UNIVERSITAT POLITÈCNICA DE VALÈNCIA

INSTITUTO DE DISEÑO Y FABRICACIÓN
DEPARTAMENTO DE INGENIERÍA DE SISTEMAS Y AUTOMÁTICA

Ph.D. Thesis

Clothoid-Based Planning and Control in Intelligent Vehicles

Author: Vicent Girbés Juan

Supervisors: Dr. Leopoldo Armesto Ángel
Dr. Josep Tornero Montserrat

Valencia, April 2016

UNIVERSITAT POLITÈCNICA DE VALÈNCIA

CLOTHOID-BASED PLANNING AND CONTROL IN INTELLIGENT VEHICLES

(AUTONOMOUS AND MANUAL-ASSISTED DRIVING)

Ph.D. in Automation, Robotics and Industrial Computer Science

Author:
Vicent Girbés Juan

Supervised by:
Dr. Leopoldo Armesto Ángel
Dr. Josep Tornero Montserrat

Instituto de Diseño y Fabricación
Departamento de Ingeniería de Sistemas y Automática
Universitat Politècnica de València

April 29, 2016

This work has been mainly supported by Generalitat Valenciana through *Programa VALi+d para investigadores en formación* (ACIF/2010/206). The author also held a predoctoral grant in the *Excellence Fellowship Program* (PAID-09-09) by Universitat Politècnica de València.

The author was recipient of two competitive grants for predoctoral stays in international research centres (BEFPI/2013/030 and BEFPI/2014/042) by Generalitat Valenciana. Support from the research team lead by Professor Alexander Lanzon in the School of Electrical and Electronic Engineering at the University of Manchester (United Kingdom) is also acknowledged, both for accepting the author in its facilities as predoctoral stay and for its valuable collaboration sharing knowledge.

This research was also funded by Generalitat Valenciana through *PROMETEO Program* and by Ministerio de Ciencia e Innovación (Spain) through the following projects: "*Sistemas de Conducción Segura de Vehículos de Transporte de Pasajeros y Materiales con Asistencia Háptica/Audiovisual e Interfaces Biomédicas (SAFETRANS)*" (DPI-2013-42302-R), "*Sistemas Avanzados de Seguridad Integral en Autobuses (SAFEBUS)*"(IPT-2011-1165-370000) and "*DIseño de un Vehículo de Inspección Submarina Autónoma para Misiones OceanográficaS (DIVISAMOS)*" (DPI-2009-14744-C03-01).

To my angel,
who encourages me when I am down,
who gives me advice when I am lost,
who makes my life meaningful.

Acknowledgements

"When you find your path, you must not be afraid.
You need to have sufficient courage to make mistakes.
Disappointment, defeat, and despair are the tools
God uses to show us the way."

Brida, Paulo Coelho.

Thanks to those who helped me follow this path, walking with me even just a few steps. Thanks to these people who in one way or another have guided me since I was born.

Thanks to my parents, Vicent and Virginia, for their unconditional support and because they always gave me the best, a good education and what is even more important, something to believe in and to fight for. Thanks to my family, especially my grandmothers and my grandfathers, although the latter are no longer with us, because without them this would not have been possible.

Thanks to my friends and brothers-in-arms in each stage of my life, I will always keep something of yours inside me. Thanks to my colleagues for what we have shared since we started the college degree, passing through the master's and the doctorate. Thanks to Ernesto, Javi, Pau, Enrique and all those who have accompanied me over the years.

Of course thanks to my thesis supervisors, Leopoldo and Josep, because they taught me to love research and because I have learned from them what a PhD really means, beyond equations, algorithms, experiments or articles.

Many thanks to those who made me fall out of step with the road, because then I learned to adapt to and to solve life's problems, or to avoid them if possible. Thanks also to all those who someday will cross my path and walk with me, it will be certainly worth it.

Last but not least, thanks to my princess, M^{a} Ángeles, because after 11 years walking together we could not be happier. Without you my life would be meaningless. I love you more than yesterday, but less than tomorrow.

Agradecimientos

Caminante, son tus huellas el camino y nada más;
caminante, no hay camino, se hace camino al andar.

Al andar se hace camino y al volver la vista atrás
se ve la senda que nunca se ha de volver a pisar.

Caminante no hay camino sino estelas en la mar.

Proverbios y Cantares,
Antonio Machado.

Gracias a todos los que me han ayudado a seguir este camino, andando conmigo aunque sólo sea unos pasos. Gracias a las personas que de un modo u otro me han guiado desde que nací.

Gracias a mis padres, Vicent y Virginia, por su apoyo incondicional y porque me han dado lo mejor, una buena educación y lo que es más importante, algo en lo que creer y por lo que luchar. Gracias a toda mi familia, en especial a mis abuelas y a mis abuelos, aunque ya no estén, porque sin ellos esto no habría sido posible.

Gracias a mis amigos y compañeros de batallas en cada una de las etapas de mi vida, siempre llevaré algo vuestro dentro de mi. Gracias a mis colegas de profesión por todo lo que hemos compartido desde que empezamos la carrera, pasando por el máster y el doctorado. Gracias a Ernesto, Javi, Pau, Enrique y a todos los que me habéis acompañado durante estos años.

Por supuesto gracias a mis directores de tesis, Leopoldo y Josep, porque me han enseñado a amar la investigación y porque de ellos he aprendido lo que significa ser doctor, más allá de ecuaciones, algoritmos, experimentos o artículos.

Mil gracias a los que han hecho que me salga del camino, porque así he aprendido a adaptarme y a solucionar los problemas de la vida, o a evitarlos si es posible. Gracias también a todos aquellos que algún día se cruzarán en mi camino y andarán conmigo, seguro que merece la pena.

Por último y no por ello menos importante, gracias a mi princesa, Mª Ángeles, porque después de 11 años caminando juntos no podíamos ser más felices. Sin ti mi vida no tendría sentido. Te quiero más que ayer, pero menos que mañana.

Abstract

Nowadays, there are many electronic products that incorporate elements and features coming from the research in the field of mobile robotics. For instance, the well-known vacuum cleaning robot *Roomba* by iRobot, which belongs to the field of service robotics, one of the most active within the sector. There are also numerous autonomous robotic systems in industrial warehouses and plants. It is the case of Autonomous Guided Vehicles (AGVs), which are able to drive completely autonomously in very structured environments.

Apart from industry and consumer electronics, within the automotive field there are some devices that give intelligence to the vehicle, derived in most cases from advances in mobile robotics. In fact, more and more often vehicles incorporate Advanced Driver Assistance Systems (ADAS), such as navigation control with automatic speed regulation, lane change and overtaking assistant, automatic parking or collision warning, among other features.

However, despite all the advances there are some problems that remain unresolved and can be improved. Collisions and rollovers stand out among the most common accidents of vehicles with manual or autonomous driving. In fact, it is almost impossible to guarantee driving without accidents in unstructured environments where vehicles share the space with other moving agents, such as other vehicles and pedestrians. That is why searching for techniques to improve safety in intelligent vehicles, either autonomous or manual-assisted driving, is still a trending topic within the robotics community.

This thesis focuses on the design of tools and techniques for planning and control of intelligent vehicles in order to improve safety and comfort. The dissertation is divided into two parts, the first one on autonomous driving and the second one on manual-assisted driving. The main link between them is the use of clothoids as mathematical formulation for both trajectory generation and collision detection. Among the problems solved the following stand out: obstacle avoidance, rollover avoidance and advanced driver assistance to avoid collisions with pedestrians.

Resumen

En la actualidad se comercializan infinidad de productos de electrónica de consumo que incorporan elementos y características procedentes de avances en el sector de la robótica móvil. Por ejemplo, el conocido robot aspirador *Roomba* de la empresa iRobot, el cual pertenece al campo de la robótica de servicio, uno de los más activos en el sector. También hay numerosos sistemas robóticos autónomos en almacenes y plantas industriales. Es el caso de los vehículos autoguiados (AGVs), capaces de conducir de forma totalmente autónoma en entornos muy estructurados.

Además de en la industria y en electrónica de consumo, dentro del campo de la automoción también existen dispositivos que dotan de cierta inteligencia al vehículo, derivados la mayoría de las veces de avances en robótica móvil. De hecho, cada vez con mayor frecuencia los vehículos incorporan sistemas avanzados de asistencia al conductor (ADAS por sus siglas en inglés), tales como control de navegación con regulación automática de velocidad, asistente de cambio de carril y adelantamiento, aparcamiento automático o aviso de colisión, entre otras prestaciones.

No obstante, pese a todos los avances siguen existiendo problemas sin resolver y que pueden mejorarse. La colisión y el vuelco destacan entre los accidentes más comunes en vehículos con conducción tanto manual como autónoma. De hecho, la dificultad de conducir en entornos desestructurados compartiendo el espacio con otros agentes móviles, tales como coches o personas, hace casi imposible garantizar la conducción sin accidentes. Es por ello que la búsqueda de técnicas para mejorar la seguridad en vehículos inteligentes, ya sean de conducción autónoma o manual asistida, es un tema que siempre está en auge en la comunidad robótica.

La presente tesis se centra en el diseño de herramientas y técnicas de planificación y control de vehículos inteligentes, para la mejora de la seguridad y el confort. La disertación se ha dividido en dos partes, la primera sobre conducción autónoma y la segunda sobre conducción manual asistida. El principal

nexo de unión es el uso de clotoides como elemento de generación de trayectorias y detección de colisiones. Entre los problemas que se resuelven destacan la evitación de obstáculos, la evitación de vuelcos y la asistencia avanzada al conductor para evitar colisiones con peatones.

Resum

En l'actualitat es comercialitzen infinitat de productes d'electrònica de consum que incorporen elements i característiques procedents d'avanços en el sector de la robòtica mòbil. Per exemple, el conegut robot aspirador *Roomba* de l'empresa iRobot, el qual pertany al camp de la robòtica de servici, un dels més actius en el sector. També hi ha nombrosos sistemes robòtics autònoms en magatzems i plantes industrials. És el cas dels vehicles autoguiats (AGVs), els quals són capaços de conduir de forma totalment autònoma en entorns molt estructurats.

A més de en la indústria i en l'electrònica de consum, dins el camp de l'automoció també existeixen dispositius que doten al vehicle de certa intel·ligència, la majoria de les vegades derivats d'avanços en robòtica mòbil. De fet, cada vegada amb més freqüència els vehicles incorporen sistemes avançats d'assistència al conductor (ADAS per les sigles en anglés), com ara control de navegació amb regulació automàtica de velocitat, assistent de canvi de carril i avançament, aparcament automàtic o avís de col·lisió, entre altres prestacions.

No obstant això, malgrat tots els avanços segueixen existint problemes sense resoldre i que poden millorar-se. La col·lisió i la bolcada destaquen entre els accidents més comuns en vehicles amb conducció tant manual com autònoma. De fet, la dificultat de conduir en entorns desestructurats compartint l'espai amb altres agents mòbils, tals com cotxes o persones, fa quasi impossible garantitzar la conducció sense accidents. És per això que la recerca de tècniques per millorar la seguretat en vehicles intel·ligents, ja siguen de conducció autònoma o manual assistida, és un tema que sempre està en auge a la comunitat robòtica.

La present tesi es centra en el disseny d'eines i tècniques de planificació i control de vehicles intel·ligents, per a la millora de la seguretat i el confort. La dissertació s'ha dividit en dues parts, la primera sobre conducció autònoma i la segona sobre conducció manual assistida. El principal nexe d'unió és l'ús de

clotoides com a element de generació de trajectòries i detecció de col·lisions. Entre els problemes que es resolen destaquen l'evitació d'obstacles, l'evitació de bolcades i l'assistència avançada al conductor per evitar col·lisions amb vianants.

Contents

List of Figures

List of Tables

Chapter 1

Introduction

1.1 Motivation

The use of motorized wheeled vehicles to transport people and materials has brought many benefits to our society. There has been an exponential evolution from the very first car to the most advanced vehicles in our days. However, despite all the advances, there are some problems that remain unresolved or can be improved. Collisions and rollovers stand out among the most common accidents of wheeled vehicles. Indeed, the difficulties of driving in unstructured environments sharing the space with other moving agents, such as cars or people, makes it almost impossible to guarantee driving without accidents. It is a fact that every year thousands of people die on the roads due to traffic accidents. Another negative indicator is the number of fatalities and injuries produced when operators are manipulating heavy vehicles in industrial environments. Some crashes are produced by machine errors, but most of them are due to human factors. In order to improve safety and reduce the number of accidents in which people are involved two different approaches can be used.

The first option is replacing humans by machines in dangerous environments with high risk of accident. This is the solution adopted in robotics, in which machines normally work autonomously, although they can also be remotely operated. In industrial warehouses, Automatic Guided Vehicles (AGV) with different guidance and navigation solutions have been widely used for transportation and goods manipulation in structured environments.

Thanks to AGVs, productivity has improved and, the most important thing, the number of accidents with humans has been reduced. However, intelligent vehicles in non-structured environments such as roads or cities are more dif-

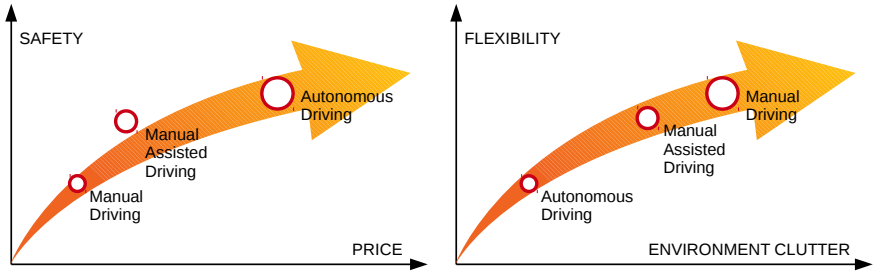

(a) (b)

Figure 1.1: Conceptual diagrams with advantages of manual-assisted driving against manual and autonomous driving.

ficult to control. A big effort has been made by researchers and engineers to develop vehicles with the ability of driving autonomously, but our society is not ready for them yet. In fact, these intelligent transportation systems would coexist with pedestrians and standard manual-driving vehicles, which is not allowed by the current legislation in Spain as well as in many countries.

On the contrary, in a second option, machines do not take the place of humans, but assist them when performing certain tasks. This is known as shared control or driving assistance in the context of intelligent vehicles and transportation systems. This field has grown exponentially in the last few decades, hand in hand with the automotive sector. Indeed, Intelligent Transportation Systems (ITS) and Advanced Driver Assistance Systems (ADAS) are two trending topics in the automotive area of knowledge.

The manual-assisted driving solution brings some advantages with respect to both manual and autonomous driving. On the one hand, as shown in Figure 1.1(a), driving assistance improves safety against manual driving without increasing much the price. At the same time, manual-assisted driving is almost as secure as autonomous driving but without being so expensive. On the second hand, regarding the relationship between flexibility and environment clutter, Figure 1.1(b) shows that the manual-assisted solution keeps the advantages of manual driving, while improving notably the flexibility against autonomous driving in high clutter scenarios.

Taking into account all these advantages and drawbacks, through this dissertation we analyse, compare and develop different solutions for both autonomous driving and manual-assisted driving. In this sense, the main goal of this thesis is to improve safety by reducing the accident ratio of vehicles transporting passengers or goods, in either urban or industrial environments.

1.2 Objectives

The aims of this thesis are described next:

- **Autonomous driving**. Analysis and comparison of path planning algorithms and control techniques used in autonomous driving.
- **Smooth path generation**. Development of a clothoid-based smooth path generation tool to plan continuous-curvature trajectories joining any pair of configurations on a Cartesian plane, with any given initial and final curvature, keeping continuity in curvature, while taking into account maximum values of curvature and its spatial derivative, the sharpness.
- **Kinematic control**. Design of a multilayer control scheme based on smooth path generation and a Look-Ahead framework, in order to solve the problem of path following with wheeled mobile robots.
- **Path/line following**. Implementation of the proposed smooth path planning algorithm to solve a vision-based line following problem.
- **Vehicle stability**. Application of the smooth control algorithm to stabilize an industrial forklift by avoiding rollovers when following a path at high speed while carrying a heavy load.
- **Obstacle avoidance**. Design and development of a new smooth obstacle avoidance algorithm to improve safety in autonomous driving.
- **Trajectory tracking**. Development of a control algorithm, based on the duality between estimation and optimal control, to close the loop in the trajectory tracking problem.
- **Manual-assisted driving**. Analysis and comparison of the existent active safety systems and Advanced Driver Assistance Systems (ADAS) in the automotive sector.
- **Driving assistance methodology**. Design of a methodology for driving assistance with haptic and audiovisual feedback to reduce the number and severity of accidents at low speed in large and heavy vehicles.
- **Applications of manual-assisted driving**. Validation and testing of the new active safety system in a driving simulator and a public bus.

1.3 Outline

The thesis has been divided in two parts: Autonomous Driving and Manual-Assisted Driving. In the first part, smooth path planning and control problems of non-holonomic wheeled robots is solved using a new clothoid-based continuous-curvature path. Whilst in the second one, a new driver assistance methodology and active safety system are developed in order to help bus drivers in manoeuvres at low speed in urban scenarios. Both approaches share a common goal, which is the development of tools and algorithms for intelligent vehicles (fully autonomous or manual-assisted vehicles), in order to improve safety and comfort, reducing collisions or rollover accidents. Moreover, as will be explained later, they both use clothoid curves as a tool to steer the vehicle, as well as collision detection and avoidance. Finally, in both cases, the vehicle speed is regulated by an algorithm in which acceleration and braking are involved, either acting directly to control the vehicle or indirectly by warning the driver.

The first part of this manuscript starts with a brief summary of the state of the art in autonomous navigation, smooth planning and control of non-holonomic vehicles. Then, a new smooth path generator based on clothoids is introduced. This path generator is able to join any arbitrary pair of postures in the plane, with curvatures distinct from zero, while taking curvature and sharpness bounds into account. This leads to safer and comfortable driving, with lower odometry errors, as will be shown. After that, how to use the proposed path generator in the context of path following is also explained, showing several applications with real and simulated vehicles, such as vision-based line following, obstacle avoidance, dynamic stability for vehicles with high risk of tip overs and optimal control.

In part two, a review of the current situation of advanced driver assistance systems is presented. There is a high number of accidents in which buses are involved, especially in urban scenarios in manoeuvres at low speed in areas of passenger loading and unloading. Therefore, there is a need to develop active safety systems in order to reduce the number and severity of accidents. Hence, a new driver assistance methodology is introduced, showing how it can be applied in a real bus. The proposed system includes pedestrian detection through smart cameras, haptic and audiovisual feedback devices to warn the driver, plus an emergency braking system to stop the vehicle in case of an imminent collision is detected. Finally, a benchmarking is carried out in a very realistic driving simulator, in order to evaluate the benefits in safety produced by the haptic feedback and emergency brake.

As explained in the last chapter, as further work we plan to analyse and compare the effect of haptics against other multi-modal inputs, such as auditive and visual feedback devices. Moreover, the clothoid-based smooth trajectory introduced in this thesis can be extended to the three-dimensional space in order to get spatial curves, which could be used to guide aerial or underwater vehicles, as discussed in the future work section of Chapter 10.

1.4 Contributions

The main highlights and research outcomes are listed in this section, such as journals and international conference publications, research awards and international stays, as well as research projects collaborations.

1.4.1 Quality Indicators of Scientific Research

It is interesting to stand out the scientific impact of the contents of this thesis, whose interest has been proven through the publication of a total of 7 peer-reviewed international conference papers and 4 articles in journals indexed in the Journal Citation Report by Thomson Reuters, plus 1 article submitted to a relevant indexed journal and 1 paper published in a non-indexed journal. Among the congress papers, most of them have been published in conferences ranked as A or B in the CORE Ranking[1].

Regarding journal articles, the scientific production of the thesis is also considerable, as one paper was published in a journal ranked in the first quartile (Q1) in the area of "Automation and Control Systems", with an impact factor 2.474. Another paper has been submitted to a Q1 journal with 2.377 of impact factor in the field of "Transportation Science and Technology". Two more papers are published or accepted in Q2 journals of the "Robotics" and "Transportation" categories with impact factors of 1.256 and 1.410, respectively. Finally, another paper was published in a "Robotics" journal classified as Q4 with 0.318 of impact factor.

[1]The CORE Conference Ranking is an ongoing activity that provides assessments of major conferences in the computing disciplines. Conference rankings are determined by a mix of indicators, including citation rates, paper submission and acceptance rates, and the visibility and research track record of the key people hosting the conference and managing its technical program. Conferences are assigned to one of the following categories: A* (flagship), A (excellent), B (good), C (meet minimum standards).

Google Scholar Metrics is another interesting source to rate publications in different areas of knowledge. Among the top 20 publications in "Engineering and Computer Science" in the category of "Robotics", there are 2 conferences and 2 journals in which at least one paper of this thesis has been published: IEEE International Conference on Robotics and Automation (1st), IEEE/RSJ International Conference on Intelligent Robots and Systems (5th), Robotics and Autonomous Systems (6th) and IEEE Transactions on Haptics (17th). In the category of "Automation and Control Theory" there are 2 publications in the top 5: IEEE Transactions on Control Systems Technology (4th) and IEEE Conference on Decision and Control (5th). In this section there is another well-known and excellent conference, the IFAC World Congress (17th). Finally, in the category of "Transportation", the IEEE Transactions on Intelligent Transportation Systems (2nd) is one of the most important journals in the field.

Google Scholar also determines individual metrics for researchers. In my case, I have an h-index of 4, which means that at least 4 of my papers have been cited 4 or more times. My contributions have been cited 53 times in total, although one of the journal papers stands out above the rest with 8 cites (only one self-cite) in less than 2 years.

1.4.2 Journal Articles

This thesis has lead to publication of several articles in very prestigious journals, which are listed below:

- V. Girbés, L. Armesto, J. Dols and J. Tornero. "Haptic Feedback to Assist Bus Drivers for Pedestrian Safety at Low Speed". IEEE Transactions on Haptics, 2016. doi: 10.1109/TOH.2016.2531686.
- V. Girbés, L. Armesto, J. Dols and J. Tornero. "An Active Safety System for Low-Speed Bus Braking Assistance". IEEE Transactions on Intelligent Transportation Systems, 2016 (submitted).
- L. Armesto, L. Arnal, J. Dols, V. Girbés and J. C. Peris. "SAFEBUS Project: Advanced Safety Systems in Buses". Revista Iberoamericana de Automática e Informática (RIAI), vol. 13, no. 1, pp. 103-114, 2016.
- L. Armesto, V. Girbés, A. Sala, M. Zima and V. Šmídl. "Duality-Based Nonlinear Quadratic Control: Application to Mobile Robot Trajectory-Following". IEEE Transactions on Control Systems Technology, vol. 23, no. 4, pp. 1494-1504, 2015.

- V. Girbés, L. Armesto and J. Tornero. "Path Following Hybrid Control for Vehicle Stability applied to Industrial Forklifts". Robotics and Autonomous Systems, vol. 62, no. 6, pp. 910-922, 2014.

- P. Muñoz-Benavent, L. Armesto, V. Girbés, J. E. Solanes, J. Dols, A. Muñoz and J. Tornero. "Advanced Driving Assistance Systems for an Electric Vehicle". International Journal of Automation and Smart Technology, vol. 2, no. 4, pp. 329-338, 2012.

1.4.3 International Conferences

During the development of the thesis a total of 7 conference papers have been published in top-ranked conferences in the field of automation, control and robotics:

- V. Girbés, L. Armesto and J. Tornero. "PISALA project. Intelligent Sensorization for Line Tracking with Artificial Vision". International Symposium on Robotics, pp. 558-563, 2010.

- V. Girbés, L. Armesto and J. Tornero. "On Generating Continuous-Curvature Paths for line Following Problem with Curvature and Sharpness Constraints". IEEE International Conference on Robotics and Automation, pp. 6156-6161, 2011.

- V. Girbés, L. Armesto and J. Tornero. "Continuous-Curvature Control of Mobile Robots with Constrained Kinematics". IFAC World Congress, pp. 3503-3508, 2011.

- V. Girbés, L. Armesto, J. Tornero and J. E. Solanes. "Smooth Kinematic Controller vs. Pure-Pursuit for Non-Holonomic Vehicles". Towards Autonomous Robotic Systems, Springer Berlin Heidelberg, 6856, pp. 277-288, 2011.

- V. Girbés, L. Armesto, J. Tornero and J. E. Solanes. "Continuous-Curvature Kinematic Control for Path Following Problems". IEEE/RSJ International Conference on Intelligent Robots and Systems, pp. 4335-4340, 2011.

- L. Armesto, V. Girbés, M. Vincze, S. Olufs and P. Muñoz-Benavent. "Mobile Robot Obstacle Avoidance Based on Quasi-Holonomic Smooth Paths". Towards Autonomous Robotic Systems, Springer Berlin Heidelberg, 7429, pp. 244-255, 2012.

- M. Zima, L. Armesto, V. Girbés, A. Sala and V. Šmídl. "Extended Rauch-Tung-Striebel Controller". IEEE Conference on Decision and Control, pp. 2900-2905, 2013.

1.4.4 Collaborations in other Research Topics

Through the years of research towards the PhD, many collaborations have been carried out with other members of our team in the fields of multi-rate control and visual-servoing.

- J. E. Solanes, P. Muñoz-Benavent, V. Girbés, L. Armesto and J. Tornero. "On improving robot image-based visual servoing based on dual-rate reference filtering control strategy". Robotica, 2015. doi: 10.1017/S0263574715000454.

- J. E. Solanes, L. Armesto, J. Tornero and V. Girbés. "Improving Image-based Visual Servoing with Reference Features Filtering". IEEE International Conference on Robotics and Automation, pp. 3083-3088, 2013.

- J.E. Solanes, V. Girbés, L. Armesto and J. Tornero. "Non-linear Dual-rate Controller for Path Following in Non-Holonomic Mobile Robots". International Symposium on Robotics, pp. 847-852, 2012.

- J. E. Solanes, J. Tornero, L. Armesto and V. Girbés. "Dual-Rate Non-Linear High Order Holds for Visual Servoing Applications". Towards Autonomous Robotic Systems, Springer Berlin Heidelberg, 7429, pp. 152-163, 2012.

- J. E. Solanes, J. Tornero, L. Armesto and V. Girbés. "Multi-rate Visual Servoing Based on Dual-Rate High Order Holds". Towards Autonomous Robotic Systems, Springer Berlin Heidelberg, 6856, pp. 195-206, 2011.

- F. A. Aguirre, A. Muñoz, P. Muñoz-Benavent, J. E. Solanes, V. Girbés, V. Colomer, L. Armesto and J. Tornero. "The complete design of the ORCA 300-AUV". World Maritime Technology Conference, 2011.

1.4.5 Research Awards and International Stays

Apart from publications in conferences and journals, the scientific productivity can be rated in other terms. For instance, it can be measured in the number and quality of international research stays, as well as research awards obtained. In this sense, during the pre-doc process, a 6-months stay was performed in a prestigious research group of the University of Manchester, collaborating with Professor Alexander Lanzon. During the stay the basis for the design of a new spatial path generator was developed. Moreover, a research work was submitted to a scientific and technological competition. Among almost 40 works, it was awarded first place for those researchers born or residents in the region Ribera del Xúquer.

- **Research Stay**: 6 months collaboration (from September 2013 to March 2014) with the research team lead by Professor Alexander Lanzon (Laboratory for Control of Uncertain Dynamical Systems) in the School of Electrical and Electronic Engineering of the University of Manchester, United Kingdom.

- **Research Award**: IX Scientific and Technical Research Award of Algemesí City for Young Researchers, received in 2014 for the work titled "Collision and rollover avoidance system for passenger and goods transportation vehicles" (prize name and work title in Catalonian: IX Premi d'Investigació Científico-Tècnic Ciutat d'Algemesí per a Joves Investigadors, "Sistema antibolcada i anticol·lisió per a vehicles de passatgers i transport de materials").

1.4.6 Research Projects Collaborations

Some research projects have influenced the results of this thesis. In some of them the author has participated directly as they are closely related with the topics of the research, while in others the collaboration was indirect through performing some specific tasks. The main projects in which the author has collaborated or is still working in are the following:

- SAFETRANS: Sistemas de Conducción Segura de Vehículos de Transporte de Pasajeros y Materiales con Asistencia Háptica/Audiovisual e Interfaces Biomédicas (DPI-2013-42302-R), Ministerio de Economía y Competitividad.

- SAFEBUS: Sistemas Avanzados de Seguridad Integral en Autobuses (IPT-2011-1165-370000), Ministerio de Economía y Competitividad.
- DIVISAMOS: DIseño de un Vehículo de Inspección Submarina Autónoma para Misiones OceanográficaS (DPI2009-14744-C03-01), Ministerio de Ciencia e Innovación.
- PROMETEO: Vehículos Eléctricos Autoguiados Propulsados por Energía Solar, Generalitat Valenciana.
- PISALA: Prototipo Industrial para el Seguimiento Automático de Líneas por Visión Artificial (PAID-06-08-3246), Universitat Politècnica de València.
- Sistema de Conducción Manual Asistida con Realimentación Háptica, Visual y Auditiva en Vehículos Industriales (Ref. 2702), Universitat Politècnica de València.
- ATECH-DGT: Actualización de Herramientas Experimentales Necesarias para la Evaluación de Conductores con Discapacidades Motoras (0100-DGT-26336), Dirección General de Tráfico - Ministerio del Interior.

Part I

Autonomous Driving

Chapter 2

State of the Art: Autonomous Navigation and Control

People used to think that robotics was something researchers and engineers did and played with in their labs. Most of them said that these machines could only be used in the industry, in very confined places, as they were dangerous and too fool to work properly in real life scenarios. However, they have been proven to be wrong and it is pretty obvious that nowadays robots are a part of our lives. They are able to help disabled people and interact with those who need rehabilitation to recover from an injury. They have learnt how to do house work, how to drive autonomously, how to speak and even how to feel or express emotions, among other applications such as rescue and surveillance (Siciliano and Khatib, 2008).

Focusing on mobile robotics, during the last decades there has been a technological explosion. The field has grown exponentially, hand in hand with advances produced in other areas of computer science. For this reason, there are more and more commercial solutions and products which incorporate robotic capabilities, specially in wheeled vehicles, with very affordable prices. For instance, the well-known vacuum cleaner *Roomba* (iRobot, 2002) or the self balancing personal transporter *Segway* (Kamen, 2001), among others.

There are many other robot platforms in the market, some of them very sophisticated, such as PR2 robot (Willow Garage, 2006) or SUMMIT XL mobile robot (Robotnik, 2002). However, probably the most advanced robotic systems with autonomous driving capabilities are those derived from DARPA Urban Challenge (Iagnemma and Buehler, 2006), in which teams had to build an autonomous vehicle capable of driving in traffic, performing complex manoeuvres such as merging, passing, parking and negotiating intersections. The

winner vehicles of the editions of 2005 and 2007 were Stanley (Stanford Racing Team. Stanford University (USA), 2005) and Boss (Tartan Racing Team. Carnegie Mellon University (USA), 2007), respectively. Another example of advanced autonomous vehicle is the Google self-driving car (Google, 2012).

From the simplest wheeled robot to the most advanced intelligent car, the basic principles that apply to drive an autonomous vehicle are the same and very simple. The robotic system needs to know where it is, where to go and what is around it. Once these aspects are clear, it is straightforward to guide the vehicle by analysing the environment, planning a collision-free trajectory as complex as necessary and follow it (Latombe, 1991; Laumond, 1998).

2.1 Clothoid-based Path Generation and Planning

The simplest approximation for trajectory generation is to use curves concatenating line segments and circles (Dubins, 1957; Jacobs and Canny, 1989; Reeds and Shepp, 1990). These trajectories are proved to be the shortest connecting two points in the Euclidean plane with bounded curvature. While Dubins curves only allow forward movement (Dubins, 1957), in RS-paths the vehicle can move both forwards and backwards (Reeds and Shepp, 1990).

Several subsequent works related to this topic (Boissonnat et al., 1991; Laumond et al., 1994; Souères and Laumond, 1994) proved the same from different approaches, i.e. these trajectories are optimal, but even though they might seem continuous in a Cartesian plane (with C^1 continuity), the resulting curvature is discontinuous (without C^2 continuity).

Therefore, the main drawback of Dubins curves and RS-paths is that a wheeled mobile robot (WMR), either in car-like or differential drive configuration, is not able to follow such trajectories. For a given speed, a curvature discontinuity implies an infinite acceleration to change the steering wheels direction instantaneously, which is physically impossible. Hence, to follow accurately a path like this, the vehicle must stop at the junction points in order to reorient the wheels and then resume the march.

In order to solve the problem of path following without stopping, a WMR needs a transition curve joining points with different values of curvature. These transition curves guarantee path generation with C^2 continuity and make trajectories feasible by non-holonomic vehicles.

2.1.1 Clothoids as Transition Curves

Several curves are used by researchers as transition curves between circular arcs and straight lines. The main approaches use the following curves: cubic

spirals (Kanayama and Hartman, 1989), clothoids (Kanayama and Miyake, 1985; Shin and Singh, 1990), splines (Delingette et al., 1991), bézier curves and other polynomial trajectories (Segovia et al., 1991; Fleury et al., 1995; Tounsi and Le Corre, 1996; Nagy and Kelly, 2001).

However, among all potential curves to generate continuous-curvature paths, clothoids stand out because of their interesting geometric properties, including a close relation between physical phenomena (normal acceleration and jerks) with the clothoid scaling parameter, which implies a potential benefit in comfort and safety. Clothoids are characterised by a constant rate of curvature with respect to the travelled path length: $\kappa = \sigma \cdot s + \kappa(0)$, with κ the curvature, s the path length and σ the sharpness, a parameter related to clothoid size. Another interesting property is that a vehicle moving with constant velocity along a clothoid segment, suffers a normal acceleration $a_N = v^2/R = v^2 \cdot \kappa$ that increases or decreases proportionally to the travelled length. Therefore, if maximum curvature and its derivative are bounded, normal acceleration too. This has a direct influence in safety and comfort when transporting people or goods. Due to the benefits of clothoids, they have been used for a long time in road and rail design (Baass, 1984; Meek and Walton, 1992; del Corral, 2001; Marchionna and Perco, 2007; McCrae and Singh, 2008), as well as in roller coasters (Weiss, 1998; Pendrill, 2005).

In addition to this, clothoids as transition curves are convenient because they provide better comfort (by increasing gradually the centrifugal), desirable arrangement for superelevation, satisfactory road appearance and side friction factor for horizontal road alignment (Krammes and Garnham, 1998; Jha et al., 2006; Kühn, 2013). The Standards usually stablish upper bounds on clothoid sharpness based on these three criteria. In addition to this, some authors, see Marchionna and Perco (2007) and the references therein, have shown the inconvenience of using too large clothoid segments since they can have a potentially negative effect on driver's curve perception and safety. As a consequence, some authors suggest lower bound on the clothoid sharpness. Moreover, mechanical constraints on orientable wheels must be also taken into account when generating a path to be followed by a car-like vehicle, as this implies a boundary on the allowed curvature.

In mobile robotics, Kanayama and Miyake (1985) introduced clothoids as transition curves between straight segments and circular arcs. In this way, it was possible to interpolate and connect two points with different curvatures, allowing non-holonomic vehicles to follow these trajectories easily. Since then, clothoids have been extensively used to solve smooth path planning pro-

blems (Iijima et al., 1981; Fraichard and Mermond, 1998; Scheuer and Xie, 1999; Yang and Sukkarieh, 2008; Labakhua et al., 2008), as well as navigation problems such as: parking (Laumond et al., 1994; Jiang et al., 1999); overtaking and lane changing (Papadimitriou and Tomizuka, 2003; Montés et al., 2007; Wilde, 2009); obstacle avoidance (Montés and Tornero, 2004; Brezak and Petrovic, 2011; Armesto et al., 2012); etc. Vision-based road identification and modelling can be also carried out using clothoids (Corridori and Zanin, 2004; Manz et al., 2010).

2.1.2 Clothoids in Continouous-Curvature Paths

In Scheuer and Fraichard (1996), Elementary paths were first introduced, a combination of two symmetrical clothoids with the same homothetic factor. The necessary condition that the coordinates of initial and final configurations must satisfy for a pair of clothoids to be symmetrical is:

$$(x_b - x_a) \cdot \sin\left(\frac{\tau_b + \tau_a}{2}\right) = (y_b - y_a) \cdot \cos\left(\frac{\tau_b + \tau_a}{2}\right) \tag{2.1}$$

being the deflection angle between both configurations $\Delta\theta = \tau_a + \tau_b$, with τ_a and τ_b the angle of each clothoid in the junction. In addition to the above equation, for the curve to be traceable, it should not exceed the physical limit imposed by the maximum rotation angle of the vehicle wheels, which is an additional restriction.

The ideas introduced in Scheuer and Fraichard (1996) were extended by the concept of Bi-Elementary paths (Scheuer and Fraichard, 1997a), combinations of two Elementary paths. The initial and final configurations of a Bi-Elementary path are not necessarily symmetric, but the loci of the intermediate configuration is restricted to a circle with specific orientations to ensure that each Elementary path contains symmetrical clothoids. The search for the correct intermediate configuration is quite simple, once coordinates $[x_i, y_i]$ are given, the goal is to find the intermediate orientation so that the following equations are satisfied:

$$(x_i - x_a) \cdot \sin\left(\frac{\tau_i + \tau_a}{2}\right) = (y_i - y_a) \cdot \cos\left(\frac{\tau_i + \tau_a}{2}\right) \tag{2.2}$$

$$(x_b - x_i) \cdot \sin\left(\frac{\tau_b + \tau_i}{2}\right) = (y_b - y_i) \cdot \cos\left(\frac{\tau_b + \tau_i}{2}\right) \tag{2.3}$$

Obviously, the solution space is significantly limited in those cases and Elementary and Bi-Elementary paths might not be appropriate to solve specific problems, specially the obstacle avoidance problem or the line following problem with bounded sharpness and curvature. In this sense, Dubins curves were the inspiration in Scheuer and Fraichard (1997b) to create the simple continuous-curvature paths (SCC-paths) and thus simplify the problem of finding optimal paths for vehicles that can go only forward, keeping curvature continuity while considering kinematic constraints by limiting the maximum allowable curvature and sharpness. That was achieved by replacing circular arcs to the called CC-turns. Each path is defined as a combination of clothoids, circular arcs and line segments. Fraichard and Scheuer (2004) extended SCC-paths, based on RS-paths, in order to create continuous-curvature paths (CC-paths) for vehicles moving both forward and backward.

In Fraichard and Ahuactzin (2001) a non-holonomic robot without curvature constraints was used to design a generic planner by combining clothoids and anti-clothoids segments. In Fraichard and Ahuactzin (2001) a generic global planner is described, with continuous-curvature path generation for car-like vehicles. It combines existing systems based on collision avoidance, introducing clothoids, lines and circles.

The authors of Brezak and Petrovic (2011) developed an algorithm for path smoothing using clothoids. They proved that paths with G^2 continuity were much easier to follow by differential drive mobile robots than paths with G^1 continuity (without clothoid segments). In Girbés et al. (2011a,b), a smooth clothoid-based continuous-curvature trajectory was proposed to solve the path following problem within the context of pure-pursuit methods.

2.1.3 Clothoid Properties

Euler or Cornu spiral, also known as Clothoid, is defined by the Fresnel integrals in $\Re^2$ as follows:

$$\mathcal{C}(\gamma) = \begin{bmatrix} C_x(\gamma) \\ C_y(\gamma) \end{bmatrix} = K \begin{bmatrix} \int_{\gamma_i}^{\gamma} \cos(\frac{\pi}{2}\xi^2) d\xi \\ \int_{\gamma_i}^{\gamma} \sin(\frac{\pi}{2}\xi^2) d\xi \end{bmatrix} \tag{2.4}$$

where K is the homothetic factor, i.e. the scale of the spiral, and $\gamma \in [\gamma_i, \gamma_f]$ comprises the integration interval between the initial and final configurations. Unfortunately, there is no closed-form solution to compute Fresnel integrals, however some interesting geometric properties of clothoids can be analytically computed.

Let $[\mathcal{C}(\gamma_i), \mathcal{C}(\gamma_f)]$ be a clothoid segment, being the so called clothoid parameter A and its factor of homothety related by $K = \sqrt{\pi}A$.

For given curvature range $\kappa \in [\kappa_i, \kappa_f]$ and sharpness σ the integration parameter is

$$\gamma = s_\sigma \kappa K / \pi \tag{2.5}$$

with $s_\sigma = \text{sign}(\sigma)$.

The Cartesian coordinates are $x = C_x(\gamma)$ and $y = s_\sigma C_y(\gamma)$, while the tangent angle τ with respect to the abscissa axis $\mathcal{X}$ of $\mathcal{C}(\gamma)$ can be defined as

$$\tau = s_\sigma \frac{\pi}{2} \gamma^2 \tag{2.6}$$

The curvature κ and length L of the clothoid $\mathcal{C}(\gamma)$ increase proportionally with γ for a given homothetic factor, being the expression for curvature

$$\kappa = s_\sigma \pi \frac{\gamma}{K} \tag{2.7}$$

and for path length with respect to the origin

$$L = K\gamma \tag{2.8}$$

It is straightforward to see that both, curvature and length are related by the clothoid parameter as

$$\kappa = \frac{L}{A^2} \tag{2.9}$$

which implies that changes on the curvature are proportional to changes on the length of the curve.

Let $\mathcal{C}(\gamma)$ be point on a clothoid curve with a constant velocity v and the sharpness $\sigma \equiv A^{-2}$, the curvature derivative of $\mathcal{C}(\gamma)$ is constant and given by

$$\dot{\kappa} = v\sigma \tag{2.10}$$

Assuming constant velocity, clothoid derivatives can be analytically computed (Schot, 1978), being he tangential and normal components of acceleration

$$a_t = 0 \tag{2.11}$$

$$a_n = v^2 \kappa \tag{2.12}$$

while the tangential and normal components of rate of acceleration (jerk) are defined by

$$j_t = -v^3 \kappa^2 \tag{2.13}$$

$$j_n = v^2 \dot{\kappa} = v^3 \sigma \tag{2.14}$$

2.1.4 Clothoid Approximation

Due to the complexity of the Fresnel integrals computation, many researchers have worked to improve their approximation. In Mielenz (1997, 2000), Fresnel integrals were approximated using a recursive method with an error less than $1 \cdot 10^{-9}$. Wang et al. (2001) approximated clothoids using B-splines and Bézier curves in the range $[0 - \frac{\pi}{2}]$, while the authors of Meek and Walton (2004) used an arc spline approximation to a clothoid.

Recently, in Montés et al. (2007, 2008), clothoids were approximated using Rational Bézier curves, providing a real-time planner using clothoid trajectories. Brezak and Petrovic (2014) introduced a new method for real-time computation of clothoid coordinates that guarantees bounded approximation error over a wide range of clothoid parameters.

Advances in this field allow very accurate approximations of clothoid segments, with very low computational cost (in the order of microseconds). So, today it is possible to use clothoids as primitive curves for smooth path planning and navigation in autonomous vehicles.

2.2 Navigation and Control

2.2.1 Path Following

During the last years, path following problems, whose goal is to develop a kinematic or dynamic control law to guide a vehicle to converge to a path, have been studied intensively because they can be applied in a wide spectrum of applications such as: parking (Laumond et al., 1994; Jiang et al., 1999; Gracia and Tornero, 2003); overtaking (Montés et al., 2007; Milanés et al., 2012); lane changing or lane lateral tracking (Papadimitriou and Tomizuka, 2003; Montés and Tornero, 2004; Wilde, 2009); vision-based line following (Manz et al., 2010; Girbés et al., 2010); vehicle navigation (Brezak and Petrovic, 2011; Villagra et al., 2012); among others. For instance, one classic approach is to generate a path that converges to a ground painted line, based on direct data from a vision system (vision-based control). Another classic application is to estimate the road profile and to provide a curvature control law that keeps the vehicle within the lane bounds.

In that sense, the well-known Pure-Pursuit method determines appropriate values of curvature and velocity that guarantee convergence to a specific path or trajectory based on current robot pose (Wallace et al., 1985; Ollero and Heredia, 1995; Ollero, 2001). It is quite common in such methods to compute

target configurations based on current vehicle's position relative to the path, which is determined by finding a point that is at least separated a given Look-Ahead distance (LA). So, they can be applied continuously by recomputing vehicle curvature and velocity based on its pose. Other approaches include linear or nonlinear control laws based on the robot model to guarantee convergence (Ollero and Amidi, 1991; Campion et al., 1996; Canudas de Wit et al., 1997),(Ollero, 2001, Chapter 9).

Indeed, most kinematic or dynamic controllers are based on current robot state and target pose, but to the best of author's knowledge, in order to solve path following problems no technique takes into account curvature continuity and constraints simultaneously. In this sense, safe and comfortable driving implies taking into account aspects such as normal and tangential accelerations and their corresponding derivatives, the jerks. These aspects become crucial in transporting people or dangerous goods. For example, this kind of solutions can be applied in transportation of materials in hostile environments in the safest possible manner. This is the case where the kind of material that is being transported must be handled with caution, because it is fragile or hazardous, or because the area where the vehicle moves contains potentially danger such as explosive area or gas pipelines. However, all these aspects have shown little attention and most of well-known path planners or kinematic controllers used in path following problems do not take continuous-curvature path generation into account and neither limit the bounds on curvature derivative or sharpness.

Furthermore, wheeled mobile robots following continuous-curvature paths might also get benefit on wheels slippage reduction and low odometry errors, since transitions are softer with constant curvature rates. A representative example in which continuous-curvature methods succeed and "standard" controllers fail is the case of a square-shaped path. In such a situation, most kinematic controllers can guarantee convergence to each square side, with null curvature in steady-time. Nevertheless, path orientation changes abruptly on square corners implying instantaneous curvature discontinuities. These aspects can affect vehicle stability in extreme cases, such as an industrial vehicle transporting heavy loads at high speeds, which could tip over easily if dynamic bounds were not properly taken into account when planning a trajectory during path following.

On the other hand, in mobile robotics some efforts have been done to improve stability and to avoid vehicle rollovers by providing the ability of load reconfiguration for robots with manipulators carrying loads. For instance,

there are some analysis about stability of vehicles carrying heavy loads, establishing dynamic models and guidelines to follow in order to avoid accidents (Korayem et al., 2004, 2010; Xinye et al., 2010). Other works use mobile manipulators so that the centre of gravity can be repositioned to avoid rollovers when travelling on slopes or on uneven terrains (Beck et al., 2009; Valls et al., 2010; Liu and Liu, 2010).

Finally, it must be remarked that applications such as path planning and kinematic control, in the context of the path following framework, differ from motion planning and obstacle avoidance methods, since they do not generally take obstacles into account, neither solve the global path planning problem[1]. Hence, to extend the solution range it is necessary to develop a tool able to generate smooth continuous-curvature references for obstacle avoidance applications.

2.2.2 Obstacle Avoidance

In robotics, motion planning and obstacle avoidance algorithms have been intensively studied in the last three decades. Classic obstacle avoidance methods determine a escape direction to avoid collisions against obstacles of the environment. This is the case of Artificial Potential Fields (APF) (Latombe, 1991), Vector Field Histogram (VFH+) (Ulrich and Borenstein, 2001), and Nearness Diagram (ND) (Minguez and Montano, 2004) to mention some of the most relevant ones. All these methods are well suited for holonomic vehicles and thus they are doomed to rely on approximations when used on non-holonomic vehicles. However, these techniques cannot guarantee that a given direction is actually followed over a long-term period, since most of these techniques assume circular motions. In addition to this, many of them only take into account obstacles of the environment when taking a direction where to move, but do not consider actual robot state (velocities). Therefore, arbitrary changes in the proposed direction cause discontinuities on either velocity or curvature profiles, which implies non-safe or non-comfortable motions. In order to ameliorate such problems some implementations may consider additional constraints, for instance including acceleration limits, which may invalidate previous computations of selecting a valid escape direction if done *a posteriori* like in Ulrich and Borenstein (2001) or Minguez and Montano (2004).

[1] For a complete reference on motion planning and obstacle avoidance methods see Chapter 35 of Siciliano and Khatib (2008).

Other methods, such as the Dynamic Window Approach (DWA) (Fox et al., 1997), provide motion commands in the configuration space. The DWA technique selects, instead of an escape direction, velocities within the feasible configuration space. For instance, the ROS implementation of DWA (Marder-Eppstein et al., 2010) for non-holonomic robots, used in this thesis, considers that obstacles are mapped into the configuration space by rolling-out arc trajectories, that is, extending the proposed velocities during a given amount of time to test the feasibility for every proposed arc. Selection within feasible velocities is normally done with the aim of a cost map (Jaillet et al., 2010) providing global convergence to the specified goal. Similarly, in Minguez and Montano (2009), authors define Arc Reachable Manifolds (ARM) by abstracting the vehicle shape, kinematics and dynamics constraints, also known as *kinodynamic* motion planning (Donald et al., 1993). More complex and rich trajectories can provide good solutions that need to be explored, instead of being limited to circular trajectories.

As already stated in Section 2.1.2, clothoids have been traditionally applied to path planning and navigation problems (Fraichard and Scheuer, 2004; Yang and Sukkarieh, 2008; Labakhua et al., 2008; Wilde, 2009), while others use other $\mathcal{C}^\infty$ curves such as splines or Bézier (Lau et al., 2009; Parlangeli et al., 2009). Continuous-curvature paths can be obtained from combinations of circular arcs, straight segments and transition curves such as clothoids. However, clothoid-based continuous-curvature paths have been studied to solve the global path generation problem rather than in the local obstacle avoidance problem.

Chapter 3

Smooth Path Generation

3.1 Introduction

In the fields of robotics and road design it is a well known fact that comfort and safety increase when generating continuous-curvature paths. Among all potential curves to generate smooth paths, clothoids have interesting geometric properties and potential benefits with respect to other curves. Therefore, in order to generate paths without discontinuities in curvature, in navigation problems many researchers have used clothoids as transitions curves between line segments and circular arcs. However, most of these approaches are focused on global path planning where initial and final curvatures are usually zero. Hence, they are not useful as local path planners because they do not take into account the current robot curvature. When an autonomous vehicle is following a reference, a big change in the target configuration, for instance to turn a corner or to avoid a collision, might imply an abrupt change in the direction of movement, which could lead to curvature discontinuities that would produce high discomfort or reduce safety by increasing the risk of wheels slippage or even lateral tip overs.

The main contribution of this chapter is to provide a method to generate continuous-curvature paths to reach a target, based on current robot configuration. In addition to this, lower and upper bounds on sharpness and curvature are simultaneously taken into account. Therefore, the type of solutions provided improve comfort and safety. Different kinds of continuous-curvature paths have been defined in order to solve problems with different complexity, all of them based on combinations of clothoids with straight segments and circular arcs. The simplest one provides continuous-curvature profiles that can-

not change from positive to negative or vice versa. More complex solutions provide a general curvature profile that can cope with changes on curvature sign, providing a more powerful tool that can be used in navigation problems.

3.2 Continuous-Curvature Path Generation

3.2.1 Problem Statement

Definition Let $\mathcal{R}$ be a non-holonomic wheeled robot moving on a 2D plane with extended state space $\mathbf{q}_R(t) = (x_R(t), y_R(t), \theta_R(t), \kappa_R(t))^T \in \Re^2 \times \mathcal{S} \times \Re$ containing the robot Cartesian positions $x_R(t)$ and $y_R(t)$, the robot orientation $\theta_R(t)$ and the curvature $\kappa_R(t)$, which is the inverse of the radius of the instantaneous centre of rotation (ICR), as shown in Figure 3.1.

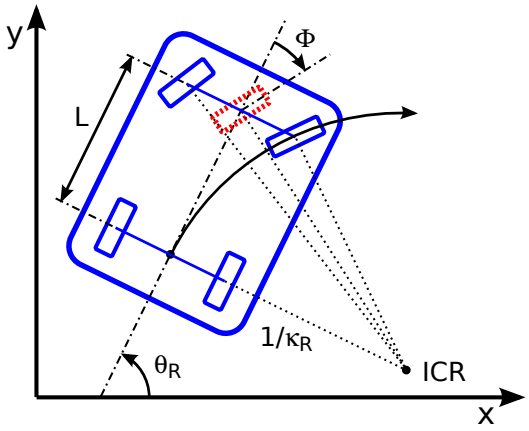

Figure 3.1: Vehicle $\mathcal{R}$ in car-like configuration with front steering wheels.

The kinematic model for $\mathcal{R}$ is:

$$\dot{\mathbf{q}}_R(t) = \begin{pmatrix} \dot{x}_R(t) \\ \dot{y}_R(t) \\ \dot{\theta}_R(t) \\ \dot{\kappa}_R(t) \end{pmatrix} = \begin{pmatrix} v_R(t)\cos\theta_R(t) \\ v_R(t)\sin\theta_R(t) \\ v_R(t)\kappa_R(t) \\ v_R(t)\sigma(t) \end{pmatrix} \tag{3.1}$$

being $v_R(t)$ the robot tangential velocity and $\sigma(t)$ the sharpness of the path.

Let's assume $\mathcal{R}$ moving with bounded curvature $\kappa_R(t) \in [-\kappa_{max}, \kappa_{max}]$ and sharpness $\sigma(t) \in [-\sigma_{max}, \sigma_{max}]$. For a vehicle with car-like configuration the steering wheels angle Φ is related to vehicle curvature κ so that $\kappa = \tan(\Phi)/L$. In this sense, curvature bounds are due to mechanical constraints of steering wheels, where the following expression stands $\kappa_{max} = \tan(\Phi_{max})/L$, being Φ_{max} the maximum steering angle and L the wheelbase or distance between front and rear axles. On the other hand, sharpness upper and lower bounds can be introduced based on the ideas suggested by Marchionna and Perco (2007) to increase safety and satisfy comfort limits, improve road appearance, etc.

The goal is to generate a continuous-curvature path $\mathcal{Q}$ connecting the current robot pose $\mathbf{q}_R(t)$ to a target $\mathbf{q}_T(t) = (x_T(t), y_T(t), \theta_T(t), \kappa_T(t))^T$, while taking curvature and sharpness upper-bounds into account. Notice that in our approach κ_R and κ_T can be any arbitrary value in the range $\pm\kappa_{max}$, more general than in Scheuer and Fraichard (1997b) or Fraichard and Scheuer (2004) that connect two configurations in the plane with null curvature only.

3.2.2 Preliminary Study

Let's study first how to solve the path generation problem to converge to a line using clothoid-based continuous-curvature paths with bounded curvature and sharpness. This preliminary study is intended to explain very quickly the necessity of a powerful path generation tool, able to solve a wide variety of problems. We are going to explain step by step how to get to the final solution adopted in this thesis.

The goal of this preliminary study is to generate a continuous-curvature path $\mathcal{Q}$ connecting an initial configuration $\mathbf{q}_A = (x_A, y_A, \theta_A, \kappa_A)^T$ (with initial null curvature $\kappa_A = 0$) to a final pose $\mathbf{q}_B = (x_B, y_B, \theta_B, \kappa_B)^T$ (with final null curvature $\kappa_B = 0$), being $x_B = d_h$ a horizontal separation, y_B a given vertical distance and θ_B the final orientation. Without loss of generality $\theta_B = \frac{\pi}{2}$ and $d_h > 0$. It can be observed that this study case is a simplification of the proposed generic path planning problem, in which initial and final curvatures are zero and the target point belongs to a straight line. Notice that $\mathcal{Q}$ may contain not only Cartesian points on the 2D plane, but also orientations (tangential directions), curvatures and sharpness or curvature derivatives along path length, which can be obtained using clothoid properties, as described in Section 2.1.3.

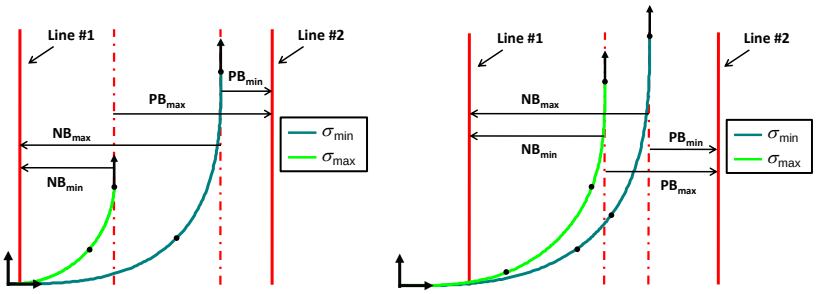

(a) Two clothoids (b) Two clothoids and circular arc

Figure 3.2: Solution space with two and four clothoids and optionally circular arcs and line segments to compensate bias and deflection angles.

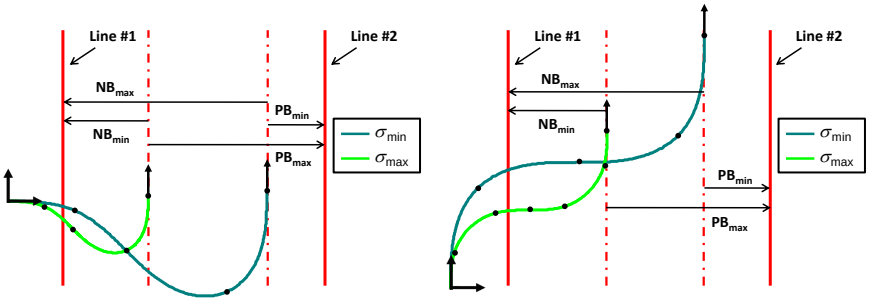

(a) Four clothoids (b) Four clothoids and circular arcs

Figure 3.3: Solution space with four clothoids and optionally circular arcs and line segments to compensate bias and deflection angles.

Figure 3.2(a) shows the type of solutions that can be obtained using two symmetric clothoids, as in Scheuer and Fraichard (1996). Depending on the angle between the line and the initial configuration (deflection angle), clothoid sharpness and curvature can be adjusted to converge parallel to the line, but in general we cannot guarantee convergence without bias and therefore an initial line segment is needed to compensate such bias. When deflection angles are too high or bounds are too tight, two symmetric clothoids cannot provide the desired final orientation and therefore a circular arc segment is needed to compensate deflection angle in addition to a line segment to compensate the bias, as shown in Figure 3.2(b). These figures illustrate the cases where the bias to be compensated with the line segments should be positive (PB) or negative (NB) for their minimum and maximum values of sharpness, σ_{min} and σ_{max} respectively.

In addition to this, there might be situations where a change on the curvature sign is mandatory, as shown in Figure 3.3(b). In that particular case, the initial and final orientations are the same, but in order to compensate the bias, we need to increase and decrease the curvature, requiring four clothoids to perform the complete path, as in Scheuer and Fraichard (1997a). Like in the previous examples, two circular arcs might be needed in case of large deflection angles or too tight bounds, each of them connecting the clothoids at their maximum curvature points. Similarly, two line segments might be required to compensate the bias, one at the beginning of the path, as shown in Figure 3.3(a), or between the intermediate clothoids, as shown in Figure 3.3(b).

3.3 Single Continuous-Curvature Paths

Definition A Single Continuous-Curvature (SCC) path is composed by a line segment, a first clothoid, an arc segment and a second clothoid, with a curvature profile like the one shown in Figure 3.4. These paths are similar to the CC-turns defined in Scheuer and Fraichard (1997b), but clothoids are not necessarily symmetric, because they can have different sharpness. As particular cases, the length of line segment and arc can be zero and so only two clothoids are necessary, known as Elementary path (Scheuer and Fraichard, 1996), which requires symmetric clothoids (with the same sharpness).

As can be inferred from Section 3.2.2, SCC paths can only cope with a limited set of solutions. For this reason, SCC paths will be only used as a basis of Double Continuous-Curvature paths described in Section 3.4. In SCC paths, the arc angle must satisfy $\theta_\Omega = \theta_B - \theta_A - \theta_{C1} - \theta_{C2}$, being $\theta_{C1} \in]0, \kappa_{max}^2 \sigma_{C1}^{-1}/2]$ the tangent angle of the first clothoid, with sharpness σ_{C1} and maximum curvature κ_{max}, and $\theta_{C2} \in]0, \kappa_{max}^2 \sigma_{C2}^{-1}/2]$ the tangent angle of the second clothoid, with sharpness σ_{C2}, where both tangent angles must satisfy $\theta_{C1} + \theta_{C2} < \delta$. Therefore, the maximum deflection angle that the clothoid-pair can achieve is $\delta_{max} \equiv \kappa_{max}^2(\sigma_{C1}^{-1} + \sigma_{C2}^{-1})/2$, which in case of symmetric clothoids with common sharpness $\sigma_C \equiv \sigma_{C1} \equiv \sigma_{C2}$ can be simplified to $\delta_{max} \equiv \kappa_{max}^2 \sigma_C^{-1}$.

Remark SCC paths have a singular situation when initial and final configurations are aligned and performing a loop is not allowed. In such cases it is quite obvious that with a curvature profile like that, i.e. which cannot change the curvature sign, it is not possible to perform an "s" shape to converge to the target pose.

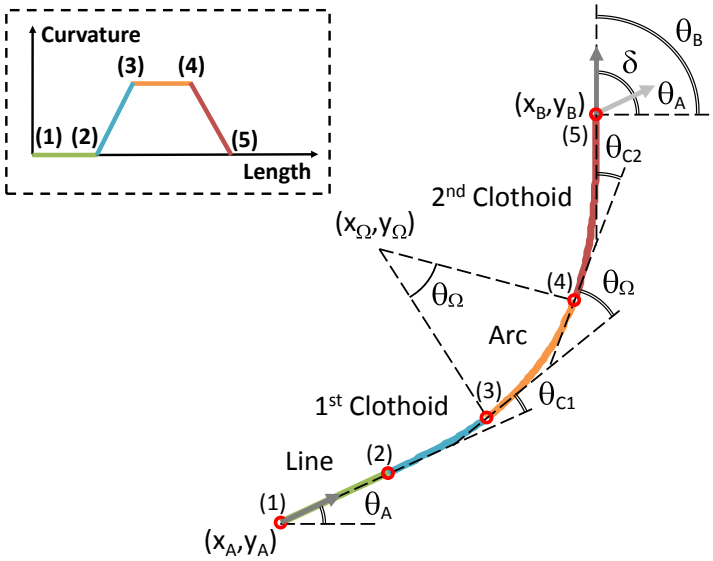

Figure 3.4: Representative example of SCC path and its curvature profile.

3.4 Double Continuous-Curvature Paths

Double Continuous-Curvature paths are inspired by the work carried out in Scheuer and Fraichard (1997b), which used two CC-turns connected with a straight segment to develop a path planner joining two arbitrary configurations with initial and final null curvatures. An extension to allow forward and backward driving was carried out in Fraichard and Scheuer (2004). However, it is interesting to remark that the formulation provided in this section is a generalization of other continuous-curvature paths based on clothoids or circles given in the literature for forward movement only. Our approach allows the generation of a wider spectrum of paths using clothoids with different sharpness that can be indistinctly combined. This is one of the main differences with respect to the continuous-curvature paths introduced in Scheuer and Fraichard (1997b).

3.4.1 Standard Double Continuous-Curvature Path

Definition A *standard* Double Continuous-Curvature (DCC) path is composed by two SCC paths plus an additional straight line segment to provide a set of general solutions guaranteeing continuity in curvature and bounded val-

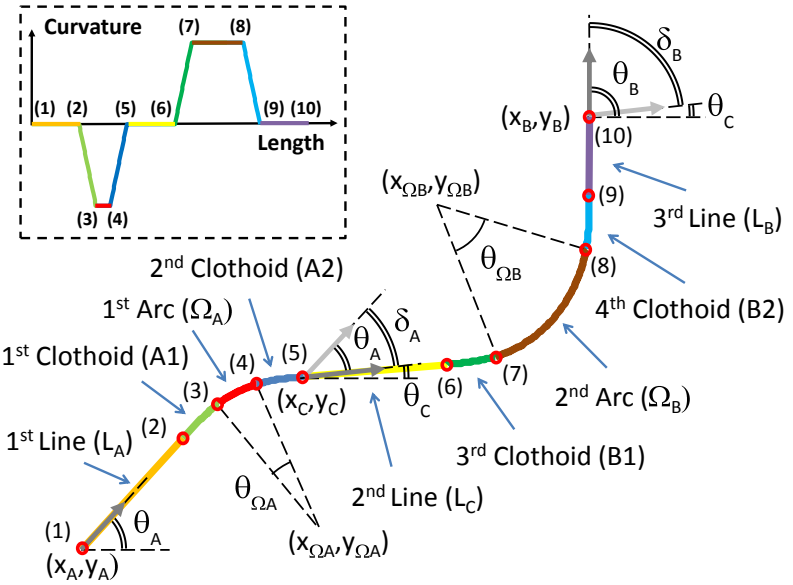

Figure 3.5: Standard DCC path definition and its curvature profile.

ues of curvature and sharpness. Therefore, DCC paths (Girbés et al., 2011a) are based on the following sequence: line-clothoid-arc-clothoid-line-clothoid-arc-clothoid-line. The first SCC path (noted with subscript A) starts at initial configuration $\mathbf{q}_A{=}(x_A, y_A, \theta_A, \kappa_A)^T$, with $\kappa_A{=}0$; while the second SCC path (noted with subscript B) finish at posture $\mathbf{q}_B{=}(x_B, y_B, \theta_B, \kappa_B)^T$, with $\kappa_B{=}0$. The pose joining both SCC paths is $\mathbf{q}_C{=}(x_C, y_C, \theta_C, \kappa_C)^T$, with $\kappa_C{=}0$ at the beginning of the common straight line segment.

Figure 3.5 shows an example of a DCC path together with its curvature profile. It can be appreciated that there are four clothoids named as $\mathbf{A1}$, $\mathbf{A2}$, $\mathbf{B1}$ and $\mathbf{B2}$ with lengths l_{A1}, l_{A2}, l_{B1} and l_{B2}, respectively. There are also two circular arcs $\mathbf{\Omega_A}$ and $\mathbf{\Omega_B}$ with lengths l_{Ω_A} and l_{Ω_B}, and three straight segments $\mathbf{L_A}$, $\mathbf{L_B}$ and $\mathbf{L_C}$ with lengths l_A, l_B and l_C. Particular solutions can be derived using only four clothoids, obtaining similar solutions to Bi-Elementary paths in Scheuer and Fraichard (1997a).

In addition, the proposed method is not forcing the same sharpness for the four clothoids namely $\sigma_{A1}, \sigma_{A2}, \sigma_{B1}, \sigma_{B2} \in [-\sigma_{max}, -\sigma_{min}] \cup [\sigma_{min}, \sigma_{max}]$, opening a wider spectrum of possibilities. Curvature signs of each SCC path are $s_A = \text{sign}(\sigma_{A1}) = -\text{sign}(\sigma_{A2})$ and $s_B = \text{sign}(\sigma_{B1}) = -\text{sign}(\sigma_{B2})$, with opposite signs for each clothoid belonging to each SCC path.

Let's assume, for the four clothoids, absolute sharpness values given by:

$$|\sigma_{A1}| = \alpha_{A1} \cdot \sigma_{max} + (1 - \alpha_{A1}) \cdot \sigma_{min} \tag{3.2}$$
$$|\sigma_{A2}| = \alpha_{A2} \cdot \sigma_{max} + (1 - \alpha_{A2}) \cdot \sigma_{min} \tag{3.3}$$
$$|\sigma_{B1}| = \alpha_{B1} \cdot \sigma_{max} + (1 - \alpha_{B1}) \cdot \sigma_{min} \tag{3.4}$$
$$|\sigma_{B2}| = \alpha_{B2} \cdot \sigma_{max} + (1 - \alpha_{B2}) \cdot \sigma_{min} \tag{3.5}$$

being $\alpha_{A1} \in [0,1]$, $\alpha_{A2} \in [0,1]$, $\alpha_{B1} \in [0,1]$ and $\alpha_{B2} \in [0,1]$ design parameters to be determined. Note that clothoids do not need to be symmetric, but for simplicity sharpness may be set to σ_{max} to get minimum path length solutions.

Remark Relaxation of the lower bound of sharpness $\sigma_{min} = 0$ is very common and in most cases feasible even when generating paths for a mobile robot, although here it has been included to provide a more general formulation.

Let $\mathcal{Q} \in \Re^2 \times \mathcal{S} \times \Re$ be a *standard* DCC path defined by a set of parameters:

$$\mathcal{Q}(\lambda, \theta_C, l_A, l_{A1}, l_{\Omega_A}, l_{A2}, l_C, l_{B1}, l_{\Omega_B}, l_{B2}, l_B, \sigma_{A1}, \sigma_{A2}, \sigma_{B1}, \sigma_{B2}, s_A, s_B) \tag{3.6}$$

where $\lambda \in [0, \lambda_B]$ is the free variable describing all possible configurations from $\mathbf{q}_A = \mathcal{Q}(0, \ldots)$ to $\mathbf{q}_B = \mathcal{Q}(\lambda_B, \ldots) + \mathbf{q}_A$, with $\lambda_B = l_A + l_{A1} + l_{\Omega_A} + l_{A2} + l_C + l_{B1} + l_{\Omega_B} + l_{B2} + l_B$.

The DCC path end configuration $\mathbf{q}_B$ can be computed as

$$\begin{aligned} \mathbf{q}_B = \mathbf{q}_A \oplus \Delta\mathbf{q}_{l_A} \oplus \Delta\mathbf{q}_{A1} \oplus \Delta\mathbf{q}_{\Omega_A} \oplus \Delta\mathbf{q}_{A2} \\ \oplus \Delta\mathbf{q}_{l_C} \oplus \Delta\mathbf{q}_{B1} \oplus \Delta q_{\Omega_B} \oplus \Delta\mathbf{q}_{B2} \oplus \Delta\mathbf{q}_{l_B} \end{aligned} \tag{3.7}$$

where

$$\Delta\mathbf{q}_{l_A} = \begin{pmatrix} l_A \cos\theta_A \\ l_A \sin\theta_A \\ 0 \\ 0 \end{pmatrix} \tag{3.8}$$

$$\Delta\mathbf{q}_{A1} = \begin{pmatrix} \mathbf{R}(\theta_A) \left[\begin{smallmatrix} x_{A1} \\ s_A \cdot y_{A1} \end{smallmatrix} \right] \\ s_A \theta_{A1} \\ s_A |\kappa_A| \end{pmatrix} \tag{3.9}$$

$$\Delta\mathbf{q}_{\Omega_A} = \begin{pmatrix} \kappa_A^{-1}\mathbf{R}(\theta_A + s_A\theta_{A1}) \begin{bmatrix} \sin\theta_{\Omega_A} \\ s_A(1-\cos\theta_{\Omega_A}) \end{bmatrix} \\ s_A\theta_{\Omega_A} \\ 0 \end{pmatrix} \tag{3.10}$$

$$\Delta\mathbf{q}_{A2} = \begin{pmatrix} \mathbf{R}(\theta_A + s_A(\theta_{A1} + \theta_{\Omega_A})) \begin{bmatrix} x_{A2} \\ s_A \cdot y_{A2} \end{bmatrix} \\ s_A\theta_{A2} \\ -s_A|\kappa_A| \end{pmatrix} \tag{3.11}$$

$$\Delta\mathbf{q}_{l_C} = \begin{pmatrix} l_C\cos\theta_C \\ l_C\sin\theta_C \\ 0 \\ 0 \end{pmatrix} \tag{3.12}$$

$$\Delta\mathbf{q}_{B1} = \begin{pmatrix} \mathbf{R}(\theta_C) \begin{bmatrix} x_{B1} \\ s_B \cdot y_{B1} \end{bmatrix} \\ s_B\theta_{B1} \\ s_B|\kappa_B| \end{pmatrix} \tag{3.13}$$

$$\Delta\mathbf{q}_{\Omega_B} = \begin{pmatrix} \kappa_B^{-1}\mathbf{R}(\theta_C + s_B\theta_{B1}) \begin{bmatrix} \sin\theta_{\Omega_B} \\ s_B(1-\cos\theta_{\Omega_B}) \end{bmatrix} \\ s_B\theta_{\Omega_B} \\ 0 \end{pmatrix} \tag{3.14}$$

$$\Delta\mathbf{q}_{B2} = \begin{pmatrix} \mathbf{R}(\theta_C + s_B(\theta_{B1} + \theta_{\Omega_B})) \begin{bmatrix} x_{B2} \\ s_B \cdot y_{B2} \end{bmatrix} \\ s_B\theta_{B2} \\ -s_B|\kappa_B| \end{pmatrix} \tag{3.15}$$

$$\Delta\mathbf{q}_{l_B} = \begin{pmatrix} l_B\cos\theta_B \\ l_B\sin\theta_B \\ 0 \\ 0 \end{pmatrix} \tag{3.16}$$

being $\mathbf{R}(\bullet)$ a rotation matrix. Where $\theta_{\Omega_A} = \delta_A - \theta_{A1} - \theta_{A2}$, $\theta_{A1} = \frac{\kappa_A^2}{2|\sigma_{A1}|}$, $\theta_{A2} = \frac{\kappa_A^2}{2|\sigma_{A2}|}$, with $s_A = \text{sign}(\theta_C - \theta_A)$ and $\delta_A = |\theta_C - \theta_A|$ the deflection angle between configurations $\angle(\mathbf{q}_A, \mathbf{q}_C)$. Similarly, $\theta_{\Omega_B} = \delta_B - \theta_{B1} - \theta_{B2}$, $\theta_{B1} = \frac{\kappa_B^2}{2|\sigma_{B1}|}$ and $\theta_{B2} = \frac{\kappa_B^2}{2|\sigma_{B2}|}$, with $s_B = \text{sign}(\theta_B - \theta_C)$ and $\delta_B = |\theta_B - \theta_C|$ the deflection angle between configurations $\angle(\mathbf{q}_C, \mathbf{q}_B)$.

Curvatures of arc segments are chosen upon the following criteria:

$$\kappa_A = \min(\sqrt{|\sigma_{A1}|\delta_A}, \sqrt{|\sigma_{A2}|\delta_A}, \kappa_{max}) \tag{3.17}$$

$$\kappa_B = \min(\sqrt{|\sigma_{B1}|\delta_B}, \sqrt{|\sigma_{B2}|\delta_B}, \kappa_{max}) \tag{3.18}$$

Thus, depending on the selected clothoid sharpness σ and deflection angle δ, a family of curvature curves is obtained, as depicted in Figure 3.6.

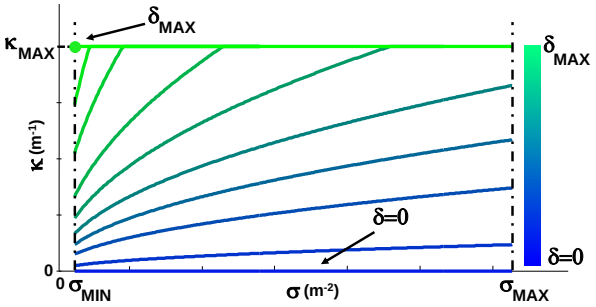

Figure 3.6: Curve selection of curvature κ for different values of σ and δ.

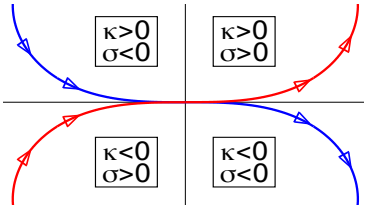

Figure 3.7: Clothoid paths defined in four quadrants.

Cartesian coordinates of clothoid segments x_{A1}, y_{A1}, x_{A2}, y_{A2}, x_{B1}, y_{B1}, x_{B2} and y_{B2} are computed for their corresponding curvature κ_A or κ_B (see Section 2.1.3). For instance, $\mathbf{q}_{A1} = (x_{A1}, y_{A1}, \theta_{A1}, \kappa_{A1})^T$ is the final point of the first clothoid given by Fresnel integrals:

$$x_{A1} = \pm\sqrt{\frac{\pi}{|\sigma_{A1}|}} \int_0^{\gamma_{A1}} \cos(\frac{\pi}{2}\xi^2)d\xi \tag{3.19}$$

$$y_{A1} = \pm\sqrt{\frac{\pi}{|\sigma_{A1}|}} \int_0^{\gamma_{A1}} \sin(\frac{\pi}{2}\xi^2)d\xi \tag{3.20}$$

$$\theta_{A1} = \pm\frac{\kappa_{A1}^2}{2|\sigma_{A1}|} \tag{3.21}$$

with $\gamma_{A1} = \sqrt{\frac{\kappa_{A1}^2}{\pi|\sigma_{A1}|}}$. Equations (3.19), (3.20) and (3.21) indicate that any clothoid combination is possible (on each quadrant) and its sign depends on the conditions needed, i.e. positive/negative curvature and positive/negative curvature rate, as shown in Figure 3.7. The configurations for the second, third and fourth clothoids ($\mathbf{q}_{A2}$, $\mathbf{q}_{B1}$ and $\mathbf{q}_{B2}$, respectively) can be similarly defined.

Since σ_{A1}, σ_{A2}, σ_{B1} and σ_{B2} are design parameters, whilst s_A and s_B depend on θ_C, it is easy to see that, in order to satisfy curvature continuity and first derivative constraints, most of the parameters of a DCC path are dependent and therefore $\mathcal{Q}$ can be re-defined as:

$$\mathcal{Q}(\lambda, \theta_C, l_A, l_B, l_C) \tag{3.22}$$

where

$$l_{A1} = |\kappa_A \sigma_{A1}^{-1}|,\ l_{A2} = |\kappa_A \sigma_{A2}^{-1}|,\ l_{\Omega_A} = |\theta_{\Omega_A} \kappa_A^{-1}| \tag{3.23}$$

$$l_{B1} = |\kappa_B \sigma_{B1}^{-1}|,\ l_{B2} = |\kappa_B \sigma_{B2}^{-1}|,\ l_{\Omega_B} = |\theta_{\Omega_B} \kappa_B^{-1}| \tag{3.24}$$

It is straightforward that the selected values for θ_{A1}, θ_{Ω_A}, θ_{A2}, θ_{B1}, θ_{Ω_B} and θ_{B2} guarantee appropriate changes on the orientation and curvature. Indeed, our approach selects the minimum admissible arc angle, so if $\delta_A > \delta_{A,min} \equiv \min(|\frac{\kappa_{max}^2}{\sigma_{A1}}|, |\frac{\kappa_{max}^2}{\sigma_{A2}}|)$ or $\delta_B > \delta_{B,min} \equiv \min(|\frac{\kappa_{max}^2}{\sigma_{B1}}|, |\frac{\kappa_{max}^2}{\sigma_2}|)$, then the corresponding arc segments will cover the remaining deflection angle. Otherwise, the DCC path will not include circular arcs and the clothoid-pairs segments will compensate such angles with appropriate curvature values at a maximum sharpness. In Section 3.4.3, we discuss that this is one of the most remarkable aspects of the proposed method compared to simple continuous-curvature paths introduced in Scheuer and Fraichard (1997b). However, the main drawback is that when this situation happens there is no analytic solution, which makes it necessary to solve an optimization problem, where the aim is to find $\mathcal{Q}^*$ such that:

$$\mathcal{Q}^* = \arg\min_{\mathcal{Q}}\ |l_A|+|l_{A1}|+|l_{\Omega_A}|+|l_{A2}|+|l_C|+|l_{B1}|+|l_{\Omega_B}|+|l_{B2}|+|l_B| \tag{3.25}$$

with

$$\mathcal{Q}(\lambda, \theta_C, l_A, l_B, l_C) = \left\{ \begin{matrix} \theta_C \in \mathcal{S}, \\ l_A, l_B, l_C \in \Re \end{matrix} \middle| \ \exists \lambda_B,\ \mathbf{q}_B = \mathcal{Q}(\lambda_B, \theta_C, l_A, l_B, l_C) + \mathbf{q}_A \right\} \tag{3.26}$$

which can be solved using, for instance, Simplex (Nelder-Mead) as optimization method, with the initialization of the starting value for θ_C as described below.

Cartesian elements of $\mathbf{q}_B$ can be written as:

$$\mathcal{P}_x + \mathcal{X}_1 \cos\theta_C + \mathcal{X}_2 \sin\theta_C = l_A \cos\theta_A + l_B \cos\theta_B + l_C \cos\theta_C \tag{3.27}$$

$$\mathcal{P}_y - \mathcal{X}_2 \cos\theta_C + \mathcal{X}_1 \sin\theta_C = l_A \sin\theta_A + l_B \sin\theta_B + l_C \sin\theta_C \tag{3.28}$$

where

$$\mathcal{P}_x = x_B - x_A - x_{A1}\cos\theta_A - x_{B2}\cos\theta_B + s_A y_{A1}\sin\theta_A - s_B y_{B2}\sin\theta_B + \\ + \kappa_A^{-1}\sin(\theta_A+\theta_{A1}) - s_B\kappa_B^{-1}\sin(\theta_B - s_B\theta_{B2}) \tag{3.29}$$

$$\mathcal{P}_y = y_B - y_A - s_A y_{A1}\cos\theta_A + s_B y_{B2}\cos\theta_B - x_{A1}\sin\theta_A - x_{B2}\sin\theta_A - \\ - s_A\kappa_A^{-1}\cos(\theta_A+\theta_{A1}) + s_B\kappa_B^{-1}\cos(\theta_B - s_B\theta_{B2}) \tag{3.30}$$

$$\mathcal{X}_1 = -x_{B1} - x_{A2} + \kappa_A^{-1}\sin\theta_{A2}\left(\cos^2\theta_A + s_A\sin^2\theta_A\right) + \kappa_B^{-1}\sin\theta_{B1} \tag{3.31}$$

$$\mathcal{X}_2 = s_B y_{B1} - s_A y_{A2} - \kappa_A^{-1}\cos\theta_{A2}\left(s_A\cos^2\theta_A + \sin^2\theta_A\right) + \kappa_B^{-1} s_B\cos\theta_{B1} \tag{3.32}$$

There are four unknowns and just two equations in (3.27) and (3.28), thus multiple solutions are possible. Since DCC paths are intended to be applied within navigation problems, we force $l_A = 0$ because convergence in path following problems cannot be guaranteed otherwise. Therefore, the problem is reduced to determine l_B, l_C and θ_C. In that case (3.27) and (3.28) can be rewritten as:

$$\mathcal{P}_x + \sqrt{(\mathcal{X}_1 - l_C)^2 + \mathcal{X}_2^2}\cos(\theta_C - \alpha) = l_B\cos\theta_B \tag{3.33}$$

$$\mathcal{P}_y - \sqrt{(\mathcal{X}_1 - l_C)^2 + \mathcal{X}_2^2}\sin(\theta_C - \alpha) = l_B\sin\theta_B \tag{3.34}$$

with $\tan\alpha = \frac{\mathcal{X}_2}{\mathcal{X}_1 - l_C}$. Equations (3.33) and (3.34) can be merged to provide a family of solutions for θ_C depending on the value l_C:

$$\theta_C = \arcsin\left(\frac{\mathcal{P}_x\sin\theta_B - \mathcal{P}_y\cos\theta_B}{\sqrt{(\mathcal{X}_1 - l_C)^2 + \mathcal{X}_2^2}}\right) + \arctan\left(\frac{\mathcal{X}_2}{\mathcal{X}_1 - l_C}\right) - \theta_B \tag{3.35}$$

To provide the shortest path l_C must satisfy the following conditions:

$$l_C = \begin{cases} \max\left(0, \mathcal{X}_1 + \sqrt{(\mathcal{P}_x\sin\theta_B - \mathcal{P}_y\cos\theta_B)^2 - \mathcal{X}_2^2}\right) & \text{if } |\mathcal{P}_x\sin\theta_B - \mathcal{P}_y\cos\theta_B| < |\mathcal{X}_2| \\ 0 & \text{otherwise} \end{cases} \tag{3.36}$$

The angle θ_C is the analytic solution for the optimization problem stated in Equations (3.25) and (3.26) when the solution implies arc segments. In any

case, this value is used as starting point of the optimization procedure because it provides deflection angles which are "close" to the optimal ones.

For a given θ_C, lengths of line segments appear as a linear combination on the Cartesian elements of Equation (3.26):

$$\begin{pmatrix} x_B \\ y_B \end{pmatrix} = \begin{pmatrix} \mathcal{P}'_x \\ \mathcal{P}'_y \end{pmatrix} + \begin{pmatrix} \cos\theta_A & \cos\theta_B & \cos\theta_C \\ \sin\theta_A & \sin\theta_B & \sin\theta_C \end{pmatrix} \cdot \begin{pmatrix} l_A \\ l_B \\ l_C \end{pmatrix} + \begin{pmatrix} x_A \\ y_A \end{pmatrix} \tag{3.37}$$

with $l_A \geq 0$ and $l_C \geq 0$, where $\mathcal{P}'_x$ and $\mathcal{P}'_y$ represent the Cartesian coordinates of the remainder of terms that do not depend on line segment lengths and are known for a given θ_C.

In order to solve (3.37), one can find many feasible solutions. However, the proposed heuristic criterion is to consider $l_A = 0$, since it is not needed in path following problems but formally introduced for path generation problems. Therefore, computation of l_C and l_B is straightforward once θ_C is given:

$$\begin{pmatrix} l_B \\ l_C \end{pmatrix} = \begin{pmatrix} \cos\theta_B & \cos\theta_C \\ \sin\theta_B & \sin\theta_C \end{pmatrix}^{-1} \cdot \begin{pmatrix} x_B - x_A - \mathcal{P}'_x \\ y_B - y_A - \mathcal{P}'_y \end{pmatrix} \tag{3.38}$$

3.4.2 DCC Path with Nonzero Curvature Profile

A *standard* DCC path is defined for $\kappa_A = 0$ and $\kappa_B = 0$, however in a navigation problem there might be situations in which robot and target curvatures are $\kappa_R \neq 0$ and $\kappa_T \neq 0$. In this sense, to satisfy curvature continuity in coherence with the actual robot and target curvatures, it is necessary to extend the scope of the problem to consider $\mathbf{q}_R \neq \mathbf{q}_A$ and $\mathbf{q}_T \neq \mathbf{q}_B$. For simplicity, from now on let's focus on the case where $\kappa_T = 0$, although configurations with non null curvatures can also be targeted with a similar procedure. Without loss of generality, let's assume that the robot is located within clothoid segment $\mathbf{A1}$ and therefore the start configuration of a DCC path is *a priori* unknown.

In that sense, the robot configuration can be expressed as:

$$\mathbf{q}_R = \mathbf{q}_A \oplus \Delta\mathbf{q}_{A1,R} \tag{3.39}$$

with

$$\Delta\mathbf{q}_{A1,R} = \begin{pmatrix} \mathbf{R}(\theta_A) \begin{bmatrix} x_{A1,R} \\ s_A \cdot y_{A1,R} \end{bmatrix} \\ s_A \cdot \theta_{A1,R} \\ \kappa_{A1,R} \end{pmatrix} \tag{3.40}$$

where all possible cases of $x_{A1,R}$, $y_{A1,R}$ and $\theta_{A1,R}$ can be computed from Fresnel integrals as in Section 2.1.3.

Henceforth, we will use notation $\Delta\mathbf{q}_{A1,R}$ to refer to the clothoid segment at the robot configuration, while $\Delta\mathbf{q}_{A1}$ to refer to the complete clothoid segment. Figures 3.8(a), 3.8(b) and 3.8(c) depict a case in which robot and target signs of curvature ($s_R = \text{sign}(\kappa_R)$ and $s_T = \text{sign}(\kappa_T)$) are the same as the signs of the generated *standard* DCC path ($s_R = s_A$ and $s_T = s_B$). While Figures 3.9(a), 3.9(b) and 3.9(c) show a situation in which they are different ($s_R \neq s_A$ and $s_T \neq s_B$). These examples are for a given pair of configurations $\mathbf{q}_R$ and $\mathbf{q}_T$, which give $s_A > 0$ and $s_B < 0$, although other combinations are possible and can be handled using the same policy. By marginalizing out $\mathbf{q}_A$ from Equation (3.39) we can obtain the appropriate starting point of the DCC path $\mathbf{q}_A = \mathbf{q}_R \ominus \Delta\mathbf{q}_{A1,R}$.

3.4.3 Comparing DCC with SCC and Dubins Paths

The proposed DCC paths might be identical to simple continuous-curvature paths in Scheuer and Fraichard (1997b), here denoted as SCC-paths, if the solution implies arc segments with large deflection angles. However, DCC paths are better suited for the path following problem as depicted in the blue line of Figure 3.10(a), where DCC paths can produce solutions where the $l_B < 0$. We name this case as *relaxed* solution, because the final negative length segment is never applied (the path is recomputed on next update as described in Chapter 4). It can be shown that this kind of converge-to-line solutions provide less oscillatory behaviour in path following problems than the solutions proposed by SCC-paths (see green dash-dotted line of Figure 3.10(a)) or even Dubins paths (Dubins, 1957), which applying maximum curvature are still not able to reach the goal without making a big turn (red dashed line in Figure 3.10(a)).

Another advantage of DCC paths with respect to SCC-paths is that the proposed solutions can provide even shorter paths for cases with small deflection angles. That is, cases where the optimization procedure of DCC provides a solution with the maximum admissible sharpness, while the solution provided by SCC-paths adapts the sharpness so that deflection angle is satisfied. This case is depicted in Figure 3.10(b), where it can be appreciated that the DCC method finds a solution with the maximum sharpness and because of that the overall path length of DCC is shorter.

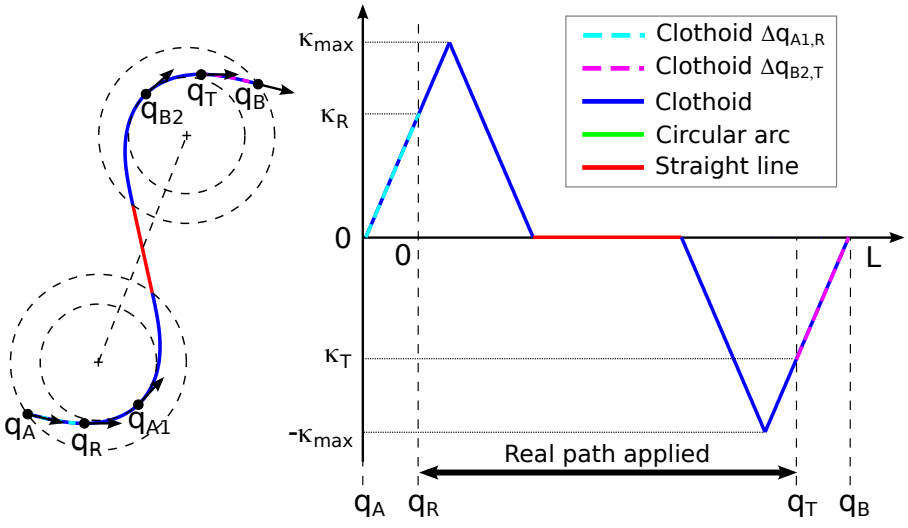

(a)

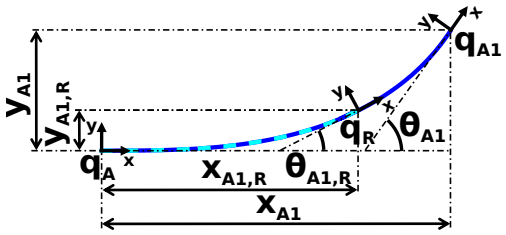

(b)

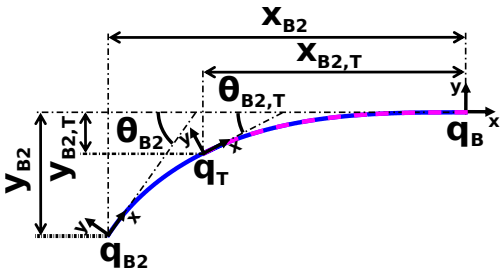

(c)

Figure 3.8: DCC paths and curvature profiles (a) for a given robot and target configuration when $s_R = s_A$. (b) Robot configuration $\mathbf{q}_R$ along clothoid $\mathbf{A1}$ and (c) Target configuration $\mathbf{q}_T$ along clothoid $\mathbf{B2}$, for DCC in (a).

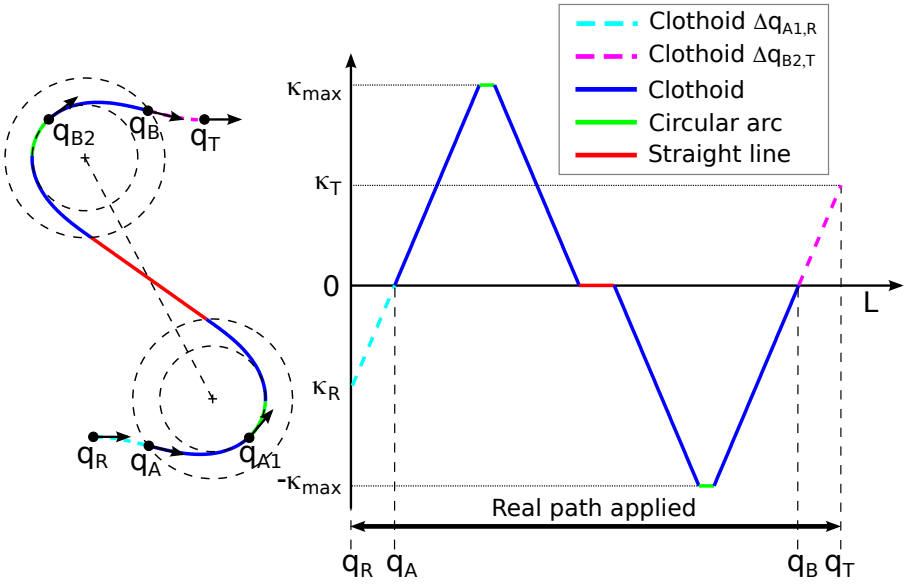

(a)

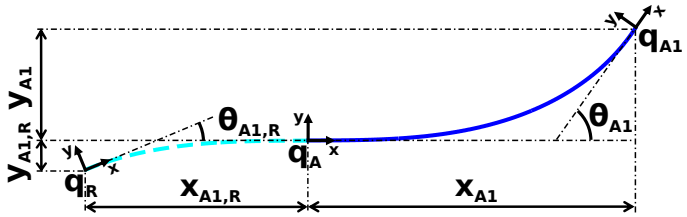

(b)

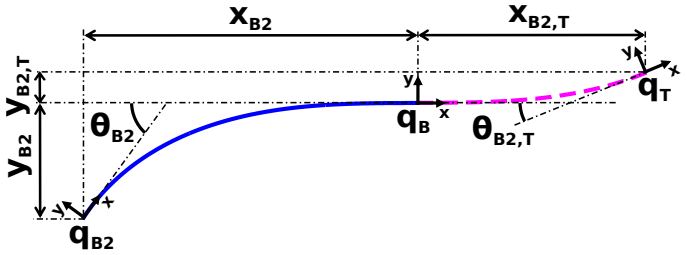

(c)

Figure 3.9: DCC paths and curvature profiles (a) for a given robot and target configuration when $s_R \neq s_A$. (b) Robot configuration $\mathbf{q}_R$ along clothoid $\mathbf{A1}$ and (c) Target configuration $\mathbf{q}_T$ along clothoid $\mathbf{B2}$, for DCC in (a).

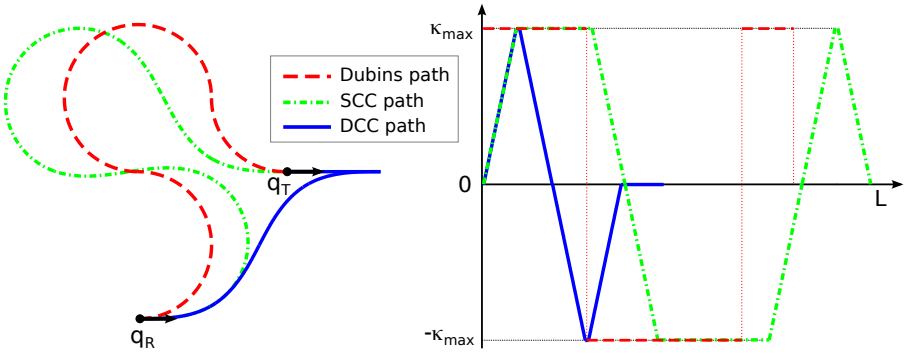

(a) Relaxation situation

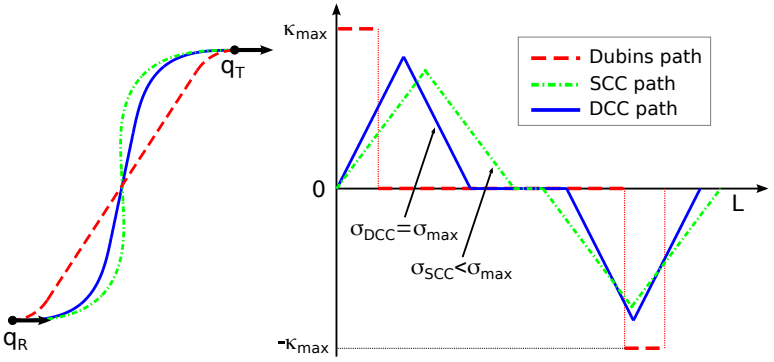

(b) Path length comparison

Figure 3.10: Comparison of Dubins (red dashed), SCC (green dash-dotted) and DCC (blue) paths.

One important drawback of SCC-paths (Scheuer and Fraichard, 1997b) in the context of path following problems is that they cannot guarantee smooth curvature changes if $\kappa_R \neq 0$. The problem arises from the fact that the sharpness that will be used in their clothoid segments cannot be known *a priori*, so they are also not able to compute the starting point of the clothoid unless $\kappa_R = 0$. For instance, if we apply the method described in Section 3.4.2, the SCC method would fail to pass even through the robot configuration $\mathbf{q}_R$ or even to have the appropriate curvature for path length $L = 0$, as shown in Figure 3.11.

Regarding the computational cost, SCC and DCC paths are equivalent when optimization procedure is not necessary, being the average time in such cases around 20μs in our implementation of both methods. However, when an optimization is performed, DCC processing time depends on the number

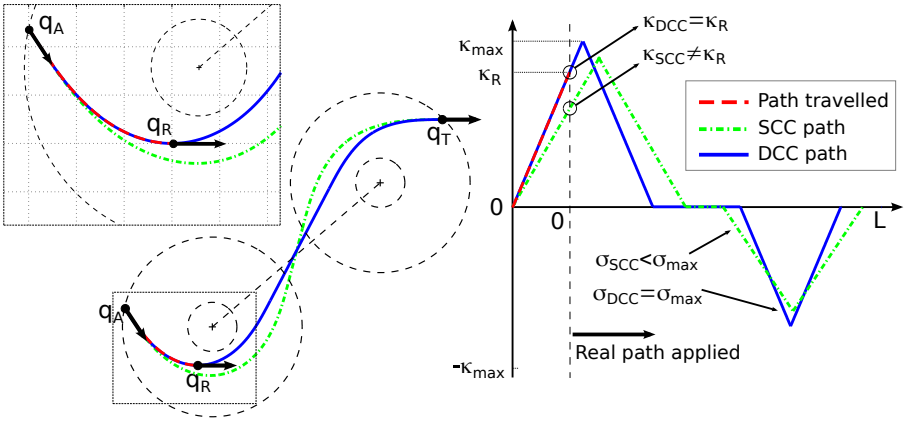

Figure 3.11: Example of path following problem in which SCC-paths cannot guarantee curvature continuity, while DCC paths always do.

of iterations required, although it has good convergence rates, being at most five times slower than SCC computation, i.e. at most 100μs. These results have been obtained in our implementation with ROS Indigo in Ubuntu 14.04 (Trusty), using a computer with processor Intel Core i7-2670QM 2.20GHz and 8GB RAM.

3.5 Conclusions

In this chapter, a method for generating clothoid-based smooth paths subject to curvature and sharpness constraints has been described. The main contribution is the development of a new path, coined as Double Continuous-Curvature path, which consists of a concatenation of line segments, circular arcs and clothoids as transition curves in order to guarantee a continuous-curvature profile.

DCC paths provide a complete set of solutions that can be applied to path planning problems where initial and final curvatures can be any arbitrary value. A proper comparison with other methods has been carried out. The main advantage of the proposed DCC path is that it can be applied to the path following problem, as explained in Chapter 4.

Chapter 5 introduces several applications in which DCC paths are used, which cover a wide range of robot autonomous navigation problems: vision-based line following, vehicle stability in industrial AGVs (Auto-Guided Vehicles), obstacle avoidance and optimal trajectory following.

Even though the benefits of planar clothoids have been proven, researchers have paid little attention to the use of such curves in the space. Among the proposed solutions, only the work carried out by Harary and Tal (2010) seems to match with the exact definition of a 3D clothoid. But, the problem is that this approach is based on a Frenet-Serret frame and requires a discrete integration. So, the final position and orientation of the curve cannot be known *a priori*. For that reason, in order to use a trajectory with such good properties in a 3D navigation problem, a new spatial clothoid should be developed, as well as smooth paths based on such curves.

In this sense, as further work we intend to develop spatial clothoids in order to include them in path planning and control problems to guide vehicles with 6-DOF (degrees of freedom) such as AUVs (Autonomous Underwater Vehicles) and UAVs (Unmanned Aerial Vehicles). Appendix A includes a preliminary study of spatial clothoids and smooth 3D paths.

Chapter 4

Smooth Control

4.1 Introduction

It is well-known that closed-loop structures increase control robustness to achieve a specific target with noises, unmodelled dynamics and disturbances. In this sense, this chapter describes the application of DCC paths as reference to control a wheeled mobile robot on static environments with dynamic (on-line) target selection. In order to close the loop two different approaches are proposed, one more related to robotics and the other closer to control theory.

In the first control scheme a trajectory based on continuous-curvature paths with velocity profile is generated by the planner to reach a given target configuration. The closed-loop control is obtained by robot current state feedback, as shown in Figure 4.1. This is the case of pure-pursuit framework or carrot-like planners. Indeed, Pure-Pursuit method implements a generic kinematic control loop, in which a target configuration is determined by finding a point that is at least separated a given Look-Ahead distance (LA) from the current robot pose, satisfying specific application conditions (in order to discard multiple solutions).

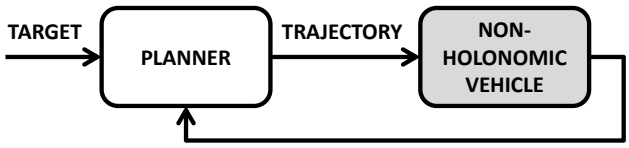

Figure 4.1: Closed-loop control with Look-Ahead based target recomputation.

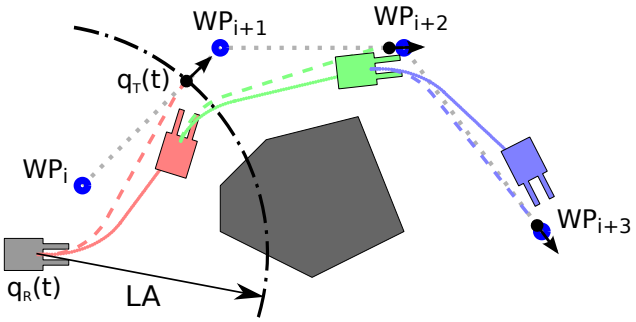

Figure 4.2: Target recomputation based on Look-Ahead distance (Pure-Pursuit framework) with odometry errors, where dashed line is the planned path and continuous line is the real path traced by the vehicle.

The proposed method can be easily combined with global planners that give some waypoints to be followed. This situation is highlighted in Figure 4.2, where a vehicle is following a meta-path (dashed grey path proposed, let's say, by a global planner) build up from a set of waypoints (blue points). It first follows a preliminary path (red path) during a certain amount of time, so it tries to converge to the meta-path based on Look-Ahead (LA) distance criterion. In the next position update, the robot might be shifted from the original path due to unmodelled dynamics or disturbances (in Figure 4.2 the update period is extremely large on purpose to highlight errors), so we need to recompute a new path based on the actual robot position (green path). Again, in the next update, the path needs to be recomputed to provide a third path based on new position update (blue path).

An exhaustive benchmarking to evaluate the performance of the proposed approach with respect to Pure-Pursuit method is provided in Section 4.2.6. As will be shown, the main advantage is that the proposed curvature profile is always continuous, taking into account actual robot curvature, as well as curvature and sharpness constraints. An exhaustive analysis to evaluate the performance of the new method with respect to classic Pure-Pursuit method has been carried out, showing that the proposed controller has better performance in terms of settling time, overshoot and robustness against design parameters.

On the other hand, the second control scheme uses an optimal controller to close the loop, as depicted in Figure 4.3. The proposed optimal controller, coined as Extended Rauch-Tung-Striebel (ERTS) controller, is defined for nonlinear unconstrained systems and it is based on two stages: prediction and smoothing. The ERTS controller is derived from a general framework based on the duality between optimal control and estimation established by

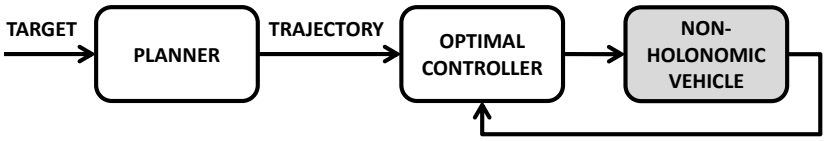

Figure 4.3: Control scheme with an optimal controller to close the loop.

Todorov (2008). The proposed controller uses an Extended Kalman Filter (EKF) that predicts (filters) future states by linearizing the nonlinear system around predicted states and then applies a backward smoothing with a Rauch-Tung-Striebel (RTS) smoother.

The proposed ERTS trajectory tracking controller can be applied to solve path following problems of non-holonomic vehicles. However, one of the main drawbacks of such a controller is the fact that is developed with assumption that the wheel slip is not possible. However, for robots with powerful wheel-driving motors (relative to their weight) wheel slip is a big concern, and therefore the proposed controller is not applicable for trajectory tracking with such robots.

Finally, another inconvenient is that ERTS controller does not take into account constraints like non-holonomicity and control actions may not be reachable by the system. In this sense, the proposed solution uses DCC paths as reference trajectory for the ERTS controller, because DCC paths are designed for non-holonomic vehicles and take into account lower and upper bounds on curvature and sharpness simultaneously. This way, although the controller is unconstrained the reference trajectory will satisfy non-holonomic restrictions and reference states will be reachable *a priori*. So, optimal unconstrained control actions from ERTS controller are expected to be close to the optimal constrained ones.

4.2 Pure-Pursuit based Control

As explained in Chapter 3, a Double Continuous-Curvature (DCC) path can be used in navigation problems assuming that current vehicle configuration $\mathbf{q}_R$ is located on a given point of the first clothoid of such DCC path, whose origin $\mathbf{q}_A$ has to be determined. In the same way, the curvature of the target configuration $\mathbf{q}_T$ might be nonzero and therefore the origin of the last clothoid or terminal point $\mathbf{q}_B$ must be also determined. However, in path following problems the vehicle has to converge to a straight line and so it can be assumed

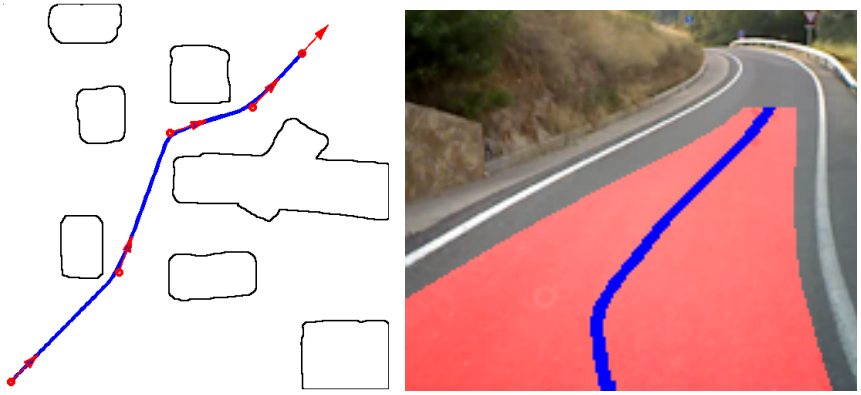

(a) Wavefront planner (b) Vision system

Figure 4.4: Waypoints generation from global planning or computer vision.

that the target curvature is $\kappa_T = 0$ and $\mathbf{q}_T = \mathbf{q}_B$. Thus, the only loose end to solve the path following problem is the dynamic recomputation of the target configuration.

4.2.1 Problem Statement

The goal is to generate a continuous-curvature path $\mathcal{Q}$ connecting the current robot pose $\mathbf{q}_R = (x_R, y_R, \theta_R, \kappa_R)^T$[1] to a target configuration $\mathbf{q}_T = (x_T, y_T, \theta_T, \kappa_T)^T$, while taking curvature and sharpness upper bounds into account, with $\kappa_R \in \pm\kappa_{max}$ and target curvature $\kappa_T = 0$, since the robot has to converge to a straight line.

The target configuration can be dynamically recomputed from a set of waypoints $w_p = \{w_{p_0}, w_{p_1}, \ldots, w_{p_N}\}$, based on a global planner method such as wavefront planner or from a vision system by detecting a path or road profile to follow, as depicted in Figure 4.4. In any case, the path formed by the poly-line as a consequence of joining waypoints might be considered as the reference path to be followed, while the target configuration can be chosen to be any point of the reconstructed poly-line. The selected $\mathbf{q}_T$ will depend on the current robot pose and a given Look-Ahead (LA) distance, a common parameter used in pure-pursuit methods that forces the robot to move ahead.

The computation of a valid set of waypoints, robot pose and map estimation, avoidance and tracking of moving obstacles are out of the scope of this

[1] In this section we make explicit time t dependency for dynamic variables of such robot configuration (including its speed and curvature), target selection, etc.

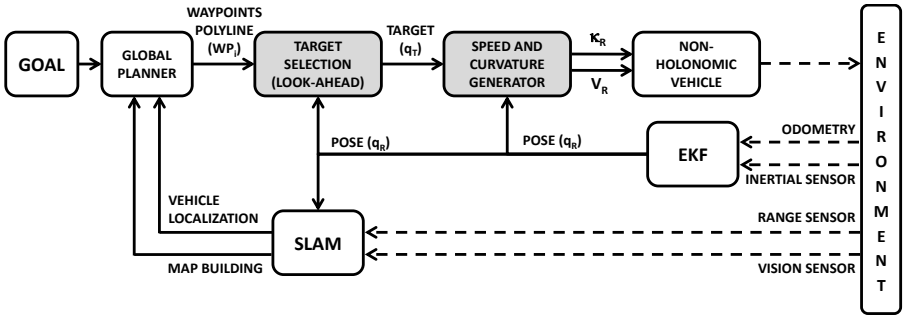

Figure 4.5: Closed-loop kinematic controller with curvature and speed profile generator for non-holonomic vehicles.

chapter, which can be seen as part of the very extensive literature on path planning methods and solutions to the SLAM problem (Montemerlo et al., 2002, 2003). Although these aspects are necessary in real-life robots, this chapter mainly focuses on the low-level aspects by considering on every control update the appropriate values of speed and curvature, while satisfying constraints on acceleration, curvature and sharpness.

4.2.2 Control Scheme

Our approach to perform a kinematic control of the vehicle is based on a cascade-loop structure, as shown in Figure 4.5. The control scheme includes speed and curvature low level controllers that require speed and curvature profiles obtained from a speed reference generator and the proposed DCC path generator, respectively. Speed reference generator simply provides a constant acceleration profile as will be explained later, while the latter has been already described in Chapter 3. In addition to this, overall closed-loop structure includes an Extended Kalman Filter (EKF) to estimate the vehicle state from inertial and odometry sensors. Target selection is based on Look-Ahead criteria, as mentioned before.

Notice that to describe a complete system in Figure 4.5 we include a high level loop with a SLAM block, as well as a Global Planner node in order to replan waypoints if needed for a specific goal. For simplicity, the environment will be considered static and therefore obstacle avoidance has not been taken into account (pure kinematic control without replanning) in the hierarchical control architecture for mobile robot navigation. Here, EKF estimation does not include stereoceptive sensors like range finders or cameras for simplicity, and no map is built because these aspects are out of the scope of this chapter.

It is interesting to remark that one of the main advantages of the proposed kinematic control is that it allows a multi-rate sampling scheme, working at different frequencies in any of the three loops: high level (SLAM and global planner), intermediate level (target selection and trajectory generation) and low level (sensorization and kinematic control).

4.2.3 Target Selection

First of all, it is necessary to remark the differences between target configurations, waypoints and goals within the context of this thesis. Target configurations $\mathbf{q}_T$ are obtained from the set of waypoints $\mathcal{W}$. On the contrary, waypoints constitute the global path to be followed based, for instance, on a global planner method such as "wavefront planner" to lead the robot to the goal $\mathbf{q}_G$, which is the last configuration to be reached.

From a given sequence of waypoints, the target configuration $\mathbf{q}_T$ can be obtained based on a Look-Ahead (LA) distance. This can be formulated as the configuration within two consecutive waypoints $\text{WP}_i = [x_{\text{WP}_i}, y_{\text{WP}_i}, \theta_{\text{WP}_i}]^T$ and $\text{WP}_{i+1} = [x_{\text{WP}_{i+1}}, y_{\text{WP}_{i+1}}, \theta_{\text{WP}_{i+1}}]^T$ with $\theta_{\text{WP}_i} = \arctan(\frac{y_{\text{WP}_{i+1}} - y_{\text{WP}_i}}{x_{\text{WP}_{i+1}} - x_{\text{WP}_i}})$:

$$\mathbf{q}_T(t) = [\lambda^*(\text{WP}_{i+1} - \text{WP}_i) + \text{WP}_i, \theta_{\text{WP}_i}, 0]^T \tag{4.1}$$

$$\lambda^* = \arg\min_{\lambda \geq \lambda_\perp} \left| \| \lambda(\text{WP}_{i+1} - \text{WP}_i) + \text{WP}_i - [x_R, y_R]^T \|_2 - LA \right| \tag{4.2}$$

$$\lambda_\perp = \arg\min_{0 \geq \lambda \geq 1} \| \lambda(\text{WP}_{i+1} - \text{WP}_i) + \text{WP}_i - [x_R, y_R]^T \|_2 \tag{4.3}$$

Equation (4.1) defines the target configuration between waypoint segments, with λ^* being the value in which the circle around the robot position with radius LA intersects with the waypoint segment (4.2). If they do not intersect then the value is selected upon the projection of the robot pose along segment (4.3).

4.2.4 Curvature Profile Generator

The curvature profile generator defines a piecewise-function based on the travelled distance along the computed DCC path. Let's assume that the vehicle is always located on the first clothoid $\mathbf{A1}$ and it has already travelled l_{A0} from DCC path origin $\mathbf{q}_A$ as a consequence of the method described

in Section 3.4.2. Thus, the distance along the DCC path is computed as $l_R(t) = \int_0^t v_R(t)dt + l_{A0}$. Then, the curvature controller uses the estimated state from EKF to compute the relative travelled distance since DCC path last update. Based on DCC path properties, the following piecewise-function is defined:

$$\kappa_R(t) = \begin{cases} 0 & \text{if } 0 \leq l_R(t) \leq l_1 \\ s_A(l_R(t)-l_1)\sigma_A & \text{if } l_1 < l_R(t) \leq l_2 \\ l_{A1}\sigma_A & \text{if } l_2 < l_R(t) \leq l_3 \\ l_{A1}\sigma_A - s_A(l_R(t)-l_3)\sigma_A & \text{if } l_3 < l_R(t) \leq l_4 \\ 0 & \text{if } l_4 < l_R(t) \leq l_5 \\ s_B(l_R(t)-l_5)\sigma_B & \text{if } l_5 < l_R(t) \leq l_6 \\ l_{B1}\sigma_B & \text{if } l_6 < l_R(t) \leq l_7 \\ l_{B1}\sigma_B - s_B(l_R(t)-l_6)\sigma_B & \text{if } l_7 < l_R(t) \leq l_8 \\ 0 & \text{if } l_8 < l_R(t) \end{cases} \tag{4.4}$$

with $l_1 = l_A$, $l_2 = l_1 + l_{A1}$, $l_3 = l_2 + l_{\Omega_A}$, $l_4 = l_3 + l_{A2}$, $l_5 = l_4 + l_C$, $l_6 = l_5 + l_{B1}$, $l_7 = l_6 + l_{\Omega_B}$, $l_8 = l_7 + l_{B2}$ and $l_9 = l_8 + l_B$.

4.2.5 Speed Profile Generator

The speed profile generator is also defined as a piecewise-function considering times for speeding up and slowing down, based on path speed and acceleration profiles (including nominal speeds and speeds at turns). When approaching a curve, humans instinctively apply a "slow-in" and "fast-out" policy, which implies to reduce velocity, i.e. v_{turn}, just before entering into a curve and then progressively increases the velocity up to a nominal value, i.e. v_{path}. The following piecewise-function defines the proposed speed profile, which includes a constant acceleration a_{path} for speeding up and a constant deceleration a_{brake} for slowing down:

$$v_R(t) = \begin{cases} v_{path} & \text{if } t \leq t_1 \\ v_{turn}\frac{t-t_1}{t_2-t_1} - v_{path}\frac{t-t_2}{t_2-t_1} & \text{if } t_1 \leq t \leq t_2 \\ v_{turn} & \text{if } t_2 \leq t \leq t_3 \\ v_{path}\frac{t-t_3}{t_4-t_3} - v_{turn}\frac{t-t_4}{t_4-t_3} & \text{if } t_3 \leq t \leq t_4 \end{cases} \tag{4.5}$$

with t_1 the time instant when the vehicle is separated $\Delta x = \frac{v_{path}^2 - v_{turn}^2}{2 \cdot a_{brake}} + LA$ far from the next waypoint. The distance $\Delta x - LA$ is indeed the required distance to reduce the velocity from v_{path} to v_{turn} with constant deceleration a_{brake}, which lasts $t_2 - t_1$ in time units. In addition to this, t_3 is the time instant when the convergence criteria indicates that the vehicle has converged to the line between current waypoint and next waypoint and t_4 is the required time to accelerate from v_{turn} to v_{path} with constant acceleration a_{path}.

4.2.6 Benchmarking: Results and Discussion

In this section, an exhaustive analysis of the proposed smooth kinematic controller based on DCC paths is performed in order to compare the benefits of this method against the classic Pure-Pursuit (PP) algorithm (Ollero, 2001) a well-known curvature controller which proposes circular arcs to reach targets, whose curvature is computed as follows:

$$\kappa_R(t) = 2 \cdot \frac{(x_T - x_R) \cdot \cos\theta_R - (y_T - x_R) \cdot \sin\theta_R}{(x_R - x_T)^2 + (y_R - y_T)^2} \tag{4.6}$$

In particular, we analyse the effects of the path following velocity v_R and the Look-Ahead distance LA, as well as maximum values of sharpness and curvature, σ_{max} and κ_{max} respectively. Although the control scheme allows variable speed, in the benchmarking the robot moves with constant velocity. The effect of a variable speed profile is evaluated in Section 5.3.

Unless specified otherwise, the default variables and parameters for the benchmarking are the following: $v_R = 0.5$ m/s and $LA = 1$ m, with $\alpha_A = 1$ and $\alpha_B = 1$ considering that the kinematic constraints are $\kappa_{max} = 4$ m^{-1} and $\sigma_{max} = 15.7$ m^{-2}, with $\sigma_{min} = 0.1\sigma_{max}$.

To evaluate the performance of the methods several metrics have been used to characterize the resulting path $\{[x_{R,0}, y_{R,0}]^T, [x_{R,1}, y_{R,1}]^T, \ldots\}$. In particular, we consider the settling time $t_s = k_s T_R$ such as $\left|\frac{\rho_l - y_{R,i}}{\rho_l}\right| < 0.02\ \forall i \geq k_s$, the mean error $\overline{e} = \sum_i \left|\rho_l - (x_{R,i}\cos\phi_l - y_{R,i}\sin\phi_l)\right|$ and the overshoot $\delta = \max\{y_{R,i}\}$. We also evaluate comfort related variables as defined in Yuste et al. (2010), such as the normalized bending energy $NBE = \frac{1}{n}\sum_{i=0}^{n}\kappa_i^2 dl$, the normalized abruptness $NA = \frac{1}{n}\sum_{i=0}^{n}\sigma_i^2 dl$, where $dl = v \cdot dt$, and the maximum normal jerk $J_{N_{max}} = v^3\sigma_{max}$.

Without loss of generality, the first set of experiments have been developed for the case in which the start robot configuration is $\mathbf{q}_R(0) = (0, 0, \pi/2, 0)$ and the path to follow is a straight line $\rho_l = x\cos\phi_l + y\sin\phi_l$ with $\rho_l = 1$m and $\phi_l = \pi/2$rad (line $y = 1$m), which represents one of the most difficult path following cases, a 90$^{\text{o}}$ corner.

From the results of Table 4.1, it can be appreciated that DCC control method performs much better by obtaining a lower settling time and therefore reaches the path earlier. DCC path generally shows an under-damped trajectory, therefore it rarely overpass the line, while the PP method clearly overpasses the path, as shown in Figure 4.6. In fact, Table 4.1 shows that Pure-Pursuit has a big overshoot with long LA distance and, in some cases,

Table 4.1: Control performance variables vs. control parameters, with Pure-Pursuit (PP) and Double Continuous-Curvature (DCC) control methods.

		$\mathbf{t_s}[\mathbf{s}]$		$\delta[\%]$		$\overline{e}(m)$	
		PP	**DCC**	**PP**	**DCC**	**PP**	**DCC**
$\mathbf{v_R}\ [\frac{\mathbf{m}}{\mathbf{s}}]$	0.2	18.90	14.26	10.06	0.56	0.188	0.189
	0.5	7.49	5.58	10.37	0.60	0.088	0.087
	1.0	3.67	2.70	10.51	0.61	0.074	0.071
	2.0	1.79	1.24	10.97	0.67	0.062	0.055
$\mathbf{LA}[\mathbf{m}]$	0.5	2.45	2.14	4.15	4.87	0.06	0.04
	1.0	3.73	2.47	9.72	0.32	0.07	0.04
	2.0	9.71	5.78	46.28	0.31	0.15	0.07
	4.0	15.0	12.01	143.4	0.19	0.66	0.10

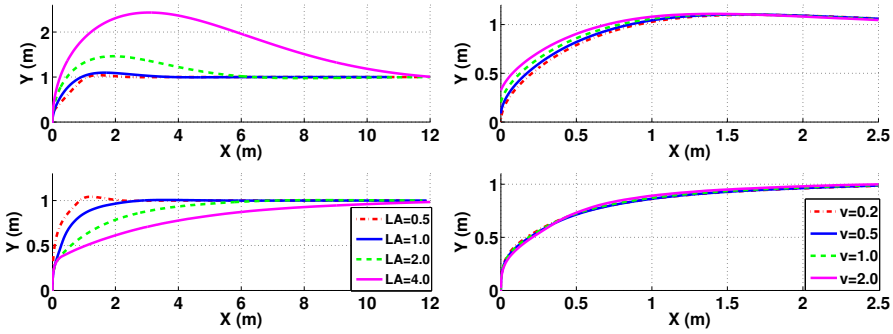

(a) XY vs. LA [m]. (b) XY vs. v_R [m/s].

Figure 4.6: DCC (below) vs. PP (above), for different values of LA and v_R.

the goal could be lost. However, with the DCC controller the behaviour is similar to those cases in which LA distance is shorter, which means that somehow the DCC control method is insensitive to LA value, probably due to the target relaxation explained in Section 3.4.3. The mean error is generally lower in DCC path method, but with the same order of magnitude as PP. The velocity has in general little influence on the metrics, but obviously it affects the settling time.

On the other hand, metrics related to comfort are analysed in Table 4.2. As can be observed, the NBE is slightly higher in the DCC which implies that the method applies, in general, higher curvatures, which can be seen as a trade-off between overshoot plus settling time and bending energy. A peculiar result is the inverse relation of the abruptness metric with respect to LA distance.

Table 4.2: Comfort performance variables vs. control parameters, with Pure-Pursuit (PP) and Double Continuous-Curvature (DCC) control methods.

		$\mathbf{NBE}[\mathbf{m}^{-1}]$		$\mathbf{NA}[\mathbf{m}^{-4}]$		$\mathbf{J}_{\mathbf{N_{max}}}[\mathbf{m/s^3}]$	
		PP	**DCC**	**PP**	**DCC**	**PP**	**DCC**
$\mathbf{v_R}\left[\frac{\mathbf{m}}{\mathbf{s}}\right]$	0.2	0.0007	0.0009	0.04	0.01	1.60	0.07
	0.5	0.0010	0.0011	0.61	0.04	51.20	2.41
	1.0	0.0021	0.0018	2.18	0.26	418.4	31.88
	2.0	0.0044	0.0030	7.86	1.57	3467	480.8
$\mathbf{LA}[\mathbf{m}]$	0.5	0.0055	0.0015	10.86	0.26	1000	95.93
	1.0	0.0013	0.0015	0.38	0.37	200.0	76.06
	2.0	0.0007	0.0017	0.05	0.49	81.03	50.60
	4.0	0.0004	0.0017	0.02	0.41	47.28	44.55

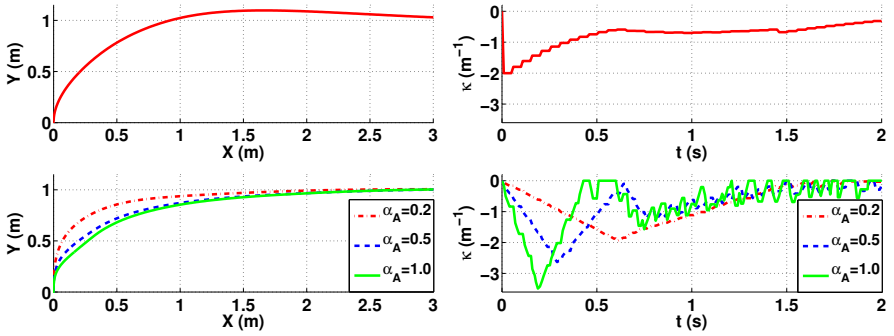

(a) XY vs. α_A. (b) κ profile vs. α_A.

Figure 4.7: DCC (below) vs. PP (above), for different values of α_A, with $\alpha_B = 1$.

In DCC method the abruptness increases slightly with LA, while in PP it decreases exponentially. Finally, the normal jerk is lower in DCC method, which supports the idea that continuous-curvature planners produce smoother and safer trajectories.

In Figure 4.7(a), it can be seen that design parameter α_A has direct influence on the abruptness. That makes perfect sense because α_A determines the maximum allowed value of sharpness for the first couple of clothoids, whilst α_B limits the second clothoid-pair. The higher the clothoid sharpness the higher the abruptness. Moreover, in Figure 4.7(b), it can be observed that the higher the clothoid sharpness the "noisier" the curvature profile in the path following. Indeed, a bang-bang sharpness control is being applied to steer the

Table 4.3: Control and comfort performance variables vs. σ_{max} and κ_{max}.

		$\mathbf{t_s}$ [s]	δ [%]	$\bar{\mathbf{e}}$ [m]	**NBE** [$\mathbf{m^{-1}}$]	**NA** [$\mathbf{m^{-4}}$]	$\mathbf{J_N}$ [$\mathbf{m/s^3}$]
$\sigma_{\mathbf{max}}[\mathbf{m^{-2}}]$	3.14	2.24	0.29	0.042	0.0012	0.02	12.65
	7.85	2.45	0.36	0.047	0.0014	0.12	29.57
	15.7	2.43	0.27	0.048	0.0018	0.48	75.87
$\kappa_{\mathbf{max}}[\mathbf{m^{-1}}]$	2.0	7.67	0.20	0.11	0.0029	0.036	15.18
	3.0	8.19	0.21	0.12	0.0031	0.084	18.17
	5.0	8.54	0.25	0.13	0.0039	0.210	33.68

vehicle. Despite of this, the curvature is still continuous, while the PP method clearly shows discontinuities (discretization effect). This happens because the PP control law does not take sharpness limits into account and therefore there might be curvature discontinuities, i.e. big steps in the value of two consecutive curvatures. This effect is magnified in the first control step of the PP method, in which initial curvature was null, but the first control input was a nonzero value. However, that does not happen when using the DCC method, as can be seen in Figure 4.7(b).

In addition to this, the analysis has been extended to evaluate the performance when varying the maximum allowable sharpness and curvature in computing the DCC path. The results obtained in Table 4.3 lead to the conclusion that the kinematic constraints affect directly to the robot behaviour. In fact, NBE, NA and J_N are proportional to the maximum curvature and curve sharpness, as expected.

Finally, we have defined a square shape path which represents one of the most challenging cases for path following problems, since at corners there is an abrupt discontinuity on the path orientation. XY-Graph in Figure 4.8(a) shows different robot traces for DCC and PP methods for mid values of LA and v_R. It can be seen that the robot follows the reference path better with a DCC control than with a PP control, since DCC has less overshoot and the settling time is faster, while PP method has, as shown in Figure 4.8(b), lower mean curvature values and sharpness, but it has higher sharpness peaks on each corner as expected, which implies less comfort and safety. Hence, the trade-off we need to pay is higher curvature values but always satisfying maximum curvature constraints. The bounds in Figure 4.8(b) and Figure 4.8(c) are included to demonstrate that the DCC path method does not exceed the maximum allowable curvature and sharpness as specified by its own design.

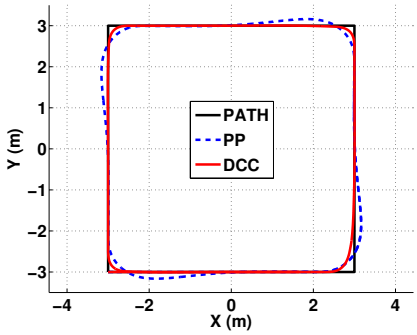

(a) Path following XY.

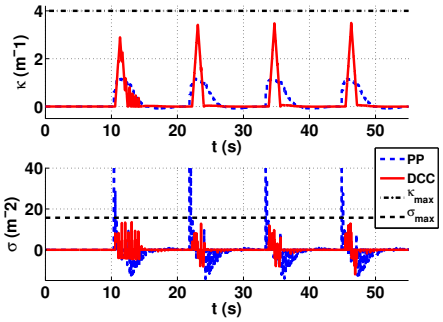

(b) Path following κ and σ profiles.

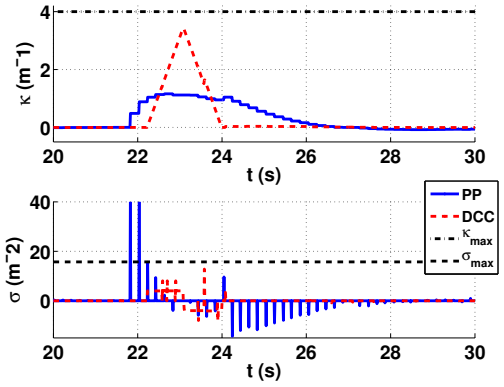

(c) Zoom of κ and σ profiles.

Figure 4.8: DCC vs. PP, following a squared path with a side of 6 m.

4.3 Optimal Control

This section is aimed to investigate efficiency of the existing tools for nonlinear stochastic smoothing to the problem of optimal control via duality. We focus on smoothing approaches with Gaussian posterior, namely the Extended Rauch-Tung-Striebel (RTS) smoother and the Unscented RTS (Sarkka, 2008). Both smoothers are analogous to the nonlinear Extended Kalman Filter (EKF) (Chui and Chen, 1987) and the Unscented Kalman Filter (UKF) (Julier et al., 2000), respectively. The distinction from the alternative linearization approaches is that ERTS linearises the trajectory using not only the system dynamic model, but also the covariance matrices representing penalizations of the cost function. The resulting algorithm uses only two passes of the horizon without any further iterations.

Therefore, based on the ideas of Toussaint (2009), this section proposes the use of non-iterative controllers, coined as Extended Rauch-Tung-Striebel (ERTS) and Unscented Rauch-Tung-Striebel (URTS) controllers, based on the duality between optimal control and estimation under certain assumptions (Todorov, 2008) for nonlinear unconstrained systems, extending Todorov's work. The proposed controllers use a Rauch-Tung-Striebel (RTS) forward-backward smoother as an state estimator that predicts (filters) future states by linearizing the nonlinear system around predicted states and then applies a backward smoothing in order to compute the original optimal control problem.

It is a two-pass technique that allows to compute linearization points based on the Extended Kalman Filter (EKF) in the first step and then to smooth such trajectory using a backward RTS smoother. The computed estimate of the next state is then used for the computation of the optimal control within a receding horizon policy. This results in an efficient controller with complexity $\mathcal{O}(N^2)$ in state dimensions. The controller is optimal for LQ systems and the extension to nonlinear settings is done by linearization along predicted trajectory where results are slightly suboptimal, as discussed later. An alternative to linearization at a single point as used in EKF is the Unscented Transform (Julier et al., 2000), which computes linearization at multiple points and thus further reduce linearization errors. Application of this transform to the smoothing problem yields the Unscented Rauch-Tung-Striebel (URTS) controller.

The performance of ERTS and URTS controllers is illustrated on the (unconstrained) trajectory-following problem of differential-drive mobile robots. This problem has been studied intensively during last years. However, proposed controllers are commonly strictly specialized on particular tasks or contain "artificial" design parameters (e.g. look-ahead distance) which have to be tuned. The new method is compared with iterative linear-quadratic regulator (iLQR) (Todorov and Li, 2005), nonlinear model predictive control (NMPC) and approximate inference approaches (AIA). Simulations show that the proposed controllers produce almost-optimal solutions with a significantly lower computing time, avoiding initialization issues in the other algorithms (in fact, they can be used to initialize them). In Chapter 5, Section 5.5, the ERTS controller is validated by an experiment using a Pioneer 3DX mobile robot (Adept Mobilerobots, 1995).

4.3.1 Introduction

Optimal control is widely used in control practice due to its advantages regarding the individual tuning of actuator amplitudes and control goals for each output, with well-known solutions for the linear case, both unconstrained (LQR) and constrained (Morari and Lee, 1997; Bemporad et al., 2002). However, it is limited to a narrow spectrum of applications because many systems in practice are inherently nonlinear. Nonlinear optimal control strategies are computationally more demanding, see Qin and Badgwell (2003); Blackmore et al. (2010); Grüne and Pannek (2011), for some model-based approaches to handling it.

The goal of model-based optimal control is designing a stabilizing control while minimizing a given performance criterion, usually in a quadratic form, assuming a deterministic plant model is available. Closed-loop solutions cannot be found analytically in a general nonlinear case since it involves obtaining the solution of the corresponding Hamilton Jacobi-Bellman equations (Yong and Zhou, 1999).

One approach to avoid this problem is the iterative solution of a finite-horizon optimal control problem for a given state with a receding horizon implementation; control approaches using this strategy are referred to as model predictive control (MPC, Morari and Lee (1997)) and nonlinear model predictive control (NMPC, Grüne and Pannek (2011)). These approaches can deal with the unconstrained and constrained problems, where both states and control inputs must satisfy particular conditions. MPC is restricted to quadratic cost functions, linear systems and linear constraints, while NMPC can optimize non-quadratic cost functions for nonlinear systems restricted to general nonlinear constraints.

Another well-accepted solution for the nonlinear case is the iterative linear quadratic regulator (iLQR) (Li and Todorov, 2004), which linearizes the cost function at given (non-optimal) state and control input trajectories and then computes optimal increments based on the linearized model. The algorithm converges with appropriate jumps on the direction of control input gradient and Hessian based on Levenberg-Marquardt approach.

The main drawback of existing approaches is the computational cost required to provide optimal solutions. Since all-known methods are iterative, they may take a large number of iterations to converge to the optimal solution depending on the chosen algorithm's initialization parameters (i.e., initial non-optimal trajectory): the choice of linearization points (gradient computations) are key for obtaining an optimal control policy for nonlinear systems;

if fact, the optimal choice would be linearising around the (not yet known) optimal trajectory.

Recent contributions propose solving the above deterministic optimal control problems by embedding them into a generic stochastic optimal control (SOC) framework (Todorov, 2008; Toussaint, 2009; Todorov, 2011). Indeed, in Todorov (2008), the well-known duality in the Riccati equations arising in the LQR and Kalman filter setups is extended to other nonlinear control cases by reformulating the problem in terms of the Kullback-Leibler divergence. In particular, Todorov proposes a forward-backward smoothing approach, different from the classic forward-only prediction in Kalman's observer.

A related approach, denoted as Approximate Inference Control (AICO), appears in Toussaint (2009). The author proposes a probability distribution over a binary variable, based on the exponential of the cost index, and solves the resulting SOC setting. In particular, the author proves equivalence between the SOC problem and estimation of the marginal distribution of the state conditioned to the binary variable readings, the latter addressed via message-passing algorithm (Yedidia et al., 2003). The resulting algorithm, when applied to nonlinear control problems, is iterative; it is non-iterative for the linear LQR case.

The fact that the covariance matrix of the optimal estimator of a linear system with Gaussian noises and Hessian of the optimal cost-to-go of a linear control problem with a quadratic loss evolves in time under similar Riccati-like equations, is known more than fifty years, Kalman (1960b). Due to this, both solutions (Kalman Filter, KF, and Linear Quadratic Controller, LQR) have the same form and as a consequence an algorithm computing KF can be used as LQR algorithm. This is known as the (Kalman's) duality between optimal control and estimation for linear-Gaussian systems. This interesting property motivated efforts for development of possible extensions to nonlinear systems, nonetheless, straightforward generalization on nonlinear cases is not known. Theoretical work introducing satisfactory extension was done in Todorov (2008), where the general (Todorov's) duality between optimal control and estimation is obtained for slightly reformulated optimal control problem based on Kullback-Leibler divergence. The new general duality applied on LQ problem does not give the same algorithm as Kalman's approach. It is because the estimation problem is different in both approaches – prediction in Kalman's case and smoothing in Todorov's.

4.3.2 Problem Definition

We are concerned with the problem of optimal control of a stochastic nonlinear dynamic system with state $\mathbf{x}_t$ and the deterministic control action $\mathbf{u}_t$ with known model:

$$\mathbf{x}_{t+1} \sim p(\mathbf{x}_{t+1}|\mathbf{x}_t, \mathbf{u}_t) \tag{4.7}$$

We seek an optimal control policy $\mathbf{u}_t = \pi_t(\mathbf{x}_t, \mathbf{s}_{t:N}) \triangleq \pi_t$ which optimizes the expected value of the following additive cost function:

$$L(\mathbf{x}_0, \mathbf{s}_{0:N}, \mathbf{u}_{0:N-1}) = q_N(\mathbf{x}_N, \mathbf{s}_N) + \sum_{t=0}^{N-1} l_t(\mathbf{x}_t, \mathbf{s}_t, \mathbf{u}_t) \tag{4.8}$$

where sequence $\mathbf{s}_{0:N} \triangleq \mathbf{s}_0, \ldots, \mathbf{s}_N$ stands for the desired quantities related to states (actually, reference trajectories for some outputs), $q_N(\mathbf{x}_N, \mathbf{s}_N)$ is an arbitrary function for the final cost and the intermediate cost is $l_t(\mathbf{x}_t, \mathbf{s}_t, \mathbf{u}_t)$. Design of the control policy is a classical problem of dynamic programming

$$J_t(\mathbf{x}_t, \mathbf{s}_{t:N}) = \min_{\pi_t} \mathsf{E}\left\{ l_t(\mathbf{x}_t, \mathbf{s}_t, \mathbf{u}_t) + J_{t+1}(\mathbf{x}_{t+1}, \mathbf{s}_{t+1:N}) \right\} \tag{4.9}$$

where E is the expected value over distribution of $\mathbf{x}_{t+1}$ and J_t is the Bellman function. Analytical solution of (4.9) exists only for limited cases such as the linear quadratic systems. For nonlinear systems, the evaluation has to be approximated. Here, we focus on reformulation of this problem into a dual problem of stochastic smoothing (Todorov, 2008) and its relations with alternative approaches.

4.3.2.1 Duality of Estimation and Control

As demonstrated in Todorov (2008), the optimization problem (4.9) can be translated into the language of probability calculus and solved as an optimal smoothing problem. This is possible if there exists a probability distribution $\bar{p}(\mathbf{x}_{t+1}|\mathbf{x}_t)$ such that the cost index can be written as

$$l_t(\mathbf{x}_t, \mathbf{s}_t, \mathbf{u}_t) = q_t(\mathbf{x}_t, \mathbf{s}_t) + \mathrm{KL}\big(p(\mathbf{x}_{t+1}|\mathbf{x}_t, \mathbf{u}_t)||\bar{p}(\mathbf{x}_{t+1}|\mathbf{x}_t)\big) \tag{4.10}$$

where KL is the Kullback-Leibler divergence (Kullback and Leibler, 1951)

$$\begin{aligned} &\mathrm{KL}(p(\mathbf{x}_{t+1}|\mathbf{x}_t, \mathbf{u}_t)||\bar{p}(\mathbf{x}_{t+1}|\mathbf{x}_t)) = \\ &\quad = \int_{\mathbb{R}^{n_x}} \log\left[\frac{p(\mathbf{x}_{t+1}|\mathbf{x}_t, \mathbf{u}_t)}{\bar{p}(\mathbf{x}_{t+1}|\mathbf{x}_t)}\right] p(\mathbf{x}_{t+1}|\mathbf{x}_t, \mathbf{u}_t)\, \mathrm{d}\mathbf{x}_{t+1} \end{aligned} \tag{4.11}$$

and $\bar{p}(\mathbf{x}_{t+1}|\mathbf{x}_t)$ is a *reference dynamics*.

Substituting (4.10) into (4.9) and using the following simplified notation $p(\mathbf{x}_{t+1}|\mathbf{x}_t, \mathbf{u}_t) \triangleq p$, $\bar{p}(\mathbf{x}_{t+1}|\mathbf{x}_t) \triangleq \bar{p}$, $q_t(\mathbf{x}_t, \mathbf{s}_t) \triangleq q_t$, $\pi_t(\mathbf{x}_t, \mathbf{s}_{t:N}) \triangleq \pi_t$ and $J_t(\mathbf{x}_t, \mathbf{s}_{t:N}) \triangleq J_t$ we obtain

$$\begin{aligned} J_t &= q_t + \min_{\pi_t} \int_{\mathbb{R}^{n_x}} \left[J_{t+1} + \log \frac{p}{\bar{p}} \right] p \, \mathrm{d}\mathbf{x}_{t+1} \\ &= q_t - \log c_t + \min_{\pi_t} \mathrm{KL} \left(p || \frac{1}{c_t} e^{-J_{t+1}} \bar{p} \right) \end{aligned} \tag{4.12}$$

where the normalizer $c_t \triangleq c_t(\mathbf{x}_t, \mathbf{s}_{t+1:N})$ is equal to

$$c_t(\mathbf{x}_t, \mathbf{s}_{t+1:N}) = \int_{\mathbb{R}^{n_x}} e^{-J_{t+1}(\mathbf{x}_{t+1}, \mathbf{s}_{t+1:N})} \bar{p}(\mathbf{x}_{t+1}|\mathbf{x}_t) \mathrm{d}\mathbf{x}_{t+1}$$

The second argument of the KL divergence (4.12) is thus a proper probability density p_π.

If there exists a control policy π_t such that $\mathrm{KL}(p||p_\pi) = \zeta_t$, where ζ_t is a constant independent of $\mathbf{x}_t, \mathbf{u}_t$, then (4.12) can be rewritten as:

$$e^{-J_t} \propto e^{\zeta_t - q_t} c_t = e^{\zeta_t} e^{-q_t} \int_{\mathbb{R}^{n_x}} e^{-J_{t+1}} \bar{p} \, \mathrm{d}\mathbf{x}_{t+1} \tag{4.13}$$

Under these assumptions, it can be proved that the optimal control problem (4.9) is dual to the problem of marginal prediction of the state (Todorov, 2008; Zima et al., 2013); with general solution of the Bellman function

$$J_{t+1}(\mathbf{x}_{t+1}, \mathbf{s}_{t+1:N}) = -\log p(\mathbf{s}_{t+1:N}|\mathbf{x}_{t+1}) + \zeta_{t+1}, \tag{4.14}$$

where

$$p(\mathbf{s}_{t+1:N}|\mathbf{x}_{t+1}) = \int_{\mathbb{R}^{n_x}} p(\mathbf{x}_{t+2:N}, \mathbf{s}_{t+1:N}|\mathbf{x}_{t+1}) d\mathbf{x}_{t+2:N} \tag{4.15}$$

is the marginal predictive model, which can be computed recursively as shown thereinafter.

The optimal policy is then defined as a minimizer of:

$$\pi_t^* = \arg\min_{\pi_t} \mathrm{KL}(\big(p(\mathbf{x}_{t+1}|\mathbf{x}_t, \mathbf{u}_t) || p_\pi(\mathbf{x}_{t+1}|\mathbf{x}_t, \mathbf{s}_{t+1:N})\big) \tag{4.16}$$

$$p_\pi(\mathbf{x}_{t+1}|\mathbf{x}_t, \mathbf{s}_{t+1:N}) \propto e^{-J_{t+1}(\mathbf{x}_{t+1}, \mathbf{s}_{t+1:N})} \bar{p}(\mathbf{x}_{t+1}|\mathbf{x}_t) \tag{4.17}$$

under the assumption that such a minimizer exists and the minimum of (4.16) is independent of $\mathbf{x}_t$. Here, $\propto$ denotes equality up to a multiplicative constant.

We note that after substitution of (4.14) into (4.17) the result is the Bayes' rule and thus a definition of the optimum smoothing problem. This problem is commonly studied and many methods has been developed for its solution.

Assume now a state-space model in the form

$$\mathbf{x}_{t+1} \sim \bar{p}(\mathbf{x}_{t+1}|\mathbf{x}_t) \tag{4.18}$$

$$\mathbf{s}_t \sim p(\mathbf{s}_t|\mathbf{x}_t) \tag{4.19}$$

where (4.18) stands for the reference dynamics from the original control problem and (4.19) is an observation model.

The marginal predictive distribution is:

$$\begin{aligned} p(\mathbf{s}_{t:N}|\mathbf{x}_t) &= p(\mathbf{s}_t|\mathbf{x}_t)p(\mathbf{s}_{t+1:N}|\mathbf{x}_t) \\ &= p(\mathbf{s}_t|\mathbf{x}_t)\int_{\mathbb{R}^{n_x}} p(\mathbf{s}_{t+1:N}|\mathbf{x}_{t+1})\bar{p}(\mathbf{x}_{t+1}|\mathbf{x}_t)\mathrm{d}\mathbf{x}_{t+1} \end{aligned} \tag{4.20}$$

Comparing (4.20) with (4.13) we can establish duality for

$$p(\mathbf{s}_t|\mathbf{x}_t) \propto e^{-q_t(\mathbf{x}_t,\mathbf{s}_t)} \tag{4.21}$$

$$p(\mathbf{s}_{t+1:N}|\mathbf{x}_{t+1}) \propto e^{-J_{t+1}(\mathbf{x}_{t+1},\mathbf{s}_{t+1:N})} \tag{4.22}$$

establishing a duality between the Bellman function and marginal prediction.

Moreover, we note that

$$p(\mathbf{x}_{t+1}|\mathbf{x}_t, \mathbf{s}_{t+1:N}) \propto p(\mathbf{s}_{t+1:N}|\mathbf{x}_{t+1})\bar{p}(\mathbf{x}_{t+1}|\mathbf{x}_t) \tag{4.23}$$

establishing duality

$$p_\pi(\mathbf{x}_{t+1}|\mathbf{x}_t, \mathbf{s}_{t+1:N}) \propto p(\mathbf{x}_{t+1}|\mathbf{x}_t, \mathbf{s}_{t+1:N}), \tag{4.24}$$

where the normalization constants absorb the constant terms in the Bellman function (i.e. the ζ_t term in (4.13)). The dual estimation problem is defined as the smoothing problem of $\mathbf{x}_{t+1}$ knowing $\mathbf{x}_t$ and the whole observation sequence $\mathbf{s}_{t+1:N}$, Todorov (2008).

The duality can be used to establish duality between the classical LQR design and the Rauch-Tung-Striebel (RTS) smoother (Rauch et al., 1965) for linear model (4.7) with quadratic cost.

4.3.2.2 Iterative Linearisation-based Optimal Control

As nonlinear optimal control problems are hard problems, linearisation around a trajectory is often used, so the systems appear as:

$$\delta \mathbf{x}_{t+1} = \mathbf{A}_t(\mathbf{x}_t)\delta \mathbf{x}_t + \mathbf{B}_t(\mathbf{x}_t)\delta \mathbf{u}_t \tag{4.25}$$

where $\delta \mathbf{x}_t$, $\delta \mathbf{u}_t$ are increments over a chosen linearisation trajectory.

The basic problem of linearisation approaches is, of course, choosing the points in which to linearise the system. Actually, it is clear that the optimal linearisation points would be those of the optimal trajectory; however, as they depend on the to-be-computed control and the control depends on such points, iterative algorithms are needed (linearise around first trajectory estimate, compute control, compute new trajectory, repeat). Current iterative linearisation-based options in literature for finding solutions to nonlinear optimal control problems are:

Iterative LQR (iLQR)

If the result of the standard LQR algorithm is used to compute a new optimal increment of control action (and the ensuing state trajectory), the system can be re-linearised around the new trajectory and this can be iterated until convergence. This is the basis of the iLQR approach proposed in Li and Todorov (2004), and of a generalisation involving linearisation of nonlinear (but affine in noise) models coined as iLQG in Todorov and Li (2005).

Nonlinear Model Predictive Control (NMPC)

Nonlinear model-predictive control minimises a finite-time quadratic cost based on open-loop predictions using standard nonlinear optimization algorithms. Most NMPC implementations compute gradients and Hessians of the quadratic cost function which, ultimately, depend on the model gradient (i.e., linearisation) at a candidate solution to be iteratively improved. It can deal with nonlinear cost functions and state and control input constraints. The reader is referred, for instance, to Grüne and Pannek (2011) for ample information on the topic.

Approximate Inference Control (AICO)

Toussaint (2009) proposes an artificial binary random variable $\mathbf{z}_t$ such that $P(\mathbf{z}_t = 1|\mathbf{x}_t, \mathbf{u}_t) = e^{-l_t(\mathbf{x}_t, \mathbf{s}_t, \mathbf{u}_t)}$. So, the control problem can be posed as a determining a trajectory which maximizes the probability of

$\mathbf{z}_t = 1$ for all times, transformed to an estimation problem via Bayes' rule. The proposed solution to the problem uses the message-passing algorithm (Yedidia et al., 2003), and in the LQR case it needs a single forward-backward pass, actually being a message-passing implementation of the RTS smoother, instead of the original Riccati one. For nonlinear systems, AICO uses an iterative approach to compute linearization points (with iterations of the message-passing algorithm which, themselves, include nested iterations to find suitable linearization points for Gaussian belief propagation).

4.3.3 Nonlinear Quadratic Control via Estimation

Consider a nonlinear model with affine control input and Gaussian disturbance

$$p(\mathbf{x}_{t+1}|\mathbf{x}_t, \mathbf{u}_t) \triangleq \mathcal{N}(\mathbf{f}(\mathbf{x}_t) + \mathbf{B}_t(\mathbf{x}_t)\mathbf{u}_t, \mathbf{V}_t) \tag{4.26}$$

for a known vector-valued function $\mathbf{f}(\mathbf{x}_t)$, matrix $\mathbf{B}_t(\mathbf{x}_t) \triangleq \mathbf{B}_t$. Consider a quadratic cost (4.8):

$$L_t = \frac{1}{2}\mathbf{e}_N^T \mathbf{Q}_N \mathbf{e}_N + \frac{1}{2}\sum_{t=0}^{N-1}(\mathbf{e}_t^T \mathbf{Q}_t \mathbf{e}_t + \mathbf{u}_t^T \mathbf{R}_t \mathbf{u}_t) \tag{4.27}$$

for $\mathbf{e}_t = \mathbf{s}_t - \mathbf{h}(\mathbf{x}_t)$ and known $\mathbf{Q}_t$, $\mathbf{R}_t$ and known vector-valued function $\mathbf{h}(\mathbf{x}_t)$.

Dual formulation of quadratic cost (4.27) in the sense of Section II.A is established for the following distributions:

$$\bar{p}(\mathbf{x}_{t+1}|\mathbf{x}_t) \triangleq \mathcal{N}(\mathbf{f}(\mathbf{x}_t), \bar{\mathbf{V}}_t), \bar{\mathbf{V}}_t = \mathbf{B}_t \mathbf{R}_t^{-1} \mathbf{B}_t^T \tag{4.28}$$

$$p(\mathbf{s}_t|\mathbf{x}_t) \triangleq \mathcal{N}(\mathbf{h}(\mathbf{x}_t), \mathbf{Q}_t^{-1}) \tag{4.29}$$

The result of substitution of these distributions into (4.10) is the quadratic cost (4.27) plus constant terms without any influence on the optimal control policy.

4.3.3.1 Linear Quadratic Regulator from KL Cost

Let us consider the LTV system with Gaussian noise (4.7) and its reference dynamics (4.28), for a special case of linear system $\mathbf{f}(\mathbf{x}_t) = \mathbf{A}_t \mathbf{x}_t$. The KL

divergence (4.11) is

$$\begin{aligned}\mathrm{KL}(p(\mathbf{x}_{t+1}|\mathbf{x}_t,\mathbf{u}_t)||\bar{p}(\mathbf{x}_{t+1}|\mathbf{x}_t)) &= \\ &= \frac{1}{2}\mathbf{u}_t^T\mathbf{B}_t^T\bar{\mathbf{V}}_t^{-1}\mathbf{B}_t\mathbf{u}_t + c_{KL}, \qquad (4.30)\\ c_{KL} &= \frac{1}{2}\left(\mathrm{tr}(\bar{\mathbf{V}}_t^{-1}\mathbf{V}_t) - \dim(\mathbf{x}_t) - \ln\frac{\det(\mathbf{V}_t)}{\det(\bar{\mathbf{V}}_t)}\right), \qquad (4.31)\end{aligned}$$

where $\dim()$ denotes vector dimension. Matching the quadratic term in (4.30) with $\mathbf{u}_t^T\mathbf{R}_t\mathbf{u}_t$ in the loss function (4.27) establishes the choice of $\bar{\mathbf{V}}_t$ in (4.28).

Without loss of generality, let us assume a reference trajectory $\mathbf{s}_{0:N} = \mathbf{0}$.

Let us now show that, indeed, both the duality-based result and the standard Riccati equations give coincident control laws. Consider Bellman function $J_N = \frac{1}{2}\mathbf{x}_N^T\mathbf{S}_N\mathbf{x}_N$ with $\mathbf{S}_N = \mathbf{Q}_N$, for $t = N-1$ the following holds:

$$\begin{aligned}p_\pi(\mathbf{x}_{t+1}|\mathbf{x}_t) &\propto e^{-\mathbf{x}_N^T\mathbf{S}_N\mathbf{x}_N}\mathcal{N}(\mathbf{A}_{N-1}\mathbf{x}_{N-1}, \bar{\mathbf{V}}_{N-1}) \qquad (4.32)\\ &= \mathcal{N}(\hat{\mathbf{x}}_\pi, \boldsymbol{\Sigma}_\pi), \qquad (4.33)\end{aligned}$$

with moments $\hat{\mathbf{x}}_\pi = \boldsymbol{\Sigma}_\pi^{-1}\bar{\mathbf{V}}_{N-1}^{-1}\mathbf{A}_{N-1}\mathbf{x}_{N-1}, \boldsymbol{\Sigma}_\pi = (\mathbf{S}_N + \bar{\mathbf{V}}_{N-1}^{-1})^{-1}$

The KL divergence (4.16) to minimize is then:

$$\begin{aligned}\mathrm{KL}(p||p_\pi) &= \frac{1}{2}\mathbf{e}_{N-1}\boldsymbol{\Sigma}_\pi^{-1}\mathbf{e}_{N-1} + c_{KL} \qquad (4.34)\\ \mathbf{e}_{N-1} &= \mathbf{A}_{N-1}\mathbf{x}_{N-1} + \mathbf{B}_{N-1}\mathbf{u}_{N-1} - \boldsymbol{\Sigma}_\pi^{-1}\bar{\mathbf{V}}_{N-1}^{-1}\mathbf{A}_{N-1}\mathbf{x}_{N-1}, \qquad (4.35)\end{aligned}$$

which is minimized for

$$\begin{aligned}\mathbf{B}_{N-1}\mathbf{u}_{N-1} &= -\mathbf{B}_{N-1}\mathbf{K}_{N-1}\mathbf{x}_{N-1}\\ \mathbf{K}_{N-1} &= \left(\mathbf{R}_{N-1} + \mathbf{B}_{N-1}^T\mathbf{S}_N\mathbf{B}_{N-1}\right)^{-1}\mathbf{B}_{N-1}^T\mathbf{S}_N\mathbf{A}_{N-1}\end{aligned}$$

with minimum $\min \mathrm{KL}(p||p_\pi) = c_{KL}$ which is independent of the state and input. Here, $\mathbf{K}_{N-1}$ was obtained using the matrix inversion lemma.

Because KL divergence term in (4.12) is constant, the cost-to-go is equal to

$$J_{N-1} = \frac{1}{2}\mathbf{x}_{N-1}\mathbf{Q}_{N-1}\mathbf{x}_{N-1} - \log c_{N-1}(\mathbf{x}_{N-1}) + c_{KL}$$

where $c_{N-1}(\mathbf{x}_{N-1}) \propto e^{-\frac{1}{2}\mathbf{x}_{N-1}^T\mathbf{A}_{N-1}^T(\mathbf{S}_N+\bar{\mathbf{V}}_{N-1}^{-1})\mathbf{A}_{N-1}\mathbf{x}_{N-1}}$. This implies that the cost-to-go remains quadratic $J_{N-1} = \frac{1}{2}\mathbf{x}_{N-1}^T\mathbf{S}_{N-1}\mathbf{x}_{N-1} + C'$ with some additional terms that do not affect the minimization and $\mathbf{S}_{N-1}$ takes the form of

the well-known Riccati equation:

$$\begin{aligned}\mathbf{S}_{N-1} &= \mathbf{Q}_N + \mathbf{A}_{N-1}^T \left(\mathbf{S}_N^{-1} + \bar{\mathbf{V}}_{N-1}\right)^{-1} \mathbf{A}_{N-1} \\ &= \mathbf{Q}_N + \mathbf{A}_{N-1}^T \left(\mathbf{S}_N \left[\mathbf{I} - \mathbf{B}_{N-1}\mathbf{K}_{N-1}\right]\right) \mathbf{A}_{N-1} \end{aligned} \tag{4.36}$$

The recursion for $t = N-2, \ldots$ leads to the standard LQR control law.

4.3.3.2 Solution of the Dual Problem

Distributions (4.28) and (4.29) form a definition of the problem of stochastic filtering, where the former is the model of system dynamics, and the latter is known as the observation model. Note that in the dual formulation, the requested values $\mathbf{s}_t$ act as observations.

The first task is to find solution of the integral (4.15). Just like the optimal control problem (4.9), solution of this equation is analytically tractable for linear systems (i.e. $\mathbf{f}(\mathbf{x}_t) = \mathbf{A}_t\mathbf{x}_t$) with Gaussian noise via algorithm known as the Rauch-Tung-Striebel (RTS) smoother (Rauch et al., 1965). The resulting distribution is Gaussian

$$p(\mathbf{x}_{t+1}|\mathbf{x}_t, \mathbf{s}_{t+1:N}) = \mathcal{N}(\hat{\mathbf{x}}_{t+1|N}, \mathbf{P}_{t+1|N})$$

which corresponds to quadratic Bellman function (4.14).

The RTS smoother uses the following steps, given a known $\mathbf{x}_t$ by assumption:

- forward pass of Kalman filter computing $p(\mathbf{x}_\tau|\mathbf{x}_t, \mathbf{s}_{t:\tau})$ for $\tau = t, \ldots, N$.
- backward pass computing the $p(\mathbf{x}_\tau|\mathbf{x}_t, \mathbf{s}_{t:N})$ for $\tau = N-1, \ldots, t+1$.

4.3.3.3 Rauch-Tung-Striebel Nonlinear Controller

If functions $\mathbf{f}(\mathbf{x}_t), \mathbf{h}(\mathbf{x}_t)$ are nonlinear, the RTS can be used for the linearized model at each trajectory point; however, optimality of the proposed estimate is no longer guaranteed. Notwithstanding, this is analogue to the Extended Kalman filter, successfully used in many control and robotics applications.

Inspired on that success, we propose to approximate the nonlinear dual problem by nonlinear extensions of the RTS smoother, such as the Extended RTS (ERTS) (Leondes et al., 1970) which is based on linearization at the point of the expected value. It is well known that Unscented Kalman Filter and Smoothers (Sarkka, 2008) provides more accurate results than EKF, by

propagating lower errors, due to linearization at multiple points given by the Unscented Transform. The Unscented RTS version (URTS) also requires a forward-backward pass and thus, assumptions done for ERTS will be also extended to URTS. Simulations and experiments later in this paper will show that, indeed, good performance in practice can be achieved using the duality via ERTS or URTS framework in the algorithms to be discussed next. In next section, a comparative analysis of accuracy and computing time is discussed in the context of a robotic application example.

A receding horizon implementation of the above ERTS/URTS control laws will be pursued; thus, at any arbitrary instant t, with known state $\mathbf{x}_t$, the needed estimate distribution will be a Gaussian distribution

$$p_\pi = p(\mathbf{x}_{t+1}|\mathbf{x}_t, \mathbf{s}_{t+1:t+N}) = \mathcal{N}(\hat{\mathbf{x}}_{t+1|t+N}, \mathbf{P}_{t+1|t+N}) \tag{4.37}$$

with mean value $\hat{\mathbf{x}}_{t+1|t+N}$ and covariance matrix $\mathbf{P}_{t+1|t+N}$.

4.3.3.3.1 Computation of Nonlinear Control Law Once the estimation problem has been solved by either of the two above proposals, duality indicates that the optimal control action should fulfil the implicit equation (4.16). The Gaussian approximation of the smoother (4.37) defines the second argument of the KL cost (4.16) yielding the implicit function to be defined as a minimizer of quadratic loss $\mathrm{KL}(p||p_\pi) = \mathbf{e}_t \mathbf{P}^{-1}_{t+1|t+N} \mathbf{e}_t$ plus constants with:

$$\mathbf{e}_t = \mathbf{f}(\mathbf{x}_t) + \mathbf{B}_t \mathbf{u}_t - \hat{\mathbf{x}}_{t+1|t+N} \tag{4.38}$$

The minimizer is found to be

$$\mathbf{u}_t = (\mathbf{B}_t^T \mathbf{P}^{-1}_{t+1|t+N} \mathbf{B}_t)^{-1} \mathbf{B}_t^T \mathbf{P}^{-1}_{t+1|t+N} (\hat{\mathbf{x}}_{t+1|t+N} - \mathbf{f}(\mathbf{x}_t)) \tag{4.39}$$

using standard minimization of quadratic functions.

Computational simplification. We note that for invertible matrices $\mathbf{B}_t$, $\mathbf{e}_t$ can be trivially made zero and hence, the variance of the smoother is irrelevant and does not need to be evaluated. This is also the case for LTV systems or when using linearisation-based approaches such as ERTS, because the smoother with perfect knowledge of $\mathbf{x}_t$ provides an estimation such that $\mathbf{f}(\mathbf{x}_t) - \hat{\mathbf{x}}_{t+1|t+N}$ always lies in the space of $\mathbf{B}_t \mathbf{u}_t$, so (4.38) can always be solved for $\mathbf{u}_t$, hence (4.39) gives the same result as

$$\mathbf{u}_t = (\mathbf{B}_t^T \mathbf{B}_t)^{-1} \mathbf{B}_t^T (\hat{\mathbf{x}}_{t+1|t+N} - \mathbf{f}(\mathbf{x}_t)) \tag{4.40}$$

Algorithm 1 ERTS Controller

[Initialization]
1: $\hat{\mathbf{x}}_{t|t} = \mathbf{x}_t$, $\mathbf{P}_{t|t} = \mathbf{0}$
[Prediction]
2: **for** $\tau = t+1, \ldots, t+N$ **do**
3: $\quad \hat{\mathbf{x}}_{\tau|\tau-1} = \mathbf{f}(\hat{\mathbf{x}}_{\tau-1|\tau-1})$
[linearization]
4: $\quad \mathbf{A}_{\tau-1} = \frac{\partial \mathbf{f}}{\partial \mathbf{x}_{\tau-1}}\Big|_{\mathbf{x}_{\tau-1}=\hat{\mathbf{x}}_{\tau-1|\tau-1}}$
5: $\quad \mathbf{H}_{\tau} = \frac{\partial \mathbf{h}}{\partial \mathbf{x}_{\tau}}\Big|_{\mathbf{x}_{\tau}=\hat{\mathbf{x}}_{\tau|\tau-1}}$
6: $\quad \mathbf{P}_{\tau|\tau-1} = \mathbf{A}_{\tau-1}\mathbf{P}_{\tau-1|\tau-1}\mathbf{A}_{\tau-1}^T + \mathbf{B}_{\tau-1}\mathbf{R}_{\tau-1}^{-1}\mathbf{B}_{\tau-1}^T$
7: $\quad \mathbf{K}_{\tau} = \mathbf{P}_{\tau|\tau-1}\mathbf{H}_{\tau}^T(\mathbf{H}_{\tau}\mathbf{P}_{\tau|\tau-1}\mathbf{H}_{\tau}^T + \mathbf{Q}_{\tau}^{-1})^{-1}$
8: $\quad \mathbf{P}_{\tau|\tau} = (\mathbf{I} - \mathbf{K}_{\tau}\mathbf{H}_{\tau})\mathbf{P}_{\tau|\tau-1}$
9: $\quad \hat{\mathbf{x}}_{\tau|\tau} = \hat{\mathbf{x}}_{\tau|\tau-1} + \mathbf{K}_{\tau}(\mathbf{s}_{\tau} - \mathbf{h}(\hat{\mathbf{x}}_{\tau|\tau-1}))$
10: **end for**
[Smoothing]
11: **for** $\tau = t+N-1, t+N-2, \ldots, t+1$ **do**
12: $\quad \mathbf{L}_{\tau} = \mathbf{P}_{\tau|\tau}\mathbf{A}_{\tau}^T\mathbf{P}_{\tau+1|\tau}^{-1}$
13: $\quad \hat{\mathbf{x}}_{\tau|t+N} = \hat{\mathbf{x}}_{\tau|\tau} + \mathbf{L}_{\tau}(\hat{\mathbf{x}}_{\tau+1|t+N} - \hat{\mathbf{x}}_{\tau+1|\tau})$
14: **end for**
[Control computation]
15: $\mathbf{u}_t = (\mathbf{B}_t^T\mathbf{B}_t)^{-1}\mathbf{B}_t^T(\hat{\mathbf{x}}_{t+1|t+N} - \mathbf{f}(\mathbf{x}_t))$

4.3.3.3.2 ERTS Control Algorithm From the above considerations, the resulting Algorithm 1, denoted as Extended Rauch-Tung-Striebel (ERTS) controller, consists of two parts: 1) computing $\hat{\mathbf{x}}_{t+1|t+N}$ via the ERTS smoother, and 2) obtaining the approximation of the optimal control (4.40). The state $\mathbf{x}_t$ is assumed to be known, so the proposed controller is a deterministic state feedback one. Due to simplification (4.40) evaluation of $\mathbf{P}_{\tau|t+N}$ can be omitted in the smoothing algorithm. Also, note that in order to provide a valid solution for the smoothing algorithm, matrix $\mathbf{P}_{\tau+1|\tau}$ must be full-rank, otherwise, its Moore-Penrose pseudo-inverse should be used in line 12. Indeed, the pseudo-inverse would provide zero correction in line 13 in the state directions in which the reference dynamics noise does have zero variance. From a duality point of view, that amounts to requiring zero control action effect on uncontrollable states.

4.3.3.3.3 URTS Control Algorithm As an alternative to the ERTS controller, Algorithm 2 implements the Unscented RTS (URTS) controller. The steps are the same with the difference that it uses the Unscented Transform

Algorithm 2 URTS Controller

[Initialization]

1: $\hat{\mathbf{x}}_{t|t} = \mathbf{x}_t$, $\mathbf{P}_{t|t} = \mathbf{0}$, $\alpha = 1$, $\beta = 0$, $\kappa = 3 - \dim(\mathbf{x}_t)$

[Prediction]

2: **for** $\tau = t+1, \ldots, t+N$ **do**

[Augmented State (system noise)]

3: $\mathbf{x}^a_{\tau-1|\tau-1} = \begin{bmatrix} \hat{\mathbf{x}}^T_{\tau-1|\tau-1} & \mathbf{0}^T \end{bmatrix}^T$

4: $\mathbf{P}^a_{\tau-1|\tau-1} = \text{block\_diag}\left(\mathbf{P}_{\tau-1|\tau-1}, \mathbf{B}_{\tau-1}\mathbf{R}^{-1}_{\tau-1}\mathbf{B}^T_{\tau-1}\right)$

[Unscented Transform & Predict]

5: $[\hat{\mathbf{x}}_{\tau|\tau-1}, \mathbf{P}_{\tau|\tau-1}] = \text{UT}(\mathbf{x}^a_{\tau-1|\tau-1}, \mathbf{P}^a_{\tau-1|\tau-1}, \mathbf{f}, \alpha, \beta, \kappa)$

[Augmented State (measurement noise)]

6: $\mathbf{x}^a_{\tau|\tau-1} = \begin{bmatrix} \hat{\mathbf{x}}^T_{\tau|\tau-1} & \mathbf{0}^T \end{bmatrix}^T$

7: $\mathbf{P}^a_{\tau|\tau-1} = \text{block\_diag}\left(\mathbf{P}_{\tau|\tau-1}, \mathbf{Q}^{-1}_{\tau}\right)$

[Unscented Transform & Update]

8: $[\hat{\mathbf{s}}_{\tau|\tau-1}, \mathbf{P}^{ss}_{\tau|\tau-1}, \mathbf{P}^{xs}_{\tau|\tau-1}] = \text{UT}(\mathbf{x}^a_{\tau|\tau-1}, \mathbf{P}^a_{\tau|\tau-1}, \mathbf{h}, \alpha, \beta, \kappa)$

9: $\mathbf{K}_\tau = \mathbf{P}^{xs}_{\tau|\tau-1}(\mathbf{P}^{ss}_{\tau|\tau-1})^{-1}$

10: $\mathbf{P}_{\tau|\tau} = \mathbf{P}_{\tau|\tau-1} - \mathbf{K}_\tau \mathbf{P}^{ss}_{\tau|\tau-1}\mathbf{K}^T_\tau$

11: $\hat{\mathbf{x}}_{\tau|\tau} = \hat{\mathbf{x}}_{\tau|\tau-1} + \mathbf{K}_\tau(\mathbf{s}_\tau - \hat{\mathbf{s}}_{\tau|\tau-1})$

12: **end for**

[Smoothing]

13: **for** $\tau = t+N-1, t+N-2, \ldots, t+1$ **do**

[Augmented State (system noise)]

14: $\mathbf{x}^a_{\tau|\tau} = \begin{bmatrix} \hat{\mathbf{x}}^T_{\tau|\tau} & \mathbf{0}^T \end{bmatrix}^T$

15: $\mathbf{P}^a_{\tau|\tau} = \text{block\_diag}\left(\mathbf{P}_{\tau|\tau}, \mathbf{B}_\tau\mathbf{R}^{-1}_\tau\mathbf{B}^T_\tau\right)$

[Unscented Transform & Smooth]

16: $[\hat{\mathbf{x}}_{\tau+1|\tau}, \mathbf{P}_{\tau+1|\tau}, \mathbf{C}_{\tau+1|\tau}] = \text{UT}(\mathbf{x}^a_{\tau|\tau}, \mathbf{P}^a_{\tau|\tau}, \mathbf{f}, \alpha, \beta, \kappa)$

17: $\mathbf{L}_\tau = \mathbf{C}_{\tau+1|\tau}\mathbf{P}^{-1}_{\tau+1|\tau}$

18: $\hat{\mathbf{x}}_{\tau|t+N} = \hat{\mathbf{x}}_{\tau|\tau} + \mathbf{L}_\tau(\hat{\mathbf{x}}_{\tau+1|t+N} - \hat{\mathbf{x}}_{\tau+1|\tau})$

19: $\mathbf{P}_{\tau+1|t+N} = \mathbf{P}_{\tau|\tau} + \mathbf{L}_\tau(\mathbf{P}_{\tau+1|t+N} - \mathbf{P}_{\tau+1|\tau})\mathbf{L}^T_\tau$

20: **end for**

[Control computation]

21: $\mathbf{u}_t = (\mathbf{B}^T_t\mathbf{P}^{-1}_{t+1|t+N}\mathbf{B}_t)^{-1}\mathbf{B}^T_t\mathbf{P}^{-1}_{t+1|t+N}(\hat{\mathbf{x}}_{t+1|t+N} - \mathbf{f}(\mathbf{x}_t))$

(UT) on lines 5, 8 and 16 to compute the mean and covariance. The UT accepts the mean and covariance of a variable $\mathbf{x}$ and returns the mean and covariance of $\mathbf{s}$ and (optionally as third argument) cross-covariance between $\mathbf{x}$ and $\mathbf{s}$ passed through a given function $\mathbf{s} = \mathbf{f}(\mathbf{x})$, where α, β and κ are well-known parameters used to spread sigma-points (Sarkka, 2008).

4.3.4 Benchmarking: Trajectory Tracking in Wheeled Robots

In this section, we analyse and discuss the benefits of the proposed algorithms compared to iLQR, NMPC and AICO. The study is based on the application to kinematic control of non-holonomic wheeled robots (Scheuer and Xie, 1999).

A vehicle state $\mathbf{x}_t{=}(x_t, y_t, \theta_t, v_t, \omega_t)^T$ in time instant t is characterized by coordinates (x_t, y_t), orientation (θ_t), linear velocity (v_t) and angular velocity (ω_t) and it evolves through input $\mathbf{u}_t = (a_t, \alpha_t)^T$ given by linear acceleration (a_t) and angular acceleration (ω_t) as

$$\mathbf{x}_{t+1} = \mathbf{f}(\mathbf{x}_t) + \mathbf{B}(\mathbf{x}_t)\mathbf{u}_t \tag{4.41}$$

$$\begin{bmatrix} x_{t+1} \\ y_{t+1} \\ \theta_{t+1} \\ v_{t+1} \\ \omega_{t+1} \end{bmatrix} = \begin{bmatrix} x_t + v_t \Delta t \cos\theta_t \\ y_t + v_t \Delta t \sin\theta_t \\ \theta_t + \omega_t \Delta t \\ v_t \\ \omega_t \end{bmatrix} + \begin{bmatrix} 0 & 0 \\ 0 & 0 \\ 0 & 0 \\ \Delta t & 0 \\ 0 & \Delta t \end{bmatrix} \begin{bmatrix} a_t \\ \alpha_t \end{bmatrix} \tag{4.42}$$

The transition matrix of linearized system is:

$$\mathbf{A}(\mathbf{x}_t) = \frac{\partial \mathbf{f}}{\partial \mathbf{x}_t} = \begin{pmatrix} 1 & 0 & -v_t \Delta t \sin\theta_t & \Delta t \cos\theta_t & 0 \\ 0 & 1 & v_t \Delta t \cos\theta_t & \Delta t \sin\theta_t & 0 \\ 0 & 0 & 1 & 0 & \Delta t \\ 0 & 0 & 0 & 1 & 0 \\ 0 & 0 & 0 & 0 & 1 \end{pmatrix}$$

being $\Delta t = 0.05s$ the simulation step (Euler integration).

Let us discuss the detailed setting of each of the compared control strategies, all of them geared towards minimising the quadratic cost (4.27) with $\mathbf{h}_t(\mathbf{x}_t){=}\mathbf{x}_t$. The aim is to drive a vehicle around a desired trajectory $\mathbf{s}_{0:N}$. The trajectory is given by a reference speed of $\bar{v}_t = 0.5ms^{-1}$, the reference positions, $\bar{x}_t = \bar{v}_t t$, $\bar{y}_t = 0m$, orientation $\bar{\theta}_t = 0rad$ and angular velocity $\bar{\omega}_t = 0rads^{-1}$, with

$$\mathbf{s}_t = (\bar{x}_t\ \bar{y}_t\ \bar{\theta}_t\ \bar{v}_t\ \bar{\omega}_t)^T \tag{4.43}$$

Penalization matrices have been set to $\mathbf{Q}_t = \text{diag}(25, 25, 1, 1, 1)$ and $\mathbf{R}_t = \text{diag}(0.5, 1)$. The tracking problem will be set up with a horizon $N = 60$, assuming that the whole the trajectory is known in advance. Note that, intentionally, due to the weights in absolute speeds (4th and 5th states) and accelerations (input variables) the optimal trajectory will have some tracking position error (small, as the position error weight is high). A comparative

between ERTS and iLQR in a case with abrupt reference changes can be found in Zima et al. (2013).

The following strategies will be compared:

1. *Iterative Linear Quadratic controller (iLQR)*. This algorithm initializes with $\mathbf{u}_{0:N-1} = \mathbf{0}$ and uses the open-loop trajectory $\mathbf{x}_{t+1} = \mathbf{f}(\mathbf{x}_t) + \mathbf{B}(\mathbf{x}_t)\mathbf{u}_t$ with $\mathbf{x}_0$ as initial linearization point. This algorithm computes on every iteration a variation of control input $\delta\mathbf{u}_t$ based on a Hessian approximation with Levenberg-Marquardt (LM) method and re-linearizes the process at the new trajectory as indicated in Todorov and Li (2005) (and implemented in Tassa (2011)).

2. *ERTS approach*, in two settings:

   - Non-iterative (standalone) ERTS. Algorithm 1.
   - *Iterative Linear Quadratic controller (iLQR) initialized with ERTS solution, denoted as ERTS+*. Obviously, the cost for iteration 1 equals the non-iterative ERTS cost.

3. *URTS approach*. Similar to ERTS approach but using Algorithm 2 instead, in the two above settings. The iterative version is denoted as URTS+.

4. *Nonlinear Model Predictive Control (NMPC)*. This algorithm performs the open-loop optimization of performance index using nonlinear model and iterations in order to compute gradients and Hessians at the optimal points. Initialization $\mathbf{u}_{0:N-1} = \mathbf{0}$ is used (based on Grüne and Pannek (2011)).

5. *Approximate Inference Control (AICO)*. The iterative forward-backward message passing algorithm implementation is Algorithm 2 in Toussaint (2009). AICO tuning parameters are set to $\alpha = 0.9$ and $\theta = 0.1$, as used in Toussaint (2009).

4.3.4.1 Analysis Setup

A set of $L = 100$ simulations have been considered with an uniformly distributed random initialization over robot state $\mathbf{x}_0^i \sim \mathcal{U}(0, [-1, 1], [-\frac{\pi}{2}, \frac{\pi}{2}], [-0.5, 0.5], [-0.5, 0.5])$, for $i = 1, \ldots, L$. For each experiment i and optimizer iteration k, the achieved performance for each of the five strategies will be denoted as $J_s(i, k)$, for $s = 1, \ldots, 5$.

On each iteration k, the method with the best cost is taken as reference to compare against other methods, i.e. $J_{best}(i,k) = \min_{1\leq s\leq 5}(J_s(i,k))$.

A cost-ratio for each experiment and iteration is defined as:

$$R_s(i,k) = \frac{J_s(i,k)}{J_{best}(i,k)}, \quad s = 1,\ldots,5 \tag{4.44}$$

Based on the definition of the cost-ratio, some useful metrics are also defined:

- Mean cost-ratio (MCR) per iteration, i.e., average of cost ratio over all simulations: $MCR_s(k) = \frac{1}{L}\sum_{i=1}^{L} R_s(i,k)$.

- Worst cost-ratio (WCR) per iteration: $WCR_s(k)$=$\max_{1\leq i\leq L}(R_s(i,k))$.

In order to suitably compare the five algorithms, some unifying conditions must be also set up:

- Note that ERTS (#2), URTS (#3) and AICO (#5) produce an estimated optimal state trajectory whereas iLQR (#1) and NMPC (#4) produce a whole batch of N future inputs. In order to compare the finite-horizon cost estimates from a particular initial condition $\mathbf{x}_0$, trajectory $\{\hat{\mathbf{x}}_{1|N}$, $\ldots$, $\hat{\mathbf{x}}_{N|N}\}$ is computed for strategies #2, #3 and #5, and future inputs $\mathbf{u}_{0:N-1}$ for the #1, #4 ones. Then, the optimal smoothed state trajectory (#2, #3, #5) is taken as "reference" to compute control inputs $\mathbf{u}_{0:N-1}$ via the Least-Squares fit (4.39) (or simplification (4.40) in ERTS) and the open-loop model (4.41). Obviously, due to linearization errors, the actual forward simulation will not be exactly coincident with the original estimated state trajectory but, anyway, performance indices are computed with such input and state sequences.

- The maximum number of iterations are fixed to 30, and cost indices are evaluated at each iteration to assess convergence speed. Here, the concept of iteration means carrying out the necessary computations such that the cost is monotonically reduced (which, in a general case, does involve *nested* iterations to assess suitable step sizes).

- Convergence (in iterative strategies) is achieved when the relative performance improvement is below a given relative threshold value such that
$\left|\frac{J_s(i,k)-J_s(i,k-1)}{J_s(i,k-1)}\right| < 10^{-4}$.

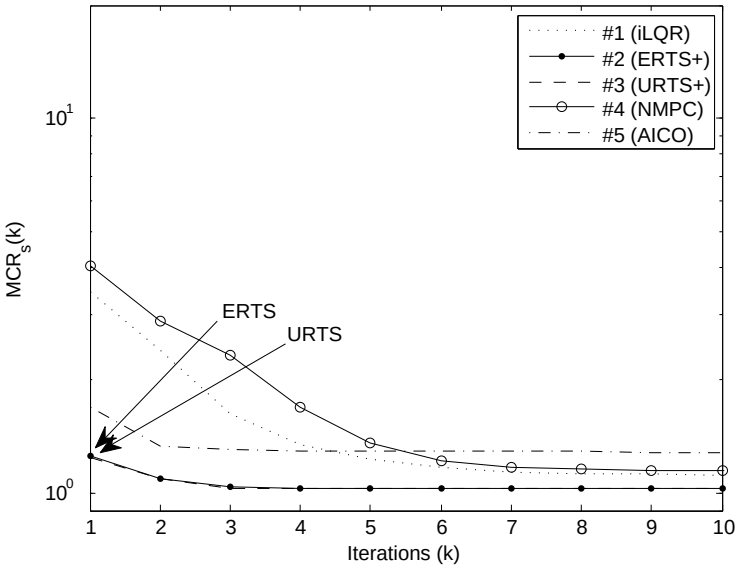

Figure 4.9: Mean-cost ratio (MCR) per iteration.

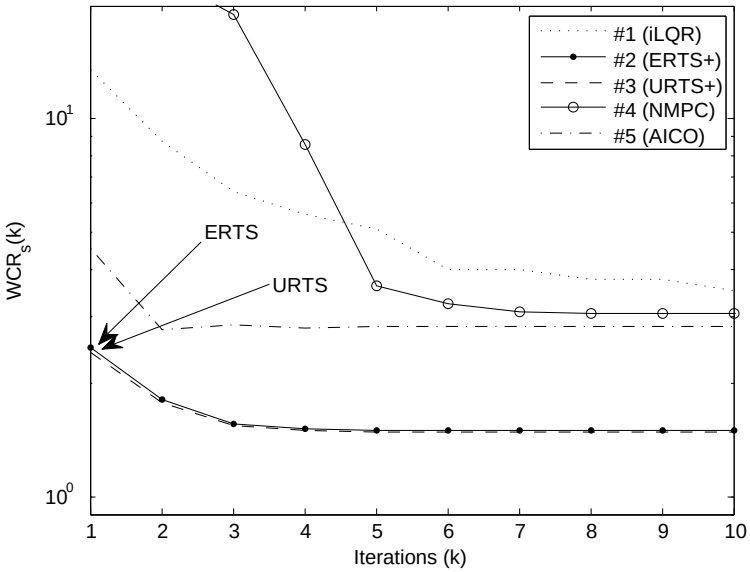

Figure 4.10: Worst-cost ratio (WCR) per iteration.

4.3.4.2 Mean-cost and Worst-cost Ratios

Figures 4.9 and 4.10 depict the above-defined mean-cost ratio $MCR_s(k)$ and worst-cost ratio $WCR_s(k)$, respectively, in logarithmic scale for first 10 iterations. It can be clearly appreciated that strategies #2, #3 and #5 provide an initial solution ($k = 1$) with a significantly lower cost than strategies #1 and #4. This was expected, due to the approximately optimal output of the proposed non-iterative ERTS, URTS and the first iteration of message-passing algorithm in AICO (#5). It can be seen that AICO ($k = 1$) shows worse performance than ERTS and URTS, likely because mean and covariance of Gaussian messages use a linearized approach (recall that ERTS use the nonlinear system to predict states and linearization to predict covariances and URTS uses the UT to account nonlinearities). After 10 iterations, iLQR initialized with ERTS or URTS provides the best performance (actually, they converge in around 4 iterations).

Table 4.4 shows the numerical results of the convergence analysis for different performances. Based on Table 4.4, some remarks about particular numerical values can be made:

- The mean cost ratio of (non-iterative) ERTS algorithm is 1.25, and the worst cost is 2.48. That is, 45% of cases yield a performance cost nearly optimal.
- The mean cost ratio of URTS algorithm is 1.24, and the worst cost is 2.41, providing only marginally better accuracy than ERTS. In this case, 48% of cases provide a cost nearly optimal.
- The mean cost ratio for ERTS+ and URTS+ is 1.03, providing even better accuracy than iLQR due to its initialization. Table 4.4 shows that $90\% - 91\%$ of cases are below 10% penalty after convergence, which is achieved in 4 iterations (in mean).
- AICO is able to improve over ERTS only in 54% of cases, while NMPC gets stuck in 18% of cases (or needs more iterations to converge).

4.3.4.3 Computational Resources

Table 4.5 shows the mean computational effort for every strategy and simulation relative to ERTS. It clearly shows that ERTS computational cost is significantly lower for the same performance with respect to iterative approaches. URTS and iLQR have a cost 2.6 and 2.65 times higher than ERTS, respectively. The ERTS+ also improves the computational cost with respect to iLQR

Table 4.4: Mean and worst-case cost ratio with respect to best result with percentage of cases better than some performance levels.

	ERTS	URTS	iLQR	ERTS+	URTS+	NMPC	AICO
MCR	1.25	1.24	1.07	1.03	1.03	1.15	1.28
WCR	2.48	2.41	2.11	1.5	1.49	3.05	2.81
$\leq$ERTS	–	100%	96%	100%	100%	91%	54%
$\leq$URTS	0%	–	96%	93%	100%	91%	52%
$\approx$Best†	45%	48%	89%	90%	91%	82%	29%

† Percentage of cases with an overcost below 10% w.r.t. J_{best}.

Table 4.5: Mean execution time ratio with respect to ERTS.

	ERTS	URTS	iLQR	ERTS+	URTS+	NMPC	AICO
$\leq$ERTS	1	2.6	2.65	1	2.6	77.6	4
$\leq$URTS	–	2.6	2.68	1.29	2.6	79.3	4.1
Converged	–	–	6.75	5.41	7.04	175.5	19.6

in $\frac{6.75}{5.41} \rightarrow 23\%$, providing even more accurate results. As a consequence, ERTS can be considered a computationally efficient way of obtaining near-optimal results in practice, either by itself or as a "seed" for other iterative approaches.

In addition to this, ERTS+ is also an attractive option considering cost/-computational time trade-off. In this sense, under real-time deadlines, we can iterate ERTS+ until deadline hit or with just very few iterations. The performance, in terms of accuracy, robustness and computational time is expected to be better than iLQR. URTS does not outperform ERTS in any meaningful way, and the other strategies require far more computing time and parameter tweaking to obtain the best results.

4.3.5 DCC Path as Reference

One of the main drawbacks of the proposed controllers is that are meant for nonlinear unconstrained systems. However, a wheeled mobile robot following a trajectory is a dynamic system with several constraints, such as non-holonomicity or bounds in the maximum value of curvature, linear and angular velocities, among other physical limitations. In this sense, a simple example of convergence to a pose in the plane is used to illustrate such a problem. Then, DCC paths are used as a reference to the ERTS controller, so that constraints are satisfied.

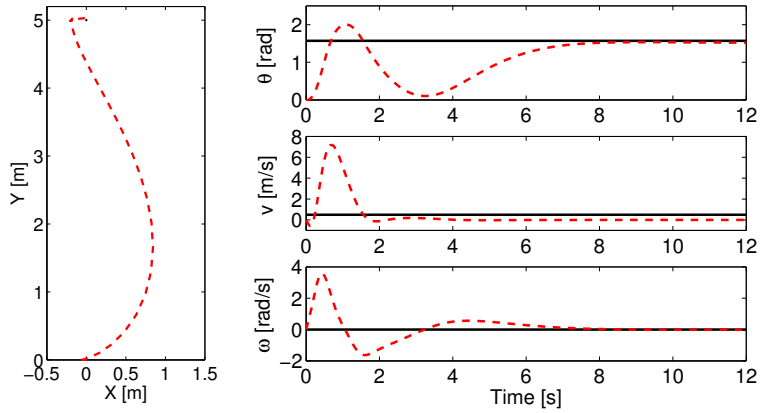

(a) (b)

Figure 4.11: ERTS controller guiding the non-holonomic vehicle. State variables evolution (dashed red line) and reference (black line).

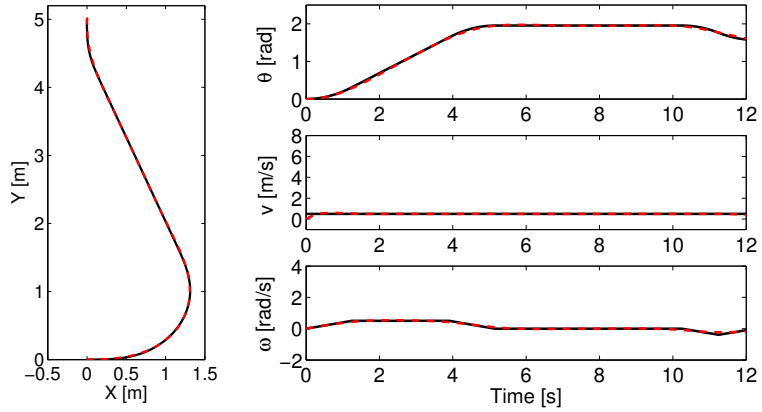

(a) (b)

Figure 4.12: ERTS controller using a DCC path as a reference to guide the non-holonomic vehicle. State variables evolution (dashed red line) and reference (black line).

Figures 4.11 and 4.12 show an example of ERTS controller guiding a non-holonomic vehicle from initial configuration $q_R = (0, 0, 0, 0)^T$ to the target $q_T = (0, 5, \pi/2, 0)^T$, where matrices for the ERTS controller are set to $R = \text{diag}(1, 1)$ and $Q = \text{diag}(100, 100, 1, 1, 1)$ The reference speed is set to $v_{ref} = 0.5$ m/s, being $\kappa_{max} = 1$ rad/m and $\sigma_{max} = 5/\pi$ rad/m^2 the maximum values of curvature and sharpness, respectively. In Figure 4.11 the original ERTS controller is used, whilst a DCC path is used as reference in Figure 4.12.

After analysing Figure 4.11(a), it can be concluded that the ERTS controller is not able to guide the vehicle to converge smoothly to the target configuration. Initially the vehicle moves backwards and then speeds up very quickly, as shown in Figure 4.11(b). At the same time it starts turning to point to the target configuration. However, when the vehicle is close to the final configuration it needs to correct its position and orientation doing some weird manoeuvres.

On the other hand, when a DCC path is used to plan a smooth trajectory, the ERTS controller performs much better. In fact, as shown in Figure 4.12(a) the vehicle reaches the final configuration minimizing the convergence error, without doing any unnatural manoeuvre. In Figure 4.12(b) it can be observed that the references for all the state variables are followed properly.

Now, let's analyse what happens with the values of curvature and sharpness in both cases, with and without DCC as reference. In Figure 4.13(a) it can be observed that the controller does not take into account the constraints and the bounds in curvature and sharpness are violated. However, Figure 4.13(b) shows that this phenomenon does not happen when using DCC paths, where curvature and sharpness are kept within bounds during the whole experiment. That result is produced by the fact that the controller follows a smooth reference that does consider such limits.

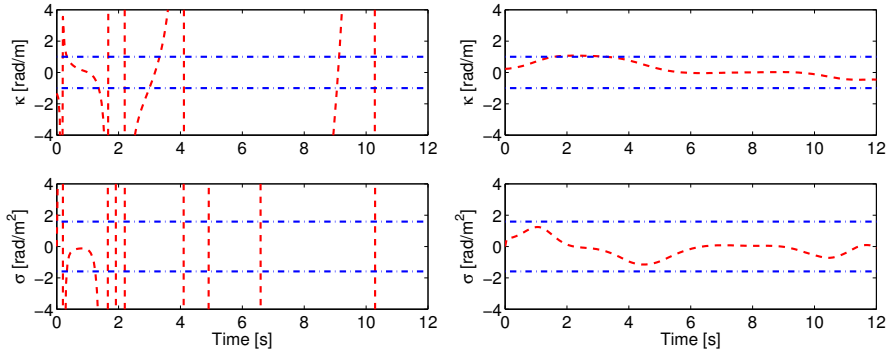

(a) Without DCC trajectory reference (b) With DCC trajectory reference

Figure 4.13: Curvature and sharpness evolution with ERTS control of the nonholonomic vehicle. Curvature and sharpness variables (dashed red line) and maximum bounds (dash-doted blue line).

4.4 Conclusions

A new method for path following using continuous-curvature paths subject to constraints on curve sharpness and maximum curvature has been introduced in Section 4.2. The method computes DCC paths from any arbitrary starting and target configurations, based on clothoids, to generate smooth references for the kinematic controller. A heuristic criterion has been implemented to find the shortest path joining both configurations. Target configurations are obtained from a sequence of waypoints computed by a global path planner or a vision-based line following system. The kinematic controller computes trajectories from a combination of DCC paths and speed profiles, based on a "slow-in" and "fast-out" policy. A closed-loop feedback structure is implemented to improve robustness in path following problems, recomputing curvatures and speed profiles, based on odometry data and Look-Ahead distance.

An exhaustive analysis to evaluate the performance of the new method with respect to Pure-Pursuit controller has also been provided. It is shown that the proposed method has better performance in terms of settling time, overshoot and error, while it has little influence on design parameters. Besides, it can also be said that the DCC method introduces improvements in comfort and safety because sharpness, normal jerk and mean abruptness are lower than with the PP control.

In Section 4.3, a duality-based Extended Rauch-Tung-Striebel (ERTS) controller has been presented, which solves the control task via the transformation of the original problem to a dual estimation problem, using future reference states as observations. The dual problem is solved via a Rauch-Tung-Striebel smoother for linearized system (non-iterative). In a linear time-varying case, the algorithm is equivalent to the well-known unconstrained LQR control. An extension using Unscented Transform has been also presented, coined as URTS. However, the performance improvement over ERTS was almost unnoticeable and the computational cost is almost 3 times higher.

Finally, the performance of the proposed ERTS and URTS controllers is studied on a trajectory-following problem of a 5th-order mobile robot and compared with well-known nonlinear iterative linearization-based algorithms such as iLQR, NMPC and AICO. Simulations show that ERTS generates nearly the same control as iLQR and NMPC controllers after convergence, but with a significant computational cost reduction. In fact, ERTS can be considered a good choice for initialization of the above iterative algorithms. Hence, accuracy and reduced computational cost makes ERTS an interesting option for real-time control *with receding horizon policies*.

Future work will consider other nonlinear estimation paradigms such as particle filter approaches for the dual estimation problem. We expect that these approaches would propose better performance than ERTS and URTS controllers when more severe nonlinearities are present. Moreover, as the assumption on Gaussian noises in the dual estimation problem implies that both state and control action are unconstrained, ERTS and URTS will fail on problems with hard constraints. On the other hand, a controller based on a particle filter does not need such assumption. In this sense, an implementation of a particle controller and case studies on problems with constraints are also left for future work.

Chapter 5

Smooth Control Applications

5.1 Introduction

In Chapters 3 and 4, smooth path generation and control methods based on Double Continuous-Curvature paths have been introduced. Here, we are going to show four different applications in which DCC paths are successfully used.

In the first application, a vision-based smooth line following application is described, where DCC paths are used as reference to converge to a line painted on the floor. An automated industrial forklift was used in the experimentation.

On the other hand, driving industrial vehicles at high speeds constitutes one of the most challenging situations in real-life problems since most of actual AGV solutions have low through-output performance characterized by providing low speed solutions. In this type of problems, standard sharpness and curvature bounds do not guarantee dynamic stability. In this sense, the contribution of the second application is to provide necessary conditions for vehicle stability with an industrial forklift carrying a heavy load at high speeds and to provide an exhaustive analysis to evaluate the performance of the new method against classic controllers.

In the third application, a subset of DCC paths, named Quasi-Holonomic Continuous-Curvature paths, are integrated into well-known obstacle avoidance algorithms in order to generate continuous-curvature references, while taking curvature and sharpness bounds into account. A proper benchmarking is carried out to show the benefits of the proposed smooth obstacle avoidance algorithm.

Finally, a trajectory following experiment has been developed in order to validate the ERTS controller, using a Pioneer 3DX mobile robot (Adept Mobilerobots, 1995). The implementation is carried out with a receding horizon policy, solving the (unconstrained) path following problem, where the goal is to track a robot along a desired path.

5.2 Vision-Based Line Following

Waypoints, typically obtained from a global path planner, can also be given by a vision system without requiring a previously computed map. The task for the vision system is to detect a path to follow from road profiles or ground-painted lines. In this sense, an industrial forklift (Nichiyu FBT15) has been automated to perform as a line-follower Autonomous Ground Vehicle (AGV), as shown in Figure 5.1. It has three wheels in tricycle configuration (an orientable rear wheel and two fixed drive wheels at the front), a PLC for low-level vehicle control, an industrial PC for high level control, encoders as odometry system, a smart camera to detected ground painted lines and determine a goal configuration to be reached (see Figure 5.1(c)) and a laser range finder to avoid obstacles and build a map if necessary. The implementation for detecting lines on images uses standard procedures of OpenCV library (Bradski and Kaehler, 2008) and therefore no particular contribution about the algorithm is claimed in this section.

Algorithm 3 describes the proposed kinematic controller particularized for the vision-based path following problem. Lines from 3 to 8 are executed every time a new image is available and as a result a new target configuration $\mathbf{q}_T(t)$ is obtained with respect to the fixed frame (i.e. the world frame) and parameters of a DCC path are also computed. Then, it computes a DCC path in lines 7 and 8 by taking into account that the lengths of the line segments must be necessarily positive, otherwise relax the solution as described in Section 3.4.3. Then compute a new robot curvature controller in lines 10 and 11. The latter part of the algorithm determines an appropriate robot speed and updates the robot position using odometry or stereoceptive sensors, i.e. based on SLAM techniques, where no more specific details are given since these two aspects are out of the scope of this section.

Target configurations $\mathbf{q}_T$ are obtained from a line detection procedure using the computer vision system. The following description represents a particular implementation, although other procedures are possible:

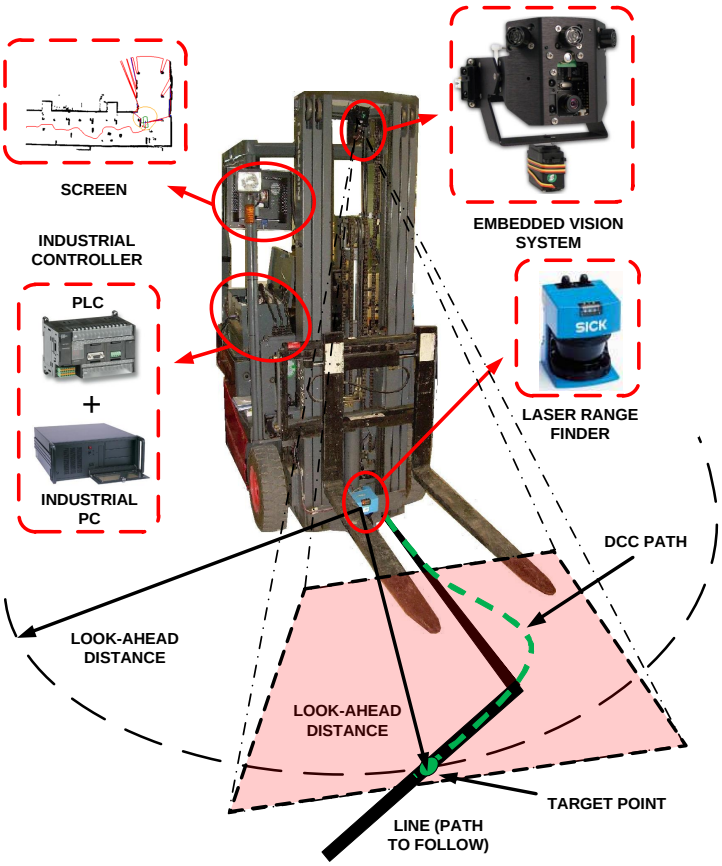

(a) Autonomous industrial forklift

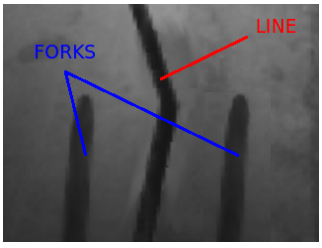

(b) Original image

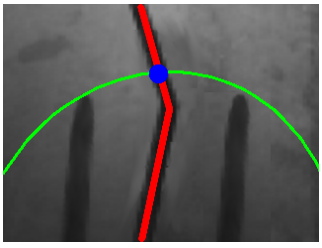

(c) Target computation

Figure 5.1: Vision-based line following application and target selection with perspective unwrap: detected line (red), look-ahead arc (green) and target (blue dot).

Algorithm 3 Vision-based Curvature Controller

while $\mathbf{q}_R(t) \neq \mathbf{q}_G$ **do**
  if a new image is available **then**
    Reset robot's travelled distance $l_R = 0$ and time $t = 0$
    Grab a new image $\mathcal{I}$
    Detect lines on image $\mathcal{I}$ and compute a set of *waypoints* $\mathcal{W}$
    Select a target configuration $\mathbf{q}_T(t)$ based on LA distance relative to robot configuration $\mathbf{q}_R(t)$ (from equations (4.1), (4.2) and (4.3)) and transform it with respect to the fixed-frame
    Estimate start configuration $\mathbf{q}_A$ and end configuration $\mathbf{q}_B$ of a standard DCC from $\mathbf{q}_R(t)$ and $\mathbf{q}_T(t)$
    Compute the shortest DCC path $\mathcal{Q}^*$ and determine the optimal values for its parameters θ_C, l_A, l_{A1}, l_{Ω_A}, l_{A2}, l_C, l_{B1}, l_{Ω_B}, l_{B2}, l_B, σ_{A1}, σ_{A2},σ_{B1}, σ_{B2}, s_A, s_B
  end if
  Update travelled distance $l_R(t)$ based on current robot velocity $v_R(t)$
  Compute $\kappa_R(t)$ using equation (4.4)
  Compute $v_R(t)$ using equation (4.5)
  Update $\mathbf{q}_R(t)$ from odometry and/or stereoceptive sensors
end while

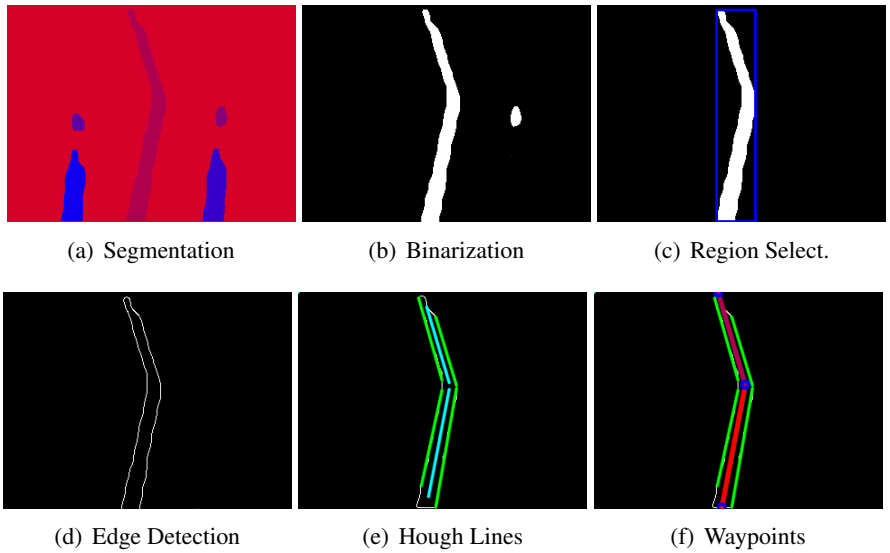

(a) Segmentation (b) Binarization (c) Region Select.

(d) Edge Detection (e) Hough Lines (f) Waypoints

Figure 5.2: Image processing steps for path detection.

- *Pyramid segmentation* uses a colour merge (over a scale that depends on the similarity of the colours to one another) in order to segment images, based on minimizing the total energy in the image, see Figure 5.2(a). In some cases, this step requires and intermediate step to smooth the image based on median or Gaussian filters to filter out potential problems such as shadows, specially in outdoor environments.

- A *threshold* operation is also applied to provide a binarized image, as shown in Figure 5.2(b).

- *Open*, *close*, *erode* and *dilation* operations are applied after image binarization in order to remove small blobs or regions as well as to fill holes of existing regions. In this case, the selected region is the one with the highest area, as shown in Figure 5.2(c).

- *Detection of multiple lines* on the selected region based on standard *Canny* edge detector, as shown in Figure 5.2(d), and then *Hough* transform, depicted in Figure 5.2(e).

- *Central line computation* by merging lines with similar characteristics, merging parallel lines with a coarser distance threshold and computing intersection points of sorted lines from bottom to top of the image which constitute a set of sorted *waypoints* with increasing distance to the mobile base as shown in Figure 5.2(f).

- *Ground plane projection* of waypoints and target selection based on a look-ahead distance LA, as depicted in Figure 5.1(c).

A sequence of images of an automated industrial forklift following a black line painted on the floor is depicted in Figure 5.3. It can be observed that the forks were lifted up during the test in order to make the problem simpler. This way the line detection processing was more robust avoiding potential instabilities due to losing the track of the line. Images show that initially the AGV is following the line completely centred. Then, it detects a corner and so it must turn to the right. The controller is smooth enough to avoid the AGV loses the track of the line and therefore the vehicle can keep following it. The controller stabilizes the autonomous vehicle after the turning, which converges to the painted line.

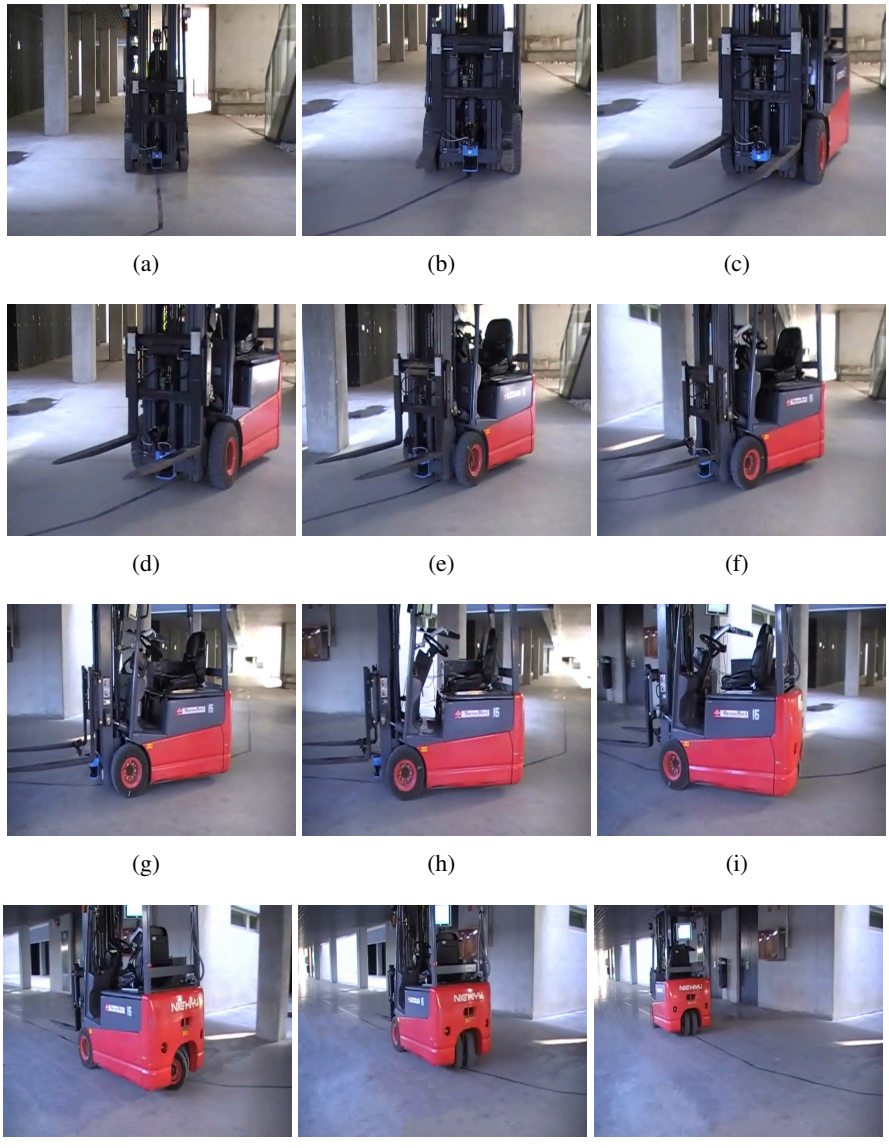

(a) (b) (c)

(d) (e) (f)

(g) (h) (i)

(j) (k) (l)

Figure 5.3: Vision-based line following application with an AGV.

5.3 Vehicle Stability Control

This section focuses on a closed-loop hybrid controller (kinematic and dynamic) for path following approaches with industrial forklifts carrying heavy loads at high speeds, where aspects such as vehicle stability, safety, slippage and comfort are considered. In particular, to solve the path following problem for non-holonomic wheeled vehicles, the kinematic controller generates velocity and curvature profiles, as described in Chapter 4. The speed profile is generated to cope with human-like driving based on "slow-in" and "fast-out" policy, while the curvature profile is planned by recomputing Double Continuous-Curvature (DCC) paths in closed-loop. The type of provided solutions gets benefit in terms of higher comfort and safety constituting a set of "natural" paths with the shortest possible length. From the generated profiles, the kinematic controller applies control inputs to drive and steer the vehicle in order to converge to a path.

In addition, a controller is proposed to guarantee vehicle stability conditions in order to avoid lateral and frontal rollovers using only odometry and inertial data. For that purpose, the controller determines lower and upper bounds on sharpness and maximum values for accelerations and curvatures, so that instantaneous vehicle stability conditions can be guaranteed. Compared to standard dynamic controllers, one of the advantages of the proposed method is that it does not require to estimate complex parameters to model the dynamics of the vehicle, such as inertial, torques and frictions. In this work we use a clothoid-based approach because they have an explicit relation with jerks, so designing clothoid-based paths implies planning paths with limited jerks, which also has direct impact on comfort and safety. Other curves such as Bézier or Splines can also provide smooth curvature profiles, but their derivatives are not limited.

The proposed vehicle stability control scheme is compared with a classic kinematic controller like Pure-Pursuit (Ollero, 2001). For that purpose, in our hybrid control structure we have just replaced the proposed kinematic controller with Pure-Pursuit. Several metrics, such as settling time, overshoot, safety and comfort have been analysed.

5.3.1 Stability Controller

Our approach to perform a kinematic control of the vehicle is based on a cascade-loop structure, as shown in Figure 5.4. Target selection is based on Look-Ahead criteria, as in the line following example explained in Section

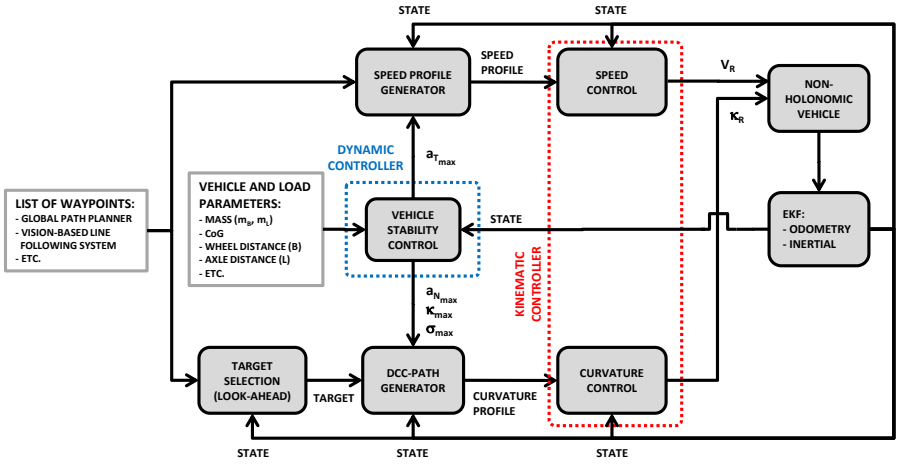

Figure 5.4: Closed-loop hybrid controller, including a kinematic controller and a vehicle stability controller.

5.2. In addition to this, the overall closed-loop structure includes a vehicle stability controller that requires an Extended Kalman Filter (EKF) to estimate the vehicle configuration from inertial and odometry sensors.

The clothoid sharpness is selected according to the following formula:

$$\sigma = (1-\alpha)\cdot\sigma_{min} + \alpha\cdot\sigma_{max} \tag{5.1}$$

where α is a design parameter.

The heuristic criteria used in the computation of α has the purpose of reducing the sharpness when the vehicle is following a straight line with high speeds, while letting it turn by increasing sharpness when necessary. Such α parameter is obtained using the following formula $\alpha = H\cdot\sin\beta_{min}\frac{v_{turn}^2}{v_R LA}$, with H a time horizon (in our case $H = 1$ s) and $\beta_{min} = \min(\beta, \pi/2)$, being $\beta = \arctan(\frac{y_T - y_R}{x_T - x_R}) - \theta_R$. Notice that α depends on v_{turn} and LA, which are included because vehicle's behaviour is sensitive to these parameters.

At this point, several criteria can be considered such as vehicle stability carrying a heavy load, horizontal alignment, wheels slippage avoidance and/or maximum curvatures due to mechanical constraints:

$$\kappa_{max} = \min(\kappa_{max,stab}, \kappa_{max,horiz}, \kappa_{max,slip}, \kappa_{max,mech}, \ldots) \tag{5.2}$$

$$\sigma_{max} = \min(\sigma_{max,stab}, \sigma_{max,horiz}, \sigma_{max,slip}, \sigma_{max,mech}, \ldots) \tag{5.3}$$

$$\sigma_{min} = \max(\sigma_{min,stab}, \sigma_{min,horiz}, \sigma_{min,slip}, \sigma_{min,mech}, \ldots) \tag{5.4}$$

where in our notation the subscript is a short name for the criterion used.

In order to increase driving safety and comfort and reduce wheels slip, many studies have been carried out to determine appropriate values for superelevation and side friction factor in horizontal road alignment (Krammes and Garnham, 1998; Marchionna and Perco, 2007). These studies also establish appropriate values for clothoid sharpness in transition curves to guarantee specific vehicle dynamic properties, according to $\sigma(t) \in [-\sigma_{max}, -\sigma_{min}] \cup [\sigma_{min}, \sigma_{max}]$ and $\kappa_R(t) \in [-\kappa_{max}, \kappa_{max}]$. In fact, in order to ensure appropriate curve visibility and comfort, one of the most accepted criteria in clothoid sharpness design (Marchionna and Perco, 2007) is related to the maximum curvature $\kappa_{max}^2 \equiv \sigma_{min} < \sigma < \sigma_{max} \equiv 9 \cdot \kappa_{max}^2$.

Focusing on stability criterion, Figure 5.5 defines main geometric parameters involved in lateral and frontal tip overs. It also shows a picture with the real forklift were values for these parameters have been taken from. Our notation considers subscript B for body and subscript L for load.

Let first compute vectors for body and load positions, velocities and accelerations for a given configuration (see Figure 5.5(d)). Let $\overrightarrow{\mathbf{p}_R} = [x_R, y_R, 0]^T \in \Re^3$ be the vehicle Cartesian coordinates where control over its position is to be performed. Positions for the centres of mass of body $\overrightarrow{\mathbf{p}_B}$ and load $\overrightarrow{\mathbf{p}_L}$ are:

$$\overrightarrow{\mathbf{p}_B} = \overrightarrow{\mathbf{p}_R} - L_B \overrightarrow{\mathbf{t}} + 0\overrightarrow{\mathbf{n}} + h_B \overrightarrow{\mathbf{z}} \tag{5.5}$$

$$\overrightarrow{\mathbf{p}_L} = \overrightarrow{\mathbf{p}_R} + L_L \overrightarrow{\mathbf{t}} + 0\overrightarrow{\mathbf{n}} + h_L \overrightarrow{\mathbf{z}} \tag{5.6}$$

being $\{\overrightarrow{\mathbf{t}}, \overrightarrow{\mathbf{n}}, \overrightarrow{\mathbf{z}}\}$ a base of orthonormal vector corresponding to the tangential, normal and binormal directions of the vehicle reference frame.

Velocities and accelerations can be easily derived:

$$\overrightarrow{\mathbf{v}_B} = v_{B_t}\overrightarrow{\mathbf{t}} + v_{B_n}\overrightarrow{\mathbf{n}} = v_R \cdot \overrightarrow{\mathbf{t}} - L_B \cdot v_R \cdot \kappa_R \cdot \overrightarrow{\mathbf{n}} \tag{5.7}$$

$$\overrightarrow{\mathbf{v}_L} = v_{L_t}\overrightarrow{\mathbf{t}} + v_{L_n}\overrightarrow{\mathbf{n}} = v_R \cdot \overrightarrow{\mathbf{t}} + L_L \cdot v_R \cdot \kappa_R \cdot \overrightarrow{\mathbf{n}} \tag{5.8}$$

$$\overrightarrow{\mathbf{a}_B} = a_{B_t}\overrightarrow{\mathbf{t}} + a_{B_n}\overrightarrow{\mathbf{n}} = \left(\dot{v}_R + L_B \cdot v_R^2 \cdot \kappa_R^2\right)\overrightarrow{\mathbf{t}} + \left(v_R^2 \cdot \kappa_R - L_B\left(\dot{v}_R \cdot \kappa_R + v_R \cdot \dot{\kappa}_R\right)\right)\overrightarrow{\mathbf{n}} \tag{5.9}$$

$$\overrightarrow{\mathbf{a}_L} = a_{L_t}\overrightarrow{\mathbf{t}} + a_{L_n}\overrightarrow{\mathbf{n}} = \left(\dot{v}_R - L_L \cdot v_R^2 \cdot \kappa_R^2\right)\overrightarrow{\mathbf{t}} + \left(v_R^2 \cdot \kappa_R + L_L\left(\dot{v}_R \cdot \kappa_R + v_R \cdot \dot{\kappa}_R\right)\right)\overrightarrow{\mathbf{n}} \tag{5.10}$$

being $\dot{\overrightarrow{\mathbf{t}}} = v_R \cdot \kappa_R \cdot \overrightarrow{\mathbf{n}}$, $\dot{\overrightarrow{\mathbf{n}}} = -v_R \cdot \kappa_R \cdot \overrightarrow{\mathbf{t}}$ and $\dot{\overrightarrow{\mathbf{z}}} = 0$ for a planar motion.

From equilibrium condition, the limit of lateral rollover stability can be computed. As shown in Figure 5.5(c), the sign criteria for the equilibrium problem is different depending on the turning direction (left and right tip

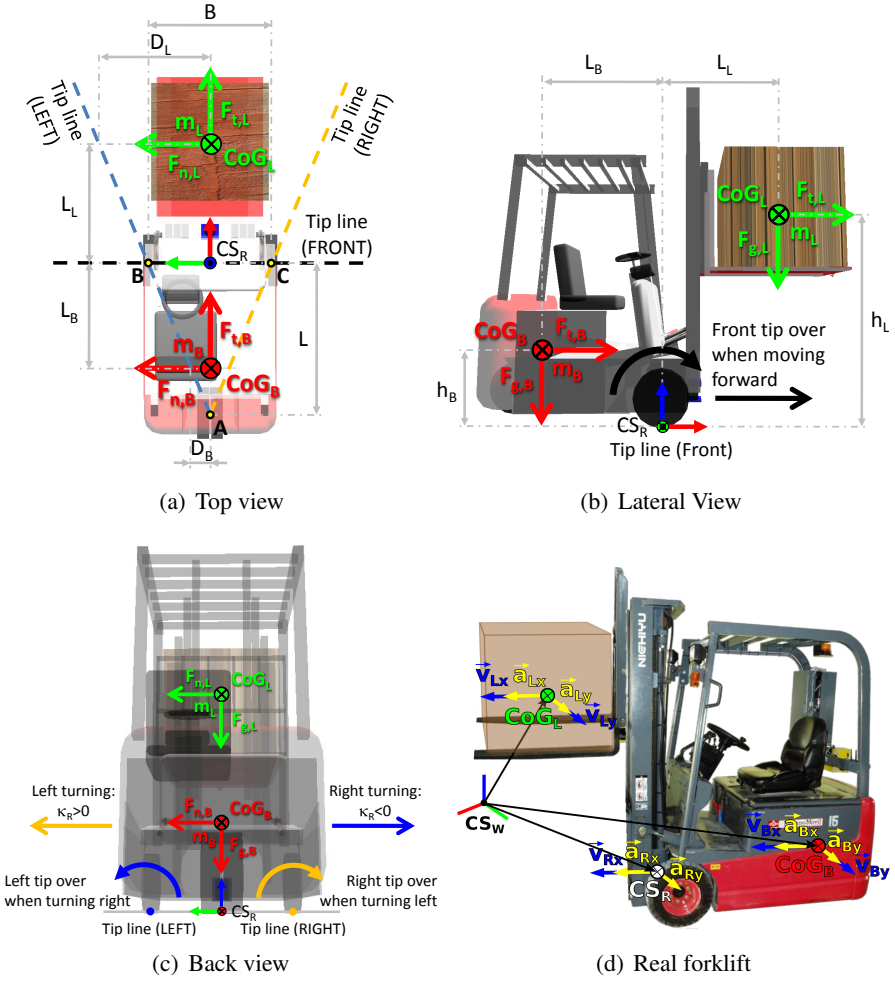

(a) Top view (b) Lateral View

(c) Back view (d) Real forklift

Figure 5.5: Different views of the industrial forklift carrying a load. CS stands for Coordinate System, while subscripts B, L, R and W refer to Body, Load, Robot and World, respectively.

lines), which turns in fact into the following inequalities depending on the case:

$$D_B{\cdot}m_B{\cdot}g{+}D_L{\cdot}m_L{\cdot}g{-}h_L{\cdot}m_L{\cdot}a_{L_n}{-}h_B{\cdot}m_B{\cdot}a_{B_n} > 0 \qquad \text{if } \kappa_R{>}0 \text{ m}^{-1} \tag{5.11}$$

$$D_B{\cdot}m_B{\cdot}g{+}D_L{\cdot}m_L{\cdot}g{+}h_L{\cdot}m_L{\cdot}a_{L_n}{+}h_B{\cdot}m_B{\cdot}a_{B_n} > 0 \qquad \text{if } \kappa_R{<}0 \text{ m}^{-1} \tag{5.12}$$

with g the gravitational acceleration, m_B and m_L the masses of body and load, $D_B = \frac{B}{2} \cdot \frac{L-L_B}{L}$ and $D_L = \frac{B}{2} \cdot \frac{L+L_L}{L}$ represent distances of the supporting triangle formed by the two front wheels and the rear wheel, L_B and L_L are longitudinal distances from vehicle coordinate system to base and load's centres of gravity respectively, h_B and h_L are heights for base and load's centres of gravity with respect to the floor, B is the front wheel separation and L is the wheel base, i.e. the axle distance.

Assuming that an inertial sensor (IMU) is located in the vehicle body's CoG and from Equation (5.10), we can marginalize out κ_R from a_{L_n} component and substitute in the marginalization of a_{L_n} in Equations (5.11) and (5.12). Thus, we can find out maximum normal load acceleration and, as a consequence, it is also possible to compute the maximum allowed curvature that guarantees instantaneous lateral stability:

$$\kappa_{max,stab} = \left| \frac{(D_L{\cdot}m_L{+}D_B{\cdot}m_B){\cdot}g{-}\ \text{sign}(\kappa_R){\cdot}(h_B{\cdot}m_B{\cdot}a_{B_n}{+}v_R{\cdot}\dot{\kappa}_R{\cdot}L_L)}{h_L \cdot m_L \cdot (v_R^2 + L_L \cdot \dot{v}_R)} \right| \tag{5.13}$$

where a_{B_N} is taken from the IMU measurement.

Similar to horizontal alignment criteria (Marchionna and Perco, 2007), the maximum sharpness from the lateral stability criteria is obtained by the following expression: $\sigma_{min,stab} = \kappa^2_{max,stab}$ and $\sigma_{max,stab} = 9 \cdot \sigma_{min,stab}$.

In order to avoid frontal rollovers due to excessive braking, we also analyse conditions for tangential equilibrium equations when braking:

$$L_B \cdot m_B \cdot g - L_L \cdot m_L \cdot g - h_B \cdot m_B \cdot a_{B_t} - h_L \cdot m_L \cdot a_{L_t} > 0 \tag{5.14}$$

Taking into account Equations (5.10) and (5.14), we can similarly proceed to derive a frontal stability condition which implies to compute maximum allowed deceleration:

$$a_{brake} \leq \frac{(L_B \cdot m_B - L_L \cdot m_L) \cdot g + h_B \cdot m_B \cdot a_{B_t}}{h_L \cdot m_L} + v_R^2 \cdot \kappa_R^2 \cdot L_L \tag{5.15}$$

5.3.2 Simulation: Results and Discussion

In order to validate our proposal, we have simulated a forklift and an environment using ROS-Gazebo with parameter values corresponding to the real forklift shown in Figure 5.5(d): body mass $m_B = 1500$ kg, load mass $m_L = 1000$ kg, with $L_B = 1.0$ m, $D_B = 0.12$ m, $h_B = 0.42$ m, $L_L = 1.01$ m, $D_L = 0.924$ m, $h_L = 2.75$ m. Simulation step time has been set to $t_{sim} = 10^{-3}$ s and control period $T_R = 0.01$ s, that is, the sampling time in which DCC paths are recomputed. Additional parameters are: gravity acceleration $g = 9.81$ m/s^2, variables related to joints and constraints for dynamic simulations based on ODE (Open Dynamics Engine), such as constraint force mixing $cfm = 0.0001$ and error reduction parameter $erp = 0.4$ as global parameter settings and damping $damp = 0.1$ and friction $fric = 10.0$ for every joint. On the other hand, a tricycle kinematic model of the vehicle has been used, with a rear steering wheel and two front driving wheels: front wheel separation $B = 1.04$ m, wheel base or axle distance $L = 1.3$ m and wheel diameter $D = 0.44$ m. From the robot configuration we can set the maximum mechanical curvature as $\kappa_{max,mech} = R_{min}^{-1} = \tan(\Phi_{max})/L = 0.7692$ m^{-1}, where R_{min} is the minimum radius of curvature, L is the wheel base and $\Phi_{max} = \pi/4$ rad is the maximum steering angle of the rear wheel.

First, we show the advantages of using the proposed hybrid-controller described in previous section. For that purpose, components of Figure 5.4 have been implemented in ROS and will be separately tested first. The implementation allows activation and deactivation of nodes and re-parametrization based on "dynamic_reconfigure" ROS package. The EKF implementation is based on the "robot_pose_ekf" ROS package, where only odometry and inertial values are considered[1].

In our first simulation scenario, the vehicle is moving almost at constant velocity $v_{path} = 3$ m/s, but it needs to make a 90^o turn (see Figure 5.6(a)). Thus, the aim of this test is to compare the behaviour of the vehicle when speed profile generator and frontal stability nodes are not active and when they are. If lateral stabilization node is off, that is, minimum and maximum sharpness and maximum curvatures are not recomputed based on IMU measurements, the DCC path generator cannot perform successfully when carrying heavy loads. Indeed, the vehicle starts turning at $t \approx 11$ s with $v_R = 3$ m/s and it tips over around $t \approx 14$ s, as shown in Figure 5.6(c) (dashed red line). It has to be mentioned that $v_{path} = 3$ m/s and $LA = 3$ m is the limit situation where the vehicle starts overturning. However, if we activate the lateral

[1]The dead-reckoning problem is out of the scope of this thesis.

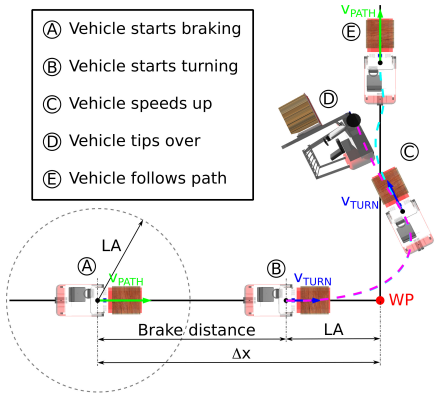

(a) Lateral Stability Test.

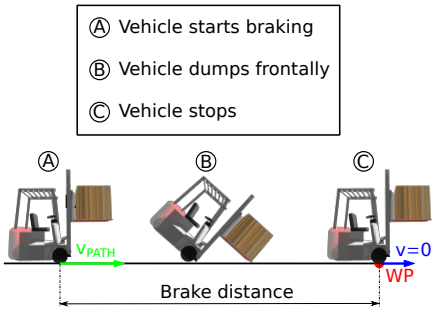

(b) Frontal Stability Test.

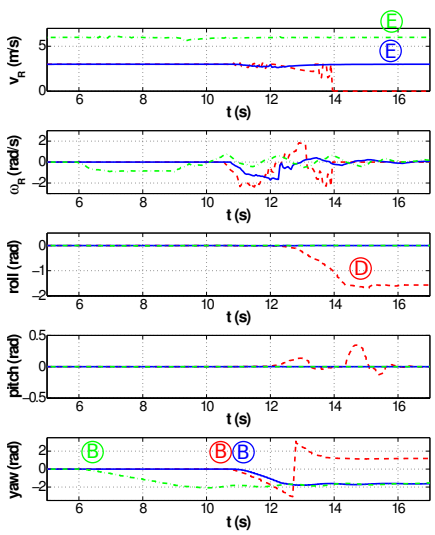

(c) Lateral Stability Analysis.

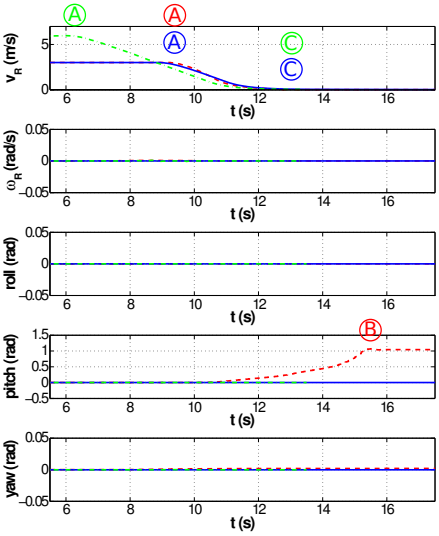

(d) Frontal Stability Analysis.

Figure 5.6: (Up) Sequences explaining experiments performed in the stability controller analysis, (a) lateral test and (b) frontal test. (Down) Stability controller analysis, (c) lateral stability with $v_{turn} = v_{path}$ and (d) frontal stability. Solid blue line corresponds to stability controller set to ON with $v_{path} = 3$ m/s, dashed red line is for the OFF state (where it starts failing) and dash-dotted green line corresponds to the maximum velocity case $v_{path} = v_{max} = 6$ m/s.

stabilization node, it can be clearly seen that the vehicle does not tip over (blue solid line in Figure 5.6(c)). This can be proved even at the maximum velocity taken from real vehicle specifications $v_{max} = 6$ m/s, where our stabilization controller still performs successfully, as depicts Figure 5.6(c) (green dash-dotted line).

Similarly, we can analyse the effect of enabling or disabling the frontal stabilization module, in which maximum allowed decelerations are recomputed. In this case, the simulation scenario includes the vehicle moving straight forward during a certain amount of time with $v_{path} = 3$ m/s and then it performs a braking, that is, it sets velocity to zero (see Figure 5.6(b)). Figure 5.6(d) shows the case in which a constant deceleration is taken as the maximum vehicle deceleration with $a_{brake} = 2$ m/s^2 for the case where the vehicle is carrying a load, where it is clearly shown that the vehicle unstabilized during braking until it dumped frontally at $t \approx 15$ s (dashed red line). In addition to this, Figure 5.6(d) also clearly shows that with frontal stabilization on, the vehicle can successfully perform the braking (solid blue line). In Figure 5.6(d), it can also be seen that the stabilization controller still performs successfully at the maximum velocity case (dash-dotted green line).

In addition to this, Figure 5.7 shows a scenario where the vehicle is following a path with a squared side of 30 m. Two different kinematic controllers are tested: blue line corresponds to our DCC path generator method, while dashed-dotted line corresponds to Pure-Pursuit (PP) method (Ollero, 2001). In both cases, lateral and frontal stabilization nodes are active and the unique difference is on how the curvature profile is computed for a given target. What we want to highlight is that if the vehicle has not properly converged after performing a turn with the appropriate heading direction, well-known policies such as "slow-in" and "fast-out" can potentially cause oscillation problems. This is the case of PP method in Figure 5.7, in which the angular rate increases as a consequence of increasing the velocity. This also may cause additional inconvenience such as increased odometry errors due to oscillatory behaviour. This error is computed as the accumulate value of error between the relative ground-truth pose (provided by Gazebo simulator[2]) and the relative estimated pose.

Moreover, let's analyse the main characteristics of the proposed DCC method against the PP method. Again, without loss of generality, the following analysis has been developed for the case in which the initial robot configuration is $\mathbf{q}_R = (0, 0, 0, 0, 0)^T$, with $v_R = 0$ m/s, and the path to follow

[2]http://gazebosim.org

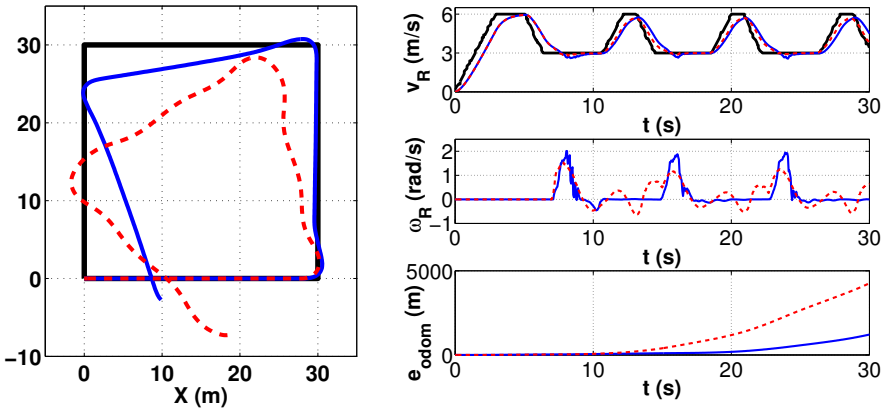

(a) XY trace (b) Integrated odometry error

Figure 5.7: DCC (blue) vs. PP (dashed red), following a square path of 30m side, with $LA = 4.5$m, $v_{path} = 6$m/s and $v_{turn} = 3$m/s.

is a straight line $\rho_l = x\cos\phi_l + y\sin\phi_l$ with $\rho_l = 20$ m and $\phi_l = 0$ rad (i.e. line $x = 20$ m), which represents one of the most difficult cases for both algorithms since it represents a 90º turn. Our purpose is to analyse the sensibility of several metrics (described below) for each method against Look-Ahead distance LA and the robot velocity v_R. Initially, the robot accelerates in a straight movement until it reaches the path reference speed and when the robot is at a distance LA to the path begins to twist until converges to the line. All simulations have been carried out with a forklift carrying a heavy load at a height of $h_L = 1.75$ m.

To evaluate the performance, several metrics have been used to characterize the resulting path $\{[x_{R,0}, y_{R,0}]^T, \ldots, [x_{R,N}, y_{R,N}]^T\}$, where N is the number of points of the simulation. In particular, we consider the following metrics: overshoot $\delta = \max\{\frac{x_{R,i}-\rho_l}{LA}\}$, settling time t_s such that $\left|\frac{x_{R,i}-\rho_l}{LA}\right| < 0.05$ and mean error $\overline{e} = \sum_i \left|\rho_l - (x_{R,i}\cos\phi_l - y_{R,i}\sin\phi_l)\right|$, with $x_{R,i}$ and $y_{R,i}$ the i-th position of the simulated path. In addition to this, we also consider additional metrics taking into account comfort and safety, so we evaluate the mean normal acceleration $\overline{a}_N = \sum_i \left|a_{N,i}\right|$, the mean curvature $\overline{\kappa} = \sum_i \left|\kappa_{R,i}\right|$ and the maximum curvature $\kappa_{max} = \max\{\kappa_{R,i}\}$, being $a_{N,i}$ the normal acceleration along the path measured with the IMU and $\kappa_{R,i}$ the robot curvature along the path obtained from odometry data.

Such metrics are reflected on Figure 5.8(a), while Figure 5.8(b) shows path trace, for different values of LA. It can be appreciated that as long as the

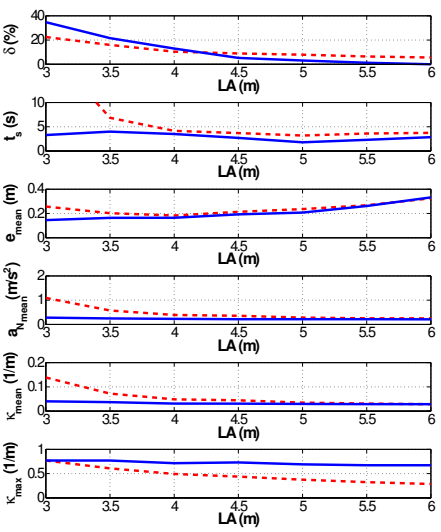

(a) Benchmark variables vs. LA.

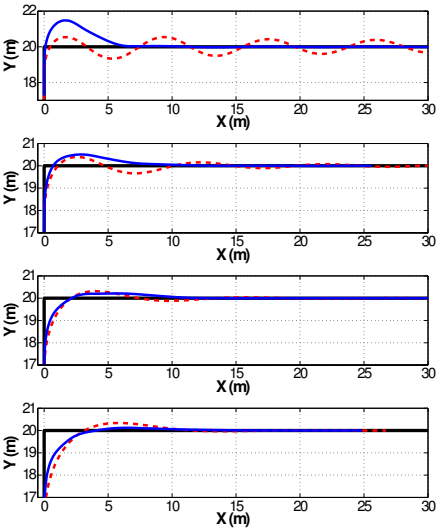

(b) XY trace vs. $LA = \{3,4,5,6\}$m (from top to bottom).

Figure 5.8: DCC (blue) vs. PP (dashed red), LA variation with $v_R = 3$ m/s.

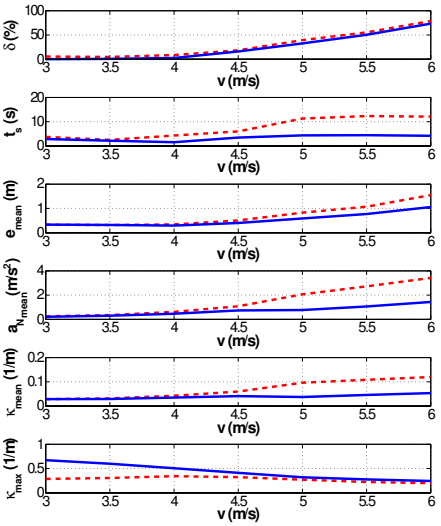

(a) Benchmark variables vs. v_R.

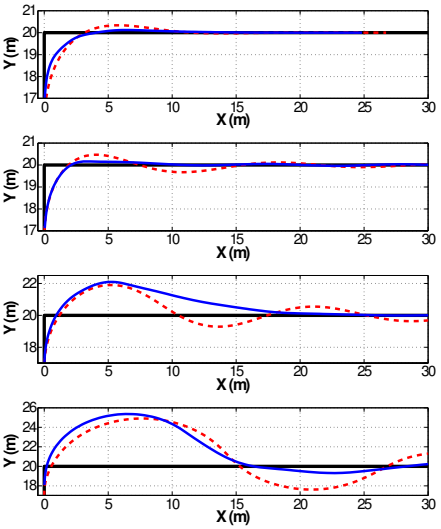

(b) XY trace vs. $v_R = \{3,4,5,6\}\frac{\text{m}}{\text{s}}$ (from top to bottom).

Figure 5.9: DCC (blue) vs. PP (dashed red), v_R variation with $LA = 6$ m.

LA distance is smaller, the PP method presents an oscillatory behaviour. In all presented cases, the convergence time for the DCC method is smaller than the PP method, as well as the mean error. Also the mean normal acceleration and curvature are lower because there is, in general, lower oscillatory effect. The maximum curvature is always higher in DCC method, which implies that it is being less conservative than PP method. So, the DCC controller is able to bring the vehicle to the limit conditions while taking into account stabilization conditions. Figure 5.9 shows the results for different velocity conditions, where similar conclusions can be drawn. DCC method performs better in terms of settling time, mean error, mean normal acceleration and curvature and maximum curvature. Here the effect is contrary to the LA parameter, that is, PP method produces higher oscillations with increasing velocity values.

5.4 Obstacle Avoidance

In this section, the Quasi-Holonomic Continuous-Curvature (QHCC) paths are introduced, which are a particular case of DCC path, without straight line segments and with particularities in the target orientation. Therefore they are considered as a subset of the family of solutions covered by DCC paths A QHCC path is generated from purely non-holonomic motions (combinations of linear and angular velocities) that mimics a holonomic motion (Cartesian and angular velocities), as shown in Figure 5.10. As QHCC paths are based on clothoids, terms such as safety and comfort are considered in the obstacle avoidance solutions proposed by this method.

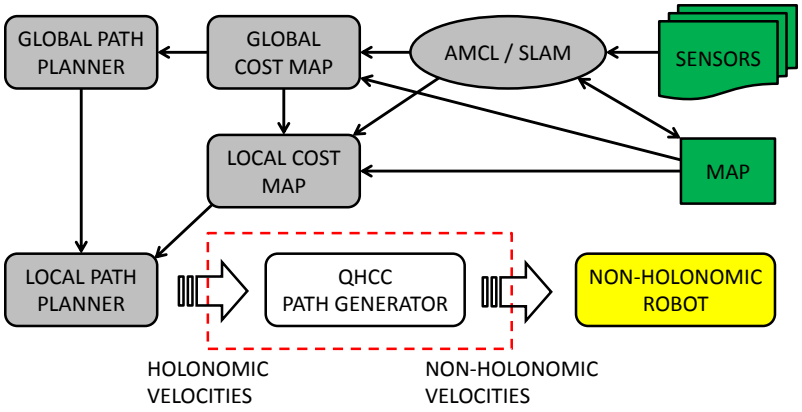

Figure 5.10: Quasi Holonomic Continuous-Curvature (QHCC) path generator within the context of global navigation problem.

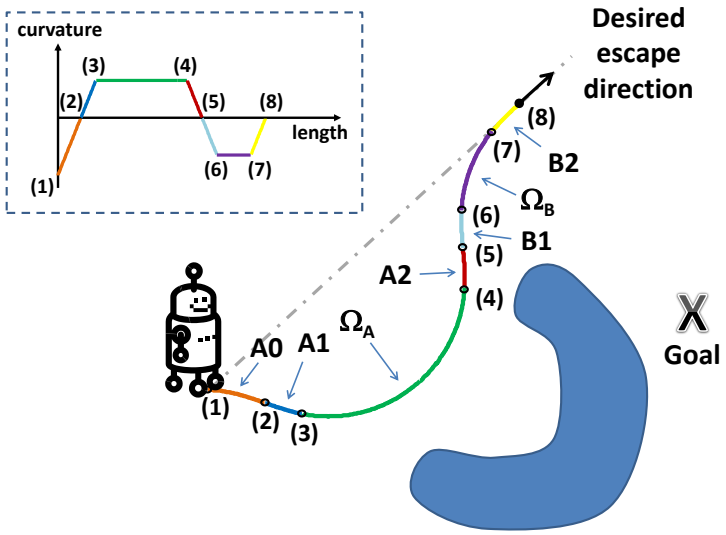

Figure 5.11: Definition of Quasi-Holonomic Continuous-Curvature Paths.

The main advantage of the method is that it can be included into well-known local-navigation methods, as well as kinematic controllers. It is interesting to remark that the method itself is not a new local-navigation algorithm, but an adaptation of existing ones. In particular, methods such as ND and DWA, have been adapted and combined with QHCC in order to evaluate the resulting path in terms of safety and comfort. Even tough there are some approaches that take into account different kind of kinematic and dynamic constraints, such as LaValle and James J. Kuffner (2001) or Pivtoraiko et al. (2009), these methods are classified into global planners, while our method is closer to local planners and kinematic controllers, since paths are continuously recomputed. Therefore, QHCC paths represent a novel contribution to the best of author's knowledge and significantly differs from approximation solutions of holonomic paths by decomposition of feasible non-holonomic paths (Lamiraux and Laumond, 2001; Sekhavat et al., 1996).

5.4.1 Quasi-Holonomic Smooth Trajectories

A Quasi-Holonomic Continuous-Curvature path is a particular case of Double Continuous-Curvature path, without straight segments, following the sequence: clothoid $\mathbf{A1}$, arc $\mathbf{\Omega_A}$, clothoid $\mathbf{A2}$, clothoid $\mathbf{B1}$, arc $\mathbf{\Omega_B}$ and clothoid $\mathbf{B2}$. Figure 5.11 shows an example of a QHCC path together with its curvature profile.

The *standard* case corresponds to null initial curvature conditions, although some situations may require to include a preliminary clothoid segment, named as $\mathbf{A0}$, which leads the curvature to zero, as shown in Figure 5.11. In other cases, the initial robot's curvature might exceed the curvature required for $\mathbf{\Omega_A}$, which implies that clothoid $\mathbf{A1}$ must be inverted.

As for the case of *standard* DCC paths, the goal of a QHCC path is to generate a continuous-curvature path $\mathcal{Q}$ connecting the robot pose $\mathbf{q}_R = [x_R, y_R, \theta_R, \kappa_R]^T$ to a target configuration $\mathbf{q}_T = [x_T, y_T, \theta_T, \kappa_T]^T$, assuming $\kappa_T = 0$, with the restriction that the target orientation is defined as

$$\theta_T = \arctan\left(\frac{y_T - y_R}{x_T - x_R}\right) \tag{5.16}$$

Note that, from now on, the time dependency is intentionally drop-off to keep notation clear. Inputs of our method are holonomic Cartesian velocities $v_{x,ref}$ and $v_{y,ref}$, angular velocity ω_{ref}, current robot linear velocity v_R and robot angular velocity $\omega_R \equiv \dot{\theta}_R$. Holonomic velocities are always referred to the robot reference frame and used to compute the target configuration.

In order to generate quasi-holonomic trajectories the following conditions must be satisfied:

$$\theta_T - \theta_R = \arctan\left(\frac{v_{y,ref}}{v_{x,ref}}\right) \tag{5.17}$$

which implies that, from the robot local frame, the target position is aligned with the Cartesian velocity vector. In addition to this, we impose a constraint to path maximum curvature $\kappa_{\Omega_{max}}$ based on angular velocity reference value ω_{ref} as follows:

$$\kappa_{\Omega_{max}} = \max\left\{\min\left\{\kappa_{ref}, \kappa_{max}\right\}, \kappa_{\Omega_{min}}\right\} \tag{5.18}$$

where $\kappa_{ref} = \frac{|\omega_{ref}|}{\sqrt{v_{x,ref}^2 + v_{y,ref}^2}}$ is the reference curvature computed from the reference turn rate and linear velocities. In this sense, they define the maximum reference curvature so the robot can converge to the same asymptotic direction but with different path profiles based on this value. As a result, the higher the turn rate the higher the convergence rate, and as a consequence, the robot will turn faster. In order to guarantee a minimum turn rate, we impose a minimum bound $\kappa_{\Omega_{min}}$.

One of the advantages of using clothoids is that sharpness parameters can be obtained from the maximum normal jerk $j_{N,max}$ criteria $\sigma_{A1} \leq \frac{j_{N,max}}{v_{max}^3}$,

where v_{max} are the maximum velocity profiles for the generated path. The same applies for the reminder of sharpness parameters. This criteria is a standard criteria used in road design (Marchionna and Perco, 2007) and adopted here for convenience. In addition to this, the maximum path curvature might be limited with the maximum curvature κ_{max}, specially for car-like vehicles. The reference curvature κ_{ref} used to generate different path profiles is based on the normal acceleration $a_{N,max}$ criteria $\kappa_{ref} \leq \frac{a_{N,max}}{v_{max}^2}$. The maximum tangential accelerations $a_{T,max}$ and jerks $j_{T,max}$ affect to the velocity-time profile, but not to the curvature-length profile.

Figure 5.12 shows some representative cases of QHCC paths. In particular, paths depicted in Figure 5.12(a) have been generated from the same holonomic motion, with different robot initial linear and angular velocities. On the other hand, Figure 5.12(b) depicts the cases of QHCC with the same robot initial conditions, but for different holonomic velocities and consequently, each path may converge to different directions, but all of them start in the same point in the curvature profile.

5.4.2 Performance Analysis

In this section, the proposed method is compared against well-known local planners such as DWA and ND to evaluate its performance. Our implementations are based on ROS Diamondback[3]. In particular, we are following the "navigation" stack (Marder-Eppstein et al., 2010) to command a non-holonomic robot in a simulated environment (Willow Garage Offices) based on Stage as provided in the "navigation_tutorials". The DWA algorithm has been limited to provide solution for non-holonomic robots, that is, only linear velocity, v_x in "X" axis, and angular velocity, ω_z in "Z" axis are allowed. In DWA the search space is $v_x \in [-0.3, 0.55]$ m/s and $\omega_z \in [-1.0, 1.0]$ rad/s, exploring 7×7 velocities combinations. Simulation time for trajectory roll-out has been set to 2.0 s. The ND implementation is based on the ND algorithm of Player-svn 3.1[4] and has been adapted to ROS following the "move_base" package specifications. Both methods have been configured in an equivalent parameter setting for tangential and normal accelerations and velocities. It should be noted that "navigation" stack include many parameters that might affect the overall performance, but they have taken default values or have been appropriately adapted.

[3]Robot Operating System - http://www.ros.org.

[4]http://playerstage.sourceforge.net

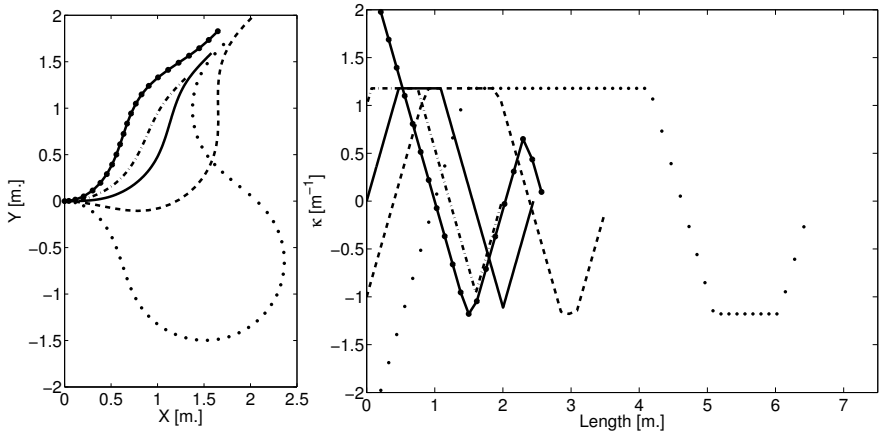

(a)

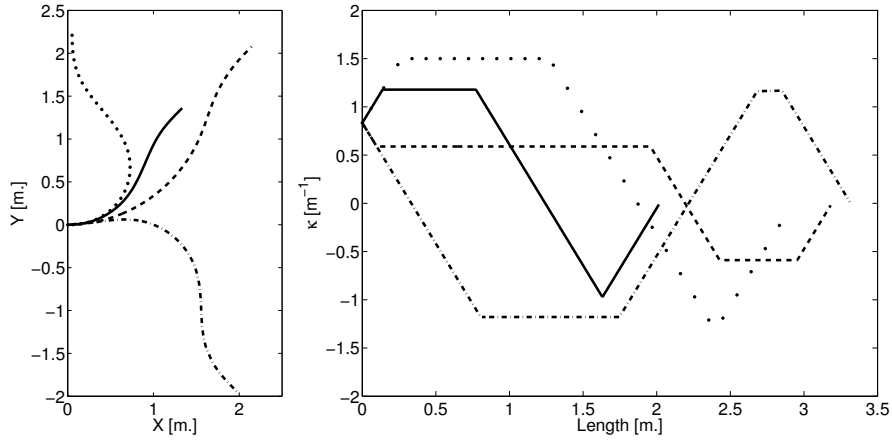

(b)

Figure 5.12: Examples of QHCC paths and continuous-curvature profiles with: (a) same holonomic motion (same convergence direction) and with different robot state (different initial curvature); (b) QHCC paths with different holonomic motion (different convergence direction) and with same robot state (same initial curvature).

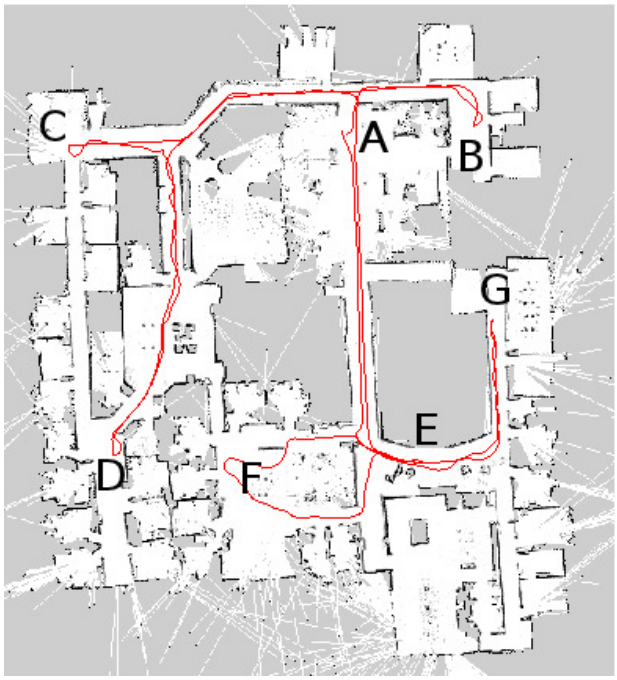

Figure 5.13: Navigation on simulated environment using QHCC-ND method.

The implementation described so far does not take into account curvature-continuity. Therefore, their equivalent counter part satisfying curvature constrains have been coined as QHCC-DWA and QHCC-ND, respectively. In particular, for QHCC-DWA the sampling space now includes velocities, $v_y \in [-0.3, 0.3]$ m/s in "Y" axis, thus treating the robot as a holonomic vehicle. The QHCC methods include additional constraints such as $a_{T,max} = 1.0$ m/s^2, $a_{N,max} = 0.63375$ m/s^2 and $j_{N,max} = 1.0$ m/s^3.

The trace of the simulated robot within the environment using QHCC-ND approach is shown in Figure 5.13. It can be appreciated that the robot traverses successfully the environment moving from goals **A**-**B**-**C**-**D**-**E**-**F**-**G**-**A**. The trace of all other methods is, indeed, very similar to the one shown in Figure 5.13 and from all simulations that have been tested the same collision-free behaviour is inherited. The differences pop-out when examining the accelerations and their derivatives. Figure 5.14 shows the accelerations and jerks for each method moving from goal **A** to **B**. It can be appreciated that tangential acceleration bounds and normal jerk bounds are continuously violated in ND and DWA methods, while in QHCC-based methods signals are always within the bounds. Obviously, such situation could be easily avoided by imposing

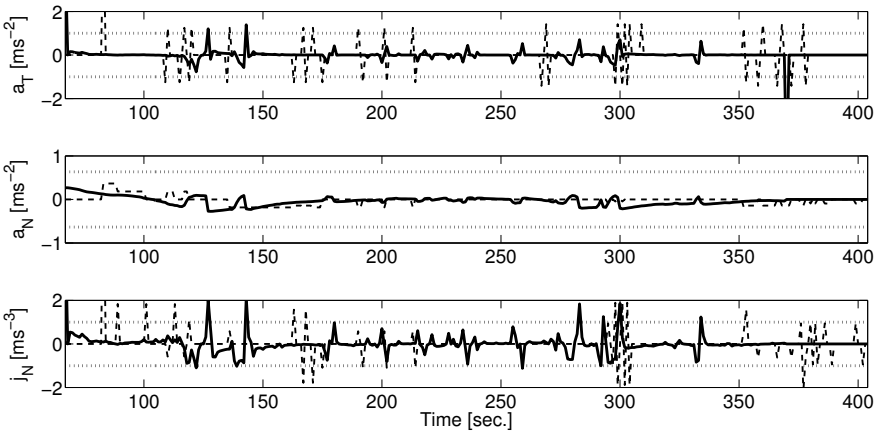

(a) ND and DWA

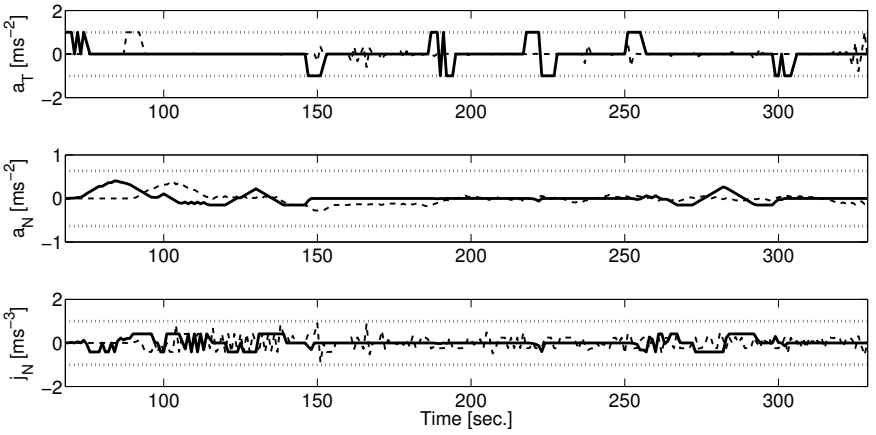

(b) QHCC-ND and QHCC-DWA

Figure 5.14: Comfort comparison between ND and QHCC-ND methods (solid lines correspond to ND and QHCC-ND methods, while dashed lines correspond to DWA and QHCC-DWA methods, bounds are represented with dotted lines).

additional kinematic and dynamic constraints to "bare" implementations, but they would need to be considered during the collision free path as well. Also smoothness and comfort would be still affected and not necessarily guaranteed. It can also be seen from Figure 5.14 that the required amount of time to complete the mission in the proposed method is lower than the original ones. This can be understood as a consequence of less manoeuvring effort due to the flexibility of the proposed path, despite of the fact that accelerations and jerks are limited.

5.5 Optimal Trajectory Following

In this section, a trajectory following experiment has been developed in order to validate the ERTS controller, using a Pioneer 3DX mobile robot (Adept Mobilerobots, 1995). The implementation is carried out with a receding horizon policy. Actual performance is stable as, indeed, the finite-time horizon is chosen long enough, so the resulting control actions are not significantly modified by variations on such horizon (indeed, stability for short horizons might need additional tweaks with the terminal cost (Mayne et al., 2000)).

The Pioneer P3-DX has differential configuration. An embedded board, model Odroid-U2 with 1.7GHz ARM Quad-Core (Cortex-A9) processor and 2GB RAM, is mounted inside the P3-DX robot. Results obtained are based on our implementation of ERTS algorithm using ROS Hydro (Quigley et al., 2009) in Ubuntu 13.10. Our C++ code implementation of ERTS takes approximately 11.28 ms with horizon $N = 60$. Obviously, computing time increases linearly with N.

The robot includes a Hokuyo URG 04LX range laser which has been used jointly with odometry measurements using an AMCL particle filter (Thrun et al., 2005) to estimate the robot position and speed without the drift that odometry-only sensing would have produced. The sensory system operates at a sampling period of 0.1 s. This is also the sampling period for the controller, which accepts linear and angular reference velocities and internally regulates wheels velocities based on a PID control. As our cost index intentionally includes acceleration weighting, the integrators of linear and angular accelerations to get velocities in the model (4.42) are actually included in the controller equations.

The goal is driving the P3-DX robot around an ∞-shape path:

$$\bar{x}_t = A\cos(\alpha_t) \tag{5.19}$$

$$\bar{y}_t = B\sin(2\alpha_t) \tag{5.20}$$

where $\alpha_t = \frac{2\pi}{T}t \in [0, 2\pi]$ rad is the angle parametrizing curve, with $T = 50$ being the trajectory period (the time closing the ∞-shape). In our experimentation, the ellipsoid major and minor semi-axis containing the ∞-shape have been set to $A = 3$m and $B = 1$m, respectively. From this path, references for angles and speeds are easily computed as:

$$\bar{\theta}_t = \arctan(\dot{\bar{y}}_t / \dot{\bar{x}}_t) \tag{5.21}$$

$$\bar{v}_t = \sqrt{\dot{\bar{x}}_t^2 + \dot{\bar{y}}_t^2} \tag{5.22}$$

$$\bar{\omega}_t = \frac{\ddot{\bar{y}}_t \dot{\bar{x}}_t - \dot{\bar{y}}_t \ddot{\bar{x}}_t}{\bar{v}_t^2} \tag{5.23}$$

so the overall state reference trajectory $\mathbf{s}_t$ in Equation (4.43) is available. The penalization matrices for the ERTS controller are set to the following values $Q = \mathrm{diag}(100, 100, 1, 1, 1)$ and $R = \mathrm{diag}(1, 1)$.

Figure 5.15 shows a screenshot at time instant $t_1 = 3$s produced by Rviz visualization software in ROS, where the robot is still far from the reference trajectory. This figure shows the reference trajectory (yellow dot indicates current value $\bar{x}_{t_1}, \bar{y}_{t_1}$; magenta line indicates the future values until $t_2 = t_1 + N \cdot \Delta t = 9$s and cyan line is the full reference), the predicted and smoothed

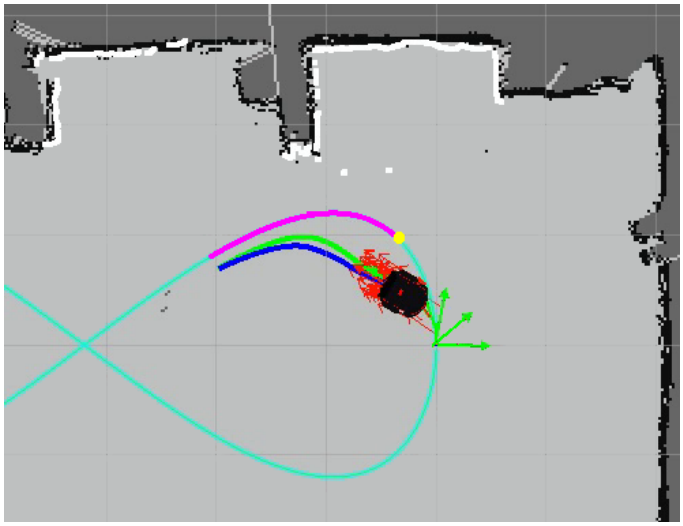

Figure 5.15: Screenshot of experiment at time $t^* = 3$s. Yellow dot, magenta line and cyan line are current, future and full reference values, respectively; blue and green are predicted and smoothed trajectories; red arrows are position estimates; grey and black is the map; white are laser dots.

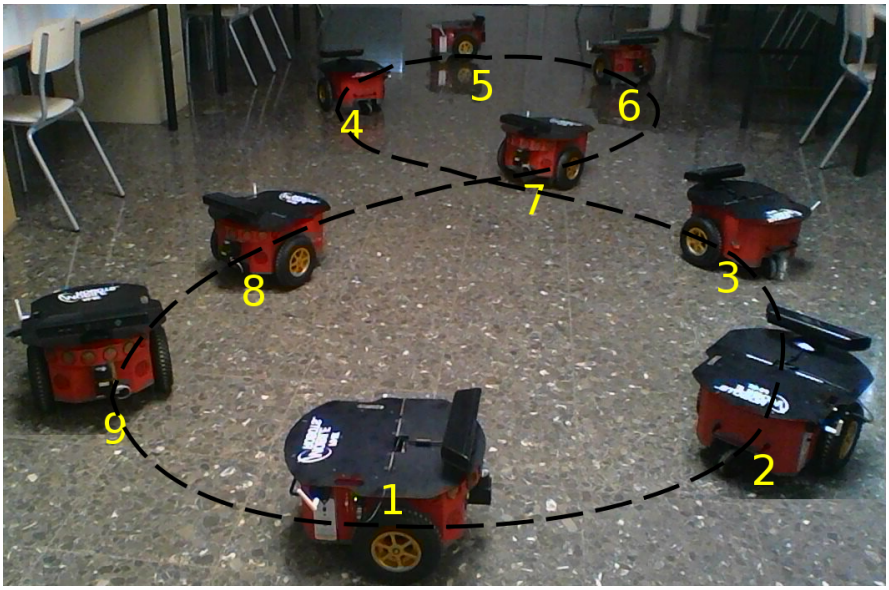

(a) Screenshots of the trajectory following experiment

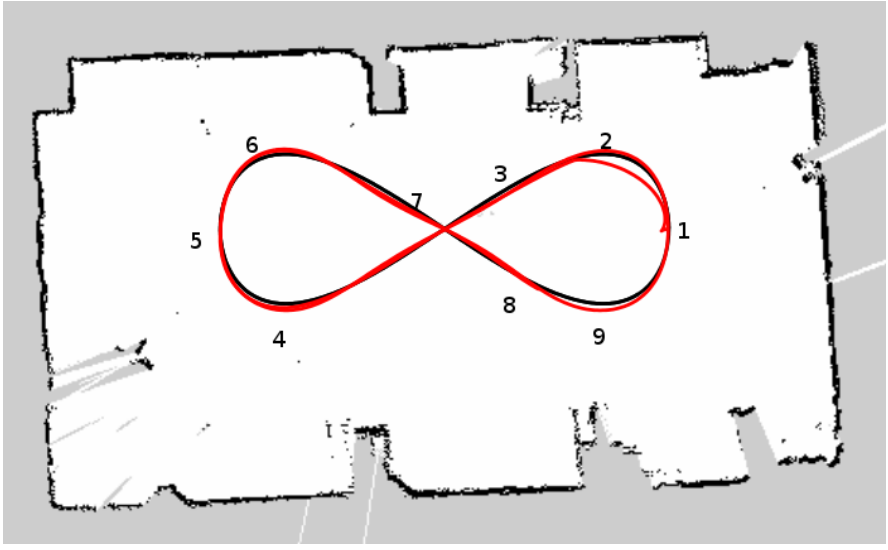

(b) XY reference trajectory (black solid line) and robot trace (red solid line)

Figure 5.16: Trajectory following with AMCL filter for vehicle localization (driftless position system).

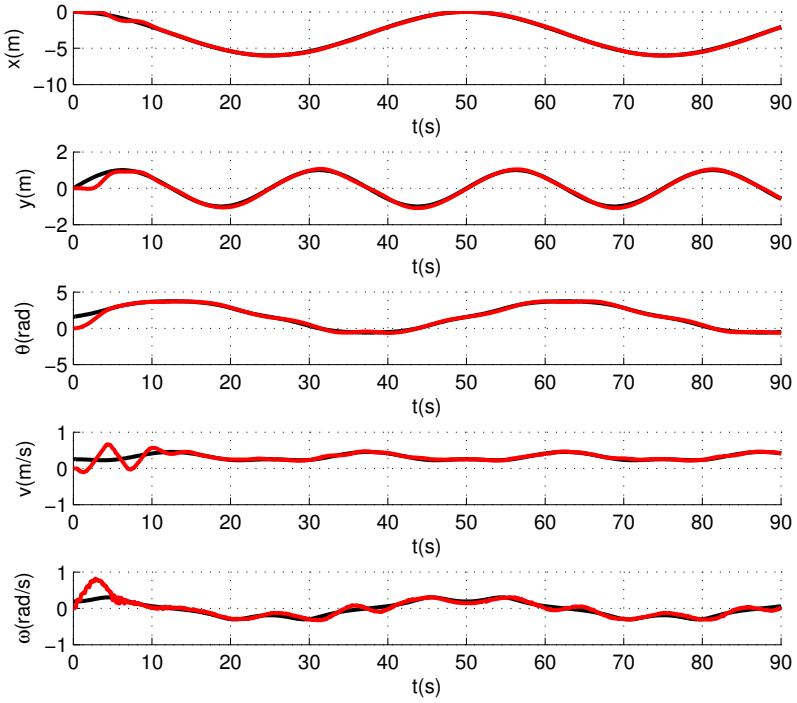

Figure 5.17: States of the system when following an infinite trajectory. References are depicted in black solid line and measured states in red solid line.

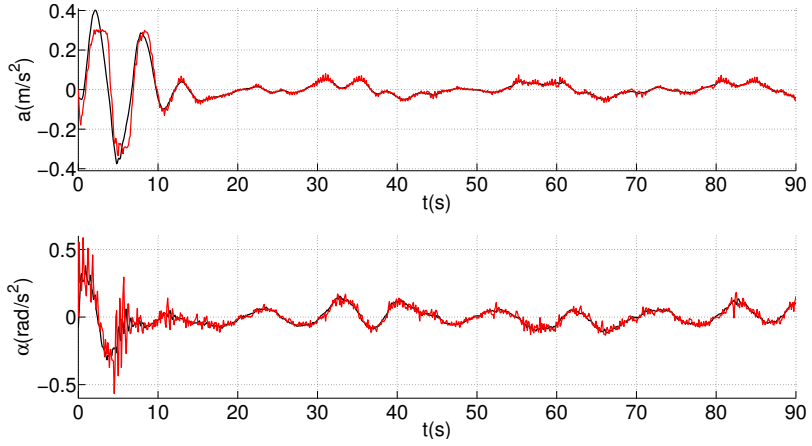

Figure 5.18: Applied control inputs (black solid line) and accelerations estimated from measurements (red solid line).

ERTS Cartesian trajectories (blue and green, respectively), AMCL particle position estimates (red arrows), the map (in gray and black) and laser scan over-imposed dots (in white).

Figures 5.16 to 5.18 show the results obtained from the experimentation of the robot following the above described trajectory. The XY-trace is depicted in Figure 5.16(b), superimposed with the map used for positioning. An actual set of frames (superimposed photographs) appears in Figure 5.16(a). On the other hand, Figure 5.17 shows system's states along time: x and y positions, orientation, linear and angular speeds. Computed inputs are shown in Figure 5.18, linear and angular accelerations (in black), together with robot accelerations (in red) estimated from measurements by suitable differentiation and filtering of odometry data.

As a conclusion of the experiments, the ERTS successfully performs the trajectory control as expected. As error figures are quite low, given that ERTS is a non-iterative algorithm with predictable computation time, it is a viable alternative to other iterative approaches whose execution time might depend on initialization and stop conditions so their real-time suitability is harder to assess beforehand.

5.6 Conclusions

The applicability of the control method using DCC paths has been proven in Section 5.2, where a vision-based path following is implemented on an industrial forklift vehicle. The global path planner was substituted by a visual-based line detection algorithm, where a smart camera detects a line painted on the floor, which is used as path to follow. As a main advantage, the trajectory takes into account lower and upper bounds of curvature and curve sharpness, which implies smoother and safer trajectories. Moreover, the proposed method can handle cases where initial and final curvature take non zero values, which is not the case of other clothoid-based smooth path methods.

In Section 5.3, we have introduced a closed-loop hybrid control for an industrial AGV, where vehicle stability, safety, slippage and comfort have been taken into account. The proposed control structure is composed by both a kinematic and a vehicle stability controller. The latter establishes bounds for DCC paths so that vehicle stability, safety and comfort are satisfied. It also includes a closed-loop feedback structure, where odometry and IMU data are used to stabilize the vehicle against rollovers. The method has been validated in different simulated scenarios, where lateral and frontal tip overs have been

analysed showing that the proposed method is able to control the industrial forklift carrying a load of 1000 kg at 2.75 m height and 6 m/s speed, which is the maximum vehicle speed for the considered vehicle. Without the stability controller the AGV overturns at 3 m/s speed.

An exhaustive analysis to evaluate the performance of the new DCC kinematic method with respect to the conventional Pure-Pursuit (PP) method is also provided. It is interesting to remark that the PP method tends to oscillate the closer the target is selected (short Look-Ahead distances). These oscillations may cause unstability and eventually frontal or lateral rollovers, as well as crashing when moving in narrow corridors. In addition, several metrics have been considered for evaluation of the performance, such as overshoot, settling time, safety and comfort. It is shown that the proposed method achieves better results.

Section 5.4 has described a new method for generating quasi-holonomic paths based on clothoids, which can be included in most local planner and obstacle avoidance algorithms, such as ND, DWA, APF, VFH+, etc. The main advantage of the proposed method is to provide a low-level path planning layer with continuous recomputation. Based on such path, a non-holonomic robot can be treated as a holonomic one, while taking into account kinematic and dynamic constraints. Accelerations and jerks are kept within specified bounds, which plays an important role in terms of safety and comfort. The method is able to generate a wide open set of trajectories converging to desired directions (faster or slower upon the desired angular velocity).

Finally, in the last part of the chapter, in Section 5.5, an implementation of the ERTS controller has been used to solve the trajectory following problem using a wheeled differential-driven mobile robot platform.

Part II

Manual-Assisted Driving

Chapter 6

State of the Art: Advanced Driver Assistance Systems

6.1 Accidents in Passenger Transportation Systems

The World Health Organization, in its global status report on road safety 2015 (WHO, 2015), states the need for governments to ensure that public Passenger Transportation Systems (PTS) are safe, affordable, accessible and sustainable, as this will lead to a reduction in the number of traffic accidents and fatalities. It is a fact that buses and coaches are essential components of PTS, which contribute to improve competitiveness and development of other sectors and have socio-economic impact on the promotion of tourism, energy saving, environmental protection, road safety, mobility and economy. Indeed, no other mean of collective passenger transport plays such an important role in all these areas at the same time. In particular, buses represent around 55% of land PTS in the European Union (EU), while other PTS - rail, tram and metro - together constitute the remaining 45% (ASCABUS, 2013).

Currently, road transportation of passengers in bus and coach is the safest in Europe, matching safety level of railways (train, metro and tram), despite the fact that they share infrastructure with other users and transportation systems. From 2004 to 2013 buses and coaches represented around 3% of registered traffic fatalities in the EU (CARE Database, 2015). In urban areas, the large flow of people using buses and walking around them implies a high risk of accident, both as occupants and as pedestrians. As an example, in 2013 in the EU about 50% of fatalities in bus or coach accidents occurred in urban areas (CARE Database, 2015). Moreover, almost 30% of those who died in

2013 in road accidents that involved buses or coaches were pedestrians and more than 20% were vehicle occupants (CARE Database, 2015). In Spain, in 2013 there were 1816 accidents with victims (mortal or with injuries) in which a bus was involved, where 85% of those accidents happened in urban areas and the remainder in non-urban roads (Seguí, 2014). Fortunately, only 2% of the total amount of accidents involved buses in 2013, compared to 80% of cars, 18% of motorcycles or 13% of trucks and vans (Seguí, 2014).

Therefore, although bus accident figures are significantly lower than other means of transport (around 3% in 2004-2013 according to CARE Database (2015)), the severity of their accidents and the fact that they are massive PTS imply a continuous search for solutions to improve active and passive safety. Even though governments and researchers have done a big effort in searching for solutions to improve active and passive safety systems for buses, there is still an urgent need to reduce the amount of fatalities and injuries all around the world. This is being one of the main fields of technological development within the sector and an absolute priority for all PTS operators. In this sense, in the last European Commission Framework Programs and H2020, there have been several projects to classify, analyse and prevent accidents (TRACE, SafetyNet, DACOTA, LIVE), while others were intended to design passive and active safety systems (ADVISORS, HASTE, WATCH-OVER).

The authors of Kirk et al. (2001) carried out a study in the United Kingdom from 1994 to 1998, and concluded that 63% of fatalities or serious injuries in which buses and coaches were involved happened in accidents with no impact, while 94% of these accidents occurred in urban areas (speed limited to 30 mph). In af Wahlberg (2002, 2004), the author characterised and classified low speed accidents with buses in public transport in order to analyse their causes and consequences. An analysis from police and hospital data regarding safety in buses (including transfers to/from bus stops) was presented in Berntman et al. (2010). In this work, the authors concluded that most injuries occurred on board, as a result of an abrupt change in vehicle speed (60% in braking and 25% in acceleration), mainly affecting elderly and disabled people. This group is shown as the most vulnerable because it represents more than 50% of accidents, both as passengers (greater harmfulness when getting off the bus than when getting on it) and as pedestrians (in the access to bus stops).

One of the most common difficulties for drivers to avoid accidents involving pedestrians is their lack of visibility, particularly accidents involving children and wheelchairs. In fact, lack of visibility and distractions are by far the most common causes of bus accidents (CARE Database, 2015). For

instance, in the USA from 2003 to 2012, 119 school-age children died in school-transportation-related crashes while they were moving around the vehicle (NHTSA's Statistics and Analysis, 2014). Moreover, most accidents (crashes and fatalities) happened due to impacts in the front and right side of the bus. Taking this into consideration, there are international standards, such as the German standard StVZO 34[a], which forces all buses that transport children to see, from driver's seat, any child above 1.2 m in height at a distance of 1 m from the front of the bus, extending also to the side till halfway of the vehicle (Garcia et al., 2003). However, in most cases the use of mirrors is insufficient since the location of a person can change quickly and the driver may be distracted. Therefore, the use of active safety systems covering the periphery of the bus is clearly necessary.

6.2 Need for Solutions

Although accident figures analysed in the previous section cannot be directly extrapolated to all areas of transport and for all countries, they prove the importance of reducing accident frequency and severity not only in vehicles travelling at high speeds, but also in vehicles that transport passengers and materials at lower speeds.

Nowadays there are a wide variety of solutions in the automotive sector. For many years, research has tried to develop more and more intelligent vehicles by increasing the autonomy and the ability to take certain decisions autonomously, with the aim of replacing the driver in a long-term period. These systems are known as Intelligent Vehicles (IV) in the robotics and transportation communities.

Among automotive companies developing IV, the following ones stand out as the most innovative: General Motors, Ford, Mercedes Benz, Volkswagen, Audi, Nissan, Toyota, BMW and Volvo, (Toyota, 2013; BMW, 2013; Nissan, 2013); each one with its own driver assistance or autonomous navigation system. Many of them have already received, from the authorities of several countries (USA, UK, Japan, etc.), the license required to perform tests on conventional roads, which opens the way for the full implementation of this kind of system in a not too distant future. As an example of such a technology, in Figure 6.1 different assistance systems are depicted, which are incorporated within the new advanced navigation system by the Japanese automotive company Nissan (Nissan, 2013).

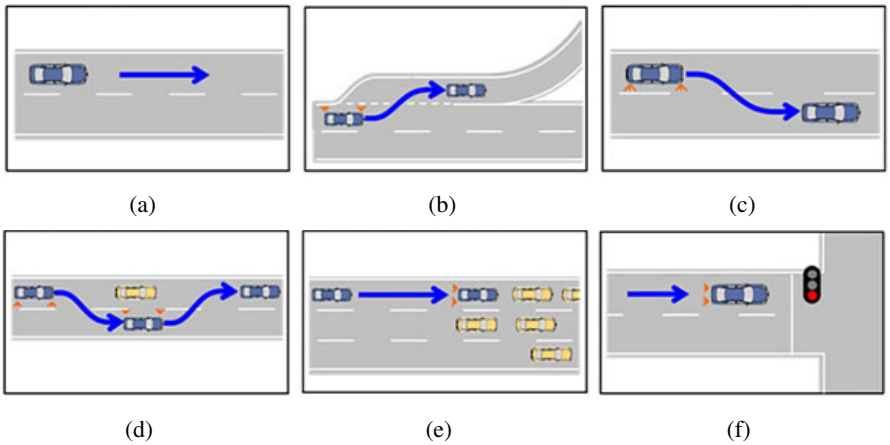

Figure 6.1: Features of the new navigation system by Nissan: (a) lane keeping, (b) automatic exit, (c) automatic lane change, (d) automatic overtaking, (e) automatic deceleration behind congestion, (f) automatic stopping at red lights.

6.3 Advanced Driver Assistance Systems

Despite all the innovations, in many cases IV with a complete autonomy fail to reach a massive scale industrial production, primarily due to high cost and lack of flexibility and adaptability. These factors, added to the high influence of driver's physical and mental conditions in safe driving, have induced the automotive industry to prioritize developing vehicles with Advanced Driver Assistance Systems (ADAS), rather than autopilots. In this sense, the automotive industry has the delicate task of integrating ADAS into their vehicles, so that drivers get acceptance and, most importantly, traffic safety is improved.

By definition, an ADAS should give support to the driver, so the purpose is not to replace the driver but to assist him. In other words, the driver remains responsible for the operation of the vehicle, but driving is monitored by an electronic system that detects and reacts in dangerous situations and manoeuvres, through haptic and audiovisual warnings. This approach seeks a collaboration between the driver and the intelligent system, where both interact and share the control of the vehicle in order to manoeuvre properly.

The final objective of ADAS is making the driving safer by reducing the probability of accident or at least mitigating the consequences of the lack of attention of the driver. In recent years, to reduce the number and severity of traffic accidents involving vehicles that transport passengers and/or materials, several ADAS technologies have been developed.

6.3.1 ADAS Classification

The number of safety systems are increasing more and more, but most of them have similar functionalities, so they can be grouped. One possible classification is related to the performed action, corrective or preventive. Hence, safety systems can be classified into two main groups:

- **Passive safety systems** act when an accident occurs and are responsible for protecting vehicle occupants in these circumstances, reducing the severity of possible injuries that occur during and after the crash. In general, passive safety systems go from the design of the car chassis or the seat belts and airbags, to the headrest or even safety devices for children.

- **Active safety systems** are those responsible for detecting and mitigating a possible dangerous situation. Some of them have been applied for long in the automotive sector, such as ABS braking system and ESP stability control. But there are other devices not so well known, such as the navigation control system, which can adjust the speed to maintain the distance to the vehicle ahead and in some cases it is able to keep the car within a road lane or perform an overtaking.

However, this is only one possible classification, but ADAS can be classified following other criteria. For instance, accordingly to the task that they develop. In this sense, a detailed classification of the ADAS available on the market regarding their functionalities is introduced in the following sections[1].

6.3.1.1 Braking Assistance

Listed below the braking assistance systems, which can be incorporated in all types of vehicles, although they are essential in buses and heavy trucks.

- **Anti-lock Braking System (ABS)**: (Bosch, 1978) ABS is an automotive safety system that allows the wheels on a motor vehicle to maintain tractive contact with the road surface according to driver inputs while braking, preventing the wheels from locking up (ceasing rotation) and avoiding uncontrolled skidding.

[1]Part of this information has been obtained from Broggi et al. (2008) and https://en.wikipedia.org/wiki/Advanced_driver_assistance_systems, as well as references therein.

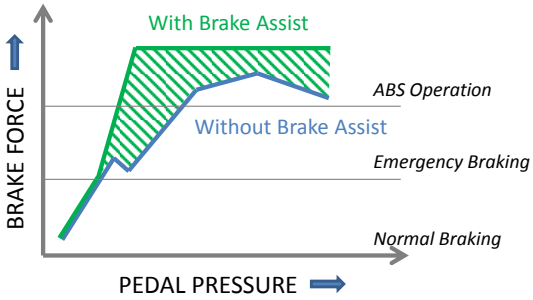

(a) Braking force

(b) Braking distances (from 100 km/h)

Figure 6.2: Performance analysis with and without BAS.

- **Emergency Brake Assist System (EBA or BAS)**: (Mercedes-Benz, 1998) BAS is a generic term for an automotive braking technology that increases braking pressure in an emergency. By interpreting the speed and force with which the brake pedal is pushed, the system detects if the driver is trying to execute an emergency stop, and if the brake pedal is not fully applied, the system overrides and fully applies the brakes until the ABS takes over to stop the wheels locking up. Figure 6.2 shows the performance of the BAS system.

- **Downhill Assist Control (DAC) or Hill Descent Control (HDC)**: (Toyota, 2013; Beever et al., 2001) HDC allows a smooth and controlled hill descent in rough terrain without the driver needing to touch the brake pedal. When on, the vehicle descends using the ABS brake system to control each wheel's speed. If the vehicle accelerates without driver input, the system automatically applies the brakes to slow down to the desired vehicle speed.

- **Active Brake Assist (ABA)**: (Mercedes-Benz, 1998) ABA is based on ACC (Labuhn et al., 1995) because it uses its sensors to explore a particular area in front of the vehicle and thus detect obstacles moving ahead. If the ABA detects a potential collision with a vehicle, progressively reacts with different levels of warning until an emergency braking is performed. Obviously ABA system cannot prevent an accident, but it makes available all the braking power to reduce the maximum speed in case of collision and thus lighten the severity and consequences of the accident.

6.3.1.2 Stability Assistance

The traction of the wheels on the ground is one of the key factors to ensure the stability of any vehicle, either transporting people or goods. For this reason, there are several systems on the market responsible for improving safety in this regard, which are explained below.

- **Electronic Stability Control (ESC) or Program (ESP)**: (Mamoru and Toshiki, 2009) ESC, also referred to as dynamic stability control (DSC), is a computerized technology that improves vehicle's stability by detecting and reducing loss of traction (skidding). When ESC detects loss of steering control, it automatically applies the brakes to help "steer" the vehicle where the driver intends to go. Braking is automatically applied to wheels individually, such as the outer front wheel to counter oversteer or the inner rear wheel to counter understeer. Some ESC systems also reduce engine power until control is regained.

- **Traction Control System (TCS)**: (Buick, 1971) TCS is typically (but not necessarily) a secondary function of the ESC on production motor vehicles, designed to prevent loss of traction of driven road wheels. TCS is activated when throttle input and engine torque are mismatched to road surface conditions.

- **Roll Stability Control (RSC)**: (Allen Brown and Carr Meyers, 2001, 2002) RSC is an active safety system that automatically intervenes if a high rollover risk is detected while driving. If a rollover threat is occurring, the system intervenes and assists the driver in minimizing the rollover risk by automatically reducing vehicle speed. RSC is designed specifically for trucks or tractors to help maintain vehicle stability and aid in reducing vehicle rollovers. RSC continuously checks and updates

the lateral acceleration of the vehicle and compares it to a critical threshold where rollover may occur. When the critical threshold is exceeded, RSC intervenes by reducing engine torque and engaging the engine retarder, while automatically applying drive axle and trailer brakes.

- **Dynamic Steering Response (DSR)**: DSR is a vehicle safety technique that corrects the rate of hydraulic or electric power steering system to adapt it to vehicle's speed and road conditions.

- **Tire-Pressure Warning System (TPWS) or Tire-Pressure Monitoring System (TPMS)**: (Doerksen and Nattinger, 1989) TPWS is an electronic system designed to monitor the air pressure inside the pneumatic tires on various types of vehicles. TPMS report real-time tire-pressure information to the driver, either via a gauge, a pictogram display, or a simple low-pressure warning light.

6.3.1.3 Visibility Enhancement

Mirrors are the traditional method used by drivers to monitor/supervise the periphery of the vehicle and detect possible dangerous situations. However, in large vehicles, such as buses or long trucks, this detection mechanism is insufficient in most cases. For this reason, during the last two decades, many systems have been incorporated in order to improve driver's visibility.

- **Blind Spot Detection (BSD)**:(Miller and Pitton, 1987) BSD is a vehicle-based sensor device that detects other vehicles located in driver's side and rear. Warnings can be visual, audible, vibrating or tactile. However, blind spot monitors are an option that may include more than monitoring the sides of the vehicle. Dead angles or blind spots are those areas where the driver cannot see directly or indirectly with the help of mirrors. The rear blind can reach up to 30 meters. Buses usually do not reverse in order to minimize the number of accidents. However, with the aim of reducing areas not visible to the driver, there are several warning and dead angle detection systems. Most of them are based on distance sensors, while others are based on cameras. A diagram with potential blind spots of a bus can be observed in Figure 6.3.

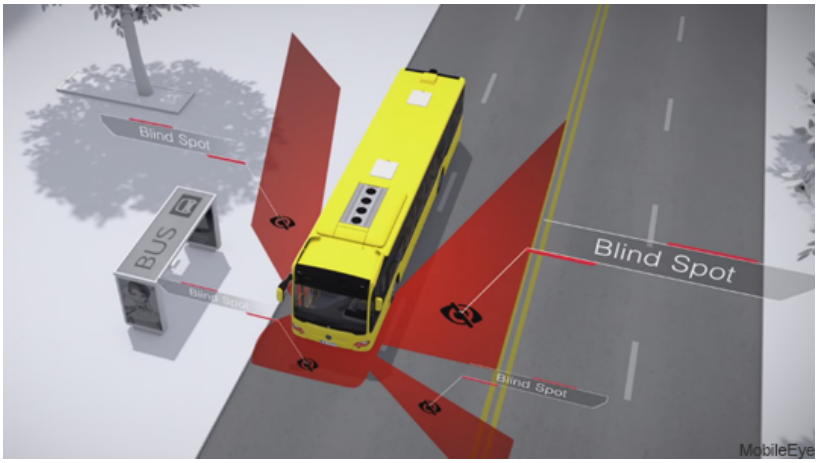

Figure 6.3: Blind spots of a bus. Courtesy of Mobileye.

Figure 6.4: Night Vision System by BMW. Courtesy of Jan-Erik Källhammer, "Imaging: The road ahead for car night-vision", Nature Photonics (2006).

- **Night Vision System (NV)**: (Windshield and Toyota, 2002) An automotive NV system uses a thermographic camera to increase driver's perception and seeing distance in darkness or poor weather beyond the reach of the vehicle's headlights. Such systems are offered as optional equipment on certain high-end vehicles. In Figure 6.4 a NV system is projecting an image of the road onto the windshield.

- **Object Detection System (ODS)**: (Grosch, 1995; Sorin Faibish et al., 1995; Juds, 1995) ODS are different types of systems that allow to inspect vehicle's surroundings, usually heavy vehicles and buses, to confirm that the space for manoeuvre is free and there is no risk of collision with objects. Therefore, the main objective is to detect objects that are in front, on the sides or in the rear of the vehicle in order to warn the driver (via visual or acoustic signals) and prevent accidents. Most ODS are based on one of the following detection technologies: LIDAR, RADAR, ultrasound and computer vision.

- **People Detection Systems (PDS)**:(Enzweiler and Gavrila, 2009; Gerónimo et al., 2010) Although people can also be detected through other simpler systems used for object detection (RADAR, ultrasound, etc.), vision-based detection systems are much better suited when it comes to detecting pedestrians, due to the versatility offered by cameras. In many cases vision systems are combined with other range sensors to obtain richer information (Milch and Behrens, 2001).

6.3.1.4 Advanced Navigation

This section describes the main active systems involved directly in driving tasks, with the aim of increasing safety by reducing the risk of rear-end or side collisions. In addition, some modern navigation and driving assistance systems are also included, which have recently been incorporated in some models of high-end vehicles (Toyota, 2013; BMW, 2013; Nissan, 2013).

- **Adaptive Cruise Control (ACC)**: (Labuhn et al., 1995; Toyota, 2013; Nissan, 2013; BMW, 2013) ACC is an optional cruise control system for road vehicles that automatically adjusts the vehicle speed to maintain a safe distance from vehicles ahead. It makes no use of satellite or roadside infrastructures nor of any cooperative support from other vehicles. Hence control is imposed based on sensor information from on-board sensors only. Cooperative Adaptive Cruise Control (CACC) further extends the automation of navigation by using information gathered from fixed infrastructure such as satellites and roadside beacons, or mobile infrastructure such as reflectors or transmitters on the back of other vehicles. Such systems use either a radar or laser sensor setup allowing the vehicle to slow when approaching another vehicle ahead and accelerate again to the preset speed when traffic allows.

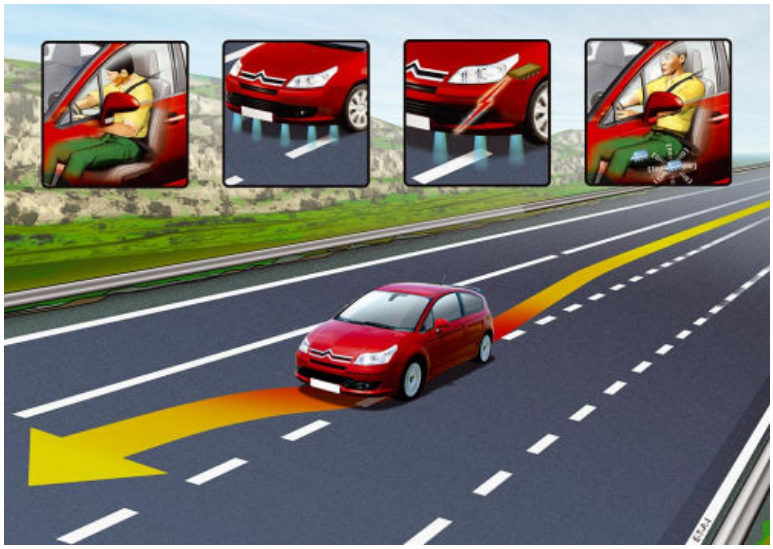

Figure 6.5: Conceptual idea of the LDW system. Courtesy of Citroën.

ACC technology is widely regarded as a key component of any future generation of intelligent cars. The impact is equally on driver safety as on economising capacity of roads by adjusting the distance between vehicles according to the conditions. One of the biggest drawbacks of the ACC is not operating at low speeds (typically below 25-30 km/h) and the fact that it does not completely stop the vehicle. Another problem is that the radar system cannot detect small size vehicles such as motorcycles.

- **Lane Departure Warning (LDW)**: (Nissan, 2001, 2013) In road transport terminology, a LDW system is a mechanism designed to warn the driver when the vehicle begins to move out of its lane (unless a turn signal is on in that direction) on freeways and arterial roads. These systems are designed to minimize accidents by addressing the main causes of collisions: driver error, distractions and drowsiness. Figure 6.5 shows an example of LDW.

- **Lane Change Assistant (LCA)**: (Kaller and Hoetzer, 2009) LCA usually works with the detection of blind spots (BSD). The system issues an audiovisual warning if the driver returns to its original lane too soon after an overtaking. If the driver ignores the warning and tries to change lanes (with possible risks of collision) a vibration in the steering wheel is used as a warning (Bishop, 2005).

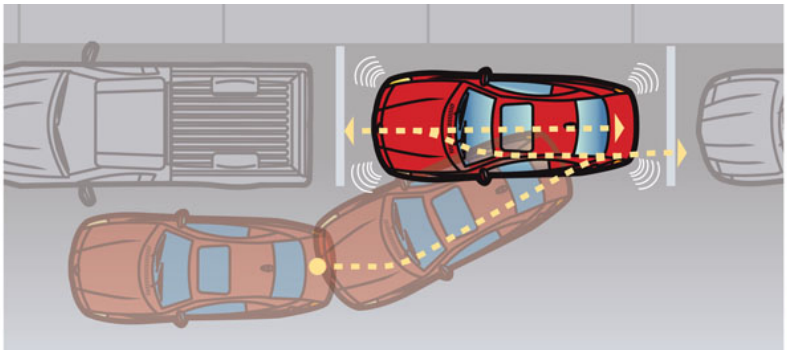

Figure 6.6: Illustration of automatic parking. Courtesy of Samuel A. Minick.

- **Automatic Lane Keeping**: Ability to drive a road without leaving it independently of the road. It is a direct extension of the LDW system, where the autonomous system takes active control of the vehicle.
- **Automatic Lane Changing**: The vehicle assists or even switches automatically between lanes. Using a BSD system, this mechanism is able to detect whether the route is free and it is possible to perform a safe lane change without risk of collision.
- **Automatic Overtaking**: The vehicle is capable of performing a fully automatic manoeuvre to overtake other vehicles driving at lower speeds or which are stopped in the roadway, whenever the action is safe. This system is a direct extension of the two previous systems.
- **Automatic Parking System (APS)**: (Macphail and Kumhyr, 2003) APS is an autonomous car-maneuvering system that moves a vehicle from a traffic lane into a parking spot to perform parallel, perpendicular or angle parking. The automatic parking system aims to enhance the comfort and safety of driving in constrained environments where much attention and experience is required to steer the car. The parking manoeuvre is achieved by means of coordinated control of the steering angle and speed, which takes into account the actual situation in the environment to ensure collision-free motion within the available space. Figure 6.6 shows an example of automatic parking system.
- **Driver Monitoring or Driver Drowsiness Detection**: (Adam Basir et al., 2004) The system is a car safety technology that helps prevent accidents caused by the driver getting drowsy. It detects the status of the driver and warns when distracted or falling asleep.

6.4 Driving Assistance Through Haptic and Audiovisual Feedback

From CARE Database (2015), it can be observed that in accidents where a pedestrian was involved, around 22% were caused by a late driver action, while in more than 32% there was no action at all. Most of those accidents could have been avoided by a warning system or a collision avoidance system with emergency braking. Indeed, a study carried out in the EC FP6 project "Cost-benefit assessment and prioritisation of vehicle safety technologies", the authors concluded that front and side collision warning systems can reduce an 8% the severity and a 12% the risk of collisions of type rear-end and head-on, as well as vehicle-pedestrian collisions. On the other hand, Intelligent Speed Adaptation (ISA) systems could reduce around a 50% the risk of collision on these types of accidents.

Among the most used ISA systems in passenger buses for executing emergency braking, basically two must be mentioned: brake assistance system (BAS) and adaptive brake assist system (ABA). On the one hand, the BAS consists of a device that acts during emergency braking of the vehicle if the driver does not reach sufficient braking force to stop the vehicle in the shortest possible distance. If the force exerted on the brake pedal is not enough in an emergency situation, the BAS activates the brake booster or the electronic braking system (EBS) hydraulic unit increasing the total force exerted. The BAS interacts with: brake booster vacuum pump, anti-lock braking system (ABS), electronic stability program (ESP) and cruise control (ACC).

On the other hand, the ABA system detects a risk of rear-end collision against a vehicle in front of the bus at a lower speed or a stationary obstacle. The system reacts in stages with different types of visual, acoustic or brake assistance actions. The ABA system operates in motorways with three radar sensors that detect the presence of such vehicles in front of the bus at a slower speed, so that it can automatically reduce the velocity to restore and maintain the safety distance. Deceleration is limited to 20% of vehicle's maximum braking effort. Normally, radar sensors are installed in the front of the vehicle and can detect obstacles up to a distance of 200 meters. In the last generation versions of this system, the operating speed range has been extended from 7 to 200 km/h (Schittenhelm, 2013).

In any traffic accident the critical pre-crash event or reason leading up to a crash can be assigned to any of the three factors involved: driver, vehicle or environment. However, the fact that between 70% and 90% among all

traffic accidents are produced by a human factor is supported by some recent road safety reports from international institutions, such as the World Health Organization (WHO), the European Union Road Federation (ERF), or the National Highway Traffic Safety Administration (NHTSA) from the USA. For instance, in NHTSA's Statistics and Analysis (2015) it was explained that in the USA a driver error was involved in $94\% \pm 2.2\%$ of crashes. Among critical reasons attributed to drivers, recognition errors ($41\% \pm 2.2\%$) and decision errors ($33\% \pm 3.7\%$) were the most significant. These causes are closely related to distractions or slow response times, which are one of the main causes of accidents.

The authors of Jurecki et al. (2012) analysed the psycho-motor reaction time (reaction time on the brake pedal) in a risky situation and showed that it varies in the range $0.42 - 0.92$ s. As stated in Ma and Andréasson (2006), a study using both a real driving environment and a simulator showed that the reaction time of drivers to an anticipated danger in a real environment has a mean value of 0.42 ± 0.14 s whereas the mean value of the reaction time distribution to an unanticipated danger by extreme braking is about 1.1 s, being around 0.9 s in a simulator (Magister et al., 2005). In the study carried out by Fambro et al. (1998), the authors proved that in real traffic situations the mean reaction time of drivers for unexpected and expected stimuli are also different, 1.3 s and 0.7 s respectively.

It is clear that anticipation of future traffic events provides potential gains in recognition and reaction times (Stahl et al., 2014). However, anticipation is not always possible in an urban environment in which pedestrians are involved, as their movements are sometimes fast and unpredictable. Moreover, there might be some manoeuvres in which the driver has low visibility, which make impossible any kind of anticipation. In this sense, the best approach to avoid accidents with pedestrians seems to be the detection of potential collisions and warning the driver to improve the reaction time. Thus, the unexpected becomes expected and driver's response time is reduced.

In Dunn et al. (2007), the authors stated that the most effective active safety systems to avoid frontal and lateral crashes are those based on side collision warning systems (SCWS), rear-end collision warning systems (RCWS) (Chang and Chou, 2009), head-on collision warning systems (Kim and Jeong, 2010) and emergency braking systems (García et al., 2013). Usually, these systems are called ODS (Object Detection System), which are based on range sensor technologies such as LIDAR, RADAR, ultrasound and ubiquitous sensor network (USN) (Wu et al., 2009; Jang et al., 2012; Gandhi and Trivedi,

2006; Geronimo et al., 2010; Brscic et al., 2013; Wu et al., 2014). Besides, since those systems use a large number of sensors and data, it has produced lots of sensor fusion works, using laser scanner (García et al., 2011) and video for detecting pedestrians (Kaempchen and Dietmayer, 2004; Geronimo et al., 2010; Ge et al., 2009; Dalal and Triggs, 2005; Schneider and Gavrila, 2013). In Gandhi and Trivedi (2006) there is a complete survey on computer vision based pedestrian collision avoidance systems.

Monitoring the vehicle environment plays an important role in the development of Advanced Driver Assistance Systems (ADAS). Among all possible ADAS for use in urban environments, those acting at low speed to detect the presence of pedestrians in the vicinity of the vehicle are particularly important, especially for buses (NHTSA's Statistics and Analysis, 2014). Indeed, active safety systems covering the periphery of a bus become necessary because mirrors are insufficient due to the size of the vehicle and the fact that the location of a person can change quickly and the driver may be distracted. In this sense, systems to support blind spots check to warn the driver of pedestrians or objects near the vehicle have been developed during the last decade (Racine et al., 2010; Morrell and Wasilewski, 2010; Chun et al., 2013). Once a pedestrian has been detected in the area surrounding the vehicle, this kind of ADAS normally produce haptic or audiovisual (HAV) warnings to make the driver aware of the danger in certain situations, with the aim of reducing the number of accidents and their severity (Dunn et al., 2007; Scott and Gray, 2008; Adell et al., 2008a,b; Straughn et al., 2009; Hogema et al., 2009; Saffarian et al., 2013; Itoh et al., 2012; Fitch et al., 2011; Jensen et al., 2011; Wu et al., 2014), for instance by avoiding a rear-end or head-on accident (Chang and Chou, 2009; Kim and Jeong, 2010; Mohebbi et al., 2009), helping in lane changing (Zheng et al., 2013), in lane keeping manoeuvres (de Nijs et al., 2014), or performing automatic emergency braking (Chang and Chou, 2009; Brannstrom et al., 2010; Geronimo et al., 2010).

Haptic interfaces such as active throttle pedal to control the deceleration are gaining more and more importance (Mulder et al., 2009). At present, there are already systems using a haptic gas pedal for active car-following with speed adaptation (Adell et al., 2008a; Mulder et al., 2010, 2011). Many of the studies focus on the development of simulation methods to evaluate and verify the quality, safety and functionality of these systems, and the analysis of the effects they cause in relation to security in terms of distance and speed (Adell et al., 2011). Some other studies have shown the benefits of including these systems in the vehicle control chain (Nilsson, 2002; Adell et al., 2008a,b, 2011). On the other hand, other researchers try to analyse the adaptation of

the driver to the new device, demonstrating that driving can be improved after a certain time of usage, making it safer (Várhelyi et al., 2004; Hjälmdahl and Várhelyi, 2004; Adell and Várhelyi, 2008).

It is pretty obvious that the driver has an important role in defining the requirements in ADAS design, which generates investigations oriented to people interaction with these systems, as in the case of driving manoeuvres selectable by the user (Kauer et al., 2010). Other studies focus on the design of user interfaces dedicated to meet the driver's needs, developing components for human-machine interaction, both visual and haptic, within the concepts of speed and safe distance (Adell et al., 2008a), combining user driving preferences and safety margins to generate optimal manoeuvres (Biral et al., 2005).

Danieau et al. (2013) stated the growing interest among researchers in integrating haptic feedback into audiovisual systems, as haptics enhances the benefits of audiovisual feedback. Particularly, the authors of Straughn et al. (2009) studied and proved the effectiveness of tactile and auditory pedestrian collision warnings in urban roads. In Mars et al. (2014) human-machine cooperation when driving with different degrees of a shared control system was investigated. They introduced direct intervention on the steering wheel and proved its effectiveness. The authors of de Nijs et al. (2014) evaluated the value of haptic feedback in the steering wheel for lane keeping. A haptic steering wheel with force-feedback was also used in Dennerlein et al. (2000); Dell'Amico et al. (2007); Jensen et al. (2011); Na and Cole (2015). See Petermeijer et al. (2015) for a detailed survey on the effect of haptic support systems on driver's performance.

It can be said that by interacting with drivers and/or braking the vehicle all these ADAS try to modify their behaviour through reactive stimuli to influence their decision making, with the aim of reducing the number of accidents and their severity. However, although there are some approaches and commercial solutions to avoid crashes between cars and pedestrians, their use in PTS is still in development and requires further research. In fact, to the best of author's knowledge, there is no system working on public PTS to avoid collisions with pedestrians at low speed. In this sense, the implantation of such a safety system into city buses would potentially reduce the frequency and severity of accidents and injuries involving this conveyance.

Chapter 7

Driver Assistance Methodology

7.1 Introduction

Buses and coaches are massive Passenger Transportation Systems (PTS), because they represent more than half of land PTS in the European Union (EU) (ASCABUS, 2013). Despite of that, accident figures for those vehicles are lower than other means of transport, but its size and weight increase the severity of accidents when they occur, even at low speed.

In urban scenarios, turnings and manoeuvres around bus stops are the main causes of accidents, mostly due to low visibility, blind spots or driver's distractions (NHTSA's Statistics and Analysis, 2014; CARE Database, 2015). Therefore, there is an increasing interest in developing driving assistance systems to avoid these accidents, among others. However, even though there are some solutions available, they are not designed to work in urban areas at low speed with the sole purpose of preventing collisions with pedestrians.

In this sense, this chapter describes an Advanced Driver Assistance System (ADAS) for buses in manoeuvres at low speed in urban scenarios (particularly with low visibility, in areas of passenger loading and unloading, as well as turnings). The main contribution is a computationally efficient algorithm with a methodology based on the following concepts: an efficient collision detection system considering driver's intention and pedestrians moving around the vehicle, which is based on arc reachable manifolds and the new concept of clothoid reachable manifold; as well as a risk evaluation system to generate warnings and emergency stop signals.

The proposed safety system consists of haptic feedback devices in throttle pedal and steering wheel, as well as an emergency brake system to stop the vehicle in situations of imminent collision. The complete active safety sys-

tem also incorporates warnings through audio-visual feedback, together with a vision-based pedestrian detection system. However, Haptic-Audio-Visual (HAV) feedback and people detection are out of the scope of this chapter and are detailed in Chapter 8.

7.2 Proposed Methodology for Driver Assistance

In autonomous driving vehicles, obstacle avoidance algorithms are used to give specific speed commands to avoid collisions (Siciliano and Khatib, 2008, Chapters 5 and 35). They typically consider the state of the vehicle, nearby obstacles (obtained either from sensor readings or from a map) and a given target goal. In that sense, to allow the integration of generic obstacle avoidance frameworks into the driving assistance problem, existing algorithms must be adapted to provide valid solutions according to driver's intention.

In order to predict potential collisions, the methodology presented in this chapter analyses not only the vehicle behaviour but also considers pedestrians wandering around it. For that purpose, it is necessary to know driver's intention based on the position of throttle, brake and steering wheel. It is interesting to remark that the vehicle dynamic model uses simplifications in order to achieve better computational performance in obstacle avoidance algorithms. This is a common approach in robotics, where all unmodeled errors are usually reduced using safety margins (Siciliano and Khatib, 2008, Chapters 5 and 35).

In addition to this, sensorization is required to provide information about each detected pedestrian in vehicle surroundings: position, speed and direction of movement relative to the vehicle. As explained in Sections 8.2 and 8.3, this is accomplished with a set of electro-mechanical components and *smart* cameras.

7.2.1 Collision Detection

7.2.1.1 Obstacle Space from Arc Reachable Manifold

To define the vehicle configuration space $\mathcal{CS}$, most collision detection algorithms and path planners use arc segments. They assume that the vehicle will keep its linear and angular speeds (v and ω) during a certain period of time. This approach is valid in the majority of situations, specially for wheeled mobile robots in indoor environments which tend to have little effects of the vehicle dynamics and can change almost instantly their linear and angular speeds.

Definition An *Arc Reachable Manifold* (ARM) is a two-dimensional manifold in $\Re^2 \times \mathcal{S}^1$ (Minguez and Montano, 2009). Let $\mathcal{CS}_{ARM}$ be the vehicle configuration space, obtained from a non-holonomic standard car-like kinematic model (*i.e.* type (1,1) in Chapters 34 and 35 of Siciliano and Khatib (2008), which is kinematically equivalent to Ackermann steering model), describing arc segments from driver's commands (linear and angular velocities). Without loss of generality, $\mathcal{CS}_{ARM}$ has its centre at (x_{ARM}, y_{ARM}) with $x_{ARM} = 0$, $y_{ARM} = \text{sign}(\alpha) \cdot R_{ARM}$ and radius $R_{ARM} = \left| \frac{L}{\tan(\alpha}) \right|$, being α the vehicle steering wheel angle and L the wheelbase, i.e. the distance between front and rear axles of the vehicle.

Now, let's define l as the distance from the rear axle to the front of the vehicle and w as the vehicle width assuming a rectangular footprint. In order to abstract pedestrians' shape, vehicle footprint is usually enlarged with the estimated radius of the circle circumscribing a pedestrian R_p. Thus, following the ideas of Minguez et al. (2006), we can obtain a parametrized rectangular shaped vehicle:

$$x_v(\lambda) = \begin{cases} dY \tan\lambda & \text{if } \tan\lambda < \frac{dX}{dY} \text{ and } \lambda < \frac{\pi}{2} \\ -dY \tan\lambda & \text{if } \tan\lambda > -\frac{dX}{dY} \text{ and } \lambda > \frac{\pi}{2} \\ dX & \text{otherwise} \end{cases} \tag{7.1}$$

$$y_v(\lambda) = \begin{cases} -dY & \text{if } \tan\lambda < \frac{dX}{dY} \text{ and } \lambda < \frac{\pi}{2} \\ dY & \text{if } \tan\lambda > -\frac{dX}{dY} \text{ and } \lambda > \frac{\pi}{2} \\ -dX \tan(\frac{\pi}{2} - \lambda) & \text{if } \tan\lambda \geq \frac{dX}{dY} \text{ and } \lambda < \frac{\pi}{2} \\ dX \tan(\frac{\lambda - \pi}{2}) & \text{if } \tan(\lambda - \frac{\pi}{2}) < -\frac{dY}{dX} \text{ and } \lambda \geq \frac{\pi}{2} \end{cases} \tag{7.2}$$

with $\lambda \in [0, \pi]$ and where $dX = l + R_p$ and $dY = w/2 + R_p$. For simplicity, only the front part of the vehicle shape is considered, because the vehicle is moving forward. However, rear part is treated in a similar way when moving backward.

Based on Minkowsky addition (Hazewinkel, 2001), the rectangular shape of the bus can be abstracted to obtain an obstacle configuration space $\mathcal{CO}_{ARM}$, which defines the region where the vehicle collides with objects by describing an ARM, allowing to treat the vehicle as a point for further computations. Indeed, the configuration obstacle for all pedestrians is $\mathcal{CO}_{ARM} = \cup_i \mathcal{CO}_{ARM,i}$, where $\mathcal{CO}_{ARM,i}$ denotes the configuration obstacle for the i-th pedestrian. However, from now on, we remove subscript i to keep notation clearer, restricting the problem to one single pedestrian case, although computations are carried out for each pedestrian.

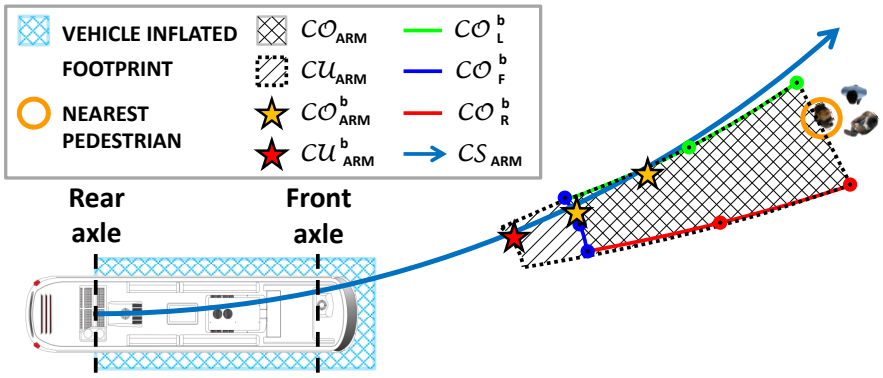

Figure 7.1: Example of collision detection using ARM.

Let's denote $\{x^b_{\mathcal{CO}}, y^b_{\mathcal{CO}}\} \in \mathcal{CO}^b$ the boundary points of $\mathcal{CO}_{ARM}$ for a given pedestrian position $\{x_p, y_p\}$. This boundary can be analytically computed for any shape (Minguez et al., 2006):

$$x^b_{\mathcal{CO}}(\lambda) = c \cdot (x_p + x_v(\lambda)) \tag{7.3}$$

$$y^b_{\mathcal{CO}}(\lambda) = c \cdot (y_p - y_v(\lambda)) \tag{7.4}$$

with $c = \frac{\left[y_p^2 - y_v^2(\lambda) + x_p^2 - x_v^2(\lambda)\right]\left[(y_p - y_v(\lambda))^2 + (x_p - x_v(\lambda))^2\right]}{(y_p - y_v(\lambda))^4 + 2(x_p^2 + x_v^2(\lambda))(y_p - y_v(\lambda))^2 + (x_p^2 - x_v^2(\lambda))^2}$.

Instead of considering the whole parametrized $\mathcal{CO}^b$ for any arbitrary shape, only mid and end points of each segment of the rectangular shape are considered. This reduces the computation of shape abstraction to a total of 7 points (coloured dots in Figure 7.1) corresponding to $\lambda_0 = 0$, $\lambda_1 = \arctan\left(dX/2dY\right)$, $\lambda_2 = \arctan\left(dX/dY\right)$, $\lambda_3 = \pi/2$, $\lambda_4 = \pi/2 + \arctan\left(dY/dX\right)$, $\lambda_5 = \pi - \arctan\left(dX/2dY\right)$ and $\lambda_6 = \pi$. Furthermore, we approximate an arc segment for every triple of points related to each side of the rectangle (backward side not considered), having a total of 3 arcs defining an approximation of $\mathcal{CO}^b$:

$$\mathcal{CO}^b \approx \mathcal{CO}^b_L \cup \mathcal{CO}^b_F \cup \mathcal{CO}^b_R \tag{7.5}$$

where $\mathcal{CO}^b_L$ denotes configuration obstacle boundary for left-side (using points with λ_0 to λ_2), $\mathcal{CO}^b_F$ corresponds to the front-side (using points with λ_2 to λ_4) and $\mathcal{CO}^b_R$ to the right-side (using points with λ_4 to λ_6). As a consequence, $\mathcal{CO}^b_{ARM}$ becomes a piece-wise function formed by 3 arc segments (green, blue and red lines in Figure 7.1), which are easier to deal with than computing the analytical *locci* as in Equations (7.3)-(7.4).

Now, let's define $\mathcal{CO}^b_{ARM} = \mathcal{CO}^b \cap \mathcal{CS}_{ARM}$ as the manifold in $\Re^2 \times \mathcal{S}^1$ in which vehicle configurations are in collision with pedestrians. This manifold

is indeed computed from geometric relations between arc segments. For every segment of the vehicle shape, we compute the intersection between the arc segment defined by $\mathcal{CS}_{ARM}$ and the approximation of $\mathcal{CO}^b$ using (7.5). If such intersection point exists and belongs to both arc segments, it is considered as a candidate collision point. The point with the minimum distance (arc-length to reach that point from the origin) is the most critical one and, thus, the one to be considered. Such distance is denoted as $d_{\mathcal{CO}}(t)$ and computed as:

$$d_{\mathcal{CO}}(t) = \min_{i \in \mathcal{C}(t)} R_v(t)\delta_i(t) \tag{7.6}$$

being $\mathcal{C}(t)$ the subset of candidate collision points and $\delta_i(t)$ their arc angle.

As defined in Minguez and Montano (2009), there exists an unsafe obstacle configuration space ($\mathcal{CU}_{ARM}$), which defines the region for inevitably collisions due to vehicle dynamics. Indeed, $\mathcal{CO}_{ARM} \subset \mathcal{CU}_{ARM}$, which contains additional vehicle configurations that are unsafe, because of the distance needed to stop the vehicle in case of emergency braking. Computing $\mathcal{CU}_{ARM}$ for a general obstacle avoidance problem is complex as it requires to compute four additional boundary points for every boundary point of $\mathcal{CO}_{ARM}$.

Fortunately, in ADAS applications only $\mathcal{CU}^b_{ARM} = \mathcal{CU}^b \cap \mathcal{CS}_{ARM}$ is of interest because it is the considered driver's intention, being $\mathcal{CU}^b$ the boundary of $\mathcal{CU}_{ARM}$. The distance of $\mathcal{CU}^b_{ARM}$ can be computed by subtracting to $d_{\mathcal{CO}}(t)$ the minimum distance to stop $d_{min}(t)$:

$$d_{\mathcal{CU}}(t) = d_{\mathcal{CO}}(t) - d_{min}(t) \tag{7.7}$$

where $d_{min}(t)$ is detailed thereinafter.

In addition to this, such distance can also be expressed as follows:

$$d_{\mathcal{CO}}(t) = \int_{t}^{t+t_C} v(\tau)d\tau \tag{7.8}$$

where t_C is the time to collision and $v(t)$ the vehicle velocity, which is used as measure of safety in the benchmarking evaluation carried out in Chapter 9.

Table 7.1 shows the algorithm performance to compute the $\mathcal{CO}^b$ using our approach (arc-based) and the approach proposed in Minguez et al. (2006) (segment-based). If we assume that there are 3 shape sides (left, front, right), the number of points to compute in the $\mathcal{CO}_{ARM}$ is $N = 3 \cdot 2^n + 1$, being n the number of times to split each vehicle shape side in a half. In our approach, since we consider three points per side, we have a fixed computational time with less significant error (case $n = 1$). To obtain the accuracy achieved in our approach the method proposed in Minguez et al. (2006) takes roughly twice

Table 7.1: Performance of segment-based vs. arc-based $\mathcal{CO}_{ARM}$ algorithm

	n	**0**	**1**	**2**	**3**	**4**
segment-based	$\mathbf{t}_{proc}$ [ms]	0.348	0.371	0.516	0.725	1.157
	$\mathbf{e}_{\mathcal{CO}}$ [mm]	51.74	22.31	8.03	0.93	0.4
arc-based	$\mathbf{t}_{proc}$ [ms]	–	0.313	–	–	–
	$\mathbf{e}_{\mathcal{CO}}$ [mm]	–	1.62	–	–	–

to compute with $n = 3$[1]. Processing times are based on Matlab implementations using a computer based on Ubuntu 14.04 with the following technical specifications: CPU Intel Core i7-2670QM 2.20GHz, with 8GB DDR3 1333 MHz.

7.2.1.2 Obstacle Space from Clothoid Reachable Manifold

For vehicles with a high dynamic component, an ARM does not fit their behaviour accurately. One of the main drawbacks of an ARM is the fact that this kind of manifold does not take into account the current curvature of the vehicle. Moreover, an ARM assumes that the vehicle can change its curvature almost instantly, but this does not happen with real vehicles. In this sense, in order to get a manifold closer to the actual behaviour of the vehicle, clothoids can be used instead of circular arcs. Indeed, clothoids can consider curvature and sharpness, which in a human-driven vehicle can be obtained instantly from driver's inputs: steering wheel angle and angular speed.

From a car-like kinematic model, we assume that the curvature of the vehicle is directly related to the wheels angle as follows:

$$\kappa(t) = \frac{\tan \alpha(t)}{L} \tag{7.9}$$

Therefore, it is possible to obtain the derivative of curvature from the angular speed at which the steering wheel is turning.

$$\dot{\kappa}(t) = \frac{\dot{\alpha}(t)}{L(1 + \tan \alpha^2(t))} \tag{7.10}$$

Then, assuming that the vehicle is following a clothoid segment, the following expression stands:

$$\sigma = \left| \frac{\dot{\kappa}(t)}{v(t)} \right| \tag{7.11}$$

[1]Error distance $e_{\mathcal{CO}_{ARM}}$ is computed as the difference between $d_{\mathcal{CO}_{ARM}}$ and the exact model of $\mathcal{CO}_{ARM}$ when $n \to \infty$.

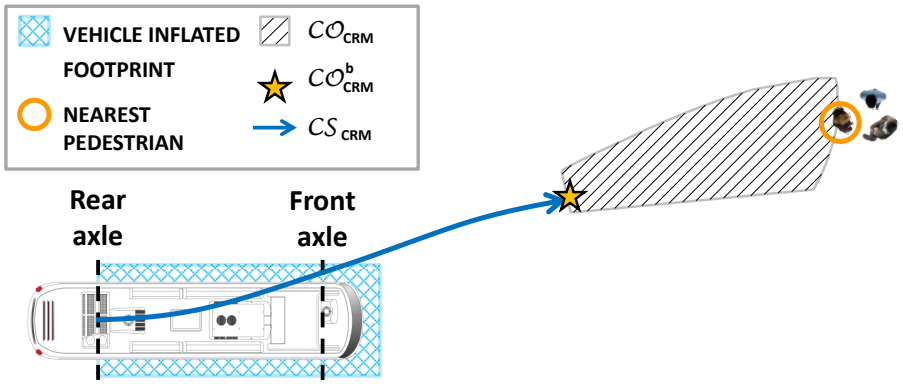

Figure 7.2: Example of collision detection using CRM.

Definition A *Clothoid Reachable Manifold* (CRM) is a two-dimensional manifold in $\Re^2 \times \mathcal{S}^1$. Let $\mathcal{CS}_{CRM}$ be the vehicle configuration space obtained from a non-holonomic standard car-like kinematic model, describing clothoid segments from driver's commands (linear velocity, steering wheel angle and steering wheel angular velocity). A point in such $\mathcal{CS}_{CRM}$ must fulfil Fresnel integrals, Equation (2.4) for the Cartesian coordinates and Equation (2.6) for the vehicle orientation.

To obtain an obstacle configuration space $\mathcal{CO}_{CRM}$ based on CRM, as for the case of ARM, it is possible to abstract pedestrians' shape by inflating the vehicle footprint with the estimated radius of the circle circumscribing a pedestrian. This $\mathcal{CO}_{CRM}$ defines the region at which the vehicle collides with objects by describing a clothoid segment or CRM, allowing to treat the vehicle as a point for further computations. Figure 7.2 shows an example of collision detection obtained from the intersection between the vehicle configuration space $\mathcal{CS}_{CRM}$ and the obstacle configuration $\mathcal{CO}_{CRM}$.

A vehicle configuration space $\mathcal{CS}_{CRM}$ starts from current vehicle curvature and its sharpness is estimated from the steering wheel angular speed. Therefore, the shape of a CRM is dependent on such initial conditions and can lead to very different obstacle configuration spaces. Indeed, the shape of a $\mathcal{CO}_{CRM}$ is very different for the same value of sharpness but different initial curvatures, as can be seen in Figure 7.3.

In Figure 7.4 there are three cases with the same initial curvature and obstacle position, but with different clothoid sharpness, which are produced by different angular speeds in the steering wheel. It can be seen that the $\mathcal{CO}_{CRM}$ remains the same in all cases for a given value of curvature, but depending on the curvature rate it might happen that a collision is detected or not.

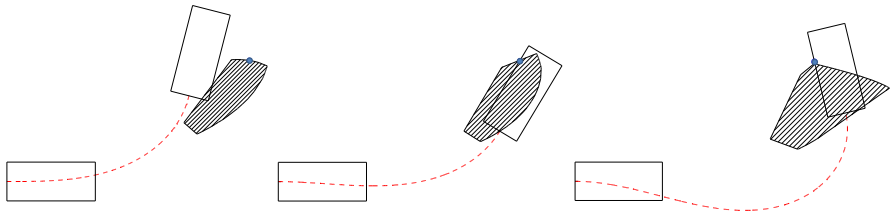

Figure 7.3: CRM with different initial curvature but the same sharpness.

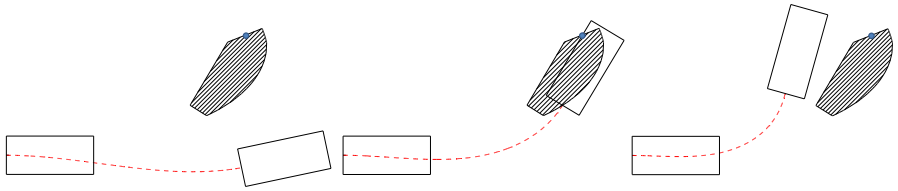

Figure 7.4: CRM with the same initial curvature but different sharpness.

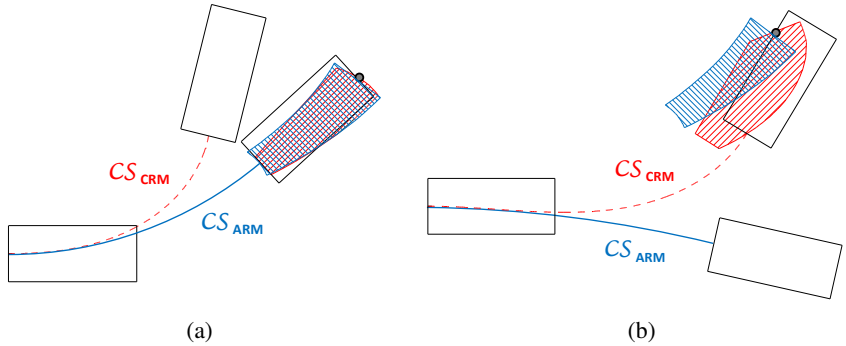

(a) (b)

Figure 7.5: Two representative cases of CRM and ARM collision detection.

It is interesting to remark that the use of CRM in the collision detection problem can help to detect potential collisions that would not be considered with ARM, see Figure 7.5(a). The opposite can happen as well, when a case detected as collision using ARM does not produce a crash if the angular speed of the steering wheel is taken into account, as depicted in Figure 7.5(b).

Working with CRM to compute the obstacle configuration space $\mathcal{CO}_{CRM}$ is more difficult in mobile robotics due to the high computational cost. However, for driving assistance it is not necessary to compute the whole collision-free space since there is only one CRM corresponding to driver's inputs. In this sense, for collision detection using CRM it is possible to implement a simple algorithm in which the vehicle trajectory is predicted from driver's intention and potential collision are checked each iteration. The remainder of

the chapter deals with the ARM approach for simplicity and its extension using CRM is left for further research work.

7.2.2 Risk Evaluation

In order to assist the speed control of the vehicles, the following collision risk factor is proposed:

$$c(t) = \text{sat}_{[0,1]}\left(\frac{d_{max}(t) - d_{\mathcal{CO}}(t)}{d_{max}(t) - d_{min}(t)}\right) = \text{sat}_{[0,1]}\left(\frac{\Delta d(t) - d_{\mathcal{CU}}(t)}{\Delta d(t)}\right) \quad (7.12)$$

being $d_{min}(t)$ and $d_{max}(t)$ distance thresholds that define a spatial window $\Delta d(t)$ where the system is active:

$$\Delta d(t) = d_{max}(t) - d_{min}(t) \quad (7.13)$$

This design parameter represents the anticipation distance at which the vehicle should reduce its speed before reaching the "inevitable collision" distance $d_{min}(t)$. Therefore, high values of $\Delta d(t)$ imply conservative solutions with anticipated warning, so the ADAS system becomes active sooner. On the contrary, low $\Delta d(t)$ values mean more aggressive solutions with sharper transition from warning to braking. As $\Delta d(t)$ is a design parameter, one can typically set it to a constant value or define an expression dependent on the vehicle velocity.

Figure 7.6 shows the definition of variables related to the computation of the risk factor for a frontal collision. The same concepts apply to any arbitrary *ARM*, where distances are indeed arc-lengths. A graphical example of Equation (7.12) is depicted in Figure 7.6, showing the range where the system is active: 1) if $c(t) = 0$ there is no risk of collision; 2) if $c(t) \in]0, 1[$ the system is not in collision, but there is a potential risk and thus warning must be activated; 3) if $c(t) = 1$ there is a maximum risk of collision and therefore emergency braking must be applied to stop the vehicle.

On the one hand, the proposed ADAS generates a warning signal $w(t)$ based on the risk factor $c(t)$, conditioned to pressing the throttle pedal, whose position is defined as $u_a(t) \in [0, 1]$[2]:

$$w(t) = \begin{cases} c(t) & \text{if } u_a(t) > 0 \text{ or } v(t) > 0 \\ 0 & \text{otherwise} \end{cases} \quad (7.14)$$

[2]When the driver stops pressing the accelerator pedal, we assume that he/she is aware of the danger and hence the warning signal is deactivated.

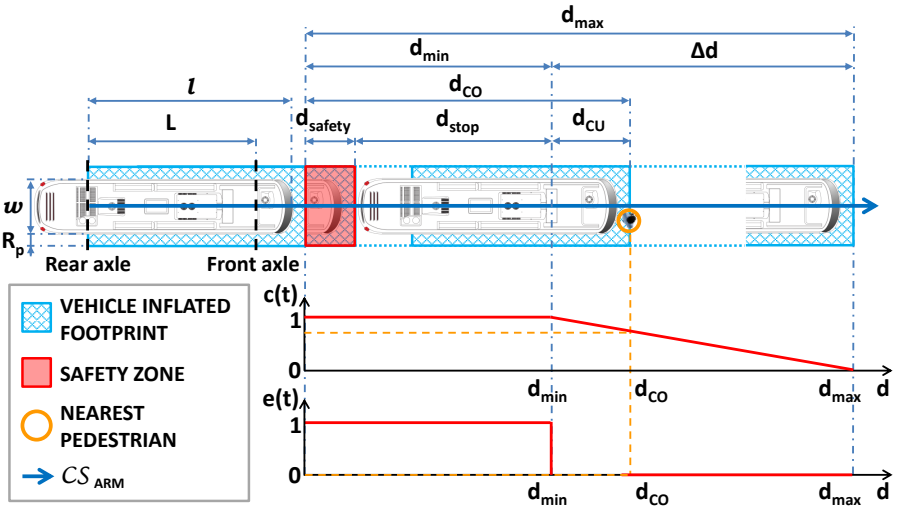

Figure 7.6: Collision risk evaluation.

On the other hand, regarding the feedback in the steering wheel, the following steering risk factor is proposed:

$$s(t) = \begin{cases} s_v & \text{if } c(t) > 0 \text{ and } s_v = s_p \text{ and } \frac{|\kappa_v| - |\kappa_p|}{\kappa_{max}} < -\epsilon, \\ -s_v & \text{if } c(t) > 0 \text{ and } s_v = s_p \text{ and } \frac{|\kappa_v| - |\kappa_p|}{\kappa_{max}} > \epsilon, \\ 0 & \text{otherwise} \end{cases} \tag{7.15}$$

with $\kappa_{max} = \sin(\alpha_{max})/L$, $\kappa_v = \sin(\alpha(t))/L$ and $\kappa_p = 2\sin(\beta)/d_p$, the maximum and current curvatures of the vehicle, and the curvature of the circular arc joining vehicle and pedestrian, respectively; where $s_v = \text{sign}(\kappa_v)$ and $s_p = \text{sign}(\kappa_p)$ are the signs of these curvatures; being $d_p = \sqrt{x_p^2 + y_p^2}$ and $\beta = \arctan(y_p, x_p)$ the distance and angle to the pedestrian position, with x_p and y_p the pedestrian's coordinates with respect to vehicle's local reference system. ϵ is a design parameter that defines a dead zone of non-blocking for curvatures with similar values. For instance, usual values for ϵ are $0.05 - 0.1$. Note that taking into account the criterion in which positive curvatures imply turning to the left, we define $s(t) = 1$ for left blocking and $s(t) = -1$ for right blocking.

An imminent collision is detected if $c(t) = 1$ and then the vehicle must stop to avoid an accident. In such cases, an emergency signal $e(t)$ is enabled in order to produce an automatic braking, although conditioned to its speed. In fact, if the velocity is higher than a given threshold $v_{e,max} = 30$ km/h, the

emergency braking is not activated, although the warning signal still works[3]:

$$e(t) = \begin{cases} 1 & \text{if } c(t) = 1 \text{ and } 0 < v(t) < v_{e,max} \\ 0 & \text{otherwise} \end{cases} \tag{7.16}$$

The minimum stop distance $d_{stop}(t)$ is dynamically computed to guarantee that the vehicle can stop by applying the maximum deceleration $a_{b,max}(t)$:

$$d_{stop}(t) = 0.5 \cdot v(t)^2 / a_{b,max}(t) \tag{7.17}$$

In order to introduce an additional safety factor, we define:

$$d_{min}(t) = d_{safety} + d_{stop}(t) \tag{7.18}$$

where d_{safety} is a safety distance where to *theoretically* stop the vehicle with respect to an object.

7.2.3 Warning and Braking Assistance Algorithm

Let's assume that from *smart* cameras (see Vasquez Govea (2007) for probabilistic approaches) it is possible to predict the motion of each pedestrian $\{x'_p, y'_p\} = f(x_p, y_p, t)$. Prediction implies that we can evaluate future pedestrian positions for a given time instant t, and thus the exact time to collision t_C can be computed.

Algorithm 4 shows an iterative procedure to determine collision risk factor for a moving pedestrian, Equation (7.12). The processing time of a C++ implementation of the proposed algorithm is $t_{proc} = 0.15 \pm 0.05$ ms, using the same computer as in Section 7.2.1.

7.3 Conclusions

A new advanced outdoor safety system for buses in urban environments at low speeds has been introduced and described. The proposed methodology is based on a computationally efficient algorithm that uses a simplified model of vehicle dynamics. This model has been proven to be applicable to collision detection with similar performance to more complex models, but with less processing load.

[3]The system is designed to be consistent with current legislation for brake assist systems.

Algorithm 4 Warning and Braking Assistance

Require: $\mathbf{u}(t)$, $v(t)$, $\{x_p, y_p\}$, H

1: Predict vehicle path, CS_{ARM}, for a given time horizon H.
2: Compute collision risk threshold distances using (7.17)-(7.18).
3: Set $t_C = t$.
4: **while** convergence **do**
5: Update pedestrian predicted position at time t_C, $\{x'_p, y'_p\} = f(x_p, y_p, t_C)$.
6: Compute 7 boundary points of $\mathcal{CO}$ corresponding to mid and end points for each segment of the vehicle rectangular shape using (7.3)-(7.4).
7: Compute 3 arc segments using each of the mid and end points previously computed.
8: Determine whether or not the vehicle path is in collision with such arc segments and compute distance to obstacle-collision, $d_{\mathcal{CO}}(t)$ using (7.6)-(7.7). If not collision is detected, then $d_{\mathcal{CO}}(t)$ is the arc length of $\mathcal{CS}_{ARM}$.
9: Find t_C at which the distance travelled by the vehicle in $\mathcal{CS}_{ARM}$ equals to $d_{\mathcal{CO}}(t)$.
10: **end while**
11: Compute collision risk using (7.12).
12: Compute throttle and steering warnings and emergency braking using (7.14), (7.15) and (7.16).
13: **return** $w(t)$, $s(t)$ and $e(t)$

The algorithm also considers driver's intention, vehicle shape and dynamics in order to evaluate the risk of collision with pedestrians moving around the vehicle, which are assumed to be given by a set of smart cameras. Once the level of risk is determined the active safety system warns the driver to make him aware of the danger. In case of imminent collision the proposed ADAS is able to perform an automatic emergency braking.

In the chapter, a new manifold has been introduced, coined as *Clothoid Reachable Manifold* (CRM). This is an extension of the well-known *Arc Reachable Manifold* (ARM), in which current vehicle curvature and sharpness are taken into account in the collision detection problem. This generalization allows to detect potential collisions that would not be considered by the ARM method, while discarding false positive collision detection cases. However, in the proposed methodology CRM are not used due to the high computational cost, compared to ARM.

Chapter 8

Pedestrian Detection and HAV Feedback in Real Bus

8.1 Introduction

A new Advanced Driver Assistance System (ADAS) to help bus drivers in urban environments at low speeds has been introduced in Chapter 7. The proposed active safety system assumes a pedestrian detection module based on *smart* cameras placed in the periphery of the bus, as well as haptic and audiovisual feedback systems. In this sense, the pedestrian detection algorithm and the safety devices, such as audiovisual feedback, haptic feedback in throttle pedal and steering wheel, as well as the emergency braking system, are explained in detail in this chapter.

8.2 Pedestrian Detection

The aim of the pedestrian detection system is to give information about the surroundings of the vehicle. This module uses a set of smart cameras to detect people in the vehicle surroundings. The set of smart cameras forms a topological network, so the system is modular and cameras can be placed anywhere, particularly in driver's blind spots. In order to cover the area nearby the vehicle, cameras are placed as follows: top front of the bus (left, centre and right) and top back of the bus (left, centre and right) pointing downwards, covering the periphery of the bus from an overhead view; two side cameras placed in both rearviews pointing backwards; and an additional camera pointing to the front, able to detect pedestrians from a greater distance (see Figure 8.1 for a zenithal view of areas covered by the smart cameras).

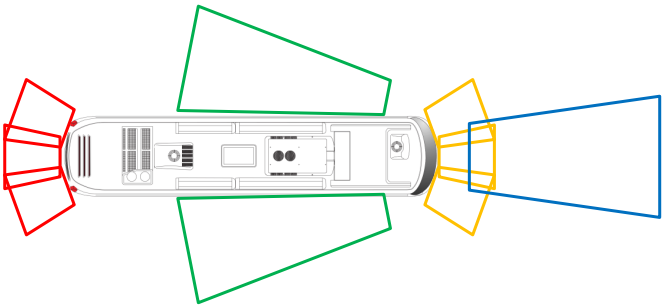

Figure 8.1: Top view of detection zones: (yellow) top front cameras, (red) top back cameras, (green) side cameras and (blue) front camera.

Each smart camera uses a set of stereo cameras that allow image acquisition to detect people by their appearance and to obtain 3D data in order to detect them by their volume. To take advantage of parallel computing in different processor cores the implementation of the algorithm uses 3 threads to distribute the computational load, as shown in Figure 8.2. For image processing nodes, OpenCV (version 2.4.2) (Bradski, 2000) and PCL (version 1.7) (Rusu and Cousins, 2011) libraries are used. To improve performance, the implementation includes parallelization by TBB (version 4.1) and OpenMP (version 3.0), as well as SIMD instructions based on NEON. Memory optimizations have also been made, including the use of cache (32Kb L1 per core and 1MB L2 common), anti-aliasing techniques ensuring no overlap in memory of certain variables, improving temporal and spatial locality of both variables and code, among others. As a result we are able to perform a high-computational demanding pedestrian detection algorithm in embedded systems in real-time.

As shown in Figure 8.2, our algorithm includes eight different processing stages, which are described below[1]:

A) Acquisition and Rectification

Acquires images at 15 FPS and applies an homogeneous transformation, obtained in system calibration, that makes them coplanar. This allows objects to appear in the same row in both images, speeding up the disparity calculation. This step generates two rectified images (left and right), see (A) in Figure 8.2 for the left camera image. A Look-Up-Table (LUT) to accelerate the calculation of the homogeneous transformation and to rectify the image has been implemented.

[1]For further details of the complete pedestrian detection algorithm and processing stages see Armesto et al. (2015) and references therein.

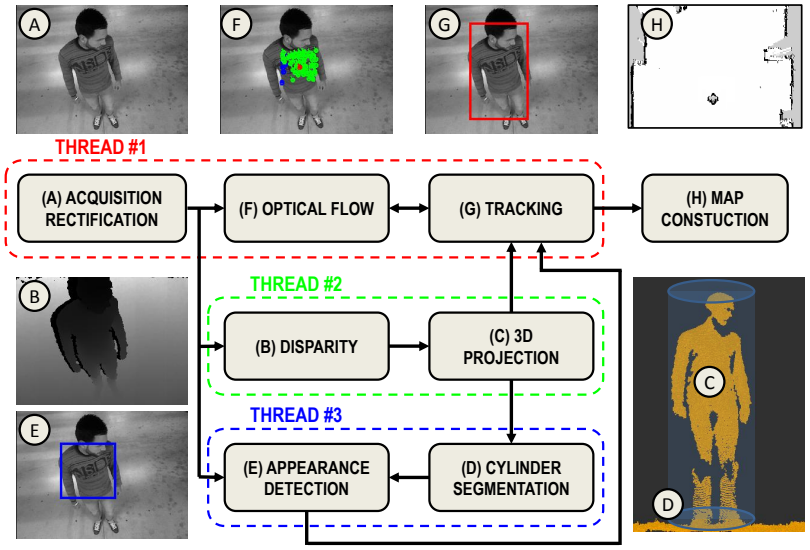

Figure 8.2: Structure of the pedestrian detection algorithm with stereo vision.

B) Disparity

Computes the disparity between left and right images based on the Sum of Absolute Differences technique (SAD) (Richardson, 2004). It generates an image disparity from the rectified image, see (B) in Figure 8.2. It uses a function whose parametrization includes a Sobel pre-filtering, a window size of 15 pixel, a disparity range $[-50, 46]$ pixels, among other settings.

C) 3D Projection

Gets a 3D point cloud based on the epipolar geometry of the stereo system (Hartley and Zisserman, 2004). Moreover, it generates a list of points corresponding to all objects in the scene, see (C) in Figure 8.2. Points next to the ground plane are routinely filtered.

D) Cylinder Segmentation

Extracts robustly cylindrical objects from 3D point cloud based on Random Sample Consensus or RANSAC technique (Fischler and Bolles, 1981). In this regard, people are clustered to cylindrical objects. Furthermore, different filters are applied to cylinders such as vertical geometric relationships and radius size. This step generates regions of interest or ROIs (in the image plane), containing objects similar to a cylinder, to be used in the step of pedestrian detection by appearance, see (D) in Figure 8.2.

E) Appearance Detection

Detects pedestrians by appearance based on Histograms of Oriented Gradients or HOG technique (Dalal and Triggs, 2005). It uses a classifier in cascade (*boost* type) to discriminate people in the picture (Zhu et al., 2006). It also generates ROIs (in the image plane) with the position and size of individuals, see (E) in Figure 8.2. Window size is 96×96 using 21 classification stages. To detect people with different sizes, the process is repeated iteratively with a reduction ratio of 1.1 with respect to the previous image.

F) Optical Flow

Gets the ROIs speed from video (consecutive sequence of images) to estimate the offset in pixels of the regions (Lucas and Kanade, 1981). To calculate the average displacement of pixels in a region, the RANSAC technique is used to filter out spurious data (pixels moving in a different direction from that of most pixels), see (F) in Figure 8.2. For the parametrization of this stage, up to 200 image features are used, based on Harris corners (Harris and Stephens, 1988), with a minimum distance between features of 5 pixels and a window size $21{\times}21$ for existing regions and 31×31 for regions initialization.

G) Tracking

Allows data fusion between ROIs position returned by the HOG classifier and velocities of these regions estimated using optical flow based on Kalman (1960a), see (G) in Figure 8.2. Kalman filter state vector contains position and velocity of the centre of the region. The position of the region obtained from HOG and its velocity through optical flow are the filter measurements. Regions correspondence maximizes the common area (Enzweiler and Gavrila, 2009).

H) Map Construction

To improve the knowledge of the environment, the system can incorporate an occupancy map that combines and fuses the information of people and objects detected by different sensors, see (H) in Figure 8.2. In this case such sensors are stereo cameras, although data could come from other sensor technologies such as LIDAR, RADAR, ultrasound or depth cameras, among others. An occupancy map $\mathcal{L}$ of size $X \times Y$ in meters is used, which indicates the occupation probability of its cells, of size c, using the log-ratio representation. It must be said that the pedestrian detection algorithm generates a point cloud $\mathcal{P}$ of people. Thus, each point $p_n = [x_n \; y_n \; h_n]^T \in \mathcal{P}$ updates the cell $\mathcal{L}_{i,j}$ of the occu-

pancy map as follows:

$$i = \left\lfloor \frac{2X - x_n}{2c} \right\rfloor \tag{8.1}$$

$$j = \left\lfloor \frac{2Y - y_n}{2c} \right\rfloor \tag{8.2}$$

$$\mathcal{L}_{i,j} \leftarrow \mathcal{L}_{i,j} + \mathcal{L}_{min} + \frac{(\mathcal{L}_{max} - \mathcal{L}_{min})(h_n - h_{min})}{h_{max} - h_{min}} \tag{8.3}$$

being $\mathcal{L}_{max}$ and $\mathcal{L}_{min}$ probability values when it is occupied and when it is not (in log-odd representation); with h_{max} and h_{min} height values returned by the previous probabilities, respectively. Moreover, the previous variables have been adjusted so that heights over 1.2 m increase the size of $\mathcal{L}_{i,j}$ corresponding to the expected height of a child, thus increasing the probability of a cell to be occupied. Before the update cycle of the map, a constant is subtracted from all cells representing a forgetting factor. At the end of the update cycle a thresholding is performed in order to obtain a binary image, which is then processed with an edge detection algorithm (Suzuki and Abe, 1985). Then, the result of this stage is used to obtain a surrounding circle. Only those circle centres whose radius are between thresholds expected to be the size of a person are used to calculate the collision risk factor.

Finally, taking into account the specific need of our application, in which pedestrians are detected with cameras oriented with a strong inclination downward (toward the ground), the classifier used in HOG was necessarily trained. Indeed, the appearance of a person from a top position is significantly different to that used by the vast majority of people detection algorithms based on HOG. For a detailed study of different techniques for people detection with multiple repositories see Dollár et al. (2009, 2012) and references. Therefore, in the context of this thesis, a dataset was made including images from different places of the city of Valencia and its surroundings. In particular, images were acquired in a train station, a hospital, a school and a university. The purpose was acquiring sample images representing a person from a top perspective, in order to get a dataset to train the cascade classifier based on HOG. Once the repository was ready, the pedestrian detection system was trained and adapted until it worked properly. In the end, it was able to detect people from a top view with a high level of accuracy and robustness.

8.3 Description of Safety Devices

As stated in Section 7.1, the aim of the proposed active safety system is to warn the driver and, if necessary, to stop the vehicle in dangerous manoeuvres. Therefore, the complete ADAS also incorporates a braking assistance system with HAV feedback. All involved safety devices are explained below.

8.3.1 Haptic Feedback

8.3.1.1 Haptic Pedal

A motorized four-bar mechanism with a lever is placed in the throttle to *block* and eject the pedal in warning situations, as shown in Figure 8.3(a). It is worth mentioning that the term *block* refers to capability of generating a torque opposite to driver's intention, to produce a kinaesthetic reaction and at the same time let the driver have complete control of the vehicle. Thus, the aim is to warn the driver to improve the reaction time for braking, while making the driver feel in control of the vehicle in collision-free situations. Indeed, a lack of control could be annoying and even dangerous. In this sense, the haptic throttle is not designed to ensure the absence of collisions, but as a warning system. When the lever tries to expel one's foot, one feels a force which is reasonably enough to warn, but at the same time, one can always push it back on purpose easily, if needed.

Figures 8.3(b), 8.3(c) and 8.3(d) show the lower (non-blocking), intermediate (partial blocking) and upper (full blocking) positions, respectively. In the non-blocking position the driver can freely push the pedal to the maximum position, while in the blocking position a force greater than 58 N must be applied on the throttle pedal to move the mechanism[2].

Although only one intermediate position is shown, the haptic feedback in the throttle is continuous from non-blocking position to full blocking. However, to avoid a noisy behaviour in the lever positioning, we have introduced hysteresis discretizing the range into 11 configurations in between the lower and upper positions of the throttle, from 0% to 100% of blocking with increments of 10%.

Additional sensing required by the system includes potentiometers on throttle and brake pedals to measure their positions ($u_a(t)$ and $u_b(t)$ in Equa-

[2]This information has been obtained experimentally in a throttle pedal with length 0.2 m, but it might vary depending on the mechanical solution adopted.

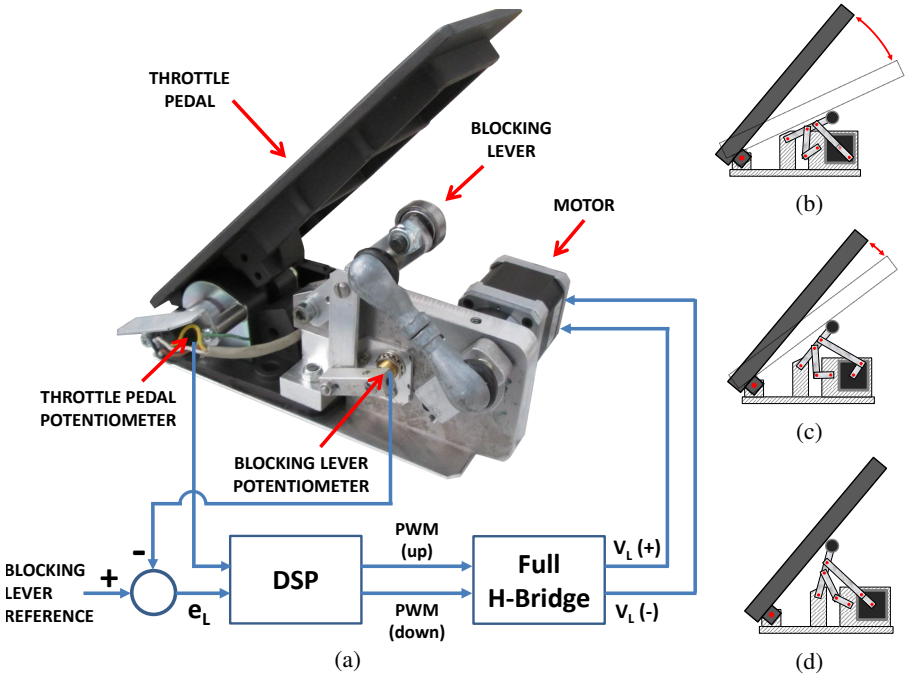

Figure 8.3: Haptic feedback pedal: (a) Active throttle with blocking lever, (b) Lower position, (c) Intermediate position, (d) Upper position.

tions (8.9) and (8.11), respectively).[3] The blocking lever also incorporates a potentiometer to measure its angular position (p_L) in order to close the loop.

For the throttle positioning, the closed-loop control scheme shown in Figure 8.3(a) is used. Either a full H-bridge or two half H-bridge drivers can be used to adapt the 2 PWM output signals from a DSP unit to control a 24V DC motor (each PWM for each motor direction). To be specific, we use the high current H-bridge Infineon BTS 7960 chip and the 24V gear motor Büehler 1.61.046.333. In this sense, a proportional controller has been designed, where the gain K_L defines how aggressive the controller is. The lever reference r_L is set taking into account the level of risk of the manoeuvre, as explained in the previous chapter in Section 7.2.2, and since the lever measured position is p_L, by definition, the error variable is $e_L = r_L - p_L$.

[3]The position of such pedals could also be obtained via CAN messages, but at a lower resolution and with a period of 100 ms, so it was decided to install potentiometers for this specific application.

PWM signals are defined as follows:

$$PWM(up) = \begin{cases} K_L \cdot e_L & \text{if } e_L > 0, \\ 0 & \text{otherwise} \end{cases} \tag{8.4}$$

$$PWM(down) = \begin{cases} K_L \cdot e_L & \text{if } e_L < 0, \\ 0 & \text{otherwise} \end{cases} \tag{8.5}$$

When the blocking lever position p_L is in the lower configuration ($p_L = 0\%$) the driver can freely push the throttle pedal to its maximum position (with an experimentally measured torque of 4.73 Nm due to the original pedal spring (Electronic Heavy Duty Throttle Pedal 962 000 series, from Mobile Control Systems)).

An initial set of experimental tests was performed in order to define the optimal torque values for the throttle haptic feedback device. In those tests, we adjusted different gains K_L so that we could select the value that optimizes a *comfort and safety* cost function. In this sense, we associate comfort to low values of the torque necessary to overcome the blocking and safety to the reaction time of the driver after the blocking device is enabled (the quicker response the higher safety). In particular, we measured the minimum torque to overcome the blocking lever torque ($T_L(K_L)$) in its upper position and the driver's reaction time ($t_R^L(K_L)$)[4] for a given gain. Let $K_L^\star$ be the optimal gain of a performance function from weighted combination of both normalized variables T_L and t_R^L in the range 0 to 1:

$$K_L^\star = \underset{K_L \in [0,\infty[}{\operatorname{argmin}} f(K_L) = \underset{K_L \in [0,\infty[}{\operatorname{argmin}} \mathbb{E}\left[a_L \cdot T_L(K_L) + b_L \cdot t_R^L(K_L)\right] \tag{8.6}$$

being a_L and b_L the weights for each component and $\mathbb{E}$ the expectation operator.

Figure 8.4(a) shows the profiles of T_L and t_R^L for different values of the controller gain K_L, while Figure 8.4(b) shows the cost function with $a_L = 0.5$ and $b_L = 0.5$. For this particular weights selection, the optimal gain is $K_L^\star = 1$ and, as a result, when the lever is in the upper position ($p_L = 100\%$) the driver must apply a torque greater than 11.62 N$\cdot$m to move the *blocking* mechanism of the throttle.

[4]Defined as the time elapsed between the instant when the blocking lever is expelled and the time in which the driver releases the throttle and significantly presses the brake pedal.

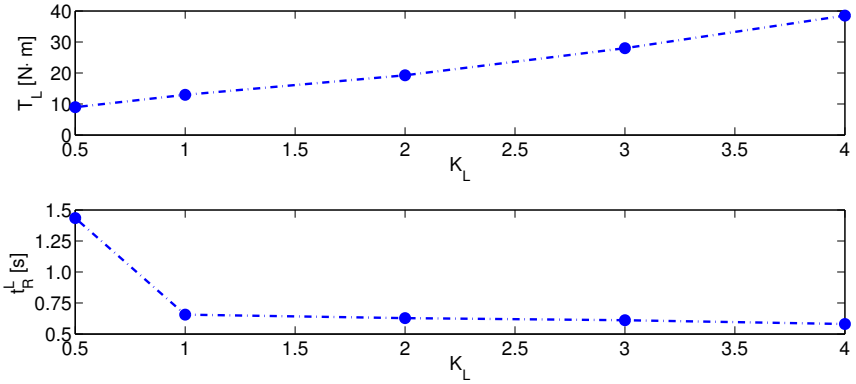

(a)

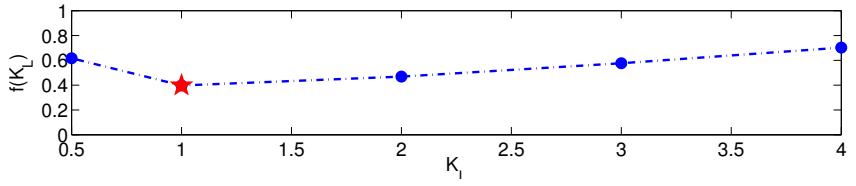

(b)

Figure 8.4: Throttle calibration. (a) Torque T_L and reaction time t_R for different values of K_L. (b) Cost function $f(K_L)$ with $a_L = 0.5$ and $b_L = 0.5$. Optimum value for gain $K_L^\star$ is the red star.

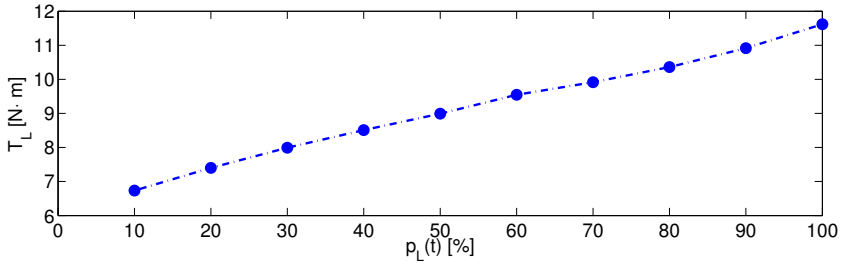

Figure 8.5: Throttle torque profile.

Another interesting aspect to show is the quasi-*linear* ratio between the lever position and the necessary torque for the selected gain, as shown in Figure 8.5. Note that there is no measure for $p_L = 0\%$, because in this case the haptic feedback is not enabled and therefore the lever is not blocking. In this situation the torque necessary to press the throttle pedal is the default value $T_T = 4.73$ N·m, which depends on throttle model and manufacturer.

8.3.1.2 Haptic Steering Wheel

A kinaesthetic steering wheel has been implemented to cover situations where the throttle pedal might not be pressed so there is no haptic feedback warning in dangerous situations, mostly when the vehicle is turning. This haptic device has been designed to be coupled in the steering wheel shaft in order to make the driver conscious of the side where the pedestrian comes from. In this sense, a braking system is placed in the steering column, which is composed by a brake disk and brake pads activated by an electromagnet (a spring retracts the brake pads when the electromagnet is disabled), as shown in Figure 8.6. In order to accurately know driver's intention and reaction, an optical encoder is also included, together with a potentiometer to measure steering wheel angle.

The system must allow normal driving when there is no collision risk, but it must make the driver aware if a potential collision is detected by *blocking* the steering wheel in the direction of a detected risk. Again here, the term *blocking* refers to introducing a momentary additional friction force on the steering wheel to produce the corresponding kinaesthetic reaction. In this way, the driver can perceive a constant resistance when moving the steering wheel towards the risky direction. The blocking force disappears as soon as the driver turns the steering wheel towards the opposite side or the risk vanishes.

A PWM signal regulates the electro-magnet voltage in the range $[0-24]$ V, which means that the brake friction can be also regulated using a half H-bridge (L293B from SGS-THOMSON). Following a similar procedure as in the throttle feedback design, we set different values of the voltage applied to the electromagnet (V_{EM}) and measured the minimum torque to overcome the blocking torque in the steering wheel (T_S). We also measured the driver's reaction time ($t_R^S(V_{EM})$), understood as the delay between the instant when the blocking steering starts working and the time in which the driver changes the sense of turning towards the non-blocking side. Figure 8.7(a) shows the profiles of $T_S(V_{EM})$ and $t_R^S(V_{EM})$ for different values of the electromagnet input voltage V_{EM}.

To get the optimum V_{EM}, we normalize variables T_S and t_S^L in the range 0 to 1 and define a cost function as a weighted combination of both components:

$$\begin{aligned} V_{EM}^{\star} &= \underset{V_{EM}\in[0,24]}{\operatorname{argmin}} \; f(V_{EM}) \\ &= \underset{V_{EM}\in[0,24]}{\operatorname{argmin}} \; \mathbb{E}\Big[a_S \cdot T_S(V_{EM}) + b_S \cdot t_R^S(V_{EM})\Big] \end{aligned} \tag{8.7}$$

where a_S and b_S are the weights of each variable.

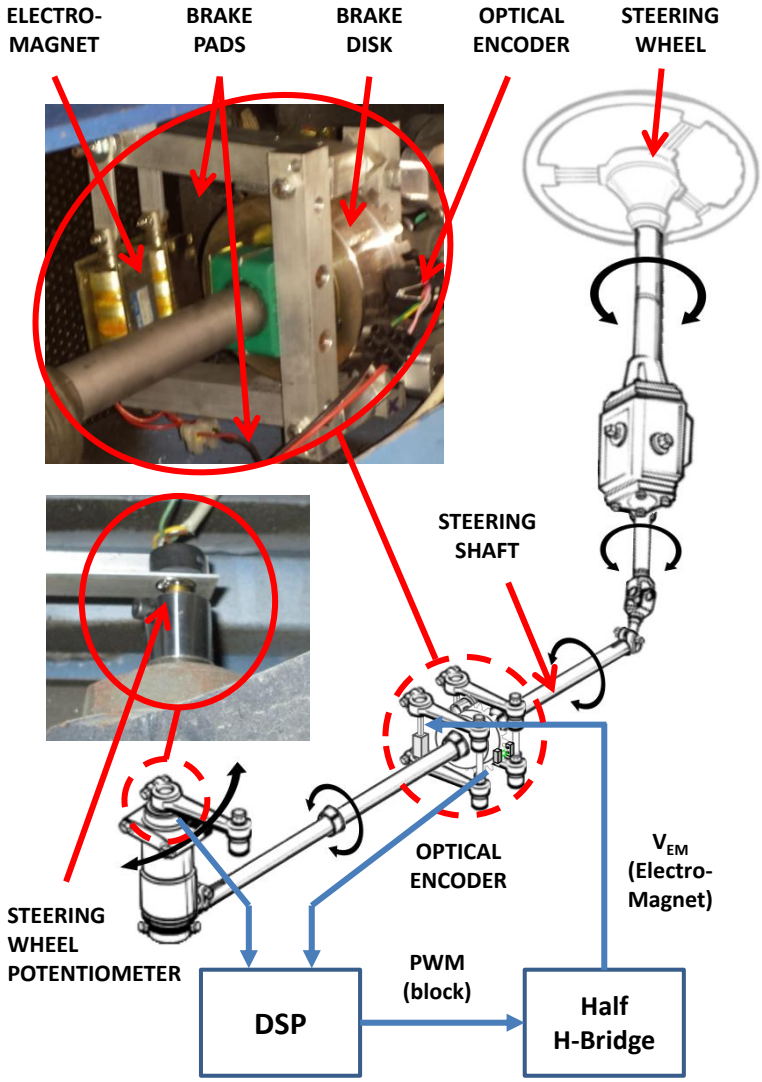

Figure 8.6: Steering column with active blocking system.

Figure 8.7(a) shows the measured values and Figure 8.7(b) the cost function with $a_S = 0.5$ and $b_S = 0.5$. It can be seen that in this particular case, for the selected weights, the optimum is $V^{\star}_{EM} = 24$ V, which suggests an ON/OFF control policy. As a result, the driver must apply a torque bigger than 4.34 N·m when the haptic device is enabled, which corresponds to the torque necessary to move the steering wheel and overcome the maximum dry friction of the electro-magnet used as blocking device.

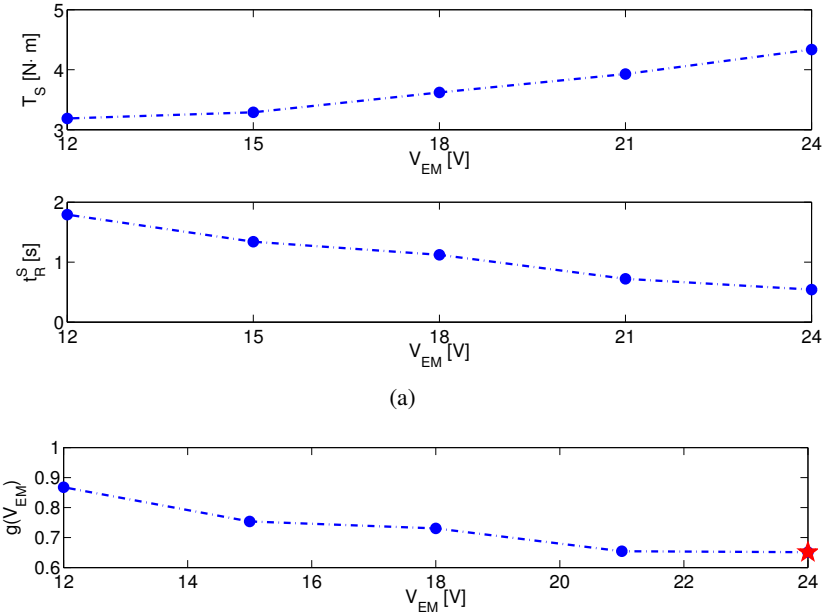

Figure 8.7: Steering calibration. (a) Torque T_S and reaction time t_R for different values of V_{EM}. (b) Cost function $g(V_{EM})$ with $a_S = 0.5$ and $b_S = 0.5$. Optimum voltage value is the red star.

Figure 8.8: Audio-visual feedback interface with images from smart cameras.

8.3.2 Audio-Visual Feedback

A monitor screen installed on the bus panel shows the set of images captured by the cameras with regions of interest for each detected person. This display provides audiovisual feedback to the driver when a warning signal is activated as described in Section 7.2.2. Figure 8.8 depicts the 8" screen installed in driver's cabin showing images taken from the smart cameras. This screen is an AFL-08A Panel PC with Intel Atom N270 1.6 GHz Fanless. It uses a Linux Ubuntu 12.04 distribution as operating system.

The screen interface shows the upper right, centre and left cameras in the top; in the lower left corner with a size four times larger the front camera is shown; while on the right side there are two more images corresponding to the two door cameras, included to improve driver visibility in the lateral part of the bus. The visual interface is a touch screen, so that the driver can choose which camera is displayed in large in the middle, helping in certain manoeuvres. When the emergency mode is activated the risk element is correspondingly indicated in the centre of each image.

The audio feedback consists of a beep on the speakers (stereo) which are integrated in the panel PC. The volume is adjusted in relation to the risk factor c_t, which plays equally on both speakers if the person is detected in the centre. On the other hand, the system only plays on the left or right speaker if the potential collision is detected in the corresponding direction.

Therefore, the proposed audio-visual feedback implementation only requires a display showing a web browser with ability to interpret *HTML5* and *javascript*. A small web server, running on the main node and designed entirely in *javascript* to show the flow of video cameras in MJPEG format. In addition, it also manages the dynamic activation of warning sounds and visual *overlays* to indicate states of emergency or warning.

8.3.3 Emergency Brake

It must be remarked that while emergency braking assistance systems such as BAS or ABA are designed to act when the bus travels at moderate speeds (over 60 km/h), the emergency braking system developed in this research has been designed to operate in passenger vehicles at low speed. Indeed, it has a threshold operation speed of up to 30 km/h, with a safety zone distance in front of the bus of about 5 m. This justifies the novelty of the research itself, since, to the best of author's knowledge, in the current market there are no ADAS developed for passenger vehicles in urban areas, with the sole purpose of preventing collisions with pedestrians.

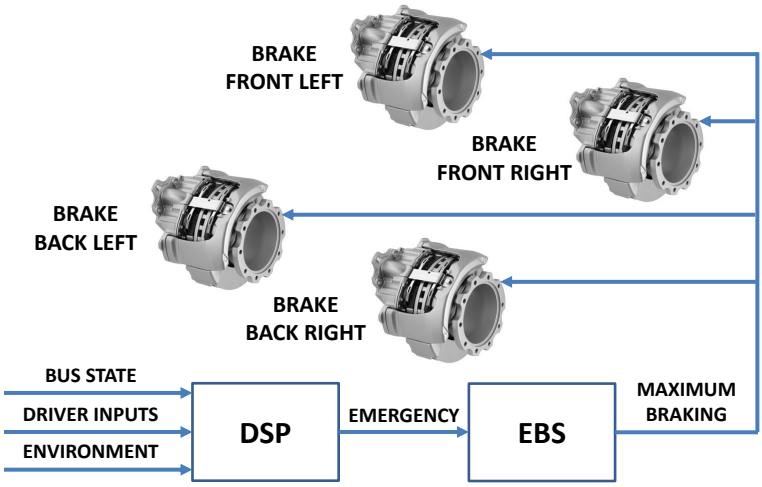

Figure 8.9: Emergency brake system.

In order to produce an automatic braking in risky situations, it is necessary to send an electronic signal to vehicle's braking system. Our implementation on a real bus in Section 8.4 (see Armesto et al. (2015)) is achieved based on the diagram of Figure 8.9. However, a virtual environment is used for the benchmarking evaluation performed in Chapter 9, and therefore the braking system is simulated by applying a maximum braking after receiving such signal.

8.4 Testing in Real Bus

A prototype of the proposed ADAS was mounted in a real bus (model TEMPUS from Castrosua S.A.). Some tests were carried out with the aim of checking if the system was able to warn the driver and stop the bus in cases of high risk of collision on a real situation. In this sense, the experimentation was a proof of concept, rather than a proper benchmarking evaluation. An in-depth evaluation of pedestrian detection module and HAV feedback performance were out of the scope of these preliminary tests.

8.4.1 Bus Prototype

The placement of the haptic and audiovisual feedback devices in the real bus is depicted in Figure 8.10. The prototype also includes a set of smart cameras, placed in the periphery of the bus to detect pedestrians in vehicle surroundings. The set of smart cameras forms a topological network, so cameras can

Figure 8.10: Implementation of the proposed safety system in a real bus: (magenta) network of smart cameras, (green) audio-visual feedback, (blue) haptic feedback in the throttle and (red) haptic feedback in the steering wheel.

be placed anywhere, particularly in driver's blind spots. In order to cover the area nearby the vehicle, cameras are placed as follows: top front of the bus (left, centre and right) and top back of the bus (left, centre and right) pointing downwards, covering the periphery of the bus from an overhead view; two side cameras placed in both rearviews pointing backwards; and an additional camera pointing to the front, able to detect people from a greater distance. Finally, as explained in previous sections, a monitor screen installed on the bus panel shows the set of images captured by the cameras with regions of interest for each detected person. This display provides audiovisual feedback to the driver when a warning signal is activated.

Figure 8.11 shows a diagram with the relationships of the different processors installed in the bus, here denoted by nodes. The nodes are based on the embedded card "ODROID-U2", which uses a quad-core ARM processor Samsung Exynos4412 Prime (Cortex-A9) at 1.7 GHz. Besides, they include a Linaro 12.11 distribution (kernel 3.8.13.14-RT30 armv7l) based on Ubuntu as OS. An agents software architecture based on ROS Groovy (Quigley et al., 2009) has been adopted for communication between different nodes. The "Master" node of Figure 8.11 is responsible for different functions of the developed application:

1. Monitoring CAN communication of DICO subsystem (Drive Control Unit), which publishes, via CAN bus, the speeds of wheels and shaft, the position of throttle and brake pedals, the engine direction or run mode DNR (Direct-Neutral-Reverse), among other information.

2. Serial communication management with a DSP that controls haptic devices (throttle and steering wheel) and the electrical signal that causes the emergency braking.

3. Construction of an occupancy map of the obstacles (pedestrians) detected from the information received by the "Smart Camera" nodes.

4. Web server of the images captured by the cameras properly combined to give visual information to the driver about vehicle's surrounding. The screen where the images are displayed, is actually a touch Panel-PC, with the main requirement of being able to run a web browser to display the images and have a stereo audio output to the beeper. The "Smart cameras" nodes are able to capture images from digital cameras, process them and send the results of processing tasks to the "Master" node.

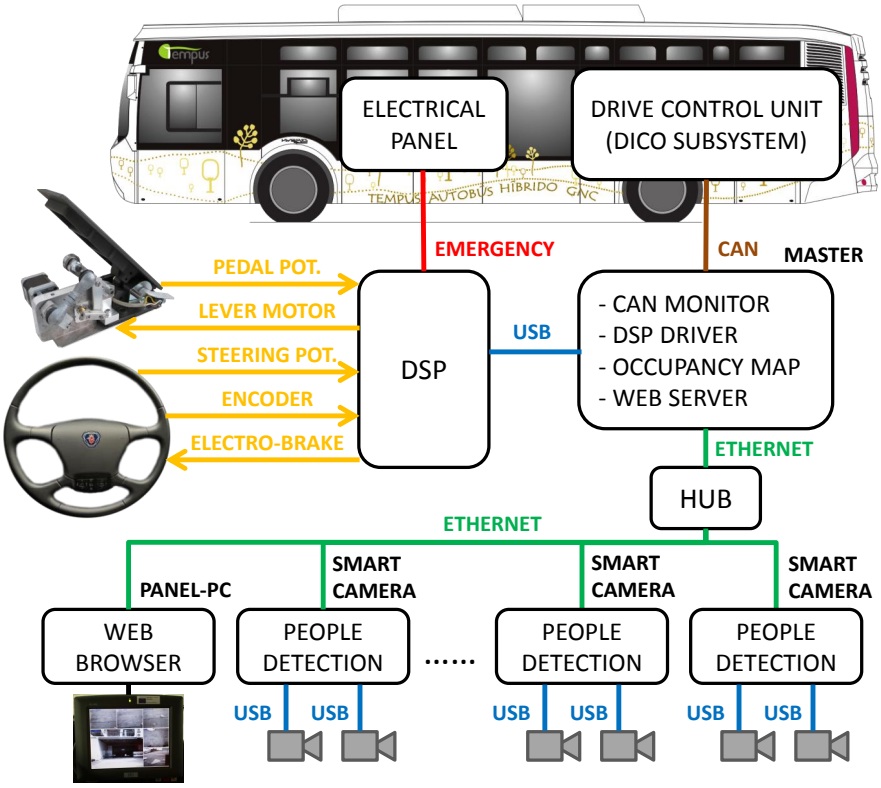

Figure 8.11: Relationship between nodes, devices and vehicle of the pedestrians detection system with HAV feedback.

8.4.2 Bus Model

Let's assume a vehicle moving in an $\Re^2$ workspace $\mathcal{W}$. So, its configuration space $\mathcal{CS}$ in $\Re^2 \times \mathcal{S}^1$ is $\mathbf{q}(t) = [x(t), y(t), \theta(t)]$, which indicates the Cartesian position and orientation of the vehicle. In addition to this, we define $\mathbf{u}(t) = [u_a(t), u_b(t), \alpha(t)]$ as the input vector containing the throttle pedal position $u_a(t)$, the brake pedal position $u_b(t)$ and the steering wheel angle $\alpha(t) \in [-\alpha_{max}, \alpha_{max}]$, with α_{max} as the maximum turning angle. We also assume that pedal ranges are normalized as follows: $u_a(t) \in [0, 1]$ and $u_b(t) \in [0, 1]$.

Our methodology is inspired by Gillespie (1992) and Pacejka (2005), where nonlinear longitudinal dynamics of a vehicle are based on physical laws. We decompose the components of the vehicle velocity $v(t) \in [0, v_{max}]$

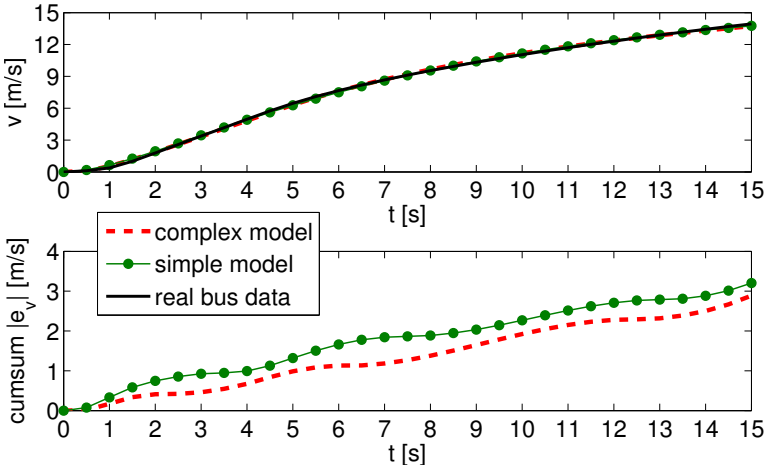

Figure 8.12: Validation with a step input pattern of complex and simple models (up). Cumulative sum of the absolute value of the velocity error e_v (down).

(with v_{max} as the maximum linear velocity) into two velocities, one related to acceleration $v_a(t)$ and another related to braking $v_b(t)$:

$$v(t) = v_a(t) + v_b(t) \tag{8.8}$$

The active safety system is designed to work at low speed, as explained in Section 7.2.2. In this sense, most of the nonlinearities can be neglected and the nonlinear model for the acceleration component is approximated by a linearised first-order system with a delay in order to take into account the transmission dynamics.

$$\frac{v_a(s)}{u_a(s)} = \frac{K \cdot e^{-\tau_d s}}{\tau s + 1}\,, \frac{d(s)}{v_a(s)} = \frac{1}{s} \tag{8.9}$$

where $d(s) \equiv \mathcal{L}[d(t)]$ is the travelled distance, $v_a(s) \equiv \mathcal{L}[v_a(t)]$ and $u_a(s) \equiv \mathcal{L}[u_a(t)]$, being $\mathcal{L}$ the Laplace transform.

In order to validate the performance of the simplified model, we have obtained velocity data from a real urban bus (TEMPUS bus manufactured by Castrosua S.A.), accelerating at full throttle during 15 seconds. The fitting performance of the simplified model to the data is $R^2 = 0.973$ and the mean squared error $MSE = 0.015$ m/s, while the best fitting we could find using longitudinal dynamics described in Gillespie (1992) and Pacejka's tire model (Pacejka, 2005) is $R^2 = 0.976$ with $MSE = 0.012$ m/s. Figure 8.12 depicts the step response of the real bus together with the two models. The cumulative

sum is also depicted, which can be expressed as $|e_v(t)| = |v_r(t) - v_m(t)|$, being $e_v(t)$ the velocity error, $v_r(t)$ the velocity data from the real bus and $v_m(t)$ the velocity of each model. It can be observed that both models have a good fitting performance, since after 15 seconds the cumulative speed error is very low and similar in both cases.

In addition to this, to simulate 15 s using a Matlab-Simulink implementation with ODE45 solver and variable simulation step, the computation time is $t_{proc} = 0.153$ s on average for the simplified first-order model. Whilst for the complex model it is $t_{proc} = 13.191$ s, around 86 times slower. The computer used in the simulation is the same as in Section 7.2.1.1.

On the other hand, an integrator models the effective deceleration:

$$\frac{v_b(s)}{a_b(s)} = \frac{1}{s} \tag{8.10}$$

with $v_b(s) \equiv \mathcal{L}[v_b(t)]$ the brake velocity component and $a_b(s) \equiv \mathcal{L}[a_b(t)]$ the brake acceleration component.

The braking deceleration $a_b(t)$ mainly depends on brake pedal position $u_b(t)$, but also on the current vehicle velocity $v(t)$, as shown in Figure 8.13. After some tests, we have detected a saturation of the braking force for values of $u_b(t)$ close to the maximum $u_b(t) > 0.8$, which makes the relation between the overall braking deceleration (inversely measured from the time to stop the vehicle at the initial velocity when the pedal was pressed) and brake pedal position slightly nonlinear. We have seen that a quadratic model as in Equation (8.11) is able to provide a good fitting performance. Using the Least Squares method and real data, we obtained a fitting of $R^2 = 0.988$ with $MSE = 0.001$ m/s^2 between these variables, although other approximations might be valid as well, for instance using neural networks.

$$a_b(t) \approx k_0 + k_1 v(t) + k_2 u_b(t) + k_3 v^2(t) + k_4 u_b^2(t) + k_5 v(t) u_b(t) \tag{8.11}$$

It is interesting to remark that using the same Pacejka's complex model for the braking deceleration (Pacejka, 2005), a parameters identification was performed in order to adjust the model as close to real data as possible. The best fitting performance obtained was $R^2 = 0.926$ and $MSE = 0.065$ m/s^2. It was found that this dynamic model differs from the real behaviour of the vehicle mostly at low speeds and with low values of braking torque, which makes more difficult to find an appropriate parameter fitting. As a conclusion, the proposed approach is more efficient computationally because the braking value is obtained directly from a polynomial equation, without the need to compute the dynamic equations of the complex model.

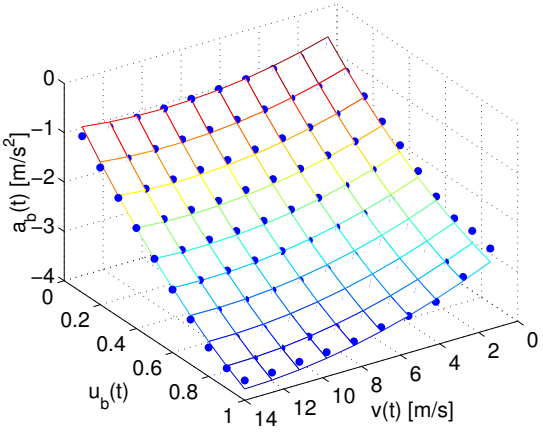

Figure 8.13: Deceleration surface of the second order polynomial model. Blue dots are the values of $a_b(t)$ measured during the braking calibration tests.

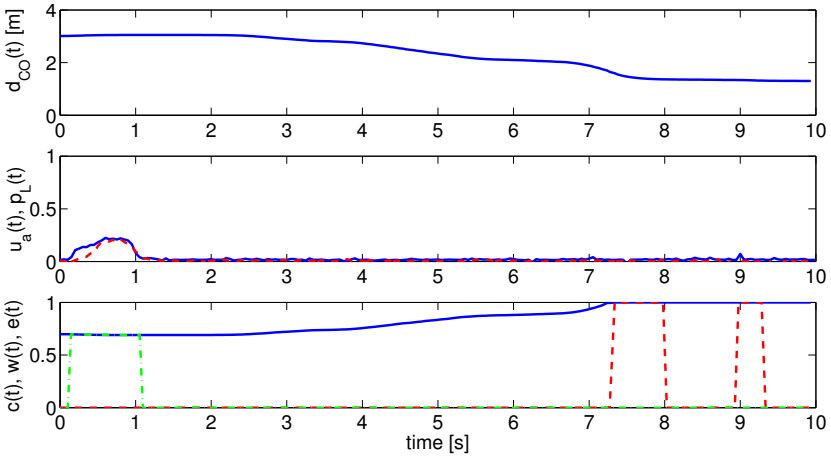

Figure 8.14: Evolution of signals in the frontal emergency experiment. In second graph $u_a(t)$ is blue and $p_L(t)$ is dashed red line, while in third graph $c(t)$ is blue, $w(t)$ is dashed-doted green and $e(t)$ is dashed red line.

8.4.3 Validation of Throttle Feedback and Emergency Braking

The main target of this experiment is the validation in a real scenario of the braking assistance module with haptic feedback together with the pedestrian detection module with audiovisual feedback. Apart from validation, the test also aims to help understand how the blocking lever and the emergency braking work.

(a) T: $t=0$ s (b) T: $t=3$ s (c) T: $t=6$ s (d) T: $t=8$ s

(e) F: $t=0$ s (f) F: $t=3$ s (g) F: $t=6$ s (h) F: $t=8$ s

(i) E: $t=0$ s (j) E: $t=3$ s

(k) E: $t=6$ s (l) E: $t=8$ s

Figure 8.15: Frontal emergency experiment with images taken at different time instants from (a-c) Top center camera (T), (d-f) Front camera (F) and (g-i) Exterior view (E).

The experiment consists of a real bus moving forward against a static person placed at a distance of $d_C = 3$ m far from the vehicle. For the experimentation the safety distance is set to $d_{safety} = 1.5$ m. In Figure 8.14, it can be observed that initially the driver presses the throttle for about one second and the vehicle accelerates smoothly, which allows the bus to move at low speed and progressively approaches to the person. At this instant of time, the blocking mechanism is activated and the throttle pedal is retracted just after

the driver stops pressing it. The acoustic warnings are equally generated in the Panel-PC. Due to bus inertia, it keeps approaching to the person even after the driver stops accelerating. When the person is 1.8 m far from the bus an emergency stop signal is activated immediately. That happens at time instant 7.3 s, i.e. about 6 s after the driver stops pressing the accelerator pedal. Finally, the bus stops completely when the pedestrian is at a collision distance of $d_{CO} = 1.3$ m, which is approximately the value of d_{safety}. As shown in Figures 8.15 (a-h) the upper-central and frontal cameras detect the person simultaneously.

8.4.4 Validation of Steering Feedback

In the test shown in Figures 8.16 and 8.17, we seek to validate the audio warning system and the steering feedback efficiency when pedestrians are detected on the side of the bus. Only the camera placed in the front door of the bus is able to register and detect the pedestrian. In the experiment, it can be observed that the driver steers the front wheels approximately 40^{o}, in order to turn to the right. Each time the driver tries to accelerate the haptic feedback gets active through the blocking lever in the throttle pedal and the blocking mechanism of the steering wheel.

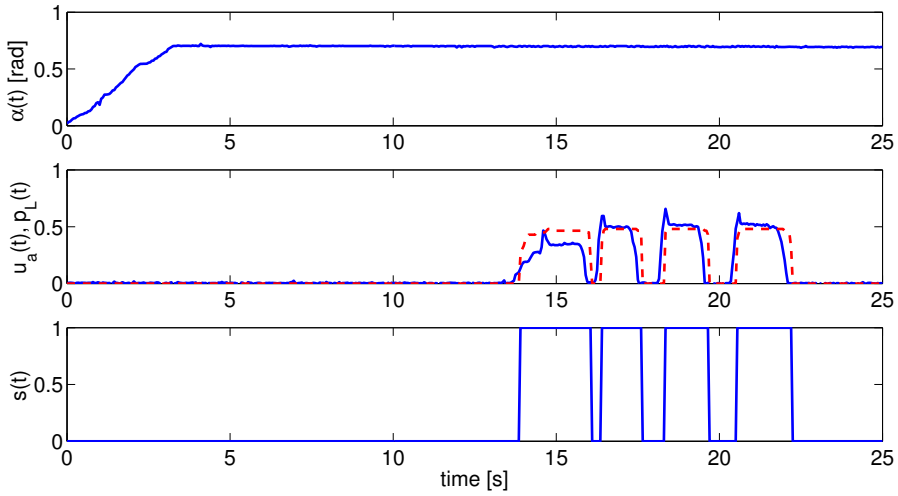

Figure 8.16: Evolution of signals in the lateral emergency experiment. In the second graph $u_a(t)$ is blue and $p_L(t)$ is dashed red line.

(a) Front door camera

(b) Side door camera

(c) Exterior view

Figure 8.17: Lateral emergency experiment with different camera images.

8.5 Conclusions

This chapter shows the complete driving assistance system implemented on a real bus, including very specific tests in a controlled scenario mainly to validate the haptic feedback and the emergency braking systems, together with the pedestrian detection module. The set of *smart* cameras is intended to detect pedestrians moving around the vehicle and evaluate any risky situation in order to warn the driver in case of dangerous manoeuvres. The haptic feedback in the throttle pedal is achieved by a blocking lever mechanism. The steering wheel also incorporates haptic feedback through an electronic brake placed in the steering shaft. Under imminent collision conditions, the safety system sends an electric signal to enable the emergency braking system. The haptic feedback has been designed to make the bus driver aware of the danger,

in order to avoid the emergency braking system to get active. By doing that driver's actions are prioritized with respect to automatic actions.

As further work, we aim to validate the complete safety system in a real scenario, using an urban transport bus. Thus, the effectiveness of the haptic feedback devices could be analysed in depth with professional bus drivers in real driving conditions. Moreover, we also want to enhance the haptic warning using audio-visual feedback devices, analysing their effects individually and together.

Chapter 9

Driver Assistance Benchmarking

9.1 Introduction

This chapter proposes the evaluation of the haptic feedback in throttle pedal and steering wheel, as well as the emergency braking of the active safety system to assist bus drivers in low-speed manoeuvres, which has been described in Chapters 7 and 8. The benchmarking methodology is based on several tests developed to evaluate the performance of the proposed ADAS. Experimentation is carried out in a driving simulation cabin with original elements from real buses, as well as a very realistic urban scenario (particularly in low visibility turnings and areas of passenger loading and unloading).

The results obtained show a statistically significant improvement in safety produced by the proposed low-speed active safety system, as the number of collisions and high risk situations are clearly minimized, reaction time to press the brake pedal is improved and time to collision with pedestrians increased in emergency situations. In addition to this, a brief discussion about current regulations for innovative safety systems on real vehicles is carried out.

9.2 Driving Simulation Cabin

A driving simulation cabin is used as a tool to evaluate the performance of the proposed ADAS. Several experiments have been carried out in order to validate the behaviour of the braking assistance system with haptic feedback on a simulated environment. As shown in Figure 9.1, the simulation platform includes the following devices: a driving cabin with a seat, a steering

Figure 9.1: Driving simulation cabin with projection system composed by 3 projectors and a semicircular screen.

wheel, pedals and a gearshift; as well as an environmental simulation system composed by three synchronised video projectors and a semicircular screen.

Regarding the simulation engine, it is based on PhysX SDK (version 3.3.1) for computation of rigid body dynamics and collisions, while OGRE (version 1.8.1) is used as a graphics engine for rendering and visualization. On the other hand, the artificial intelligence for vehicles and pedestrians is based on a navigation graph, used to guide vehicles and pedestrians around the scenario in a realistic manner. The decision making and path planning of vehicles and people has been developed considering target nodes for each one. The management of semaphores and traffic with collision avoidance has been also developed. Details describing such artificial intelligence included on vehicles and pedestrians are not included as this is out of the scope of this thesis.

The computer used in the simulator is based on Ubuntu 13.04 and has the following technical specifications: CPU Intel Core i7-3820 3.6GHz, with 8GB DDR3 and a graphics card Nvidia GeForce GTX650Ti 1GB GDDR5. Projectors have an image resolution XGA 1024x768 and 3000 lumen.

Our simulator is capable of rendering images at 32 FPS (in average) with an urban scenario 0.8 km^2 of a specific area of the city of Valencia (Spain) with 200 cars and 200 animated pedestrians (including skeleton motion).

9.3 Experimental Setup

The dynamic model of the simulated bus has been adjusted to be equivalent to the real bus used in Section 8.4 (Armesto et al., 2015). The vehicle type used for experimentation has the following parameters: mass $m = 10630$ kg (tare or unladen weight), length $l = 7$ m, width $w = 2.6$ m, axles distance $L = 6$ m and maximum turning angle $\alpha_{max} = \pi/4$ rad. After identification using the step response method, we obtained a first-order model as in Equation (8.9), with $K = 16.81$, $\tau = 12.47$ s and $\tau_d = 0.1$ s. On the other hand, the braking model in Equation (8.11) is approximated using the following values: $k_0 = 0$, $k_1 = -0.03$, $k_2 = -5.97$, $k_3 = 4.41 \cdot 10^{-4}$, $k_4 = 1.79$ and $k_5 = 0$, with a maximum deceleration of $a_{b,max} \approx -4.5\,\text{m/s}^2$.

Unless specified otherwise, in all tests the parameters for the ADAS were set to the following values: safety distance $d_{safety} = 1$ m and $\Delta d = 10$ m, with $R_p = 0.3$ m as a constant radius to define pedestrians shape.

Emergency braking: mass influence

The aim of this experiment is to evaluate the robustness of the emergency braking system against modelling errors, for different bus loads (assuming a capacity of 58 passengers and approximately 70 kg per passenger): $m = 11000$ kg (empty, with kerb weight), $m = 13000$ kg (half loaded) and $m = 15000$ kg (full loaded). In this test, the pedestrian is placed initially at a distance of $d_{CO} = 40$ m far from the bus. Then the driver starts pressing the throttle and the vehicle speeds up and moves straight forward against the obstacle. The haptic warning is disabled to evaluate only the emergency braking effect. Indirectly, we also want to show how d_{safety} can be obtained to guarantee the absence of collision even when the vehicle model has uncertainties.

Haptic warning: distance range influence

In order to evaluate the influence of the distance range Δd in which the warning is active, we perform a series of 7 tests varying from $\Delta d = 0$ m to $\Delta d = 30$ m, with increments of 5 m. Initially, the pedestrian is placed at $d_{CO} = 40$ m, the bus is half loaded $m = 13000$ kg and the safety distance is set to $d_{safety} = 1$ m. The driver proceeds as in the previous experiment, but in this case reacting as soon as he feels the haptic feedback in the throttle. This experiment also shows how to get an appropriate value of Δd, justifying the value used in the experimentation carried out in Section 9.4.6.

Haptic warning: driving behaviour influence

Through this experimentation, we evaluate the influence of the haptic feedback under different driving modes, from conservative to aggressive. As in the previous test, the vehicle moves forward in 1D against a static pedestrian placed at $d_{CO} = 14$ m far from the front of the bus. The driver was addressed to brake the vehicle when considered necessary. In the expected behaviour the driver reacted as soon as he/she felt the haptic feedback, whilst the subject with a more aggressive driving did not take the warning into account. In this experiment the bus was also half loaded $m = 13000$ kg.

Through this experimentation, we evaluate the influence of the haptic feedback under different driving behaviours or styles, from expected to aggressive. As in the previous test, the vehicle moves forward against a static pedestrian placed at $d_{CO} = 14$ m far from the front of the bus. The driver is addressed to brake the vehicle when he/she considers necessary. In the expected behaviour the driver reacts as soon as he/she feels the haptic feedback. In the second attempt, the subject is addressed to drive in a more aggressive way, without taking the haptic warning into account. In this experiment the bus is also half loaded $m = 13000$ kg.

Emergency in Arrival and Departure Manoeuvres

These experiments show two particular cases of tests carried out in Section 9.4.6, where a pedestrian forces the system to stop when approaching to or departing from a bus stop. In particular, we show a sequence of images for each situation and how the corresponding signals are activated. The analysis of these experiments helps to understand how the haptic warning and emergency braking work.

Benchmarking Evaluation

Two different tests are carried out to evaluate and compare certain aspects of the safety system. The goal of the first set of experiments is to evaluate the efficiency of the haptic feedback in the throttle pedal and the emergency braking performance. On the contrary, the second set of tests is designed to analyse the potential benefits of the force feedback in the steering wheel.

The set of experiments for the benchmarking involved 20 different drivers (19 males and 1 female with ages between 18 and 55, mean age 30 ± 5.6), each one driving for about an hour around an urban scenario. A specific area of the city of Valencia (Spain) was modelled, reproducing very realistic driv-

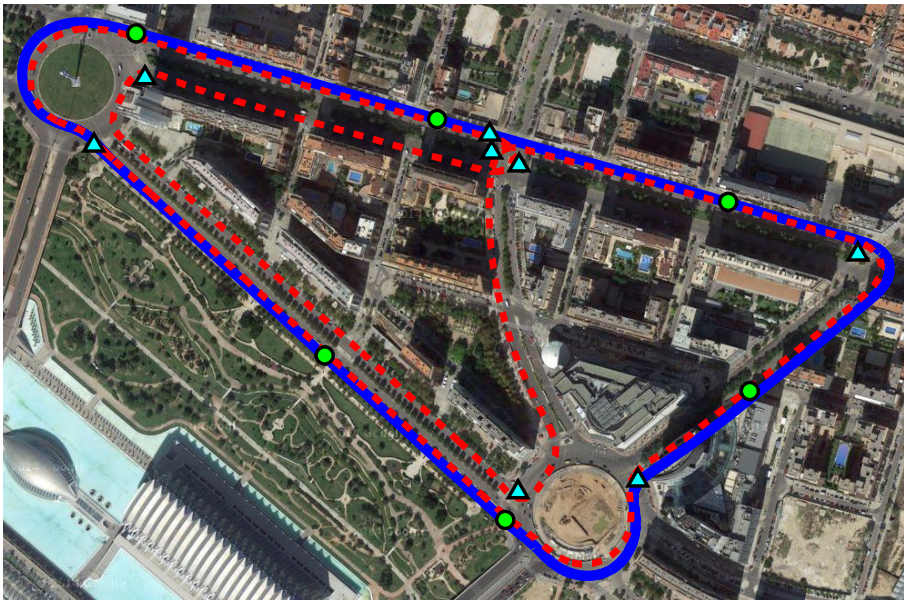

Figure 9.2: Urban scenario with two different bus routes. The first route (blue line) has 6 bus stops (green dots) and it is used to evaluate the performance of the haptic throttle and the emergency braking. The second bus route (red dashed line) has 8 turnings (cyan triangles) and allows the evaluation of the haptic feedback in the steering wheel in risky situations in corners.

ing conditions including traffic management, artificial intelligence of cars and pedestrian logic. Even though users were not expert bus drivers, all of them had driving licence (experience of 8 ± 3.4 years in average) and used to drive their cars frequently. Before starting, the subjects experienced the driving simulator for as long as they needed, in order to get used to it and to the circuit.

For the first set of experiments, drivers were addressed to take 4 loops to the first route, stopping the vehicle on each of the 6 bus stops (blue line and green dots in Figure 9.2). The first bus route was more than 2.2 km long, so each subject drove for about 9 km and did 24 bus stops. In order to force unexpected dangerous situations around bus stops, pedestrians showed up randomly walking in front of the bus, either when the vehicle was approaching or leaving bus stops. It is worth mentioning that people participating on the test did not know when or where a pedestrian was going to appear and, furthermore, half the times the haptic throttle and the emergency braking were randomly disabled, so the driver did not know whether the system was active or inactive.

To evaluate the performance of the haptic feedback in the steering wheel, a different route with more turnings is proposed (red dashed line and cyan triangles in Figure 9.2). As in the first set of experiments, the subjects were addressed to drive normally around the city and to take 4 loops to a predefined circuit, but in this case they did not have to stop. On each turn, randomly, a pedestrian appeared walking in front of the bus from either the left or the right side of the street. By doing this, subjects did not expect when and where pedestrians were going to show up from. In this experimentation, the throttle safety system was always enabled (haptic warning and emergency braking), but half the times the haptic feedback in the steering wheel was randomly disabled, in order to evaluate its performance and possible benefits.

The aim of such experiments is to compare the performance when the safety system is enabled against cases in which it is disabled. Several metrics are analysed in Section 9.4.6, such as percentages of low, medium, high risk incidents and collisions, as well as driver's reaction time in warning situations and time to collision in emergency situations. In the experimentation, we consider the following risk conditions:

- **Low**: when $d_{min} < d_{CO} \leq d_{max}$.
- **Medium**: when $d_{safety} < d_{CO} \leq d_{min}$.
- **High**: when $0.1\text{m} < d_{CO} \leq d_{safety}$ and $v > 1.5$ m/s.
- **Collision**: when $d_{CO} \leq 0.1\text{m}$ and $v > 0.6$ m/s.

Accordingly, the three proposed safety systems are expected to be effective upon the cases shown in Table 9.1.

Table 9.1: Safety system effectiveness

System	Low	Medium	High	Collision
Haptic throttle pedal	X	-	-	-
Haptic steering wheel	X	-	-	-
Emergency brake	-	X	X	X

As stated in Chapter 6, drivers' reaction time t_R is approximately between 0.4 s and 0.9 s on average (Jurecki et al., 2012). In our experimentation, the time of reaction is measured as the delay between the instant in which a pedestrian appears and the time instant when the driver presses the brake pedal at least a 10% of its range. Empirically, we obtained that t_R varies from 0.3 s to 1.2 s. In this sense, we discarded values of $t_R < 0.3$ s because either, the

driver was already pressing the brake pedal or we consider that driver's intention was to brake before even seeing any potential risk. For this analysis, we distinguish between situations where the bus slows down to stop (approach manoeuvres), from those in which the bus starts its movement (departure manoeuvres). It is interesting to remark that the collision risk evaluation system is computed in any case. That is, with the ADAS system enabled or disabled in order to compare the performance in a fair way.

In addition to this, we also measure the time to collision, as the time that the vehicle travels d_{CO} (7.8). In both metrics, we want to obtain the worst case per driver, so the following formulas are applied:

$$m_C^{[i]} = \min \mathbf{t}_C^{[i]} \tag{9.1}$$

$$m_R^{[i]} = \max \mathbf{t}_R^{[i]} \tag{9.2}$$

where i denotes the i-th driver, being $\mathbf{t}_C^{[i]}$ and $\mathbf{t}_R^{[i]}$ the lists corresponding to metrics with all medium risk, high risk or collision incidents involving the i-th driver. It is interesting to remark that the reaction time t_R is computed for all cases, whilst for the time to collision t_C only emergency situations are considered, which involve incidents of medium and high risk, plus collisions.

9.4 Results

9.4.1 Emergency braking: mass influence

This set of tests shows the influence of bus mass in an emergency braking and how d_{safety} can be set to guarantee no collision even with modelling errors. In this experiment, a model of the bus half loaded considering a mass of $m = 13000$ kg is used for the collision detection. As the safety distance is set to $d_{safety} = 1$ m, the vehicle should stop at such distance far from the obstacle (dashed blue line in Figure 9.3). However, if the model is not accurate enough the vehicle does not behave as expected, braking before or after it should (green and dotted red lines in Figure 9.3, respectively). In the worst case scenario, we would be using a model of the bus completely empty for the collision detection, when in fact it would be full. This would imply braking too late in some situations and therefore adding an extra safety distance is necessary to avoid crashes. Such distance d_{safety} should be at least the difference between the distance travelled by the vehicle (moving approximately at the maximum speed at which the emergency braking works) when it is full loaded and when it is loaded as the model used in the collision detection.

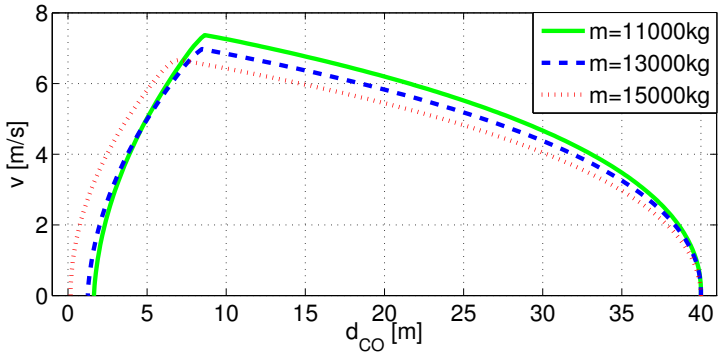

Figure 9.3: Phase diagram of distance $d_{CO}(t)$ versus velocity $v(t)$ for different values of vehicle mass m.

9.4.2 Haptic warning: distance influence

In this experimentation the influence of the distance Δd is evaluated. To do so, we have used the following longitudinal metrics: Mean Normalized Total Jerk ($MNTJ$) and Warning-Emergency Ratio (WER).

On the one hand, $MNTJ$ takes into account changes in acceleration or deceleration and is defined as:

$$MNTJ = \frac{1}{N}\sum_{i=0}^{N} \left| \frac{da_{x,i}}{dt} \right| \tag{9.3}$$

being $a_{x,i}$ the longitudinal acceleration.

On the other hand, WER considers the ratio between the travelled distance in a warning situation $d_{warning}$ and the distance when an emergency braking is produced $d_{emergency}$.

$$WER = \frac{d_{warning}}{d_{emergency}} \tag{9.4}$$

After analysing the results obtained for different values of the distance Δd, in Figure 9.4 it can be observed that the shorter Δd is the higher the $MNTJ$ and the sharper the emergency braking. In the limit of $\Delta d = 0$ m, there is no warning at all as $WER = 0$ and therefore there is no transition between a non-collision situation and an emergency situation. We consider that a $WER \approx 1$ is good, because lower values imply more aggressive safety actions without warning, while values too big can be annoying to the driver as the system starts working when the pedestrian is still too far away. In this sense, we choose $\Delta d = 10$ m for the experimentation carried out in Section 9.4.6.

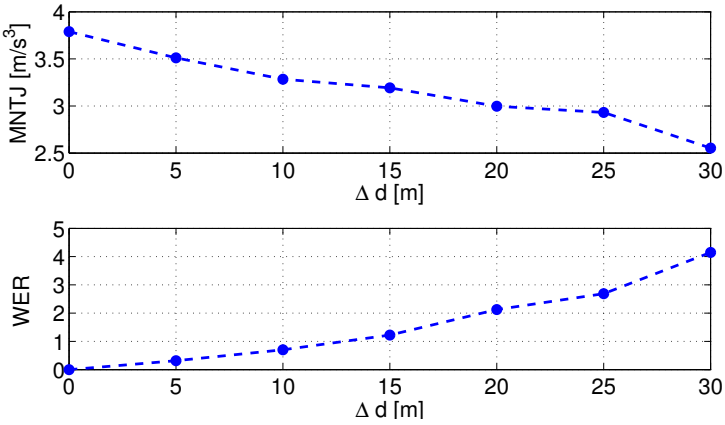

Figure 9.4: Mean Normalized Total Jerk $MNTJ$ and Warning-Emergency Ratio WER for different values of Δd.

9.4.3 Haptic warning: driving behaviour influence

Figure 9.5 shows two cases representing different driver's behaviour: expected and aggressive. In Figure 9.5(a), in the first case (red line) the driver intentionally does not react when the blocking lever tries to eject the throttle so he/she keeps pressing it, let's define that as aggressive driving. The second situation (dashed blue line) is an expected behaviour that happens when the driver reacts immediately releasing completely the throttle after feeling some force in the pedal. Obviously, between this two extreme situations there is a range of behaviours depending on driver's reaction time after feeling the haptic feedback.

On the other hand, in Figures 9.5(b) and 9.5(c) longitudinal acceleration and jerk are depicted, respectively. In the instant $t \approx 8$ s the driver stops pressing the throttle in the expected behaviour (dashed blue line), which implies a slight negative deceleration before the emergency braking is produced at $t \approx 9$ s. This behaviour implies that the maximum jerk suffered by the vehicle is lower and therefore more comfortable than the one produced by a more aggressive driving (red line). It is interesting to remark the equivalence between aggressive driving and a more conservative or expected driving without haptic warning, i.e. with $\Delta d = 0$ m. In fact, in both situations the emergency braking is applied directly without the driver reacting previously.

Finally, Figure 9.5(d) depicts the phase diagram of the proposed deceleration control law in order to analyse the performance of the safety system under each driver behaviour. The abscissa axis represents vehicle velocity, while the

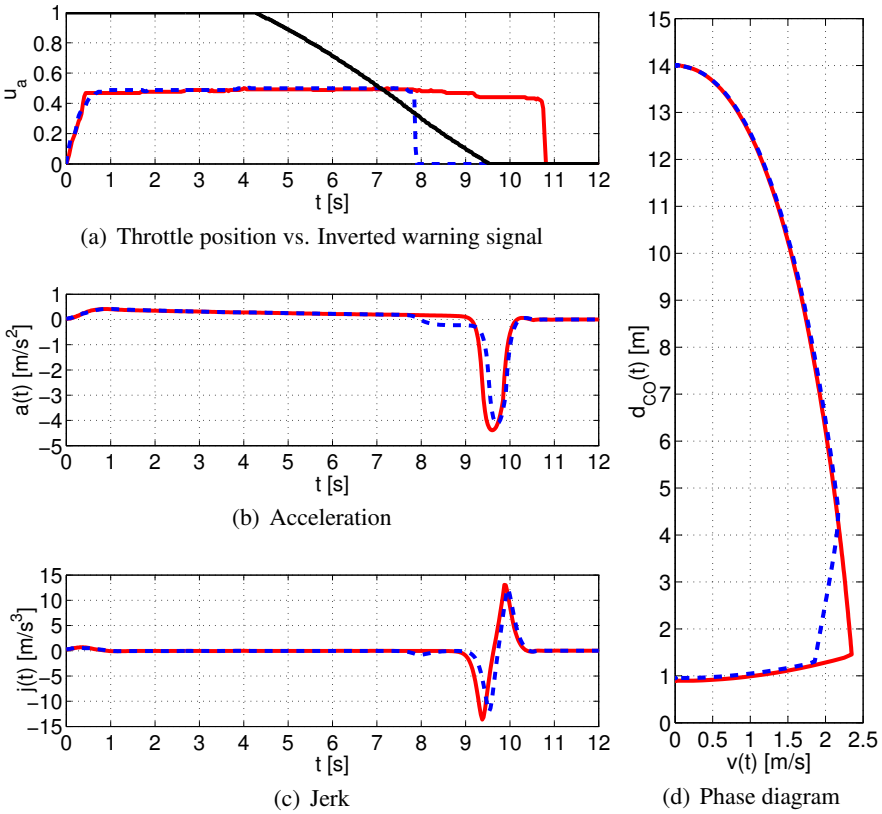

(a) Throttle position vs. Inverted warning signal

(b) Acceleration

(c) Jerk

(d) Phase diagram

Figure 9.5: Experiments with two opposite driver's reaction to the haptic feedback device: aggressive (red) and expected (dashed blue). Black line represents the allowed range to press the gas pedal, computed as $b(t) = 1 - w(t)$. In both cases the vehicle moves forward against an obstacle at $d_{CO} = 14$ m.

ordinate axis represents the distance of the vehicle to collide (without taking into account the length of the bus, since distances are measured from its front part). Initially, the pedestrian is placed at $d_{CO} = 14$ m far from the vehicle. Then the driver starts pressing the throttle and the vehicle speeds up. When the obstacle is at $d_{CO} < d_{max}$ the blocking system becomes active and ejects the throttle pedal. Finally, as soon as $d_{CO} < d_{min}$ an emergency braking is applied guaranteeing that when the bus is fully stopped the pedestrian is at a distance around d_{safety} far from the front part of the vehicle. It can be seen that the proposed control law cancels out driver actions and safely stops the vehicle before crashing in all considered situations. Indeed the safety system is effective even in cases of aggressive driving or with late reactions.

9.4.4 Emergency in an arrival manoeuvre

This experiment is aimed to explain what happens when the vehicle is approaching to a bus stop and suddenly a pedestrian appears in front of the vehicle. A sequence of images of such a dangerous situation is shown in Figure 9.6(a-i). As can be seen in Figure 9.6(j) the bus is initially moving at a speed $v \approx 7.5$ m/s and the driver is not pressing the throttle pedal u_t because he intends to stop. At the time instant 57.2 s the system detects a potential collision at $d_{CO} \approx 10$ m. Then, the collision risk factor c_t increases as d_{CO} decreases. However the warning haptic feedback is not activated until the throttle is pressed, which happens at instant $t \approx 57.7$ s. At this instant of time, the blocking mechanism b_t is activated and then the driver stops pressing the throttle around time instant $t \approx 58$ s (here the throttle pedal is pressed intentionally to force an activation of the warning system). Due to the inertia of the bus, it keeps approaching to the pedestrian even after the driver stops accelerating. When the pedestrian is at a distance $d_{CO} = 5$ m far from the bus an emergency stop signal e_t is enabled immediately. The emergency signal is deactivated when the vehicle is completely stopped at time instant $t \approx 59.5$ s.

9.4.5 Emergency in a departure manoeuvre

The goal of this experiment is to analyse what happens when the vehicle departs from a bus stop and suddenly a pedestrian shows up in the front part, let's say walking a pedestrian cross after a bus stop (as shown in Figure 9.7(a-i)). As can be seen in Figure 9.7(j), the bus is initially stopped and at time instant $t \approx 107.6$ s the driver presses the throttle to start moving. A second later the pedestrian is detected at a distance $d_{CO} \approx 2.2$ m and so the warning system becomes active immediately. As soon as the driver feels the haptic feedback he stops pressing the throttle. However, the inertia of the vehicle makes the potential collision get closer, which triggers the emergency braking at instant $t \approx 109$ s. Such signal is active until the vehicle stops its movement.

9.4.6 Benchmarking Evaluation

9.4.6.1 Haptic Throttle and Emergency Braking

The experimentation carried out for the benchmarking produced 606 incidents (half with the safety system disabled and half with it enabled) classified as low risk (Low), medium risk (Med), high risk ($High$) and collision (Col).

(a) Top centre 1 (b) Top center 2 (c) Top centre 3

(d) Front 1 (e) Front 2 (f) Front 3

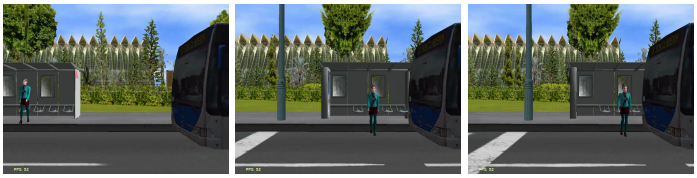

(g) Exterior view 1 (h) Exterior view 2 (i) Exterior view 3

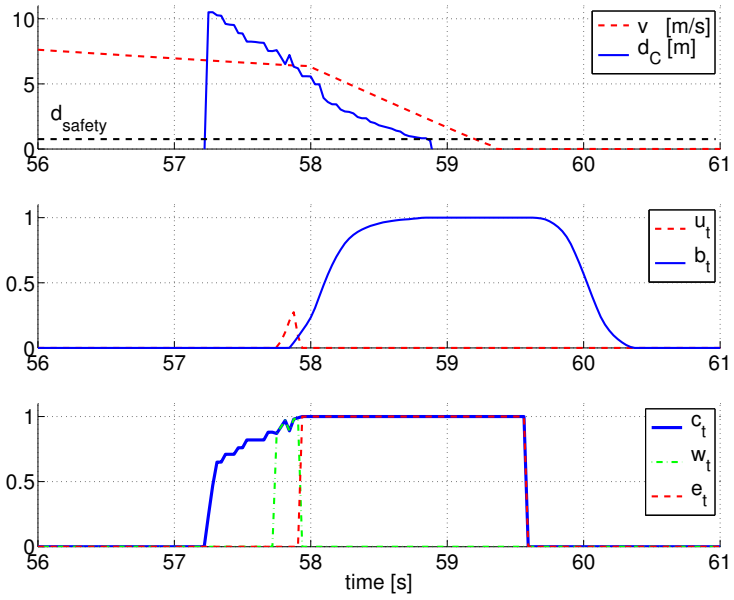

(j) Signals generated

Figure 9.6: Frontal emergency in an arrival manoeuvre (STOP).

(a) Top centre 1 (b) Top centre 2 (c) Top centre 3

(d) Front 1 (e) Front 2 (f) Front 3

(g) Exterior view 1 (h) Exterior view 2 (i) Exterior view 3

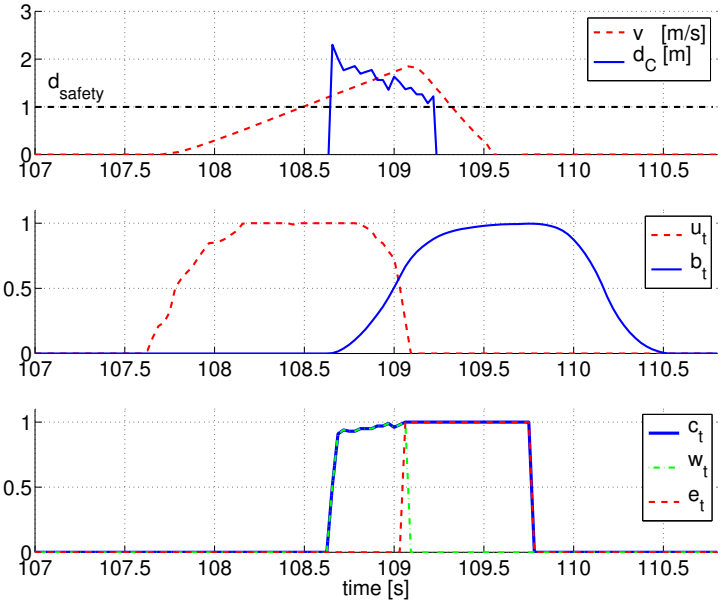

(j) Signals generated

Figure 9.7: Frontal emergency in a departure manoeuvre (START).

If we analyse Table 9.2, when the system was disabled there were 179 situations considered as low risk incidents (59.08%), 83 medium risk incidents (27.06%), 39 high risk (13.2%) and 2 collisions (0.66%). On the contrary, when the haptic throttle and the emergency braking were enabled, it can be clearly seen that a total of 30 previous cases, including high risk and collisions, were now considered as low or medium risk incidents. Moreover, there were no collisions and the high risk situations were reduced to 11 (a mere 3.63%).

Table 9.2: Risk evaluation of tests with haptic throttle and emergency braking disabled (OFF) and enabled (ON).

Haptic Feedback	RISKY INCIDENTS				
	Low	Medium	High	Collision	Total
OFF	179	83	39	2	303
ON	184	108	11	0	303

In our opinion, this phenomena can be mainly attributed to the emergency braking, which is able to stop autonomously the vehicle avoiding a crash when the driver does not react in time. Although, it also means that the haptic feedback in the throttle is being effective, because such a warning system makes the driver aware of a dangerous situation earlier, which avoids unnecessary emergency braking and indirectly reduces de number of medium risk situations. In other words, some of the medium and high risk situations with no haptic feedback have become medium and low risk incidents because the driver reacted in time thanks to the haptic feedback.

In Figure 9.8, a bar diagram with all incidents around bus stops of every driver is plotted. For each subject, the left graph is for cases with the haptic feedback and emergency braking disabled (OFF), while the right bar diagram is for incidents in which the haptic and emergency systems are enabled (ON). As can be clearly seen in Figure 9.8, the system improves reducing the number of high risk incidents and collisions to all drivers. In general, the number of these incidents are reduced although there are 5 cases in which the ratio increases (individuals 6, 11, 12, 17, 18). However, in those cases the ratio of low risk incidents is higher, which implies that the haptic system was effective despite of the high number of incidents.

Furthermore, after analysing the average values for all drivers of the different risky incidents, a considerable improvement can be observed. When the safety system is OFF, drivers on average tend to have 59.66% of low risk, 27.62% of medium risk and 12.18% of high risk incidents, with a 0.54% of probability of collision. On the contrary, when the system is ON a 62.13%

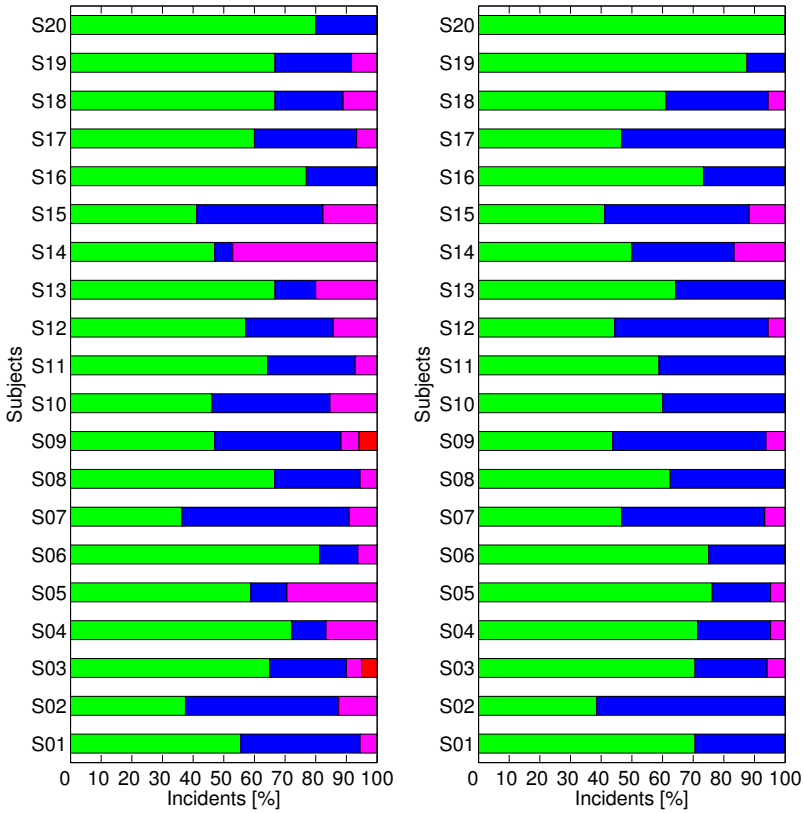

(a) OFF (b) ON

Figure 9.8: Bar diagram with incidents happened to each driver around bus stops, with haptic throttle and emergency braking (a) disabled and (b) enabled: (green) low risk, (blue) medium risk, (magenta) high risk and (red) collision.

of incidents are low risk, 34.48% are medium risk and 3.39% are high risk, without any probability of collision. Hence, it can be said that the force feedback in the throttle and the emergency braking help to reduce the number of high risk incidents and collisions. At the same time, the ratios of low risk and medium risk incidents are increased, which is an improvement in safety.

Now, let's focus on analysing separately situations where the vehicle is approaching the bus stop (STOP) and those in which it departs (START). In both cases, we compare the results when the safety haptic system is disabled (OFF) and when it is enabled (ON). Figure 9.9 shows the results considering the reaction time t_R, while Figure 9.10 depicts the results obtained for the time to collision t_C.

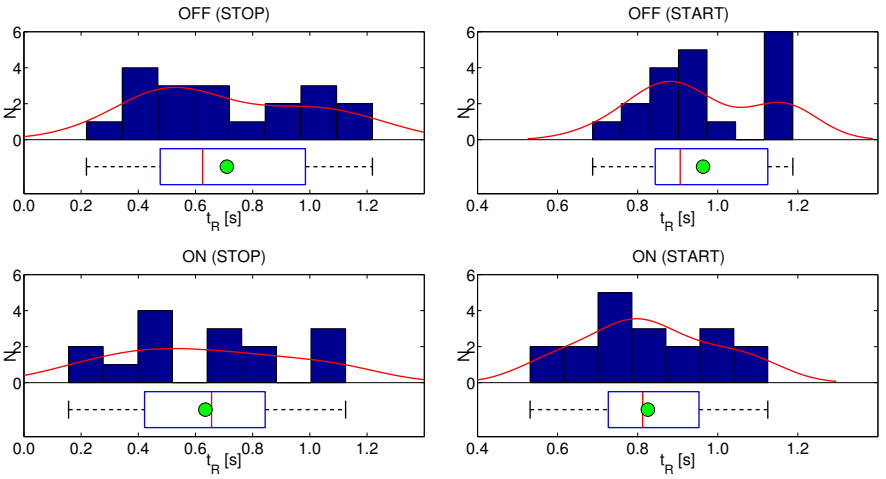

(a) Approach (b) Departure

Figure 9.9: Histograms and distributions of reaction time t_R, when ADAS is OFF (up) and ON (down): (a) t_R in approach manoeuvres (STOP) and (b) t_R in departure manoeuvres (START).

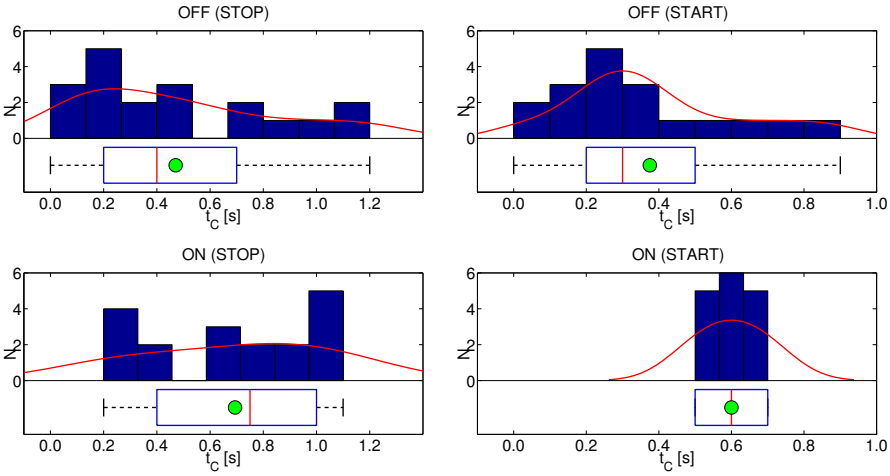

(a) Approach (b) Departure

Figure 9.10: Histograms and distributions of time to collision t_C in emergency situations, when ADAS is OFF (up) and ON (down): (a) t_C in approach manoeuvres (STOP) and (b) t_C in departure manoeuvres (START).

In order to highlight the benefits provided by the warning system, we evaluate driver's reaction time t_R in low risk cases. In Figure 9.9(a) it can be observed that in approach manoeuvres the reaction time is slightly better when the haptic throttle is enabled (mean value $t_R \approx 0.63$ s) than when it is disabled (mean value $t_R \approx 0.71$ s). In addition to this, when departing the haptic system becomes more effective with an improvement around 15% faster regarding the reaction time: mean value $t_R \approx 0.82$ s when ON against $t_R \approx 0.96$ s when OFF in mean, as shown in Figure 9.9(b).

Besides, since the haptic feedback reduces the reaction time, the expected velocity in these situations is also reduced. We obtained, from these experiments, a mean velocity value of $\bar{v} = 2.8$ m/s when the system is enabled compared to $\bar{v} = 4.5$ m/s when the system is disabled in those situations. Therefore, we can induce that safety is also improved as the severity in case of collision is reduced by reducing the speed of the vehicle.

Now, let's analyse the time to collision t_C in emergency situations (corresponding to cases of medium risk, high risk or collision) in order to highlight the benefits of the autonomous braking. In Figure 9.10(a) it can be observed that the probability distribution function of the time to collision when approaching is a combination of two Gaussian distributions. On one side, there are people who react later and produce lower times to collision $t_C \approx 0.3$ s, on average. Whilst on the other side, some drivers are more conservative and their mean time to collision is much higher $t_C \approx 0.9$ s. However, with the haptic throttle enabled the distribution function tends to move to the right (increases the number of time to collision cases with $t_C \geq 0.6$ s). Furthermore, as shown in Figure 9.10(b), the time to collision in departure situations is clearly improved, reducing considerably the standard deviation (SD) and moving the mean value from $t_C \approx 0.37$ s to $t_C \approx 0.6$ s (roughly twice).

In order to validate results, an analysis of variance (a two-way ANOVA) has been performed to evaluate whether the observed differences are statistically significant considering the factors *haptic feedback* and *driver*. The purpose is to determine whether data from levels of the factor *haptic feedback* (OFF/ON), and levels of the factor *driver* corresponding to each subject, have a common mean or, on the contrary, are significantly different.

From ANOVA tests, we get that the p-value corresponding to the reaction time t_R when the vehicle approaches the bus stop for the factor *haptic feedback* is $p = 0.124$, and for the factor *driver*, we get $p = 0.091$. This means that either null hypothesis cannot be rejected at the 0.05 significance level. Therefore, we can conclude that the observed differences in the reaction

time are not statistically significant. So the haptic feedback does not improve safety when the vehicle approaches the bus stop. On the contrary, analysing the reaction time in departure manoeuvres, after ANOVA analysis, we get that $p=0.01$ for the factor *haptic feedback*. Therefore, we reject the null hypothesis and can conclude that both groups of data are statistically different with a significance of 5%. Hence, the haptic feedback in the throttle do influence the time of reaction in departure manoeuvres. On the other hand, the factor *driver* provides $p = 0.196$. So, we cannot reject the null hypothesis and prove that the two samples are not statistically different (with 5% of significance level) and hence the reaction time is not influenced by the factor *driver*. This is also interesting because it means that the haptic feedback performance is similar for all type of drivers (let's say normal, conservative, aggressive).

Finally, we consider the ANOVA analysis regarding the time to collision t_C in approach manoeuvres involving the factor *emergency brake*, which takes its two possible levels OFF/ON and the factor *driver*. The factor *emergency brake* clearly provides a statistic significance of 5%, since $p=0.03$. Whilst the factor *driver* has not significance because $p=0.132$. Therefore, we state that the observed improvements in t_C are due to the usage of the proposed emergency brake system, but are not influenced by the driver. Regarding departure manoeuvres the results are similar. From ANOVA we get that the factor *emergency brake* affects the time to collision because $p=0.006$. But, as $p=0.512$ for the factor *driver*, t_C does not vary significantly for different drivers.

9.4.6.2 Haptic Steering Wheel

As can be observed in Table 9.3, the test produced an amount of 346 incidents, combining cases in which the haptic steering feedback was disabled with cases when it was enabled (we registered 173 incidents on each situation). When the feedback in the steering wheel was disabled there were 112 situations considered as low risk incidents. Whilst when it was enabled there were 135 low risk cases, reducing the number of medium risk, high risk and collision incidents. This means that the steering feedback improves safety, as this warning helps the driver react faster and avoids unnecessary emergency braking. Moreover, if we consider emergency situations there is also an improvement, because only 5 of the incidents were classified as high risk, with no collisions when the steering feedback was ON. However, the combination of haptic throttle and emergency braking, without steering feedback, is proved not to be enough for unexpected dangerous situations when the bus is turning, because 9 incidents implied high risk incidents and there were 4 collisions.

Table 9.3: Risk evaluation of tests performed with the steering feedback disabled (OFF) and enabled (ON).

Steering Feedback	RISKY INCIDENTS				
	Low	Medium	High	Collision	Total
OFF	112	48	9	4	173
ON	135	33	5	0	173

On the other hand, Figure 9.11 shows the results obtained per individual, where again there are situations in which the system tends to reduce the number of incidents. Now, if we analyse the average values for all drivers of the different risky incidents we observe an improvement. When the system is OFF, drivers tend to have 68.41% of low risk, 23.76% of medium risk and 6.61% of low risk incidents, with a 1.21% of probability of collision. On the contrary, when the system is ON a 78.46% of incidents are low risk, 19.78% are medium risk and 1.76% are low risk, with no collisions. So, the haptic feedback in the steering wheel tends to increase the percentage of low risk incidents while reducing the number of high risk and collision accidents.

Finally, let's analyse and compare the reaction time t_R when the steering feedback is disabled (OFF) and when it is enabled (ON). As shown in Figure 9.12(a), in turnings when the steering feedback is OFF the average time of reaction is $t_R \approx 0.91$ s, which is 15% slower than when it is ON ($t_R \approx 0.77$ s). After analysing the ANOVA results we conclude that the differences are statistically significant because $p = 0.0196$. On the other hand, it is worth mentioning that we also have analysed the time to collision t_C (see Figure 9.12(a)), which provides no significance according to the ANOVA analysis. This makes perfect sense, since the haptic steering feedback is only effective at low risk situations as shown in Table 9.1.

9.4.6.3 Usability

In order to analyse the usability of the safety system from drivers' experience, after finishing the driving tests they were asked to complete a short questionnaire regarding their opinion about comfort and safety. They had different options to choose in a range from 1 to 5 to refer to the degree of agreement with the statement (the higher the better).

Table 9.4 shows the results of the survey. Questions 1-3 are related to comfort, whilst questions 4-7 are about safety. In general the results are good, as most items have a mark above 4 out of 5. Questions Q2 and Q3 are the

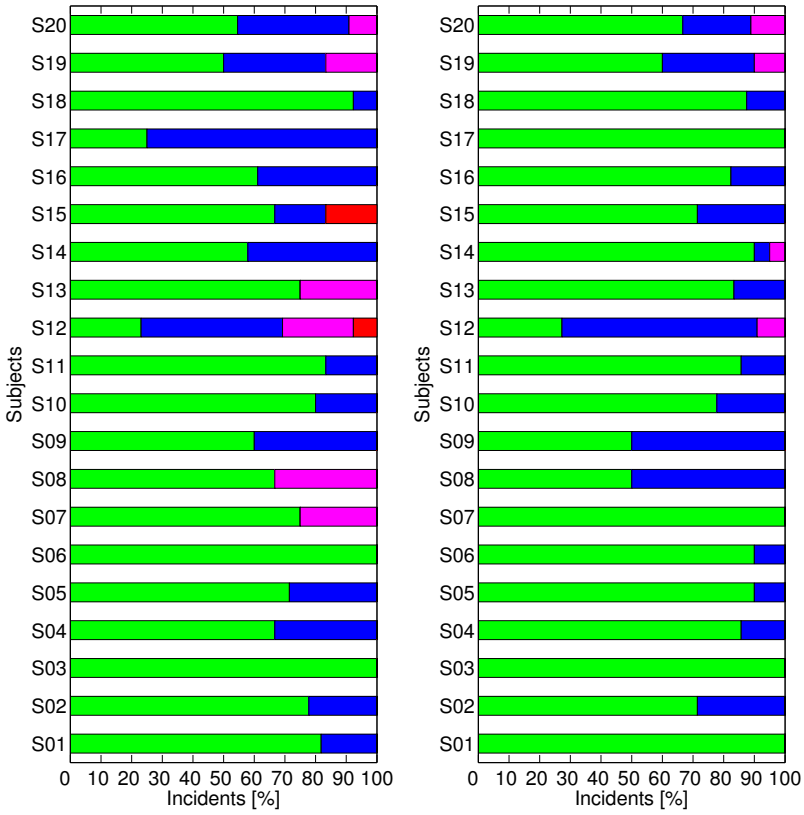

(a) OFF (b) ON

Figure 9.11: Bar diagram with incidents happened to each driver in turnings, with the steering feedback (a) disabled and (b) enabled: (green) low risk, (blue) medium risk, (magenta) high risk and (red) collision.

Table 9.4: Results from users experience after driving tests.

Questions	Answers
Q1. The ADAS is not annoying in normal driving situations.	4.6
Q2. The blocking torque in the throttle pedal is correct.	3.9
Q3. The blocking torque in the steering wheel is correct.	4.1
Q4. The haptic warning in the throttle pedal is helpful.	4.5
Q5. The haptic warning in the steering wheel is helpful.	4.3
Q6. The haptic feedback works in low risk situations.	4.5
Q7. The emergency stop works in dangerous situations.	4.6

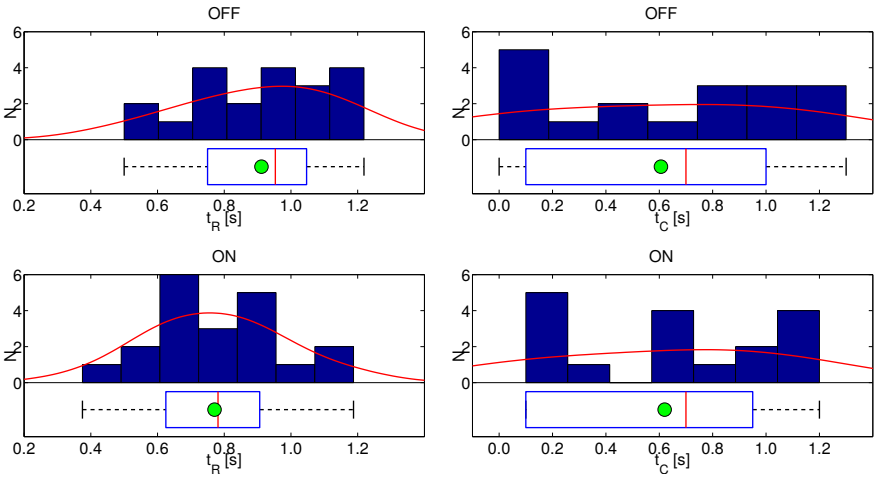

(a) Reaction time t_R (b) Collision time t_C

Figure 9.12: Histograms and distributions of t_R and t_C in turning incidents.

lowest ones, close to 4. The answers derived from these items might imply that people using the system felt some slight kind of discomfort, however this could be simply attributed to their lack of previous experience using the safety system.

9.5 Discussion

As stated in Section 9.1, the main contribution of this chapter is the testing of a new ADAS to help bus drivers in low-speed manoeuvres in urban environments, mostly in areas of passenger loading and unloading. The novelty lies in the fact that, after doing our own research and among all the papers cited in the extensive survey carried out by Petermeijer et al. (2015), we did not find any approach using haptic feedback in the throttle in order to avoid crashes with pedestrians.

Following the classification proposed in Petermeijer et al. (2015), we consider that the active safety system for bus braking assistance proposed in this thesis could be described as a warning system with automatic emergency braking (function level), intended for collision avoidance and speed adaptation at a manoeuvring level (task level), that uses a haptic throttle (channel level) applying a counterforce to communicate with the driver (signal level).

In works such as Várhelyi et al. (2004); Hjälmdahl and Várhelyi (2004); Adell et al. (2008b, 2011), the authors use an active gas pedal applying a counterforce when the speed limit is exceeded. This is very similar to what is done here, although applied to "safe speed and safe distance" (SASPENCE). In this sense, our findings are consistent and also show a statistically significant reduction in driver's reaction time when the haptic warning is enabled. Furthermore, we have also shown how a haptic throttle pedal can help to reduce the number of high risk incidents and collisions.

In other works, haptic warnings are used to avoid rear-end collisions with vehicles using vibro-tactile and/or audiovisual feedback (Chang and Chou, 2009; Kim and Jeong, 2010; Mohebbi et al., 2009). Similar works were carried out for collision avoidance problems using a haptic seat (Fitch et al., 2011), a haptic steering wheel (Jensen et al., 2011) or auditory feedback and a haptic pedal (Adell et al., 2008a,b). However, only two studies have been found regarding collision avoidance with pedestrians. They use either auditory and tactile feedback (Straughn et al., 2009) or haptic steering guidance (Itoh et al., 2012). But, none of them evaluates the effect of an active gas pedal as a warning to reduce the risk of collision with pedestrians. Therefore, our approach can be considered as a new contribution in the field because there are no previous solutions to this problem.

As in most of the mentioned papers, our findings prove that the active throttle with haptic feedback reduces driver's reaction time, so the average speed is reduced and the time to collision increased, which indirectly decreases the number of medium and high risk situations in which an emergency braking is necessary. Moreover, we have also shown that using a haptic warning reduces the abruptness when braking and therefore injuries occurred on board can be decreased. On the other hand, in medium or high risk incidents the emergency braking is an extra safety device able to reduce the speed automatically when the driver does not react in time, which helps to reduce the number of crashes.

The implantation of the proposed active safety system into city buses seeks to reduce the frequency and severity of accidents related to buses. However, their implementation in real systems is not immediate, requiring compliance with current legislation and relevant approvals. We believe that the haptic steering wheel feedback is compliant with the vehicle's steering equipment (Regulation UN/ECE 79), because the driver remains in primary control of the vehicle but may be helped by the steering system being influenced by signals initiated on-board vehicles of type M3 (buses). On the other hand, Regulations

UN/ECE 13 and UN/ECE 131 might apply for the vehicle's emergency braking, which might imply the integration within the Electronic Braking System (EBS). Finally, regarding the haptic feedback in the throttle pedal, the system does not affect the original vehicle configuration. Besides, as far as we know there is no-regulation regarding the maximum force that can be applied to the throttle pedal, it only depends on the bus manufacturer. In any case the torque necessary to overcome the lever force is small enough to allow a normal driving.

All these regulation aspects have been taken into account during the tests carried out in the context of the SAFEBUS Project, whose main goal was to develop a solution to reduce the severity of accidents between buses and pedestrians (see Armesto et al. (2015) for further details). Even though a prototype was developed before the end of the project, only a few preliminary tests were performed using a real bus, which constituted a proof of concept for the proposed ADAS, but without a proper benchmarking evaluation. However, the developments and results obtained in SAFEBUS have been extended in the next project named SAFETRANS. In this sense, we seek to design an industrialized version of the proposed active safety system, which will be able to universally be adapted to any heavy vehicle.

9.6 Conclusions

The advanced outdoor safety system for buses in urban environments at low speeds introduced in Chapters 7 and 8 has been tested. We have analysed the influence of the main parameters affecting the proposed method. Besides, the effectiveness of the developed safety system has been tested through some experiments carried out using a real prototype of the haptic throttle in a driving simulator. These experiments demonstrate that the haptic feedback in the throttle pedal is able to warn and interact with the driver when a dangerous manoeuvre happens, which reduces the reaction time and the number of situations in which the emergency braking system gets active. If a dangerous manoeuvre persists, the emergency braking guarantees collision-free situations, which is an improvement in safety.

An ANOVA analysis has been performed to test the significance of the proposed safety systems. From the results obtained, it can be concluded that there is a significant improvement on the time of reaction using the haptic throttle pedal, particularly when departing (accelerating). There is also a significant improvement on the time to collision as a consequence of the emergency brake, particularly when approaching to a bus stop (decelerating).

It has also been proven that there is no influence of the driver, which means that the safety system improves driving performance independently of driver's skills. In addition to this, the haptic steering wheel has also shown to be influential, particularly in turns, reducing the time of reaction even more when combined with the haptic throttle pedal. Therefore, it can be concluded that the proposed system improves safety significantly when a dangerous manoeuvre happens, thanks to haptic warnings and by enabling an emergency braking when there is a high risk of collision with a pedestrian.

Chapter 10

Conclusions and Future Work

At the beginning of the present research, the topic of smooth planning and control based on clothoids was not very extended within our research team. Just a few papers had been published in international conferences, but the topic was abandoned given that the application of this mathematical formulations was not clear. However, as a result of the research carried out towards the PhD degree, the publication of several good quality journal and conference papers has proved that this is a very interesting approach for many applications related to intelligent transportation systems, as well as advanced driver assistance systems. Moreover and not less important, there are still some niches that can be explored, which predicts a promising future ahead.

The research described in this thesis is focused on two main issues: 1) smooth planning and control techniques in autonomous driving and 2) active safety systems for manual-assisted driving. In both issues, the main objective is safety improvement and reduction in the frequency and severity of accidents in the context of intelligent vehicles. In this sense, through this chapter some conclusions are drawn from the obtained results, in addition to the main milestones and achievements of the research carried out. Finally, future work and perspectives are introduced, explaining several directions that can be taken from this point on.

10.1 Conclusions

In Chapter 2, it is pointed out that there are no trajectory generation tools for local path planning and control of non-holonomic robots that consider curvature continuity and maximum bounds in curvature and sharpness simultane-

ously. When an autonomous vehicle is following a reference, a big change in the target configuration, for instance to turn a corner or to avoid a collision, might imply an abrupt change in the direction of movement, which can lead to curvature discontinuities that would produce high discomfort or reduce safety by increasing the risk of wheels slip or even lateral rollovers. Therefore, the development of a path generation tool in order to guarantee smooth behaviours with curvature continuity is necessary to improve safety and comfort in intelligent vehicles.

A clothoid-based local path planner is developed in Chapter 3, inspired by the work of Scheuer and Fraichard (1997b) for smooth global planning in continuous-curvature paths. The proposed path, coined as Double Continuous-Curvature (DCC) path, is able to join any pair of arbitrary configurations in a Cartesian plane, keeping curvature continuity, while taking into account lower and upper bounds on sharpness and curvature. A proper comparison between DCC paths and the single continuous-curvature paths proposed in Scheuer and Fraichard (1997b) is carried out. It has been proven that DCC paths can be used as local planners while SCC-paths not, because they are meant for global planning where initial and final path curvatures are usually zero.

Then, in Chapter 4 two different approaches are introduced to prove the applicability of DCC paths to the control of mobile wheeled robots. The first control scheme is based on a Pure-Pursuit framework in which the target is recomputed from robot position and a Look-Ahead distance, very typical in the robotics field. While in the second approach, an optimal controller is used to close the loop, which is more common in the control systems area. In both cases, DCC paths can be used as a reference in the path following problem. In this context, a complete benchmarking is carried out to compare the DCC controller and the well-known Pure-Pursuit algorithm (Ollero, 2001). The benefits of the proposed controller are supported by the results obtained from the experimentation. In Section 4.2.6, it has been shown that the proposed method has better performance in terms of settling time, overshoot and error, while it has little influence on design parameters. Besides, DCC control introduces improvements in comfort and safety because the sharpness, normal jerk and mean abruptness are lower than with the PP control.

Regarding the optimal control approach, in Section 4.3.4, the performance of the proposed optimal controllers, named as ERTS and URTS, has been studied on a trajectory-following problem of a mobile robot and compared with nonlinear iterative linearization-based algorithms such as iLQR, NMPC and AICO. Simulations show that ERTS generates nearly the same control as

iLQR and NMPC controllers after convergence, but with a significant computational cost reduction. In fact, ERTS can be considered a good choice for initialization of the above iterative algorithms. Hence, accuracy and reduced computational cost makes ERTS an interesting option for real-time control *with receding horizon policies*.

With the aim of proving that the proposed control scheme can be successfully used, four different applications are solved in Chapter 5: vision-based line following of AGVs, rollover avoidance of industrial forklifts carrying heavy loads at high speeds, obstacle avoidance of non-holonomic wheeled robots and path following of mobile robots using optimal controllers.

Every year thousands of people die in traffic accidents, as stated in Chapter 6, being a human factor the cause of the crash in most cases. Even though there are some approaches and commercial solutions to assist drivers in order to avoid accidents between cars and pedestrians, their use in passenger transportation systems is still in development requiring further research. In this sense, in the second part of the thesis, a new Advanced Driver Assistance System (ADAS) has been introduced to reduce the frequency and severity of accidents in which buses are involved, specially in low-speed manoeuvres in urban scenarios (particularly with low visibility, such as turnings or areas of passenger loading and unloading).

The main contribution of Chapter 7 is the development of a methodology for assisted driving and a computationally efficient algorithm, based on three main concepts: 1) an efficient collision detection system considering driver's intention and pedestrians moving around the vehicle, which is based on arc reachable manifolds and the new concept of clothoid reachable manifold; 2) a risk evaluation system to generate warnings and emergency stop signals; 3) a simplified model of the vehicle applicable to collision detection with similar performance to more complex models, but with less processing load.

The proposed safety system consists of haptic feedback devices in throttle pedal and steering wheel, as well as an emergency brake system to stop the vehicle in situations of imminent collision. The complete active safety system also incorporates warnings through audio-visual feedback, together with a vision-based pedestrian detection system. Haptic-Audio-Visual (HAV) feedback and pedestrian detection systems are detailed in Chapter 8. Besides, some preliminary tests have been carried out using a prototype of the active safety system in a real public bus.

Finally, in Chapter 9 the effectiveness of the developed safety system is analysed through some experiments carried out using a simulated scenario. These experiments demonstrate that the haptic feedback of the safety system is able to warn and interact with the driver in risky situations. If a dangerous manoeuvre persists an emergency braking is enabled to guarantee collision-free situations. The number of medium and high risk situations as well as the number of collisions are clearly reduced, given that driver's reaction time when braking is also lower and average time to collision increases with respect to situations where the system is disabled.

10.2 Achievements

A list summarizing the main achievements of the thesis is presented next:

- Generation of a new clothoid-based smooth trajectory, coined as Double Continuous-Curvature (DCC) path, able to join any arbitrary pair of planar configurations, keeping curvature continuity while taking into account lower and upper bounds on curvature and sharpness.
- DCC paths can be used as reference to control non-holonomic mobile robots, since the current curvature of the vehicle is taken into account. In this regard, using real and simulated wheeled mobile robots, several navigation problems have been solved, such as vision-based line following, vehicle stability to avoid tip overs, as well as obstacle avoidance.
- A new controller has been developed based on the duality between estimation and optimal control. This control algorithm is used to close the loop in the trajectory following of mobile robots.
- A methodology for driver assistance to reduce the number and severity of accidents in low-speed manoeuvres in large vehicles such as buses has also been developed.
- A new tool for collision detection in manual-assisted driving, coined as Clothoid Reachable Manifold (CRM), has been introduced.
- The proposed ADAS is based on pedestrian detections using artificial vision, as well as haptic and audiovisual feedback to warn the driver of dangerous manoeuvres. The system incorporates an emergency braking mechanism capable of stopping the vehicle in dangerous situations where the driver does not react in time.

- The active safety system has been tested using a public bus. Moreover, a benchmarking evaluation using a very realistic driving simulator with 20 drivers has been carried out in order to validate the haptic feedback and emergency braking systems. According to the tests, times are improved and the risk of collision is reduced, which is an important improvement in safety.

10.3 Future Work

10.3.1 Spatial Smooth Paths

Even though the benefits of planar clothoids have been proven, researchers have paid little attention to the use of such curves in the space. A few works proposed the use of clothoids in path planning for UAVs (Yang and Sukkarieh, 2008; Wan et al., 2011). Others instead, approached a similar problem from the field of computer graphics (Li Guiqing and Hua, 2001; Harary and Tal, 2010; Saracoglu, 2012). Nevertheless, only one seems to match with the exact definition of a 3D clothoid (Harary and Tal, 2010). But, the problem is that this approach is based on a Frenet-Serret frame and requires a discrete integration. Moreover, since they are generated from the linear equations of curvature and torsion, it is not possible to know a priori the increment in position and orientation with respect to the origin of the curve. For that reason, in order to use a trajectory with such good properties in a 3D navigation problem, a new spatial clothoid should be developed. In this sense, Appendix A includes a preliminary study to develop spatial smooth paths to guide AUVs (Autonomous Underwater Vehicles) and UAVs (Unmanned Aerial Vehicles) in navigation problems.

10.3.2 Clothoid Reachable Manifold Mathematics

Some concepts have been introduced in this manuscript regarding Clothoid Reachable Manifolds. However, the development of the Mathematics requires further research in order to get analytical solutions or at least an efficient computation of the obstacle space based on CRM. This will allow to use CRM not only in the context of ADAS but to solve motion planning problems in mobile robotics too.

10.3.3 Driver Guidance in Parking Manoeuvres

In the context of ADAS, there are several research lines to follow. For instance, force-feedback in the steering wheel has been introduced in the driving simulation platform through a gear and a DC motor connected to the steering shaft. In this sense, we plan to use DCC paths to assist and guide bus drivers in parking manoeuvres and when approaching to bus stops. The expected result is an improvement in the performance and repeatability of those manoeuvres, so that the vehicle stops parallel to the sidewalk and exactly near the bus stop, because some studies have proven that this could reduce the number of accidents when people get on and off the bus.

10.3.4 Haptic and Audio-Visual Feedback Benchmarking

As stated in Chapter 8, a further work will imply the development of an industrialized version of the proposed active safety system for bus driver assistance. A complete benchmarking will be performed using real buses with professional drivers in order to test the ADAS in real driving conditions. Apart from the haptic feedback in the throttle and the steering wheel, we aim to evaluate in-depth the benefits of using auditive and visual feedback. Different approaches for audiovisual and haptic feedback are intended to be developed and compared, in order to find which give better performances.

Bibliography

ADAM BASIR, O., BHAVNANI, J. P., KARRAY, F. and DESROCHERS, K. Drowsiness detection system. 2004.

ADELL, E. and VÁRHELYI, A. Driver comprehension and acceptance of the active accelerator pedal after long-term use. *Transportation Research Part F*, vol. 11(1), pages 37–51, 2008. ISSN 1369-8478.

ADELL, E., VARHELYI, A., ALONSO, M. and PLAZA, J. Developing human-machine interaction components for a driver assistance system for safe speed and safe distance. *Intelligent Transport Systems, IET*, vol. 2(1), pages 1–14, 2008a. ISSN 1751-956X.

ADELL, E., VÁRHELYI, A. and DALLA FONTANA, M. The effects of a driver assistance system for safe speed and safe distance - a real-life field study. *Transportation Research Part C: Emerging Technologies*, vol. 19(1), pages 145 – 155, 2011. ISSN 0968-090X.

ADELL, E., VÁRHELYI, A. and HJÄLMDAHL, M. Auditory and haptic systems for in-car speed management - a comparative real life study. *Transportation Research Part F*, vol. 11(1), pages 445 – 458, 2008b. ISSN 1369-8478.

ADEPT MOBILEROBOTS. Pioneer 3dx. 1995.

ALLEN BROWN, T. and CARR MEYERS, J. Rollover stability control for an automotive vehicle. 2001.

ALLEN BROWN, T. and CARR MEYERS, J. Rollover stability control for an automotive vehicle. 2002.

ARMESTO, L., ARNAL, L., DOLS, J., GIRBÉS, V. and PERIS, J. C. Safebus project: Advanced safety systems in buses. *RIAI (In press)*, pages 1–12, 2015.

ARMESTO, L., GIRBÉS, V., VINCZE, M., OLUFS, S. and MUÑOZ-BENAVENT, P. Mobile robot obstacle avoidance based on quasi-holonomic smooth paths. In *Advances in Autonomous Robotics*, vol. 7429 of *Lecture Notes in Computer Science*, pages 244–255. Springer Berlin Heidelberg, 2012.

ASCABUS. El sector carrocero de autobuses y autocares y el transporte de viajeros en cifras. technical report, Asociación Española de Carroceros de Autobuses y Autocares, 2013.

BAASS, K. G. The use of clothoid templates in highway design. *Transportation Forum*, vol. 1, pages 47–52, 1984.

BECK, C., VALLS, J. and DISSANAYAKE, G. Trajectory optimisation for increased stability of mobile robots operating in uneven terrains. In *IEEE Int. Conf. on Control and Automation*, pages 1913–1919. 2009.

BEEVER, P. A., GALLERY, M. J. and PARSONS REGINALD, K. G. A wheeled vehicle with hill descent control. 2001.

BEMPORAD, A., MORARI, M., DUA, V. and PISTIKOPOULOS, E. N. The explicit linear quadratic regulator for constrained systems. *Automatica*, vol. 38(1), pages 3 – 20, 2002. ISSN 0005-1098.

BERNTMAN, M., WRETSTRAND, A. and HOLMBERG, B. Bus travel safety - a travel chain perspective. In *International conference on Mobility and Transport for Elderly and disabled Persons*, page 10. 2010.

BIRAL, F., DA LIO, M. and BERTOLAZZI, E. Combining safety margins and user preferences into a driving criterion for optimal control-based computation of reference maneuvers for an adas of the next generation. In *Intelligent Vehicles Symposium, 2005. Proceedings. IEEE*, pages 36–41. 2005.

BISHOP, R. *Intelligent Vehicle Technology And Trends*. Artech House Its Library, 2005.

BLACKMORE, L., ONO, M., BEKTASSOV, A. and WILLIAMS, B. A probabilistic particle-control approximation of chance-constrained stochastic predictive control. *Robotics, IEEE Transactions on*, vol. 26(3), pages 502–517, 2010. ISSN 1552-3098.

BMW. Technology guide: Safety. 2013.

BOISSONNAT, J.-D., CÉREÉZO, A. and LEBLOND, J. Shortest paths of bounded curvature in the plane. technical report, INRIA Sophia Antipolis, 1991.

BOSCH. Anti-lock braking system (abs). 1978.

BRADSKI, G. The OpenCV Library. *Dr. Dobb's Journal of Software Tools*, 2000.

BRADSKI, G. and KAEHLER, A. *Learning OpenCV*. O'Reilly Media Inc., 2008.

BRANNSTROM, M., COELINGH, E. and SJOBERG, J. Model-based threat assessment for avoiding arbitrary vehicle collisions. *Intelligent Transportation Systems, IEEE Transactions on*, vol. 11(3), pages 658–669, 2010. ISSN 1524-9050.

BREZAK, M. and PETROVIC, I. Path smoothing using clothoids for differential drive mobile robots. In *18th IFAC World Congress, Milano, Italy*, vol. 28, pages 1133–1138. 2011.

BREZAK, M. and PETROVIC, I. Real-time approximation of clothoids with bounded error for path planning applications. *Robotics, IEEE Transactions on*, vol. 30(2), pages 507–515, 2014. ISSN 1552-3098.

BROGGI, A., ZELINSKY, A., PARENT, M. and THORPE, C. E. S*pringer* H*andbook of* R*obotics. Chapter 52: Intelligent Vehicles*. Springer-Verlag New York Inc., 2008.

BRSCIC, D., KANDA, T., IKEDA, T. and MIYASHITA, T. Person tracking in large public spaces using 3-d range sensors. *Human-Machine Systems, IEEE Transactions on*, vol. 43(6), pages 522–534, 2013. ISSN 2168-2291.

BUICK. Maxtrac traction control. 1971.

CAMPION, G., BASTIN, G. and DANDREA-NOVEL, B. Structural properties and classification of kinematic and dynamic models of wheeled mobile robots. *IEEE Transactions on Robotics and Automation*, vol. 12(1), pages 47–62, 1996.

CARE DATABASE. Traffic safety basic facts: Heavy goods vehicles and buses. technical report, European Road Safety Observatory, 2015.

DO CARMO, M. *Differential geometry of curves and surfaces*. Prentice Hall, 1976.

CHANG, C.-Y. and CHOU, Y.-R. Development of fuzzy-based bus rear-end collision warning thresholds using a driving simulator. *Intelligent Transportation Systems, IEEE Transactions on*, vol. 10(2), pages 360–365, 2009. ISSN 1524-9050.

CHUI, C. K. and CHEN, G. *Kalman Filtering with Real-time Applications*. Springer-Verlag New York, Inc., New York, NY, USA, 1987. ISBN 0-387-18385-7.

CHUN, J., LEE, I., PARK, G., SEO, J., CHOI, S. and HAN, S. H. Efficacy of haptic blind spot warnings applied through a steering wheel or a seatbelt. *Transportation Research Part F: Traffic Psychology and Behaviour*, vol. 21, pages 231 – 241, 2013. ISSN 1369-8478.

DEL CORRAL, I. *Topografía de obras*. Edicions UPC, 2001.

CORRIDORI, C. and ZANIN, M. High curvature two-clothoid road model estimation. In *Intelllgenl Trsnsportation Systems Conference*. 2004.

DALAL, N. and TRIGGS, B. Histograms of oriented gradients for human detection. In *In CVPR*, pages 886–893. 2005.

DANIEAU, F., LÉCUYER, A., GUILLOTEL, P., FLEUREAU, J., MOLLET, N. and CHRISTIE, M. Enhancing audiovisual experience with haptic feedback: A survey on hav. *IEEE Transactions on Haptics*, 2013.

DELINGETTE, H., HEBERT, M. and LKEUCHI, K. Trajectory generation with curvature constraint based on energy minimization. In *IEEE Int. Conf. on Intelligent Robots and Systems*. 1991.

DELL'AMICO, M., MARZANI, S., MININ, L., MONTANARI, R., TESAURI, F., MARIANI, M., IANI, C. and TANGO, F. Design of an adaptive feedback based steering wheel. In *Proceedings of the 2007 International Conference on Ergonomics and Health Aspects of Work with Computers*, pages 180–188. Springer-Verlag, Berlin, Heidelberg, 2007. ISBN 978-3-540-73332-4.

DENNERLEIN, J. T., MARTIN, D. B. and HASSER, C. Force-feedback improves performance for steering and combined steering-targeting tasks. pages 423–429. ACM Press, 2000.

DOERKSEN, B. F. and NATTINGER, D. M. Tire pressure monitoring system. 1989.

DOLLÁR, P., WOJEK, C., SCHIELE, B. and PERONA, P. Pedestrian detection: A benchmark. In *IEEE Conf. on Computer Vision and Pattern Recognition*, pages 304–311. 2009.

DOLLÁR, P., WOJEK, C., SCHIELE, B. and PERONA, P. Pedestrian detection: An evaluation of the state of the art. *IEEE Transactions on Pattern Analysis and Machine Intelligence*, vol. 34(4), pages 743–761, 2012.

DONALD, B., XAVIER, P., CANNY, J. and REIF, J. Kinodynamic motion planning. *J. ACM*, vol. 40, pages 1048–1066, 1993. ISSN 0004-5411.

DUBINS, L. E. On curves of minimal length with constraint on average curvature, and with prescribed initial and terminal positions and tangents. *American Journal of Mathematics*, vol. 79(3), pages 497–516, 1957.

DUNN, T., LAVER, R., SKORUPSKI, D. and ZYROWSKI, D. Assessing the business case for integrated collision avoidance systems on transit buses. fta-omb no. 0704-0188. technical report, US Department of Transportation, 2007.

ENZWEILER, M. and GAVRILA, D. Monocular pedestrian detection: Survey and experiments. *IEEE Transactions on Pattern Analysis and Machine Intelligence*, vol. 31(12), pages 2179–2195, 2009.

FAMBRO, D., KOPPA, R., PICHA, D. and FITZPATRICK, K. Driver perception-brake response in stopping sight distance situations. *Transportation Research Record, 1628: 1–7*, 1998.

FISCHLER, M. A. and BOLLES, R. C. Random sample consensus: A paradigm for model fitting with applications to image analysis and automated cartography. *Commun. ACM*, vol. 24(6), pages 381–395, 1981.

FITCH, G. M., AMD BRIAN M. KLEINER, J. M. H. and DINGUS, T. A. Driver comprehension of multiple haptic seat alerts intended for use in an integrated collision avoidance system. *Transportation Research Part F: Traffic Psychology and Behaviour*, vol. 14(4), page 278–290, 2011.

FLEURY, S., SOUÉRES, P., LAUMOND, J. and CHATILA, R. Primitives for smoothing mobile robot trajectories. *IEEE Trans. Robotics and Automation*, vol. 11, pages 441–448, 1995.

FOX, D., BURGARD, W. and THRUN, S. The dynamic window approach to collision avoidance. *Robotics Automation Magazine, IEEE*, vol. 4(1), pages 23 –33, 1997. ISSN 1070-9932.

FRAICHARD, T. and AHUACTZIN, J. M. Smooth path planning for cars. In *IEEE International Conference on Robotics and Automation, 2001*, vol. 4, pages 3722–3727 vol.4. 2001. ISSN 1050-4729.

FRAICHARD, T. and MERMOND, R. Path planning with uncertainty for car-like robots. In *Robotics and Automation, 1998. Proceedings. 1998 IEEE International Conference on*, vol. 1, pages 27–32 vol.1. 1998. ISSN 1050-4729.

FRAICHARD, T. and SCHEUER, A. From reeds and shepp's to continuous-curvature paths. In *IEEE Trans. on Robotics and Automation*, 6, pages 1025–1035 vol. 20. 2004. ISSN 1552-3098.

GANDHI, T. and TRIVEDI, M. Pedestrian collision avoidance systems: a survey of computer vision based recent studies. In *IEEE Intelligent Transportation Systems Conference*, pages 976–981. 2006.

GARCIA, A., SANCHEZ, M., MARTIN, A., LOPEZ, S., HASSMAN, C. and VALDEPEÑAS, J. Estudio para la mejora de las condiciones de seguridad y ergonomía del puesto de conducción en autocares. technical report, Instituto Universitario de Investigación del Automóvil (INSIA), 2003.

GARCÍA, F., JIMÉNEZ, F., NARANJO, J., ZATO, J., APARICIO, F. and DE LA ESCALERA, A. Laser scanner como sistema de detección de entornos viales. *Revista Iberoamericana de Automática e Informática Industrial {RIAI}*, vol. 8(1), pages 44 – 53, 2011. ISSN 1697-7912.

GARCÍA, F., JIMÉNEZ, F., PUERTAS, E., NARANJO, J., ARMINGOL, J. and FERNÁNDEZ, J. Pre-collision systems for urban environment accidents avoidance. *Securitas Vialis*, pages 1–9, 2013. ISSN 1888-9697.

GE, J., LUO, Y. and TEI, G. Real-time pedestrian detection and tracking at nighttime for driver-assistance systems. *Intelligent Transportation Systems, IEEE Transactions on*, vol. 10(2), pages 283–298, 2009. ISSN 1524-9050.

GERÓNIMO, D., LÓPEZ, A., SAPPA, A. and GRAF, T. Survey of pedestrian detection for advanced driver assistance systems. *IEEE Transactions on Pattern Analysis and Machine Intelligence*, vol. 32(7), pages 1239–1258, 2010.

GERONIMO, D., LOPEZ, A., SAPPA, A. and GRAF, T. Survey of pedestrian detection for advanced driver assistance systems. *Pattern Analysis and Machine Intelligence, IEEE Transactions on*, vol. 32(7), pages 1239–1258, 2010.

GILLESPIE, T. D. *Fundamentals of Vehicle Dynamics*. Society of Automotive Engineers, 1992. ISBN 9781560911999.

GIRBÉS, V., ARMESTO, L. and TORNERO, J. Pisala project: Intelligent sensorization for line tracking with artificial vision. In *International Symposium on Robotics*, pages 558–563. 2010.

GIRBÉS, V., ARMESTO, L. and TORNERO, J. On generating continuous-curvature paths for line following problem with curvature and sharpness constraints. In *IEEE International Conference on Robotics and Automation*, pages 6156–6161. 2011a.

GIRBÉS, V., ARMESTO, L., TORNERO, J. and SOLANES, J. Smooth kinematic controller vs. pure-pursuit for non-holonomic vehicles. In *Towards Autonomous Robotic Systems*, vol. 6856 of *Lecture Notes in Computer Science*, pages 277–288. Springer Berlin Heidelberg, 2011b. ISBN 978-3-642-23231-2.

GOOGLE. Google self-driving car. 2012.

GRACIA, L. and TORNERO, J. Geometric parallel parking planner for car-like vehicles. In *Int. Industrial Simulation Conf.*. 2003.

GRAUSTEIN, W. *Differential Geometry*. Dover, 2006.

GROSCH, T. O. Radar sensors for automotive collision warning and avoidance. In *Proceedings of SPIE - The Int. Society for Optical Engineering*, pages 239–247. 1995.

GRÜNE, L. and PANNEK, J. *Nonlinear Model Predictive Control: Theory and Algorithms*. Communications and Control Engineering. Springer, 1st ed. edition, 2011.

HARARY, G. and TAL, A. 3d euler spirals for 3d curve completion. In *Symposium on Computational Geometry*. 2010.

HARRIS, C. and STEPHENS, M. A combined corner and edge detector. In *In Proc. of Fourth Alvey Vision Conference*, pages 147–151. 1988.

HARTLEY, R. I. and ZISSERMAN, A. *Multiple View Geometry in Computer Vision*. Cambridge University Press, ISBN: 0521540518, second edition, 2004.

HAZEWINKEL, M., editor. *Minkowski addition*, vol. Encyclopedia of Mathematics. Springer, 2001.

HJÄLMDAHL, M. and VÁRHELYI, A. Speed regulation by in-car active accelerator pedal. effects on driver behaviour. *Transportation Research Part F*, vol. 7(1), pages 77–94, 2004. ISSN 1369-8478.

HOGEMA, J. H., VRIES, S. C. D., ERP, J. B. V. and KIEFER, R. J. A tactile seat for direction coding in car driving: Field evaluation. *IEEE Transactions on Haptics*, vol. 2(4), pages 181–188, 2009.

IAGNEMMA, K. and BUEHLER, M. Special issues on the darpa grand challenge. *Journal on Field Robotics*, vol. 23, pages 461–835, 2006.

IIJIMA, J., KANAYAMA, Y. and YUTA, S.-I. A locomotion control system for mobile robots. In *Int. Conf. on Artificial Intelligence*, pages 779–784 vol. 2. 1981.

IROBOT. Roomba vacuum cleaning robot. 2002.

ITOH, M., INAGAKI, T. and TANAKA, H. Haptic steering direction guidance for pedestrian-vehicle collision avoidance. In *Systems, Man, and Cybernetics (SMC), 2012 IEEE International Conference on*, pages 3327–3332. 2012.

JACOBS, P. and CANNY, J. Planning smooth paths for mobile robots. In *Int. Conf. on Robotics and Automation*. 1989.

JAILLET, L., CORTÉS, J. and SIMÉON, T. Sampling-based path planning on configuration-space costmaps. *Trans. Rob.*, vol. 26, pages 635–646, 2010.

JANG, J.-A., CHOI, K. and CHO, H. A fixed sensor-based intersection collision warning system in vulnerable line-of-sight and/or traffic-violation-prone environment. *Intelligent Transportation Systems, IEEE Transactions on*, vol. 13(4), pages 1880–1890, 2012. ISSN 1524-9050.

JENSEN, M. J., TOLBERT, A. M., WAGNER, J. R., SWITZER, F. S. and FINN, J. W. A customizable automotive steering system with a haptic feedback control strategy for obstacle avoidance notification. *IEEE Transactions on Vehicular Technology*, vol. 60(9), page 4208–4216, 2011.

JHA, M., SCHONFELD, P., JONG, J.-C. and KIM, E. *Intelligent Road Design*. WIT Press, 2006. ISBN 1-84564-003-9.

JIANG, K., ZHANG, D. and SENEVIRATNE, L. A parallel parking system for a car-like robot with sensor guidance. *Journal of Mechanical Engineering Science*, vol. 213(6), pages 591–600, 1999. ISSN 0954-4062.

JUDS, S. Collision avoidance system for vehicles. 1995.

JULIER, S., UHLMANN, J. and DURRANT-WHYTE, H. A new method for the nonlinear transformation of means and covariances in filters and estimators. *Automatic Control, IEEE Transactions on*, vol. 45(3), pages 477–482, 2000. ISSN 0018-9286.

JURECKI, R., JAŚKIEWICZ, M., GUZEK, M., LOZIA, Z. and ZDANOWICZ, P. Driver's reaction time under emergency braking a car - research in a driving simulator. *Maintenance and Reliability*, vol. 14(4), page 295–301, 2012.

KAEMPCHEN, N. and DIETMAYER, K. Fusion of laserscanner and video for advanced driver assistance systems. In *11th World Congress on Intelligent Transportation Systems (ITS), Japan*, pages 1–5. 2004.

KALLER, J. and HOETZER, D. Lane-change assistant for motor vehicles. 2009.

KALMAN, R. E. A New Approach to Linear Filtering and Prediction Problems. *Transactions of the ASME – Journal of Basic Engineering*, pages 35–45, 1960a.

KALMAN, R. E. A new approach to linear filtering and prediction problems. *Journal of basic Engineering*, vol. 82, pages 35–45, 1960b.

KAMEN, D. Segway personal transporter. 2001.

KANAYAMA, Y. and MIYAKE, N. Trajectory generation for mobile robots. In *Int. Symp. on Robotic Research*. 1985.

KANAYAMA, Y. J. and HARTMAN, B. I. Smooth local-path planning for autonomous vehicles. *Int. J. Rob. Res.*, vol. 16(3), pages 263–284, 1989. ISSN 0278-3649.

KAUER, M., SCHREIBER, M. and BRUDER, R. How to conduct a car? a design example for maneuver based driver-vehicle interaction. In *Intelligent Vehicles Symposium (IV), 2010 IEEE*, pages 1214–1221. 2010.

KIM, T. and JEONG, H.-Y. Crash probability and error rates for head-on collisions based on stochastic analyses. *Intelligent Transportation Systems, IEEE Transactions on*, vol. 11(4), pages 896–904, 2010. ISSN 1524-9050.

KIRK, A., GRANT, R. and BIRD, R. Bus and coach passenger casualties in non-collision incidents. vehicle safety research centre & ice ergonomics. technical report, Loughborough University, UK, 2001.

KORAYEM, M., GHARIBLU, H. and BASU, A. Maximum allowable load of mobile manipulators for two given end points of end effector. *Int. J. Adv. Manuf. Technol*, vol. 24, pages 743–751, 2004.

KORAYEM, V., M. H.AZIMIRAD, NIKOOBIN, A. and BOROUJENI, Z. Maximum load-carrying capacity of autonomous mobile manipulator in an environment with obstacle considering tip over stability. *Int. J. Adv. Manuf. Technol.*, vol. 46, pages 811–829, 2010.

KRAMMES, R. A. and GARNHAM, M. A. Worldwide review of alignment design policies. In *Int. Symp. on Highway Geometric Design Practices*, pages 19:1–17. 1998.

KÜHN, W. *Fundamentals of Road Design*. WIT Press, 2013. ISBN 978-1-84564-097-2.

KULLBACK, S. and LEIBLER, R. A. On information and sufficiency. *Ann. Math. Statist.*, vol. 22(1), pages 79–86, 1951.

LABAKHUA, L., NUNES, U., RODRIGUES, R. and LEITE, F. S. Smooth trajectory planning for fully automated passengers vehicles. spline and clothoid based methods and its simulation. *Springer. Informatics in Control Automation and Robotics*, 2008.

LABUHN, P. I., CHUNDRLIK, J. and WILLIAM, J. Adaptive cruise control. 1995.

LAMIRAUX, F. and LAUMOND, J.-P. Smooth motion planning for car-like vehicles. *IEEE Transactions on Robotics and Automation*, vol. 17, pages 498–502, 2001.

LATOMBE, J. C. *Robot Motion Planning*. Kluwer Academic Press, 1991.

LAU, B., SPRUNK, C. and BURGARD, W. Kinodynamic motion planning for mobile robots using splines. In *Intelligent Robots and Systems, 2009. IROS 2009. IEEE/RSJ International Conference on*, pages 2427 –2433. 2009.

LAUMOND, J.-P., editor. *Robot Motion Planning and Control*. Springer. Lectures Notes in Control and Information Sciences, 1998.

LAUMOND, J.-P., JACOBS, P., TAIX, M. and MURRAY, R. A motion planner for nonholonomic mobile robots. *Robotics and Automation, IEEE Trans. on*, vol. 10(5), pages 577–593, 1994. ISSN 1042-296X.

LAVALLE, S. M. and JAMES J. KUFFNER, J. Randomized kinodynamic planning. *The International Journal of Robotics Research*, vol. 20(5), pages 378–400, 2001.

LEONDES, C., PELLER, J. and STEAR, E. B. Nonlinear smoothing theory. *Systems Science and Cybernetics, IEEE Transactions on*, vol. 6(1), pages 63–71, 1970. ISSN 0536-1567.

LI, W. and TODOROV, E. Iterative linear quadratic regulator design for nonlinear biological movement systems. In *ICINCO*, pages 222–229. 2004.

LI GUIQING, L. X. and HUA, L. 3d discrete clothoid splines. In *Computer Graphics International*, pages 321–324. 2001.

LIU, Y. and LIU, G. Interaction analysis and online tip-over avoidance for a reconfigurable tracked mobile modular manipulator negotiating slopes. *IEEE/ASME Transactions on Mechatronics*, vol. 5(4), pages 623 – 635, 2010.

LUCAS, B. D. and KANADE, T. An iterative image registration technique with an application to stereo vision. In *International Joint Conference on Artificial Intelligence (IJCAI)*, pages 674–679. 1981.

MA, X. and ANDRÉASSON, I. Driver reaction time estimation from the real car following data and its application in gm-type model evaluation. *Transportation Research Record*, 2006.

MACPHAIL, M. G. and KUMHYR, D. B. System and method for automated parking. 2003.

MAGISTER, T., KRULEC, R., BATISTA, M. and BOGDANOVIĆ, L. The driver reaction time measurement experiences. In *Innovative Automotive Technology (IAT'05) conference*. 2005.

MAMORU, S. and TOSHIKI, M. Vehicle stability control system. 2009.

MANZ, M., VON HUNDELSHAUSEN, F. and WUENSCHE, H.-J. A hybrid estimation approach for autonomous dirt road following using multiple clothoid segments. In *IEEE Int. Conf. on Robotics and Automation*, pages 2410–2415. 2010. ISSN 1050-4729.

MARCHIONNA, A. and PERCO, P. A proposal to update the clothoid parameter limiting criteria of the italian standard. In *Int. Società Italiana Infrastrutture Viarie Congress*. 2007.

MARDER-EPPSTEIN, E., BERGER, E., FOOTE, T., GERKEY, B. P. and KONOLIGE, K. The office marathon: Robust navigation in an indoor office environment. In *International Conference on Robotics and Automation*. 2010.

MARS, F., DEROO, M. and HOC, J.-M. Analysis of human-machine cooperation when driving with different degrees of haptic shared control. *IEEE Transactions on Haptics*, vol. 7(3), pages 324–333, 2014.

MAYNE, D., RAWLINGS, J., RAO, C. and SCOKAERT, P. Constrained model predictive control: Stability and optimality. *Automatica*, vol. 36(6), pages 789 – 814, 2000. ISSN 0005-1098.

MCCRAE, J. and SINGH, K. Sketching piecewise clothoid curves. In *Workshop on Sketch-Based Interfaces and Modeling*. 2008.

MEEK, D. and WALTON, D. An arc spline approximation to a clothoid. *Journal of Computational and Applied Mathematics*, vol. 170, pages 59–77, 2004.

MEEK, D. S. and WALTON, D. J. Clothoid spline transition spirals. *Mathematics of computation*, vol. 59(199), pages 117–133, 1992.

MERCEDES-BENZ. Brake assist. 1998.

MIELENZ, K. D. Computation of fresnel integrals. *Journal of Research of the National Institute of Standards and Technology*, vol. 102(3), pages 363–365, 1997.

MIELENZ, K. D. Computation of fresnel integrals ii. *Journal of Research of the National Institute of Standards and Technology*, vol. 105(4), pages 589–590, 2000.

MILANÉS, V., LLORCA, D. F., VILLAGRÁ, J., PÉREZ, J., FERNÁNDEZ, C., PARRA, I., GONZÁLEZ, C. and SOTELO, M. A. Intelligent automatic overtaking system using vision for vehicle detection. *Expert Systems with Applications*, vol. 39(3), pages 3362 – 3373, 2012. ISSN 0957-4174.

MILCH, S. and BEHRENS, M. Pedestrian detection with radar and computer vision. 2001.

MILLER, B. A. and PITTON, D. Vehicle blind spot detector. 1987.

MINGUEZ, J. and MONTANO, L. Nearness diagram (nd) navigation: Collision avoidance in troublesome scenarios. *IEEE Transactions on Robotics and Automation*, vol. 1(20), pages 45–59, 2004.

MINGUEZ, J. and MONTANO, L. Extending collision avoidance methods to consider the vehicle shape, kinematics, and dynamics of a mobile robot. *IEEE Transactions on Robotics*, vol. 25(2), pages 367–381, 2009. ISSN 1552-3098.

MINGUEZ, J., MONTANO, L. and SANTOS-VICTOR, J. Abstracting vehicle shape and kinematic constraints from obstacle avoidance methods. *Autonomous Robots*, vol. 20(1), pages 43–59, 2006. ISSN 0929-5593.

MOHEBBI, R., GRAY, R. and TAN, H. Z. Driver reaction time to tactile and auditory rear-end collision warnings while talking on a cell phone. *Human Factors*, vol. 51(1), pages 102–110, 2009.

MONTEMERLO, M., THRUN, S., KOLLER, D. and WEGBREIT, B. Slam: A factored solution to the simultaneous localization and mapping problem. In *Proc. of the AAAI*. 2002.

MONTEMERLO, M., THRUN, S., KOLLER, D. and WEGBREIT, B. Fastslam 2.0: An improved particle filtering algorithm for simultaneous localization and mapping that probably converges. In *Proc. of the IJCAI*. 2003.

MONTÉS, N., HERRAEZ, A., ARMESTO, L. and TORNERO, J. Real-time clothoid approximation by rational bezier curves. In *IEEE Int. Conf. on Robotics and Automation*. 2008.

MONTÉS, N., MORA, M. and TORNERO, J. Trajectory generation based on rational bezier curves as clothoids. In *IEEE Intelligent Vehicles Symposium*, pages 505–510. 2007. ISSN 1931-0587.

MONTÉS, N. and TORNERO, J. Lane changing using s-series clothoidal approximation and dual-rate based on bezier points to controlling vehicle. In *WSEAS Int. Conf. on Systems Theory and Scientific Computation*, pages 1–6 vol. 17. 2004. ISBN 111-6789-99-3.

MORARI, M. and LEE, J. H. Model predictive control: Past, present and future. *Computers and Chemical Engineering*, vol. 23, pages 667–682, 1997.

MORRELL, J. and WASILEWSKI, K. Design and evaluation of a vibrotactile seat to improve spatial awareness while driving. In *Haptics Symposium, 2010 IEEE*, pages 281–288. 2010.

MULDER, M., ABBINK, D., VAN PAASSEN, M. and MULDER, M. Design of a haptic gas pedal for active car-following support. *Intelligent Transportation Systems, IEEE Transactions on*, vol. 12(1), pages 268–279, 2011. ISSN 1524-9050.

MULDER, M., VAN PAASSEN, M., MULDER, M., PAUWELUSSEN, J. and ABBINK, D. Haptic car-following support with deceleration control. In *IEEE Int. Conference on Systems, Man and Cybernetics*, pages 1686–1691. 2009. ISSN 1062-922X.

MULDER, M., PAUWELUSSEN, J., VAN PAASSEN, M., MULDER, M. and ABBINK, D. Active deceleration support in car following. *Systems, Man and Cybernetics, Part A: Systems and Humans, IEEE Transactions on*, vol. 40(6), pages 1271–1284, 2010. ISSN 1083-4427.

NA, X. and COLE, D. Game-theoretic modeling of the steering interaction between a human driver and a vehicle collision avoidance controller. *Human-Machine Systems, IEEE Transactions on*, vol. 45(1), pages 25–38, 2015. ISSN 2168-2291.

NAGY, B. and KELLY, A. Trajectory generation for car-like robots using cubic curvature polynomials. In *Field and Service Robots*. 2001.

NHTSA'S STATISTICS AND ANALYSIS. School-transportation-related crashes. technical report, National Highway Traffic Safety Administration (U.S. Department of Transportation), 2014.

NHTSA'S STATISTICS AND ANALYSIS. Critical reasons for crashes investigated in the national motor vehicle crash causation survey. technical report, National Highway Traffic Safety Administration (U.S. Department of Transportation), 2015.

DE NIJS, S., MULDER, M. and ABBINK, D. The value of haptic feedback in lane keeping. In *Systems, Man and Cybernetics (SMC), 2014 IEEE International Conference on*, pages 3599–3604. 2014.

NILSSON, R. Evaluation of a combined brake-accelerator pedal. *Accident Analysis and Prevention*, vol. 34(1), pages 175–183, 2002. ISSN 0001-4575.

NISSAN. Lane departure warning system. 2001.

NISSAN. Nissan safety shield technologies. 2013.

OLLERO, A. *Robótica. Manipuladores y robots móviles*. Marcombo, S.A., Barcelona, 1 edition, 2001.

OLLERO, A. and AMIDI, O. Predictive path tracking of mobile robots. application to the cmu navlab. In *International Conference on Advanced Robotics, 'Robots in Unstructured Environments'*, pages 1081–1086 vol.2. 1991.

OLLERO, A. and HEREDIA, G. Stability analysis of mobile robot path tracking. In *Int. Conf. on Intelligent Robots and Systems*, pages 461–466 vol.3. 1995.

PACEJKA, H. B. *Tire and Vehicle Dynamics, 2nd edition*. SAE International, 2005. ISBN 0768017025.

PAPADIMITRIOU, I. and TOMIZUKA, M. Fast lane changing computations using polynomials. In *American Control Conf.*, pages 48–53 vol.1. 2003. ISSN 0743-1619.

PARLANGELI, G., OSTUNI, L., MANCARELLA, L. and INDIVERI, G. A motion planning algorithm for smooth paths of bounded curvature and curvature derivative. In *Mediterranean Conf. on Control and Automation*, pages 73 –78. 2009.

PENDRILL, A.-M. Rollercoaster loop shapes. *Physics Education*, vol. 40(6), pages 517–521, 2005.

PETERMEIJER, S. M., ABBINK, D. A., MULDER, M. and DE WINTER, J. C. F. The effect of haptic support systems on driver performance: A literature survey. *IEEE Transactions on Haptics*, 2015.

PIVTORAIKO, M., KNEPPER, R. A. and KELLY, A. Differentially constrained mobile robot motion planning in state lattices. *Journal of Field Robotics*, vol. 26(CMU-RI-TR-), pages 308–333, 2009.

QIN, S. J. and BADGWELL, T. A. A survey of industrial model predictive control technology. *Control engineering practice*, vol. 11(7), pages 733–764, 2003.

QUIGLEY, M., CONLEY, K., GERKEY, B. P., FAUST, J., FOOTE, T., LEIBS, J., WHEELER, R. and NG, A. Y. Ros: an open-source robot operating system. In *ICRA Workshop on Open Source Software*, vol. 3, page 5. 2009.

RACINE, D., CRAMER, N. and ZADEH, M. Active blind spot crash avoidance system: A haptic solution to blind spot collisions. In *IEEE International Symposium on Haptic Audio-Visual Environments and Games*, pages 1–5. 2010.

RAUCH, H. E., TUNG, F. and STRIEBEL, C. T. Maximum likelihood estimates of linear dynamic systems. 1965.

REEDS, J. and SHEPP, L. Optimal paths for a car that goes both forwards and backwards. *Pacific Journal of Mathematics*, vol. 145(2), pages 367–393, 1990.

RICHARDSON, I. *H.264 and MPEG-4 Video Compression: Video Coding for Next-generation Multimedia*. Wiley, 2004. ISBN 9780470869604.

ROBOTNIK. SUMMIT-xl robot. 2002.

RUSU, R. B. and COUSINS, S. 3D is here: Point Cloud Library (PCL). In *IEEE Int. Conf. on Robotics and Automation*, pages 1–4. 2011.

SAFFARIAN, M., DE WINTER, J. and HAPPEE, R. Enhancing driver car-following performance with a distance and acceleration display. *Human-Machine Systems, IEEE Transactions on*, vol. 43(1), pages 8–16, 2013. ISSN 2168-2291.

SARACOGLU, S. On generalized euler spirals in e3. In *Differential Geometry*. 2012.

SARKKA, S. Unscented rauch–tung–striebel smoother. *Automatic Control, IEEE Transactions on*, vol. 53(3), pages 845–849, 2008. ISSN 0018-9286.

SCHEUER, A. and FRAICHARD, T. Planning continuous-curvature paths for car-like robots. In *IEEE Int. Conf. on Intelligent Robots and Systems*, pages 1304–1311 vol.3. 1996.

SCHEUER, A. and FRAICHARD, T. Collision-free and continuous-curvature path planning for car-like robots. In *IEEE Int. Conf. on Robotics and Automation*, pages 867–873 vol.1. 1997a.

SCHEUER, A. and FRAICHARD, T. Continuous-curvature path planning for car-like vehicles. In *IEEE Int. Conf. on Intelligent Robots and Systems*, pages 997–1003 vol.2. 1997b.

SCHEUER, A. and XIE, M. Continuous-curvature trajectory planning for manoeuvrable non-holonomic robots. In *IEEE-RSJ Int. Conf. on Intelligent Robots and Systems*, vol. 3, pages 1675–1680. 1999.

SCHITTENHELM, H. Advanced brake assist – real world effectiveness of current implementations and next generation enlargements by mercedes-benz. In *23rd International Technical Conference on the Enhanced Safety of Vehicles (ESV)*, 13-0194. 2013.

SCHNEIDER, N. and GAVRILA, D. Pedestrian path prediction with recursive bayesian filters: A comparative study. In *Pattern Recognition*, vol. 8142 of *Lecture Notes in Computer Science*, pages 174–183. Springer Berlin Heidelberg, 2013. ISBN 978-3-642-40601-0.

SCHOT, S. H. Jerk: The time rate of change of acceleration. *American Journal of Physics*, vol. 46, pages 1090–1094, 1978.

SCOTT, J. J. and GRAY, R. A comparison of tactile, visual, and auditory warnings for rear-end collision prevention in simulated driving. *Human Factors*, vol. 50(2), pages 264–275, 2008.

SEGOVIA, A., ROMBAUT, M., PRECIADO, A. and MEIZEL, D. Comparative study of the different methods of path generation for a mobile robot in a free environment. In *International Conference on Advanced Robotics, 'Robots in Unstructured Environments'*, pages 1667–1670 vol.2. 1991.

SEGUÍ, M. Main figures on road safety data: Spain 2013. Dirección General de Tráfico (DGT), 2014.

SEKHAVAT, S., SVESTKA, P., P. LAUMOND, J. and OVERMARS, M. H. Multi-level path planning for nonholonomic robots using semi-holonomic subsystems. *Int. J. Robot. Res*, vol. 17, pages 840–857, 1996.

SHIN, D. H. and SINGH, S. Path generation for robot vehicles using composite clothoid segments. technical report CMU-RI-TR-90-31, Robotics Institute, Pittsburgh, PA, 1990.

SICILIANO, B. and KHATIB, O., editors. S*pringer* H*andbook of* R*obotics*. Springer-Verlag New York Inc., 2008.

SORIN FAIBISH, I., EZRA SHAMAY, K. B. and SHALOM SHTECKELMAN, K. H. Collision avoidance and warning system. 1995.

SOUÈRES, P. and LAUMOND, J. Shortest path synthesis for a car-like robot. *Transactions on Automatic Control*, vol. 41(5), pages 672–688, 1994.

STAHL, P., DONMEZ, B. and JAMIESON, G. Anticipation in driving: The role of experience in the efficacy of pre-event conflict cues. *Human-Machine Systems, IEEE Transactions on*, vol. 44(5), pages 603–613, 2014. ISSN 2168-2291.

STANFORD RACING TEAM. STANFORD UNIVERSITY (USA). Stanley vehicle. 2005.

STRAUGHN, S. M., GRAY, R. and TAN, H. Z. To go or not to go: Stimulus-response compatibility for tactile and auditory pedestrian collision warnings. *IEEE Transactions on Haptics*, vol. 2(2), pages 111–117, 2009.

SUZUKI, S. and ABE, K. Topological structural analysis of digitized binary images by border following. *Computer Vision, Graphics, and Image Processing*, vol. 30(1), pages 32–46, 1985.

TARTAN RACING TEAM. CARNEGIE MELLON UNIVERSITY (USA). Boss vehicle. 2007.

TASSA, Y. iLQG/DDP package. 2011.

THRUN, S., BURGARD, W. and FOX, D. *Probabilistic robotics*. MIT press, 2005.

TODOROV, E. General duality between optimal control and estimation. In *Decision and Control, 2008. CDC 2008. 47th IEEE Conference on*, pages 4286–4292. 2008. ISSN 0191-2216.

TODOROV, E. Finding the most likely trajectories of optimallycontrolled stochastic systems. In *In World Congress of the International Federation of Automatic Control (IFAC*. 2011.

TODOROV, E. and LI, W. A generalized iterative lqg method for locally-optimal feedback control of constrained nonlinear stochastic systems. In *American Control Conference, 2005. Proceedings of the 2005*, pages 300–306. IEEE, 2005.

TOUNSI, M. and LE CORRE, J. Trajectory generation for mobile robots. *Mathematics and Computers in Simulation*, vol. 41(3-4), pages 367 – 376, 1996. ISSN 0378-4754.

TOUSSAINT, M. Robot trajectory optimization using approximate inference. In *International Conference on Machine Learning*, pages 1049–1056. ACM, New York, NY, USA, 2009. ISBN 978-1-60558-516-1.

TOYOTA. Safety technology. 2013.

ULRICH, I. and BORENSTEIN, J. Vfh*: Local obstacle avoidance with look-ahead verification. In *IEEE Int. Conf. Robotics and Automation*, pages 2505–2511. 2001.

VALLS, J., DUMONTEIL, G., BECK, C. and DISSANAYAKE, G. A kyno-dynamic metric to plan stable paths over uneven terrain. In *IEEE/RSJ Int. Conf. on Intelligent Robots and Systems (IROS)*, pages 294–299. 2010. ISSN 2153-0858.

VÁRHELYI, A., HJÄLMDAHL, M., HYDÉN, C. and DRASKÓCZY, M. Effects of an active accelerator pedal on driver behaviour and traffic safety after long-term use in urban areas. *Accident Analysis and Prevention*, vol. 36(1), pages 729–737, 2004.

VASQUEZ GOVEA, D. A. *Incremental Learning for Motion Prediction of Pedestrians and Vehicles*. Theses, Institut National Polytechnique de Grenoble - INPG, 2007.

VILLAGRA, J., MILANÉS, V., PÉREZ, J. and GODOY, J. Smooth path and speed planning for an automated public transport vehicle. *Robotics and Autonomous Systems*, vol. 60(2), pages 252 – 265, 2012. ISSN 0921-8890.

AF WAHLBERG, A. Characteristics of low speed accidents with buses in public transport. *Accident Analysis and Prevention*, vol. 34, pages 637–647, 2002.

AF WAHLBERG, A. Characteristics of low speed accidents with buses in public transport: Part ii. *Accident Analysis and Prevention*, vol. 36, pages 63–71, 2004.

WALLACE, R., STENTZ, A., THORPE, C. E., MORAVEC, H., WHITTAKER, W. and KANADE, T. First results in robot road-following. In *Int. Conf. on Artificial Intelligence*. 1985.

WAN, T. R., TANG, W. and CHEN, H. A real-time 3d motion planning and simulation scheme for nonholonomic systems. In *Simulation Modelling Practice and Theory*. 2011.

WANG, L., MIURA, K., NAKAMAE, E., YAMAMOTO, T. and WANG, T. An approximation approach of the clothoid curve define in the interval $[0, \frac{\pi}{2}]$ and its offset by free-form curves. *Computer Aided Design*, vol. 33, pages 1049–1058, 2001.

WEISS, D. L. *Dynamic Simulation and Analysis of Roller Coasters*. doctoral thesis, University of California, Davis, 1998.

WHO. Global status report on road safety 2015. technical report, World Health Organization, 2015.

WILDE, D. K. Computing clothoid segments for trajectory generation. In *Int. Conference on Robotics and Automation*. 2009.

WILLOW GARAGE. Pr2 robot. 2006.

WINDSHIELD, L. C. and TOYOTA. Night vision. 2002.

CANUDAS DE WIT, C., SICILIANO, B. and BASTIN, G., editors. *Theory of Robot Control*. Springer, 1997.

WU, C., PENG, L., HUANG, Z., ZHONG, M. and CHU, D. A method of vehicle motion prediction and collision risk assessment with a simulated vehicular cyber physical system. *Transportation Research Part C*, vol. 47, pages 179–181, 2014.

WU, S., DECKER, S., CHANG, P., CAMUS, T. and ELEDATH, J. Collision sensing by stereo vision and radar sensor fusion. *Intelligent Transportation Systems, IEEE Transactions on*, vol. 10(4), pages 606–614, 2009. ISSN 1524-9050.

XINYE, W., XIAOHONG, G. and HONGWU, H. Study on vehicle rollover avoidance. In *IEEE Int. Conf. on Measuring Technology and Mechatronics Automation*, pages 681–684. 2010.

YANG, K. and SUKKARIEH, S. Real-time continuous curvature path planning of uavs in cluttered environments. In *Int. Symp. on Mechatronics and its Applications*, pages 1–6. 2008.

YEDIDIA, J. S., FREEMAN, W. T. and WEISS, Y. Understanding belief propagation and its generalizations. *Exploring artificial intelligence in the new millennium*, vol. 8, pages 236–239, 2003.

YONG, J. and ZHOU, X. *Stochastic Controls: Hamiltonian Systems and HJB Equations*. Applications of mathematics. Springer New York, 1999. ISBN 9780387987231.

YUSTE, H., ARMESTO, L. and TORNERO, J. Benchmark tools for evaluating agvs at industrial environments. In *IEEE Int. Conf. on Intelligent Robots and Systems*, pages 2657–2662. 2010.

ZHENG, Z., AHN, S., CHEN, D. and LAVAL, J. The effects of lane-changing on the immediate follower: Anticipation, relaxation, and change in driver characteristics. *Transportation Research Part C*, vol. 26, pages 367–379, 2013.

ZHU, Q., YEH, M.-C., CHENG, K.-T. and AVIDAN, S. Fast human detection using a cascade of histograms of oriented gradients. In *Computer Vision and Pattern Recognition, 2006 IEEE Computer Society Conference on*, vol. 2, pages 1491–1498. 2006. ISSN 1063-6919.

ZIMA, M., ARMESTO, L., GIRBES, V., SALA, A. and SMIDL, V. Extended rauch-tung-striebel controller. In *Decision and Control (CDC), 2013 IEEE 52nd Annual Conference on*, pages 2900–2905. 2013.

Appendix A

Preliminary Study of Spatial Smooth Paths

A spatial curve $\mathcal{C}(s)$ is determined by its curvature $\kappa(s)$ and its torsion $\tau(s)$. Intuitively, a curve can be obtained from a straight line by bending (curvature) and twisting (torsion). The authors of Harary and Tal (2010) characterised 3D clothoids and developed a novel algorithm, which produces continuous curves to join two configurations in the space. The main contribution was the use of a Frenet-Serret frame (do Carmo, 1976; Graustein, 2006), where for given curvature $\kappa(s) > 0$ and torsion $\tau(s)$, according to the fundamental theorem of the local theory of curves (Graustein, 2006), there exists a unique (up to rigid motion) spatial curve, parametrized by the arc-length s, defined by its Frenet-Serret equations as:

$$\begin{aligned} \frac{d\overrightarrow{T}(s)}{ds} &= \kappa(s)\overrightarrow{N}(s), \\ \frac{d\overrightarrow{N}(s)}{ds} &= -\kappa(s)\overrightarrow{T}(s) + \tau(s)\overrightarrow{B}(s), \\ \frac{d\overrightarrow{B}(s)}{ds} &= -\tau(s)\overrightarrow{N}(s), \end{aligned} \tag{A.1}$$

where $\overrightarrow{T}$, $\overrightarrow{N}$ and $\overrightarrow{B}$ are the tangential, normal and binormal unit vectors of an orthonormal basis, respectively.

The curve $\mathcal{C}(s)$ is defined by:

$$\mathcal{C}(s) = \int_0^s \overrightarrow{T}(\upsilon)d\upsilon + \vec{x_0} = \int_0^s \left[\int_0^t \overrightarrow{T}(u)du + \overrightarrow{T_0}\right]dt + \vec{x_0} \tag{A.2}$$

Finally, they characterised the curve from its arc-length, being its curvature and torsion defined as follows:

$$\kappa(s) = \kappa_0 + \sigma_\kappa s, \qquad \tau(s) = \tau_0 + \sigma_\tau s \tag{A.3}$$

It is interesting to mention the geometric characteristics of the 3D clothoid. Since its shape comes from a combination of two inputs, curvature and torsion derivatives, it is difficult to demonstrate the scalability. In other words, given two unitary curvature and torsion derivatives it is not possible resize the unitary 3D clothoid while keeping its shape. In fact, by definition the torsion twists any curve so scalability is not possible, due to infinite possible combinations of these two parameters. Moreover, any point in the curve is related to the previous one. So, even though the proposed trajectory is continuous because it is formed by two continuous and derivable functions, for given arc-length it is not possible to know *a priori*, without a discrete integration, the configuration (position and orientation) of a point along the clothoid. For that reason, a new spatial clothoid must be defined.

A preliminary investigation has been performed related to spatial clothoids and smooth paths. Although it needs further research, a few ideas are sketched out. From the concept of circular helix, a smooth curve in 3-dimensional space with constant curvature and torsion, it is possible to define spatial clothoids as a combination of two planar clothoids. This approach makes it easier to compute 3D clothoids than the one proposed by Harary and Tal (2010), and it allows to know the final configuration (position and orientation) in the three-dimensional path planning task. Furthermore, curvature and torsion profiles of this new trajectory are really close to the ideal ones, and in any case the values of those variables are equal or less than the ones from the actual spatial clothoid.

Following the same ideas as in circular helices, a 3D clothoid can be developed from a combination of two planar clothoids. Using a clothoid to get x,y,ψ coordinates and another clothoid to get z and θ. The following equations define such a trajectory:

$$\begin{aligned} x(t) &= K_\kappa \int_0^{\gamma_\kappa} \cos(\frac{\pi}{2}\xi^2) d\xi, \\ y(t) &= K_\kappa \int_0^{\gamma_\kappa} \sin(\frac{\pi}{2}\xi^2) d\xi, \\ z(t) &= K_\tau \int_0^{\gamma_\tau} \sin(\frac{\pi}{2}\xi^2) d\xi \end{aligned} \tag{A.4}$$

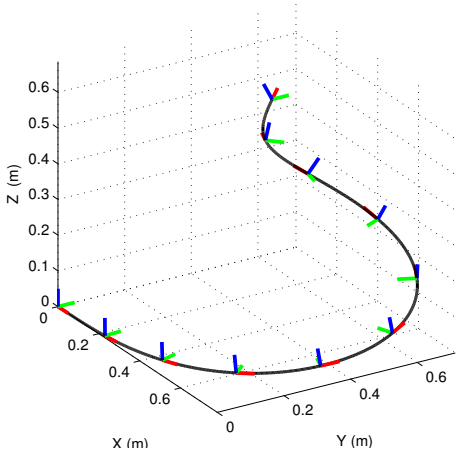

(a) 3D clothoid

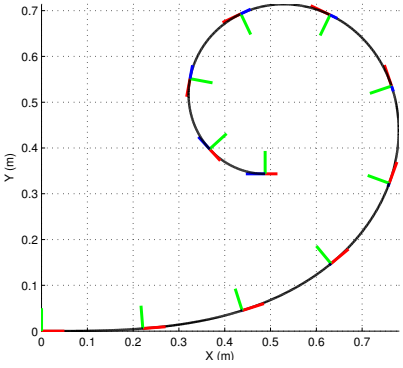

(b) x-y projection

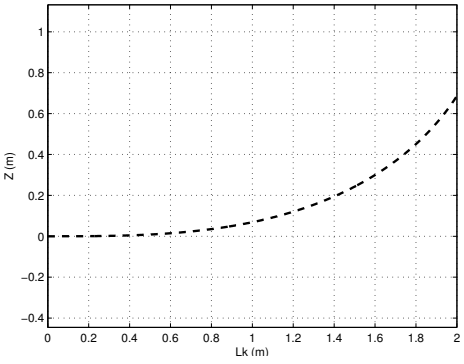

(c) L-z profile

Figure A.1: Spatial clothoid projected and unrolled.

where K_κ is the clothoid homothetic factor of the trajectory projected onto global xy-plane which produces curvature κ, and K_τ is the clothoid homothetic factor of the trajectory projected onto global xz-plane, which induces torsion τ.

Figure A.1 shows an example of the proposed three-dimensional clothoid. It can be observed that when the spatial clothoid is unrolled and projected another clothoid shows up, as shown in Figure A.1(c)). The x-axis is the length s of the first clothoid, the y-axis is the height z of the spatial curve and the length of this clothoid is the overall path length L. Figure A.2 shows, for the spatial clothoid of Figure A.1(a), its Cartesian orientations, curvature and torsion profiles, and sharpness in both curvature and torsion.

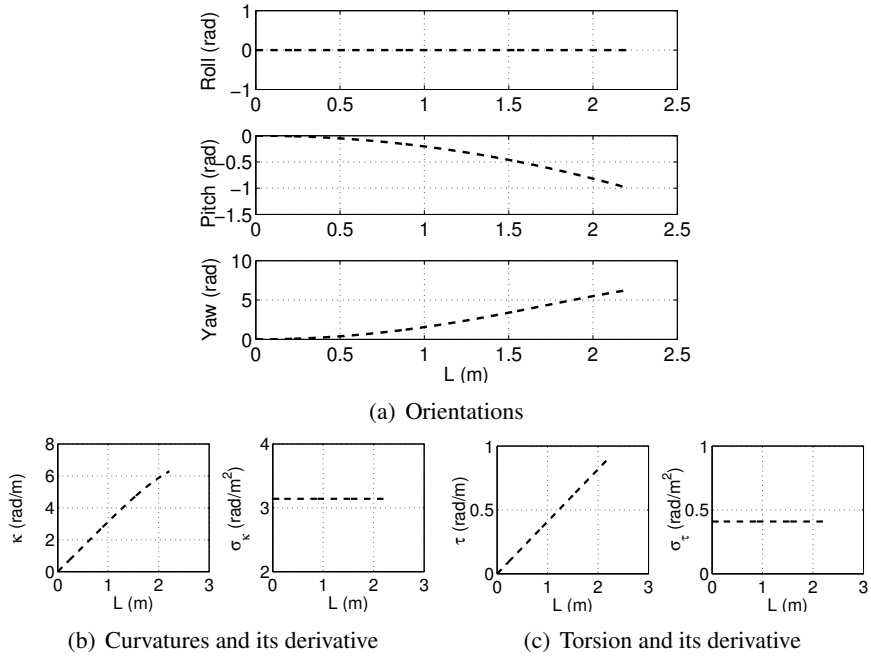

(a) Orientations

(b) Curvatures and its derivative

(c) Torsion and its derivative

Figure A.2: 3D clothoid helix-like with clothoidal slope, orientations, curvature and sharpness profiles.

Applying the same concepts as in planar geometry, once the basic element for creating the path is defined, from two symmetric spatial clothoids a smooth turn can be computed. A smooth turn consists of a concatenation of two symmetric spirals joined at points of maximum curvature and torsion. In the first segment curvature and torsion increase from zero to the value needed to rotate the predefined angles, while the second clothoid segment does just the opposite, reducing the value of both variables to zero. Figure A.3 is an example of generation of such a path, where bounds in sharpness of curvature and torsion were set to $\sigma = 1$ rad/m^2, while desired angles for the final configuration were: $\theta = 0$ rad, $\phi = 0.5$ rad, and $\psi = \pi/2$ rad. Figure A.3(c) and Figure A.3(d) show that none of the sharpness exceed maximum values, while in Figure A.3(b) vehicle's orientation variables converge to desired values.

The only downside of this path is that, although orientation is compensated effectively as explained, the final position cannot be specified, because it is very restricted and is imposed by clothoids sizes, which are function of the sharpness in curvaure and torsion. Furthermore, the intermediate point has nonzero curvature and torsion values, it is not possible to include a straight segment to compensate the offset position, because this way continuity in cur-

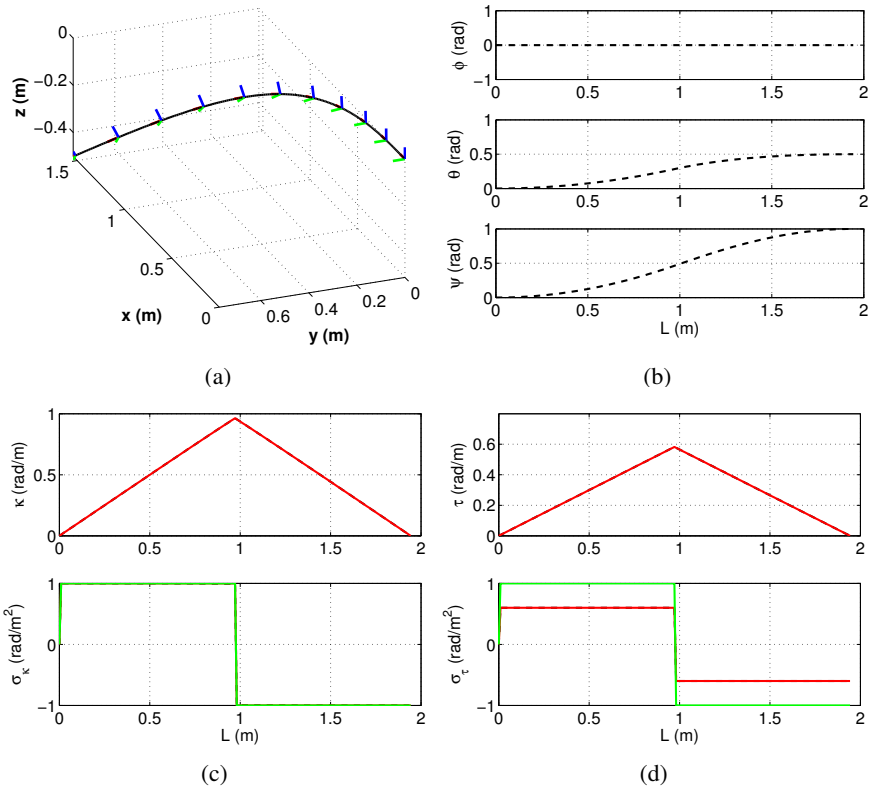

Figure A.3: Example of smooth turn based on spatial clothoids: (a) path, (b) orientations, (c) profiles of curvature κ and its derivative σ_κ, (d) profiles of torsion τ and its derivative σ_τ.

vature would be broken. For this reason there is an evident need to include an extra "smooth turn", as happens with DCC paths in the plane.

Using two 3D smooth turns it is possible to reach any orientation. An example of a spatial path based on three-dimensional clothoids is depicted in Figure A.4, where bounds in sharpness of curvature and torsion were set to $\sigma = 2$ rad/m^2, desired angles were $\theta = 0$ rad, $\phi = 0.5$ rad, and $\psi = 2$ rad, while final configuration's position was $x = 4$ m, $y = 2$ m, $z = 1$ m. As can be seen in Figure A.4, the path converges to the desired configuration while the overall path length is minimized. The variable used in the optimization is the intermediate orientation (ϕ and ψ angles, since θ is always zero), since it is the only free parameter. As in the case of planar DCC paths, once intermediate orientation is obtained the lengths of the 3 segments are obtained by solving a system of three linear equations with three unknowns.

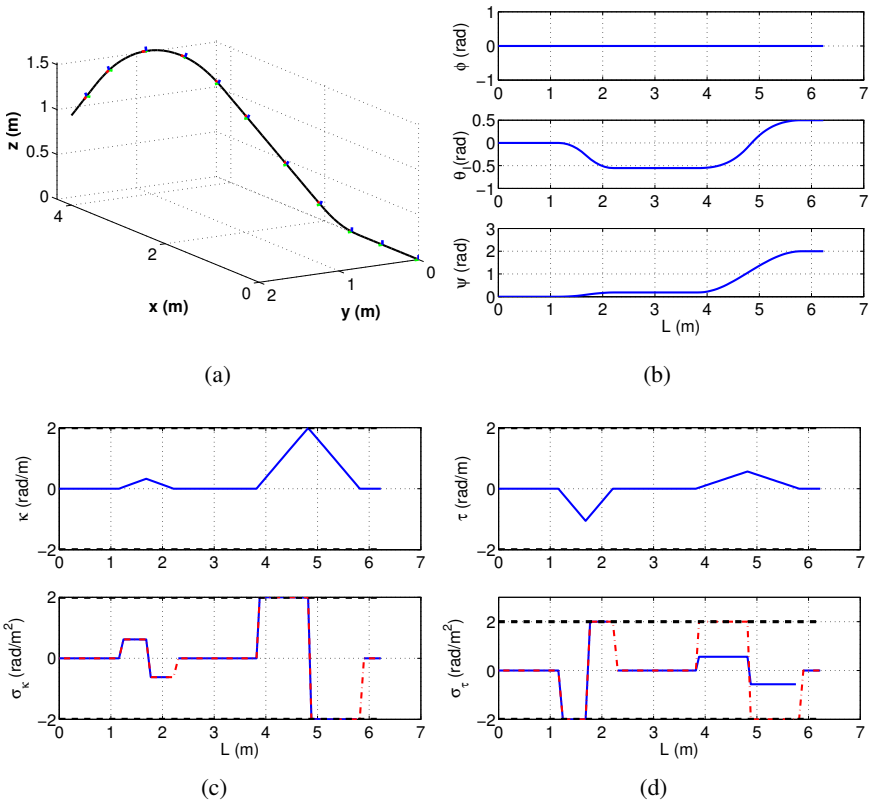

Figure A.4: Example of smooth path based on spatial clothoids: (a) path, (b) orientations, (c) profiles of curvature κ and its derivative σ_κ, (d) profiles of torsion τ and its derivative σ_τ.